

Deep UV Initiated Excited State Dynamics of Flavins

A Thesis

Submitted in partial fulfillment of the requirements for

the degree of

Doctor of Philosophy

by

Sudeb Ghosh

20113125



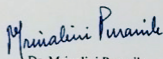
Indian Institute of Science Education and Research

Pune - 411 008

Certificate

Certified that the work incorporated in the thesis entitled "*Deep UV Initiated Excited State Dynamics of Flavins*" submitted by Sudeb Ghosh was carried out by the candidate under my supervision. The work presented here or any part of it has not been included in any other thesis submitted previously for the award of any degree or diploma from any other university or institution.

Date 31st October, 2017



Dr. Mrinalini Puranik

Thesis Supervisor

e-mail: puranik.mrinalini@gmail.com

Address: Indian Institute of Science Education and Research
Pune, Maharashtra.

Current address: Unilever Research and Development Centre,
64 Whitefield Road, Bangalore - 560066

Declaration

I declare that this thesis is a presentation of my original research work. Wherever contributions of others are involved, every effort is made to indicate this clearly, with due reference to the literature, and acknowledgment of collaborative research and discussions. I also declare that I have adhered to all principles of academic honesty and integrity and have not misrepresented or fabricated or falsified any idea/data/fact/source in my submission. I understand that violation of the above will be cause for disciplinary action by the Institute and can also evoke penal action from the sources which have thus not been properly cited or from whom proper permission has not been taken when needed.

Sudeb Ghosh

Sudeb Ghosh

Date: 31/10/2017

ID - 20113125

To,

Maa and Baba

Acknowledgements

I would like to express my sincere gratitude to my supervisor Dr. Mrinalini Puranik for giving me an opportunity to work in her lab, for her valuable guidance during my Ph.D. and for making this all possible. I also want to thank her for encouraging me to do hard work and helping me to grow as an independent researcher. I would like to thank to my RAC members Dr. Pankaj Mondal and Dr. Jeetender Chugh for useful discussions and suggestions to my research projects. I am immensely grateful to Prof. K N Ganesh for taking care of me as an institute supervisor during the last year of my Ph.D.

The work which has been included in this thesis would not have been completed without the help of my labmates. So, I am incredibly grateful to all my labmates including Sayan, Yashwant, Anil, Shahila, Sidhhartha, Vishakha, Kalyan and Erix. I express my gratitude to Sayan who has not only introduced me to the laser instruments but also taught me how to troubleshoot and analyze my research problems. I am also grateful to him for giving me valuable suggestions to improve my manuscripts and for his constant support during my Ph.D. Thanks to Yashwant, Anil and Shahila for helping me during my experiments and correcting my manuscripts. I want to thank to all of them for making the friendly environment and keeping the lab lively. It was a great pleasure to working with all of them.

I want to thank to all of my friends inside and outside of IISER Pune. Among them, I want to especially thank to Avishek, Reja, Sunil, Anupam, Abhik, Arindam, Supratik, Chandramouli, Barun and Partho with whom I have spent most of my spare times playing football, discussing many things, making foods and doing parties. I will never forget our Saturday parties and travel to different places. I have enjoyed playing football with Amit, Arindam, Reja, Soumen, Maidul, Avishek, Arunavo, Supratik, Shyama and others. I am going to miss all of them. Thanks to Manoj, Mriganka, Ambar, Mala and Kalam for their constant support during all these years.

I would like to thank to all staffs of academic, non-academic and technical departments at IISER Pune for their support. I want to thank to Chair Chemistry, Prof. M Jayakannan, for his support in my difficult times.

Finally, I want to thank my parents and my brother for their unconditional support and keeping patience during all these years. Without their constant support and love, it would not have been possible to reach the end of this road.

Sudeb Ghosh

Abstract

Flavins are redox-active chromophores in blue light activated enzymes and hence play crucial roles in several photobiological processes. Photophysics of flavin compounds has been the subject of intense research due to the involvement of its electronic excited states in those photochemical and photobiological processes. In majority of the published literature, the excited states corresponding to absorption at 450 and 375 nm of flavins have been investigated to deduce the underlying molecular mechanism of these photoinduced processes. However, the photodynamics in the excited state associated with 266 nm absorption band has not been investigated. These highly absorbing singlet excited states are important because solar flux contains a considerable amount of UV light along with low energetic visible photons. Through a comprehensive resonance Raman experiments, theoretical calculations and classical wave-packet dynamics simulations, we have determined the sub-100 femtosecond structural dynamics of flavins upon photoexcitation to their 266 nm excited state. We have also determined the mode-specific reorganization energies along each observed vibrational modes. Our simulation method can partition the total spectral broadening into homogeneous and inhomogeneous broadening components contributing to both absorption and Raman line shapes. We find upon excitation, the first solvation shell inertially responds with an ultrafast timescale of ~ 30 fs for all of the flavins. Initial excited state parameters obtained from our simulation will impact studies on flavin containing proteins that utilize flavin as a probe of protein dynamics.

Contents

Table of Contents	
Contents	1
Acronyms and Abbreviations	5
Synopsis	7
Chapter 1: Introduction	11
1.1 Flavins.....	11
1.2 History of flavins and flavoenzymes	11
1.3 Structures of flavins	12
1.4 Properties of flavins	12
1.5 Flavins in biology	13
1.5.1 DNA photolyase.....	14
1.5.2 Cryptochromes	15
1.5.3 The BLUF domain	15
1.5.4 Phototropins	15
1.6 Absorption and emission properties of flavins and alloxazines	15
1.7 Ultrafast excited state photophysics of flavins and motivation of this work	18
1.8 Goals of this project	21
1.9 Measuring the photophysics in the UV region of absorption.....	22
1.10 Organization of the thesis	23
References.....	24
Chapter 2: Experimental and Theoretical Methods	29
2.1 Theoretical methods.....	32
2.1.1 Quantum mechanical description of the resonance Raman intensity.....	32
2.1.2 Time-dependent wave packet propagation (TDWP) theory	34
2.1.3 Contribution of homogeneous and inhomogeneous broadenings to the total spectral linewidth	38
2.1.4 Model for solute-solvent bath interaction	41
2.1.5 Total reorganization energy	43
2.1.6 Conversion from normal mode to internal coordinates.....	43
2.2 Experimental Methods	44

2.2.1 Experimental set-up for UVRR experiments	44
2.2.2 Depolarization ratio measurement	45
2.2.3 Spectrometer and detector efficiency	47
2.2.4 Self-absorption correction.....	48
2.2.5 UVRR cross section determination.....	49
2.2.6 Total differential Raman cross-section of the internal standard	49
2.2.7 Experimental absorption cross-section	50
2.3 Quantum chemical calculations	50
References.....	51
Chapter 3: Initial Excited State Structural Dynamics of Lumiflavin upon Ultraviolet Excitation.....	56
3.1 Introduction.....	56
3.2 Experimental and Theoretical Methods	59
3.2.1 Sample Preparation	59
3.2.2 UVRR Spectroscopy	59
3.2.3 UVRR Cross-section Determination.....	59
3.2.4 Computational Method - Simulation of Experimental REP and Absorption Spectrum.....	60
3.2.5 Deconvolution of Absorption Spectrum	61
3.2.6 DFT Calculations	61
3.3 Results and Discussion	62
3.3.1 Electronic structure	62
3.3.2 UVRR Spectra and Experimental Raman excitation profile.....	65
3.3.3 Simulation of Absorption and Experimental REPs.....	70
3.4 Conclusion	79
References.....	80
Chapter 4: Deep UV Initiated Excited State Dynamics of Riboflavin (RF) and Flavin mononucleotide (FMN).....	83
4.1 Introduction.....	83
4.2 Experimental and Computational Methods.....	87
4.2.1 Sample Preparation	87
4.2.2 UVRR Spectroscopy	87
4.2.3 UVRR Cross-section Determination.....	87
4.2.4 Computational Method - Simulation of Experimental REP and Absorption Spectrum.....	89

4.2.5 Deconvolution of the Absorption Spectrum	89
4.2.6 Quantum Chemical Computations	89
4.3 Results and Discussion	90
4.3.1 Electronic structure	90
4.3.2 UVRR Spectra and Experimental Raman excitation profile.....	93
4.3.3 Simulation of Absorption and Experimental REPs.....	97
4.4 Conclusion	106
References.....	107
Chapter 5: Is the photophysics of Flavin and adenine rings of FAD coupled?.....	110
5.1 Introduction.....	110
5.2. Experimental and Computational Methods.....	113
5.2.1 Sample Preparation	113
5.2.2 UVRR Spectroscopy	113
5.2.3 UVRR Cross-section Determination.....	114
5.2.4 Computational Method - Simulation of Experimental REP and Absorption Spectrum.....	115
5.2.5 Quantum Chemical Computations	115
5.3 Results and Discussion	116
5.3.1 Electronic Structure	116
5.3.2 UVRR Spectra of FAD and Adenine	119
5.3.3 Simulation of Absorption and Experimental REPs.....	125
5.3.4 Structural Dynamics upon Photoexcitation.....	128
5.3.5 Linewidth Broadening.....	130
5.4 Caveats and Future prospects.....	131
5.5 Conclusion	132
Figure and Tables of Wave-packet Dynamics Simulations of AMP	133
References.....	135
Chapter 6: Initial Excited state dynamics of Lumichrome (LC) upon Ultraviolet Excitation	138
6.1 Introduction.....	138
6.2 Experimental Methods	140
6.2.1 Sample Preparation	140
6.2.2 UVRR Spectroscopy	141
6.2.3 UVRR Cross-section Determination.....	141

6.2.4 Computational Method - Simulation of Experimental REP and Absorption Spectrum.....	142
6.2.5 DFT Calculations	142
6.3 Results and Discussion	144
6.3.1 Electronic Structure	144
6.3.2 UVRR Spectra	146
6.3.3 Simulation of Absorption and Experimental REPs.....	150
6.4 Conclusion	157
References.....	158
7 : Conclusion and Future Perspective	161
7.1 Conclusion	161
7.2 Future perspective	164

Acronyms and Abbreviations

LF: Lumiflavin

RF: Riboflavin

FMN: Flavin mononucleotide

FAD: Flavin adenine dinucleotide

LC: Lumichrome

AMP: Adenosine-5'-monophosphate

GMP: Guanosine-5'-monophosphate

B3LYP: Becke, three-parameter, Lee-Yang-Parr

BBO: Barium borate

Str: bond stretching vibration involving two atoms

Be: bending vibration involving three atoms

CCD: Charge Couple Device

DFT: Density Functional Theory

FTIR: Fourier-Transform Infrared

fs: femtosecond

ns: nanosecond

ps: picosecond

FSRS: femtosecond stimulated Raman spectroscopy

FWHM: full width at half maxima or bandwidth

GS: ground state

D: Deuterium atom

HF: Hartree-Fock

HOMO: highest occupied molecular orbital

LUMO: lowest unoccupied molecular orbital

LBO: lithium borate

Nd-YLF: Neodymium-doped yttrium lithium fluoride

PED: Potential Energy Distribution

PES: Potential energy surface

QM: Quantum Mechanical

QC: Quantum Chemical

ref: reference

TD-DFT: Time-dependent density functional theory

Ti-Sapph: Titanium-doped sapphire crystal ($\text{Ti}^{3+}:\text{Al}_2\text{O}_3$)

UVRR: Ultraviolet resonance Raman spectroscopy

UV/Vis: Ultraviolet-visible

Synopsis

Introduction

Flavins belong to a broad class of bioactive cofactors found in several redox enzymes and photoreceptors. In blue-light photoreceptors, absorption of blue-light by the flavin chromophore initiates the signaling processes detected in plants and other organisms. These processes include light-induced DNA-repair, regulation of circadian rhythm and control of the photosynthetic movement of plants and microorganisms. Flavin adenine dinucleotide (FAD) and flavin mononucleotide (FMN) are found to be the key redox cofactors in photoreceptor enzymes. Riboflavin (RF) is the component of vitamin B2 complex, and is the precursor of biologically important cofactors, FAD and FMN. Furthermore, RF is an essential component in our everyday diet and it acts as an effective photosensitizer in various foods and beverages. Another compound of flavin family is Lumiflavin which is the main photoproduct formed by the UV-Vis photolysis of other three flavins. All of the flavins have the same chromophoric ring known as isoalloxazine ring which has electron transfer capability. In addition to that RF and FMN contain a ribityl side chain that also plays important biological roles. FAD constitutes an adenine moiety together with a ribityl chain.

Due to the involvement of excited states of flavin cofactors in several blue light activated processes, the excited state photophysics of flavin molecules have become the topic of intense research over the decades. Photophysics of flavins in its oxidized and reduced forms has been extensively studied following photoexcitation to their long wavelength absorption bands at around 450 and 375 nm. Time-resolved spectroscopic techniques having time resolution from femtoseconds (fs) to nanoseconds (ns) have been applied to examine excited state properties of flavins in solution and inside the protein core in the lowest energy singlet (S_1) excited state at ~ 445 nm. All of the flavins show excited state lifetime of several ns in the S_1 state, except FAD which decays in a faster picosecond (ps) timescale. Time-resolved vibrational spectroscopies, such as femtosecond mid-IR and stimulated Raman spectroscopy (FSRS) in conjunction with quantum chemical calculations are also routinely applied to deduce the structural changes in flavins following photoexcitation to the S_1 excited state.

Apart from the S1 state (~ 445 nm), flavins have strong $\pi\pi^*$ transitions in the ultraviolet (UV) region of the absorption spectrum. A number of reports investigating photophysics of these heavily absorbing electronic states are limited. As we know that the harmful UV radiations are always reaching the earth surface, it is important to determine the effect of these radiations on the highly absorbing singlet excited states of flavins. One of the methodologies to study excited state structural dynamics of a photoexcited chromophore is through analysis of experimental resonance Raman (RR) excitation profiles. RR intensities of a chromophore are sensitive to structural changes that happen within 100 fs of photon absorption and interaction with the local environment. Modeling of Raman excitation profiles (REP) using the time-dependent formulation of RR intensities has been applied to extract ultrafast structural dynamics of several natural and modified nucleobases.

I have employed RR intensity analysis to extract the excited state structural dynamics of lumiflavin (LF), riboflavin (RF), flavin mononucleotide (FMN), flavin adenine dinucleotide (FAD) and lumichrome (LC) following photoexcitation to their excited state centered at around 266 nm. The structural distortions were determined in terms of changes in internal coordinates of the electronic ground state and were compared. Total internal reorganization energies measured was distributed into each specific Raman active modes. Additionally, through modeling of solute-solvent interaction within the Brownian oscillator spectral density model, the time scale and amplitude of the inertial component of solvation were also extracted for all the flavin compounds and were compared with those reported dynamics of different molecules.

Key findings

Chapter 3: Initial Excited State Structural Dynamics of Lumiflavin upon Ultraviolet Excitation

A quantitative measurement of the resonance Raman cross-section across the 264 nm absorption band (257-275 nm) of LF is performed, and REPs of all RR active modes are constructed. I have simulated the REPs and absorption cross-section using time dependent wave packet propagation (TDWP) formalism to extract initial excited state dynamics of LF within 50 fs after photoexcitation. We find that structural changes happen all along the isoalloxazine ring modes following photoexcitation to the 264 nm excited state. The amount of distortions of the excited

state structure from that of the ground state is reflected in total internal reorganization energy that is determined at 469 cm^{-1} . By comparing the excited state structural changes between S1 state and 264 nm excited state, we found that different molecular distortions occur following photoexcitation to those two different states. The contribution of inertial component of solvent response towards the total reorganization energy was obtained at 1070 cm^{-1} . Additionally, our simulation also yields an instantaneous response of the first solvation shell within an ultrafast timescale, $\tau \sim 30\text{ fs}$, following photoexcitation. It is worthy to note here that, though theoretically predicted, the inertial component of solvation that occurs within few tens of fs has been detected in very few experimental reports.

Chapter 4: Deep UV Initiated Excited State Dynamics of Riboflavin (RF) and Flavin mononucleotide (FMN)

Excited state structural dynamics of RF and FMN were studied using RR intensity analysis following photoexcitation to their 266 nm excited state. Here also we find that structural changes happen along all over the isoalloxazine ring with a contraction in most of the isoalloxazine ring coordinates. Similar to LF, it has been found for RF and FMN that the Raman band at 1583 cm^{-1} contributes maximum to the total internal reorganization energy. Deduced structural changes of the isoalloxazine ring of RF are compared with those obtained for LF and we find that excitation to similar excited states, these two flavins show different molecular distortions. We have also measured an ultrafast inertial water response timescale at $\sim 30\text{ fs}$ for both the molecules. Despite the addition of ribityl chain in RF and FMN, the homogeneous and inhomogeneous broadening values obtained for these two molecules are observed to be in the same order as that obtained for LF.

Chapter 5: Is the photophysics of Flavin and adenine rings of FAD coupled?

Contributions of both flavin and adenine rings were observed in the UVRR spectra of FAD, because both can absorb UV radiations. We have observed significant Raman hypochromism in FAD, consistent with stacking interaction between flavin and adenine rings. It was found that excited state structural dynamics of FAD lie along both flavin and adenine ring coordinates. Here, we found a little higher solvent reorganization energy for FAD as compared to RF and FMN and it suggests that existence of AMP moiety in FAD structure leads to a stronger dipole

interaction with the surrounding water molecules than photoexcited RF and FMN. Similar to other three flavins, we also determined for FAD that upon excitation the first solvation shell inertially responds with an ultrafast timescale of around ~ 30 fs.

Chapter 6: Initial Excited state dynamics of Lumichrome (LC) upon Ultraviolet Excitation

Initial excited state structural dynamics of LC was determined following photoexcitation within the absorption band centered at around 260 nm. Upon photoexcitation, it has been found that major structural distortions happen in ring II and ring III of the alloxazine structure. The structural changes obtained for LC are completely different than that determined for flavins. We found a lower homogeneous broadening linewidth for alloxazine structure in comparison to the isoalloxazine structures, whereas the inhomogeneous broadening values obtained are comparable. The fastest response of dynamic water solvation was detected within 23.1 fs timescale due to the inertial response of water.

Chapter 1: Introduction

1.1 Flavins

Flavin chemistry has drawn much scientific attention over the past decades due to the discovery of a large number of flavoenzymes, which play significant roles in many important biological processes.^{1,2} The yellow coloured compounds with the basic structure of 7,8-dimethylisoalloxazine, or to be precise 7,8-dimethylbenzo[g]pteridine-2,4(3H,10H)-dione, (Fig. 1.1(a)) are ubiquitously recognized as Flavins. Flavins act as a cofactor in flavoenzymes and involves in various biochemical reactions in the context of redox reactions.³ The structurally very similar alloxazine derivatives are not generally regarded as flavins (see Fig 1.1(b)).⁴

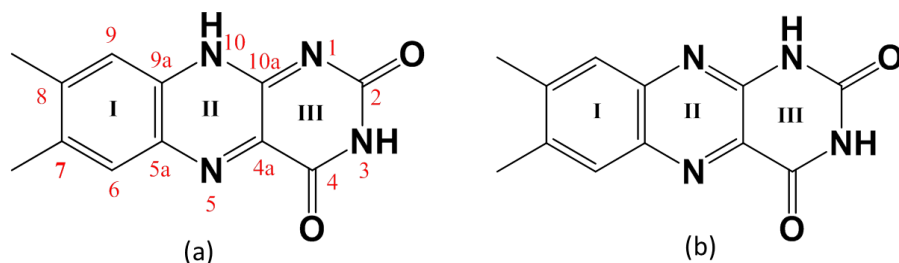


Fig. 1.1 Structures of (a) 7,8-dimethylisoalloxazine with conventional atom numbering and (b) 7,8-dimethylalloxazine (lumichrome). The rings are also numbered with Roman numbers.

1.2 History of flavins and flavoenzymes

It was about a century ago, when an English chemist by the name of A. Wynter Blyth isolated a bright yellow pigment in cow's milk and he named it as lactochrome.^{3,5} Then, in the late 1920s and early 1930s, the yellow pigment with a bright greenish fluorescence was isolated from a large variety of sources.³ Much interest on these pigments was evolved when they were identified to be a constituent of the vitamin B complex. In the subsequent years, the two foremost chemists, Richard Kuhn in Heidelberg and Paul Karrer in Zurich determined the structure of the pigment and also proved it by chemical synthesis.^{3,6,7} They named the yellow pigment as riboflavin (RF) in replace of other previous names such as lactoflavin and ovoflavin. After the discovery of flavin structure, Hugo Theorell, a Swedish biochemist discovered the catalytic activity of flavin as a cofactor in enzymes while working on the catalytic oxidation of NADPH by yeast using oxygen as a substrate.⁸ Ever since, the finding of Hugo Theorell's work, which

established the role of flavin as a cofactor in enzyme catalysis, stimulated to the discovery and characterization of more than a hundred of flavoenzymes.

1.3 Structures of flavins

The three biologically important flavin molecules are riboflavin (RF), flavin adenine dinucleotide (FAD) and flavin mononucleotide (FMN). In flavoproteins, flavins are found in the form of FAD and FMN.⁵ The structures of different flavin compounds are shown in Fig. 1.2. Flavin compounds are different by the respective substituents at the N10 position of the isoalloxazine ring structure. RF, FMN and FAD have substituents such as a ribityl chain, a ribityl chain plus phosphate group and a ribityl chain plus phosphate group plus adenine 5'-monophosphate nucleotide respectively. Other derivatives of flavin, lumiflavin (LF) and lumichrome (LC) are the photoproducts formed by the photodegradation of RF, FMN and FAD.

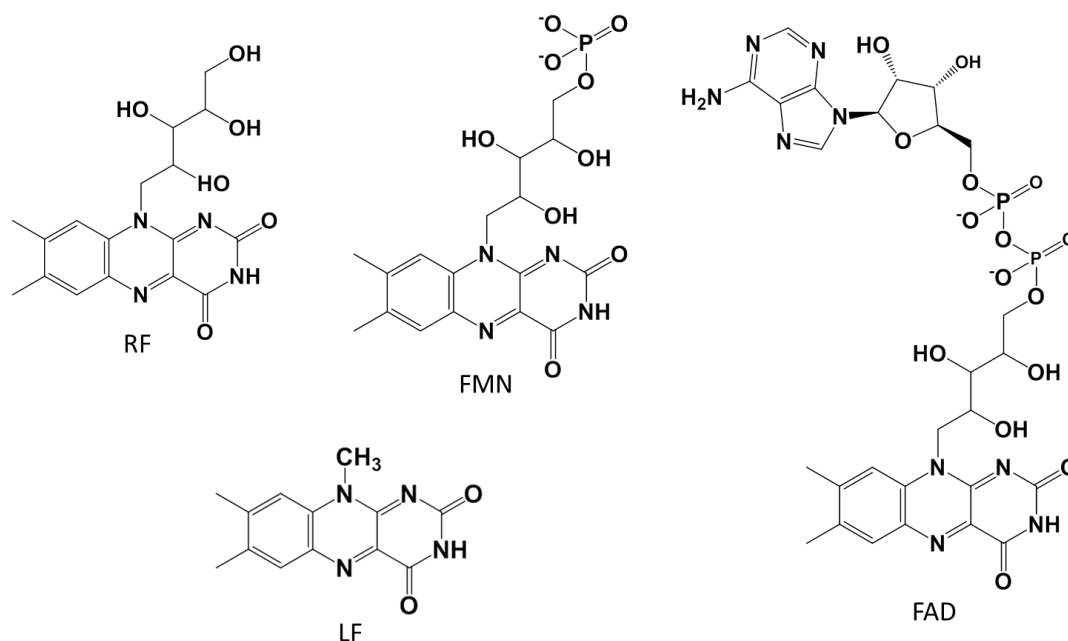


Fig. 1.2 Chemical structures of riboflavin (RF), flavin mononucleotide (FMN), flavin adenine dinucleotide (FAD) and lumiflavin (LF).

1.4 Properties of flavins

Flavins have the unique ability to accept or donate one or two electrons due to their versatile redox active properties.⁴ They can exist in three different redox states; oxidized, radical semiquinone (by one electron reduction) and fully reduced hydroquinone (by two electron

reduction). Each redox state can undergo in different protonation forms depending upon the change in pH of the solution (shown in Fig. 1.3).⁹ The radical semiquinone form is not stable in solution because two semiquinones can undergo disproportionation to form one oxidized and one fully reduced flavin.¹⁰ Semiquinone forms can be stabilized inside the protein core and micelles¹¹⁻¹³ and also by chemical modification.¹⁴

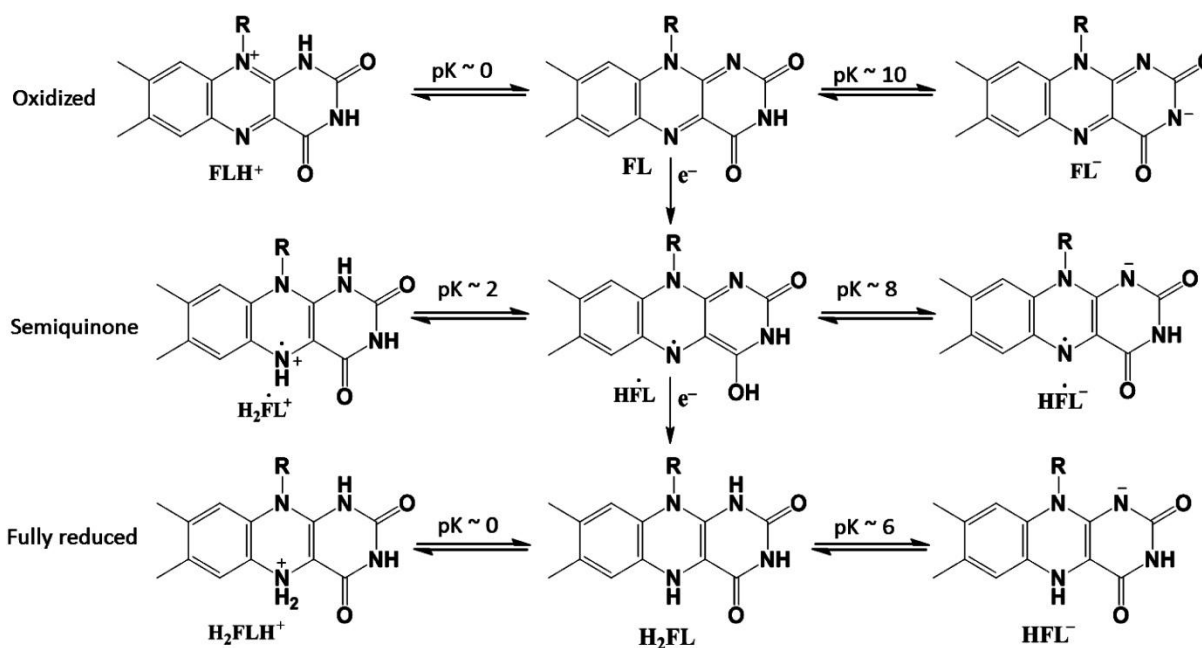


Fig. 1.3 Redox and acid-base equilibria of flavins.

1.5 Flavins in biology

The main photoactive chromophores in living organisms which use blue light to carry out biological activities are carotenoids, billins, chlorophylls, flavins and pterins. Among them flavins have become the important cofactors in biology in the last few decades due to the discovery of a large number of flavoenzymes. Flavoenzymes participate in a wide range of chemical reactions as a catalyst in the presence or absence of light.¹⁵ FAD and FMN are found to be the key redox active cofactors in these enzymes and functions as an intermediary in either one or two electron transfer processes. Most of the flavoenzymes discovered are light independent,^{3,16,17} and a few of them are photoactive.^{2,18}

It has been established that sensing the blue light is crucial for a diverse range of organisms. For example plants, algae and photosynthetic microorganisms all depend on blue

light to control growth, development and optimization for photosynthesis, whereas organisms like drosophila and mice use blue light in mediating circadian rhythms.¹⁹ Flavin containing photoreceptors are found to involve in these light activated processes. Until today, four different kinds of blue-light sensing flavoprotein families are identified, namely, DNA photolyase, cryptochromes, blue-light-using FAD (BLUF) family and phototropins.^{18,20,21} Here we have discussed some of the functions of photoactive flavoenzymes and the role of flavins as a cofactor in those photoreceptors.

1.5.1 DNA photolyase

The most popular light-driven flavoenzyme is the DNA photolyase which uses blue or near UV light of 360 to 500 nm as the energy source to repair the cyclobutane pyrimidine dimer (CPD) lesions in DNA.^{18,22-24} These repair enzymes are abundant in plants, microorganisms and some higher organisms like wood frogs and Australian Kangaroos.²³ Humans and other mammals lack of this enzyme. All of the photolyases identified contain a noncovalently bound cofactor FAD in the active site and a noncovalently bound second cofactor methenyltetrahydrofolate (MTHF). In the active site, the catalytic cofactor, FAD exists in the fully reduced form (FADH⁻) which carries out the repair process upon excitation by resonance energy transfer from MTHF which

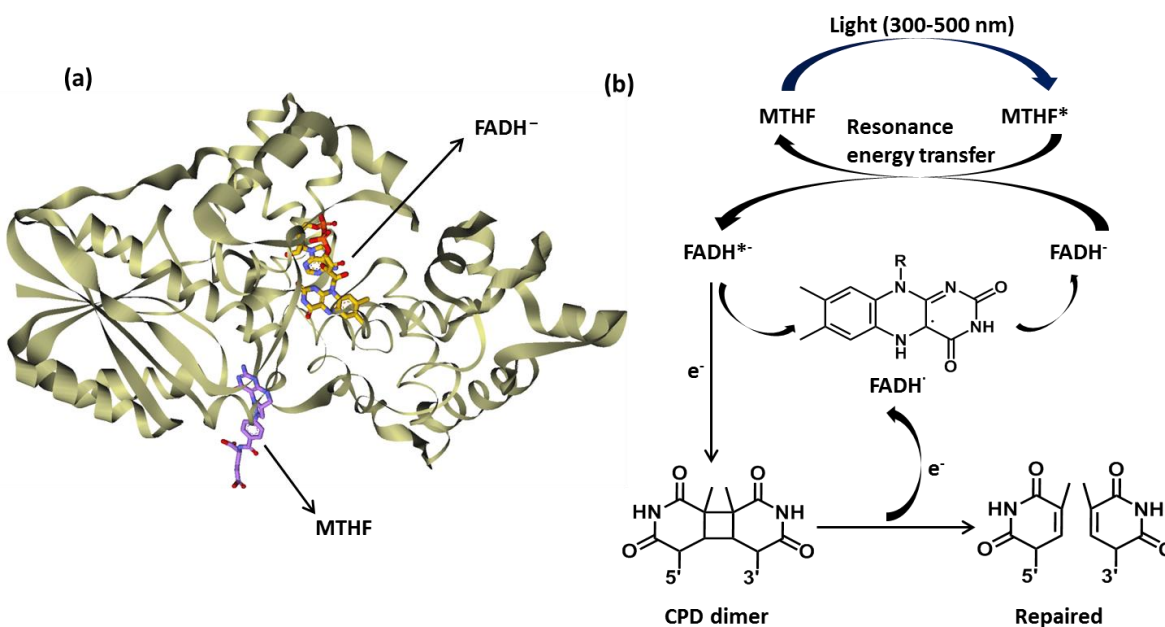


Fig. 1.4 (a) Crystal structure of *E. coli* photolyase containing the cofactors, (b) DNA-repair mechanism by photolyase adapted from A. Sancar. (ref. 18)

acts as a light harvesting cofactor.²⁵ The repair mechanism (Fig. 1.4 (b)) starts with the binding of photolyase enzyme to the damage site of DNA in dark state.^{26–28} Then FADH⁻ anion upon photoexcitation transfers an electron to the CPD lesion to split the cyclobutane ring.^{18,29,30} The radical anion formed in this process then transfers back one electron to the radical semiquinone FADH⁻ cofactor to complete the cycle.²⁷

1.5.2 Cryptochromes

The second one in the light-driven flavoenzyme family is cryptochromes, which are structurally very similar to photolyases and they have same cofactors, FAD and MTHF noncovalently bound to the enzyme.^{18,31} Cryptochromes are discovered to function as photoreceptors in plants, animals and also in humans.^{31,32} They regulate the circadian rhythm in animals, growth and development in plants supposedly by photoinduced electron transfer.^{18,31–34}

1.5.3 The BLUF domain

Another class of FAD containing light activated flavoenzyme is the BLUF domain family detected in microorganisms such as cyanobacteria and flagellate algae.³⁵ These proteins absorb blue light to trigger the photosynthetic movement of microorganisms in order to locate the minimum light conditions for photosynthesis.^{35,36} The conformational change in the protein active site influenced by coupled proton and electron transfer between FAD and protein residues initiates the photomovement.³⁷

1.5.4 Phototropins

Phototropins are the fourth kind of photoreceptors in the class of light triggered flavoenzymes which use FMN as its light sensitive chromophore.^{38,39} They are found in plants and involves in mediating phototropism, chloroplast relocation, rapid inhibition of stem growth and stomata opening.³⁸ The phototropins consist of two domains known as LOV1 and LOV2, each binding FMN as a chromophore.³⁹ The LOV photochemistry that regulates kinase activation and signal transduction is based on the formation of a covalent adduct between the flavin atom and conserved cysteine upon blue light illumination.^{38,40}

1.6 Absorption and emission properties of flavins and alloxazines

The photophysical and photochemical properties of flavins are mainly dominated by the isoalloxazine core ring. All of the flavins show similar experimental absorption and emission characteristics. The absorption spectra of flavins in aqueous solution (Fig. 1.5) extended in visible and ultraviolet (UV) regions of spectrum show four structureless absorption bands centered at around 446, 375, 266 and 222 nm. The absorption band of flavins at 222 nm is blueshifted to 213 nm for FAD may be due to the presence of adenine nucleotide. All four absorption bands exhibit high molar extinction coefficients⁴¹ which indicate of $\pi\pi^*$ type transitions. Various quantum chemical calculations using CASPT2,⁴² DFT/MRCI,^{43,44} SAC-CI⁴⁵ and TDDFT^{44,46-54} methods precisely assign the two long wavelength absorption bands to $\pi\pi^*$ transitions.

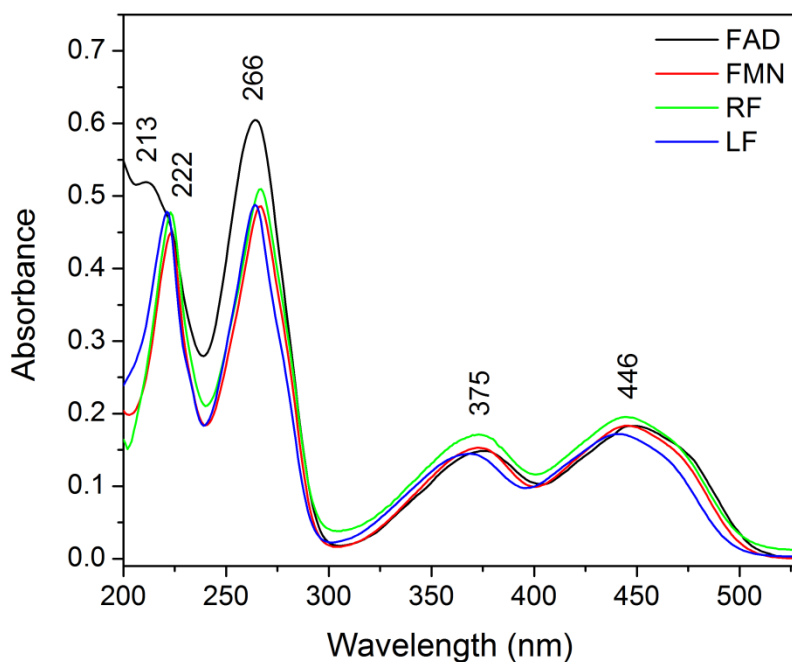


Fig. 1.5 Experimental absorption spectra of FAD (2×10^{-5} M), FMN (2.2×10^{-5} M), RF (2.2×10^{-5} M) and LF (2.2×10^{-5} M) in pH 7 phosphate buffer solution. Absorption bands are labeled with λ_{\max} (in nm) values.

Although the first absorption band centered at 446 nm is structureless in aqueous solution, it shows vibronic structure with three peaks in less polar solvents such as ethanol (EtOH), acetonitrile (ACN) and 2-methyltetrahydrofuran (MTHF).^{55,56} Apart from showing the vibronic structures due to the reduction in solvent-solute interactions, the position of this band is practically unaffected upon moving from water to less polar solvents. In opposite to that, the

second absorption band shows a prominent solvatochromism.^{51,56,57} In less polar solvents like dioxane (DX)⁵¹ and MTHF,⁵⁶ a noticeable blueshift (around 40 nm) is observed for this band. Experiments hereby have revealed that the influence of solvent polarity on the position of this band might be due to hydrogen bonding between the flavin and solvent.^{51,58}

The third experimentally observed band (maxima at 264-267 nm) in the UV region is the most intense band in the absorption spectra of flavins (Fig. 1.5). This band also experiences a little influence upon changing the solvent polarity, similar to the first absorption band.⁵⁹ Theoretical calculations and experimental results on different isoalloxazine molecules concluded that this band is a combination of more than one $\pi\pi^*$ transitions. PPP-CI calculations⁶⁰ and circular dichromism experiments⁵⁹ on various RF derivatives have shown two weak $\pi\pi^*$ transitions to the both sides of the strong $\pi\pi^*$ transition centered at around 265 nm. Two strong $\pi\pi^*$ transitions at 4.57 and 4.96 eV were computed contributing to the 266 nm absorption band for LF using SAC-CI method,⁴⁵ whereas CASPT2⁴² (at 4.69 eV, 5.00 eV and 5.37 eV) and TDDFT^{44,47,48,51-54} calculations assign three $\pi\pi^*$ transitions within this absorption band. The fourth absorption band at 222 nm is also close in intensity to the 266 nm absorption band. Theoretical assignment for this band is scarce.

Oxidized flavin compounds exhibit a bright yellow fluorescence emission with a peak maximum at around 530-545 nm in aqueous solution.^{52,61} The position of the peak is mostly unaffected by different solvent environments, whereas the fluorescence quantum yield (Φ_F) increases in non-polar, aprotic solvents.^{51,57} The fluorescence quantum yield observed for LF in aqueous solution ranges within 0.14 to 0.29 depending upon the pH ($\Phi_F = 0.16$ at pH 2.2,⁶¹ $\Phi_F = 0.14$ at pH ≈ 6 ,⁵¹ $\Phi_F = 0.25$ at pH 7,⁵⁷ $\Phi_F = 0.29$ at pH 7⁶¹). For, RF and FMN almost identical fluorescence properties are obtained, while the quantum yield found for FAD in neutral aqueous solution ($\Phi_F = 0.038$)⁶¹ is ten times weaker than the other three flavins. It has been reported that the intramolecular electron transfer with a stacked conformation between the isoalloxazine ring and the adenine moiety is the reason behind the quenching of FAD fluorescence.⁶²⁻⁶⁵ For all of the flavins, the strongest competition for the spin-allowed radiative relaxation arises due to triplet formation. Quantum yields (Φ_T) found for triplet formation ranges between 0.4^{66,67} and 0.6^{68,69}.

Despite the structural similarity to isoalloxazine compounds, alloxazines exhibit very distinct absorption and fluorescence properties as compare to isoalloxazine compounds. All

alloxazines absorb in the near UV and UV regions of the spectrum. The experimental absorption spectrum of lumichrome (LC), a derivative of alloxazine family, is shown in Fig. 1.6. In aqueous solution, the absorption spectrum of LC shows an absorption band at around 353 nm with a shoulder near 385 nm in the near UV region.

These two absorption bands are assigned to two independent $\pi\pi^*$ transitions by various quantum chemical calculations.^{51,52,70–74}

Calculations predicted optically dark $n\pi^*$ states closely spaced to each of those $\pi\pi^*$ transitions. The positions of both the bands are found to depend on solvent polarity and show blueshift with decreasing polarity and hydrogen bonding ability of solvent.^{51,75} In

the UV region, the absorption spectrum is dominated by two bands analogous to the flavin spectra containing peak maxima at

around 260 and 219 nm. Both the UV absorption bands possess high molar extinction coefficients indicating to $\pi\pi^*$ transitions, though assignments for these bands are not available yet by quantum chemical calculations. It is found that the absorption band at 260 nm splits into two with a new band at around 250 nm in less polar solvents such as EtOH and DX.⁴¹

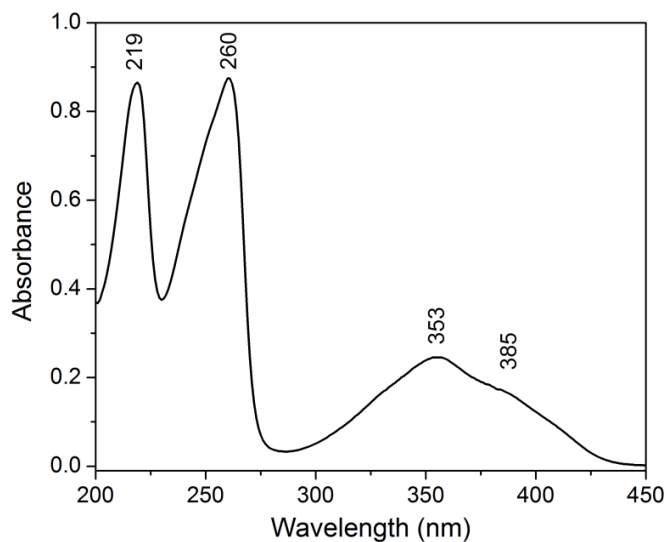


Fig. 1.6 Experimental absorption spectrum of LC (4.8×10^{-5} M) in phosphate buffer solution at pH 7. Absorption bands are labeled with λ_{max} (in nm) values.

The maximum of fluorescence emission spectrum of LC in aqueous solution is reported to shift to the short wavelengths about 50 nm (near 475 nm), relative to that of flavins which exhibit much broader fluorescence band than alloxazines.^{51,52,76} The fluorescence quantum yield ($\Phi_F = 0.088$ in water) found for LC is one order smaller than that of flavins due to the lower non-radiative decay rates in the latter compounds.^{51,71,73,76} The position of the fluorescence maximum blueshifts and quantum yield decreases in polar aprotic solvents ($\Phi_F = 0.028$ in ACN, 0.032 in methanol, 0.027 in DX),⁵¹ if compared to LC in polar protic solvents.^{51,74,77} The quantum yield for triplet formation (Φ_T) is found to be 0.71 and 0.45 for LC and alloxazine respectively in aqueous solution.⁶⁸

1.7 Ultrafast excited state photophysics of flavins and motivation of this work

The primary photoactivation step for some light sensitive chromophores such as phytochromobilin, retinal and coumarin involves E/Z isomerization, whereas flavin structure restrains to strong conformational changes.⁷⁸ Nonetheless, flavins are extremely versatile redox cofactors, whose activation mechanism is aided by protein environment. It is established that the signaling state formation in LOV domain involves intersystem crossing of FMN singlet excited state in picosecond (ps) timescale upon blue light illumination, followed by a covalent adduct formation between flavin and nearby cysteine in microsecond timescale.^{40,79–83} In BLUF proteins, the signaling state formation is characterized by a 20 cm^{-1} red shifted IR absorption in carbonyl stretching frequencies concomitant with the red shifted absorption spectrum.^{36,37,84–87} A hydrogen bonding rearrangement around the chromophore happens involving the hydrogen bond formation with flavin C4=O carbonyl group to form the BLUF light state.^{36,37,84–93} Femtosecond (fs) resolved infrared and transient absorption studies proposed that the signaling state formation appears in 100 ps (picosecond) timescale in the singlet state manifold involving electron and proton transfers.^{37,84–86} The mechanism also includes the change in the orientation of tryptophan and glutamine residues.^{37,84} In cryptochromes, a conformational change in the protein occurs following photoreduction of flavin to its semiquinone form, but the complete mechanism is still under debate.^{30,33,34,94,95}

In blue light photoreceptors, it is often become complicated in the measurement of spectroscopic properties due to the spectral overlap from different contributions. Here we concentrate on the excited state photophysics of flavin, free in solution instead of inside the photoreceptors. If we can accurately measure its electronic and structural properties including the response to the solvents, then this information can be applied to deconvolve the inhomogeneity in proteins. That's why, flavin photophysics is studied by using several spectroscopic techniques including fs stimulated Raman, absorption and fluorescence techniques having time resolution from femtosecond (fs) to nanosecond (ns) timescales.

The photochemistry of flavin depends on its different redox forms (oxidized, semireduced and fully reduced) which again can undergo in different protonation states depending on pH. In the thesis work, we focus on the neutral oxidized form of flavin that exists in the pH range 2-8 in polar solvents. The lowest singlet (S_1) and triplet excited (T_1) states of

flavin are assigned to $\pi\pi^*$ symmetry.^{43,46,96} Following excitation to the S_1 state all of the flavins decays to the ground state in nanosecond (ns) timescale except FAD which exhibits an ultrafast decay in picosecond (ps) timescale.¹³ In polar solvents, FAD favors a stacked conformation between the adenine and the isoalloxazine ring and an intramolecular electron transfer from adenine to the isoalloxazine ring is proposed.^{13,64,97-99} Transient absorption, fluorescence and infrared studies find a timescale of 5-10 ps for charge transfer and subsequently charge recombination in 30-40 ps.^{13,97-99} Although this mechanism is unarguably accepted, spectroscopic measurements are unable to capture the intermediates in the charge transfer process. Theoretical calculations predicted a dark $n\pi^*$ state in close proximity to the S_1 ($\pi\pi^*$) state.^{43,50,96} The vibronic coupling strength between these two states is found to be dependent on dynamic polar solvation and temperature.^{50,99} The solvation dynamics in S_1 excited state is observed as a dynamic Stokes shift of the emission band.⁹⁹

Time resolved vibrational spectroscopies (fs transient mid-IR to visible and stimulated Raman spectroscopy) have been applied on flavin molecules to determine the structural changes following excitation to S_1 state by observing shifts in the normal modes of the chromophore.^{100,101} Major change is observed in the loss of double bond character between C4a and N5 atoms in the isoalloxazine ring.¹⁰⁰⁻¹⁰² It is found that the double bond stretching frequencies (C=O, C=C and C=N) in the flavin ring downshifts upon excitation from S_0 to S_1 . In addition, several quantum chemical calculations also predicted similar changes in the structure of flavin upon excitation to lowest energy singlet state.^{45,50,53,103,104} In S_1 state, TD-B3LYP/TZVP calculations find a maximum change of ~ 0.05 Å bond elongations and contractions in the isoalloxazine ring.^{50,103}

All of the above studies demonstrate the photophysics of flavins upon excitation to the lowest energy, $\pi\pi^*$ electronic state, while to our knowledge there has been no study as yet on the excited state photodynamics within their UV regions of absorption. Flavin absorbs more efficiently in the UV regions (see Fig. 1.4) comprising two absorption bands at 260 and 223 nm, compared to the visible and near visible regions. Nonetheless, Copeland and Spiro¹⁰⁵ reported the Resonance Raman (RR) spectra of FAD and FMN molecule with visible as well as UV excitations at 488, 355, 266, 240, 218 and 200 nm. Distinct change in the relative intensity of RR bands varying excitation wavelengths suggest different distortions

occurring at the Franck-Condon (FC) region to the corresponding excited states. **In this work, we determine the excited state photophysics of flavins following photoexcitation to their most intense UV absorption band having a maximum at around 266 nm.**

As we know that harmful UV radiations (ranging 100-400 nm) from the sun are always reaching in the earth surface, which has many hazardous effects such as causing depletion in the DNA nucleobases.¹⁰⁶⁻¹⁰⁸ This harmful radiation can be classified into three categories, long wavelength UVA (400-320 nm), medium wavelength UVB (320-280) and short wavelength UVC (280- 100 nm).¹⁰⁶ However, the ozone layer of about 3 mm thick above the earth surface shields and absorbs most of the UV radiations of the solar spectrum upto 310 nm from reaching the earth surface.¹⁰⁷ But, in the modern era, as the stratospheric ozone layer is experiencing continuous depletion due to increase in many pollutants, an increased amount of UV radiations containing UVB and even UVC is also reaching in the earth surface.^{107,108} **So, to understand the effects of UVB and UVC radiations on blue light photoreceptors, it is important to understand the excited state photophysics of flavin cofactors within their strong $\pi\pi^*$ electronic states in the UV region of absorption.**

1.8 Goals of this project

Photoexcitation induces a change in the structure of a molecule in solution as well as on the surrounding environments. Upon optical excitation there is an excess vibrational energy of a solute molecule which dissipates via the specific vibrational modes in a radiationless manner. The energy released in this process is known as vibrational reorganization energy. In addition, initially the surrounding solvent molecules remain in equilibrium with the ground state dipole moment of the solute. The solvent molecules then have to reorient themselves in response to the change in the direction of the excited state dipole moment of the solute. Solvent releases energy in this reorientation process known as solvent reorganization process. Fig. 1.7 shows the various processes involved after the optical excitation of a solute.

So, here our aim is to determine the reorganization energies and structural changes for different flavin molecules following excitation to their 266 nm excited state. As we know that flavin molecules differ by the respective substituents at N10 position. So, we also want to know that how the substituents affect the reorganization energies in different flavins.

Nowadays, the crystal structures of several flavoproteins are reported, which reveals that the majority of flavin-protein interaction involves with the ribityl chain of FMN and FAD.^{109–113} So, **the effect of the ribityl chain in the excited state dynamics for RF and FMN is to be investigated as compare to the LF which contains a methyl group as a substituent. This study is also extended in FAD where we want to understand the effect of adenine moiety on flavin dynamics.**

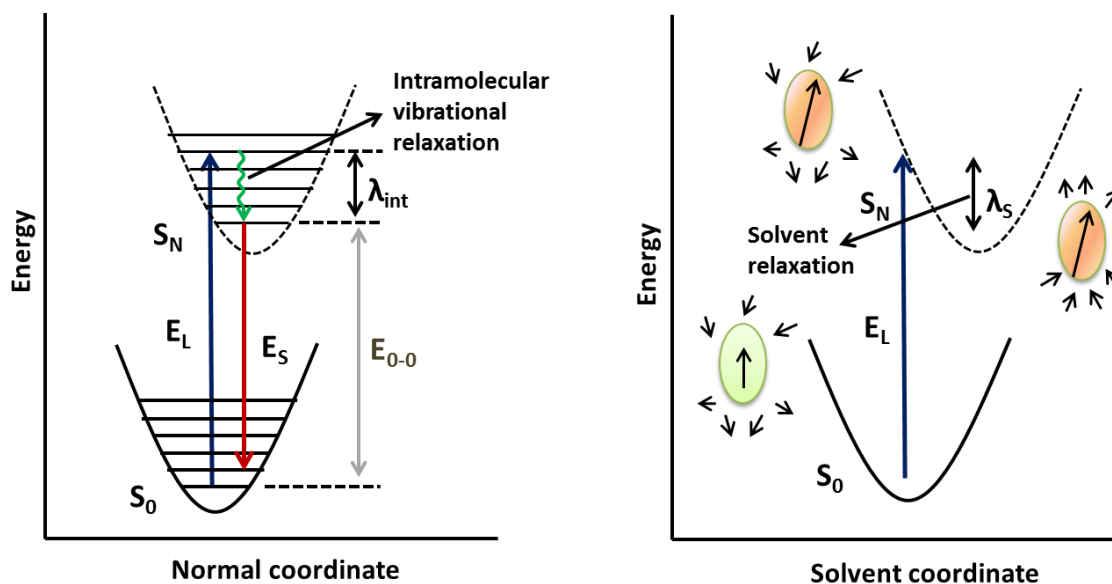


Fig. 1.7 Schematic representation of the ground and excited state potential energy surfaces as function of the (a) normal mode and (b) solvent coordinates. E_L and E_S are the incident and scattered photon energies, E_{0-0} is the 0-0 transition energy, λ_{int} and λ_s are the internal reorganization energy of the solute and the reorganization energy of the solvent respectively. The arrows represent the permanent dipole moment of the solute and solvent molecules.

1.9 Measuring the photophysics in the UV region of absorption

Apart from the time-resolved RR spectroscopy which can monitor the ultrafast response of structural changes in a solute and solvation dynamics in real time, there is another indirect approach which has been employed for the same purpose. **In this case, the information of the excited state dynamics contains within the intensity of RR spectrum itself.**¹¹⁴ RR intensity analysis has been successfully applied to probe the excited state structural dynamics for several natural and modified Nucleobases within their lowest energy (~ 260 nm) $\pi\pi^*$ electronic states.^{115,116,116–123}

The wavenumbers of bands in the Raman spectrum of a molecule report the structure in the ground electronic state. Additionally, in RR spectroscopy in which the Raman excitation lies within the electronic absorption of a molecule, the intensity of a band encodes the information of the resonant excited state. Intensity of a RR band is proportional to the slope at the potential energy surface (PES) of the resonant excited state along that normal coordinate. Thus greater the structural distortion in the excited state compared to that in the ground state along the normal coordinate, higher the intensity of the resulting RR band. From experimentally measured RR cross-section, the structural distortions in the excited state with respect to that in the ground state molecular structure can be determined. Resonance Raman (RR) spectroscopy is the only experimental technique that can determine vibrational mode-specific instantaneous structural distortions of a molecule, subsequent to photoexcitation to an electronic state.

Moreover, the line shape analysis of the Raman excitation profile (REP), i.e., the excitation wavelength dependence of RR cross sections can reveal the response of the effect of solvent environments through line broadening. This approach has the advantage of being able to differentiate between the contributions of the homogeneous and inhomogeneous broadening effects to the absorption spectral lineshape. The contributions of the long time scale dynamics will be manifested in the inhomogeneous broadening linewidth which also provides a quantitative estimate of the different ground state structural conformations of the chromophore. Through measurement and modeling of experimental REP and absorption spectrum, it is possible to extract the parameters corresponding to the initial excited state structural dynamics of flavin within tens of femtoseconds of excitation.

1.10 Organization of the thesis

This thesis is organized into six chapters. In chapter 2, a detailed description of the theoretical and experimental methodologies is given. In chapter 3, the initial excited state structural dynamics of LF in water upon excitation within the 265 nm absorption band is studied by using time-dependent wave packet propagation theory and a Brownian oscillator model to account for the solute-solvent interaction. The contribution of the solute and solvent to the total reorganization energy as well as the inhomogeneous broadening linewidth are determined. Specifically, an estimated value of the inertial solvent response and the change in internal coordinates has been obtained. In the subsequent chapters, the initial excited state structural

dynamics of RF, FMN (chapter 4), FAD (chapter 5) and LC (chapter 6) are studied using the same methodology as that used for LF. We find very similar reorganization energies and broadening parameters for RF, FMN and FAD, while the internal coordinate changes found in the isoalloxazine ring in those molecules are different. The excited state dynamics of LC determine lower internal reorganization energy for alloxazine structure than flavins. At the end we have added the conclusion of all chapters.

References

- (1) Fraaije, M. W.; Mattevi, A. *Trends Biochem. Sci.* **2000**, 25 (3), 126.
- (2) Losi, A. *Photochem. Photobiol.* **2007**, 83 (6), 1283.
- (3) Massey, V. *Biochem. Soc. Trans.* **2000**, 28 (4), 283.
- (4) Gelalcha, F. G. *Chem. Rev.* **2007**, 107 (7), 3338.
- (5) Vincent, A. S. *PhD Thesis Photochem. Sci.* **2011**, Bowling Green State University.
- (6) Kuhn, R, Reinemund, K. and Weygand, F. *Ber* **1934**, 67, 1460.
- (7) Karrer, P., Schopp, K. and Benz, F. *Helv. Chim. Acta* **1935**, 18, 426.
- (8) Theorell, H. *Biochem. Z.* **1935**, 275, 344.
- (9) Heelis, P. F. *Chem. Soc. Rev.* **1982**, 11 (1), 15.
- (10) Massey, V.; Hemmerich, P.; Knappe, W. R.; Duchstein, H. J.; Fenner, H. *Biochemistry* **1978**, 17 (1), 9.
- (11) Massey, V.; Palmer, G. *Biochemistry* **1966**, 5, 3181.
- (12) Bretz, N.; Mastalsky, I.; Eisner, M.; Kurreck, H. *Angew. Chem. Int. Ed. Engl.* **1987**, 26, 4.
- (13) Kao, Y.; Saxena, C.; He, T.; Guo, L.; Wang, L.; Sancar, A.; Zhong, D. *J. Am. Chem. Soc.* **2008**, 130 (39), 13132.
- (14) Kemal, C.; Chan, T. W.; Bruice, T. C. *Proc. Natl. Acad. Sci.* **1977**, 74 (2), 405.
- (15) Joosten, V.; van Berkel, W. J. *Curr. Opin. Chem. Biol.* **2007**, 11 (2), 195.
- (16) Ghisla, S.; Thorpe, C. *Eur. J. Biochem.* **2004**, 271 (3), 494.
- (17) Bruice, T. C. *Acc. Chem. Res.* **1980**, 2772 (eq 5), 256.
- (18) Sancar, A. *Chem. Rev.* **2003**, 103 (6), 2203.
- (19) Briggs, W. R.; Huala, E. *Annu. Rev. Cell Dev. Biol.* **1999**, 15 (1), 33.
- (20) Losi, A.; Gärtner, W. *Photochem. Photobiol.* **2011**, 87 (3), 491.
- (21) Anderson, S.; Dragnea, V.; Masuda, S.; Ybe, J.; Moffat, K.; Bauer, C. *Biochemistry* **2005**, 44 (22), 7998.
- (22) Heelis, P. F.; Hartman, R. F.; Rose, S. D. *Chem. Soc. Rev.* **1995**, 24 (4), 289.
- (23) Sancar, A. *Biochemistry* **1994**, 33 (1), 2.
- (24) Malhotra, K.; Kim, S.-T.; Sancar, A. *Biochemistry* **1994**, 33 (29), 8712.

- (25) Tan, C.; Guo, L.; Ai, Y.; Li, J.; Wang, L.; Sancar, A.; Luo, Y.; Zhong, D. *J. Phys. Chem. A* **2014**.
- (26) Vande Berg, B. J.; Sancar, G. B. *J. Biol. Chem.* **1998**, *273* (32), 20276.
- (27) Mees, A. *Science (80-.)*. **2004**, *306* (5702), 1789.
- (28) Torizawa, T.; Ueda, T.; Kuramitsu, S.; Hitomi, K.; Todo, T.; Iwai, S.; Morikawa, K.; Shimada, I. *J. Biol. Chem.* **2004**, *279* (31), 32950.
- (29) Wang, H.; Saxena, C.; Quan, D.; Sancar, A.; Zhong, D. *J. Phys. Chem. B* **2005**, *109* (4), 1329.
- (30) Kao, Y.-T.; Tan, C.; Song, S.-H.; Öztürk, N.; Li, J.; Wang, L.; Sancar, A.; Zhong, D. *J. Am. Chem. Soc.* **2008**, *130* (24), 7695.
- (31) Öztürk, N.; Song, S.-H.; Özgür, S.; Selby, C. P.; Morrison, L.; Partch, C.; Zhong, D.; Sancar, a. *Cold Spring Harb. Symp. Quant. Biol.* **2007**, *72*, 119.
- (32) Hoang, N.; Schleicher, E.; Kacprzak, S.; Bouly, J. P.; Picot, M.; Wu, W.; Berndt, A.; Wolf, E.; Bittl, R.; Ahmad, M. *PLoS Biol.* **2008**, *6* (7), 1559.
- (33) Kottke, T.; Batschauer, A.; Ahmad, M.; Heberle, J. *Biochemistry* **2006**, *45* (8), 2472.
- (34) Giovani, B.; Byrdin, M.; Ahmad, M.; Brettel, K. *Nat. Struct. Biol.* **2003**, *10* (6), 489.
- (35) Gomelsky, M.; Klug, G. *Trends Biochem. Sci.* **2002**, *27* (10), 497.
- (36) Wu, Q.; Gardner, K. H. *Biochemistry* **2009**, *48* (12), 2620.
- (37) Stelling, A. L.; Ronayne, K. L.; Nappa, J.; Tonge, P. J.; Meech, S. R. *J. Am. Chem. Soc.* **2007**, *129* (50), 15556.
- (38) Christie, J. M.; Swartz, T. E.; Bogomolni, R. A.; Briggs, W. R. *Plant J.* **2002**, *32* (2), 205.
- (39) Briggs, W. R.; Beck, C. F.; Cashmore, a R.; Christie, J. M.; Hughes, J.; Jarillo, J. a; Kagawa, T.; Kanegae, H.; Liscum, E.; Nagatani, a; Okada, K.; Salomon, M.; Rüdiger, W.; Sakai, T.; Takano, M.; Wada, M.; Watson, J. C. *Plant Cell* **2001**, *13* (5), 993.
- (40) Kottke, T.; Heberle, J.; Hehn, D.; Dick, B.; Hegemann, P. *Biophys. J.* **2003**, *84* (2), 1192.
- (41) Koziol, J. *Photochem. Photobiol.* **1966**, *5* (1), 41.
- (42) Climent, T.; González-Luque, R.; Merchán, M.; Serrano-Andrés, L. *J. Phys. Chem. A* **2006**, *110* (50), 13584.
- (43) Salzmann, S.; Tatchen, J.; Marian, C. M. *J. Photochem. Photobiol. A Chem.* **2008**, *198* (2–3), 221.
- (44) Neiss, C.; Saalfrank, P.; Parac, M.; Grimme, S. *J. Phys. Chem. A* **2003**, *107* (1), 140.
- (45) Hasegawa, J.; Bureekaew, S.; Nakatsuji, H. *J. Photochem. Photobiol. A Chem.* **2007**, *189* (2–3), 205.
- (46) Sikorska, E.; Khmelinskii, I.; Komasa, A.; Koput, J.; Ferreira, L. F. V.; Herance, J. R.; Bourdelande, J. L.; Williams, S. L.; Worrall, D. R.; Insińska-Rak, M.; Sikorski, M. *Chem. Phys.* **2005**, *314* (1–3), 239.
- (47) Zenichowski, K.; Gothe, M.; Saalfrank, P. *J. Photochem. Photobiol. A Chem.* **2007**, *190* (2–3), 290.
- (48) Kowalczyk, M.; Sikorska, E.; Khmelinskii, I. V.; Komasa, J.; Insińska-Rak, M.; Sikorski, M. *J. Mol. Struct. THEOCHEM* **2005**, *756* (1–3), 47.
- (49) Sikorska, E.; Khmelinskii, I. V.; Koput, J.; Bourdelande, J. L.; Sikorski, M. *J. Mol. Struct.* **2004**, *697* (1–3), 137.
- (50) Klaumünzer, B.; Kröner, D.; Lischka, H.; Saalfrank, P. *Phys. Chem. Chem. Phys.* **2012**, *14* (24), 8693.
- (51) Sikorska, E.; Khmelinskii, I. V.; Prukala, W.; Williams, S. L.; Patel, M.; Worrall, D. R.; Bourdelande, J. L.; Koput, J.; Sikorski, M. *J. Phys. Chem. A* **2004**, *108* (9), 1501.

- (52) Sikorska, E.; Khmelinskii, I. V.; Worrall, D. R.; Koput, J.; Sikorski, M. *J. Fluoresc.* **2004**, *14* (1), 57.
- (53) Choe, Y.-K.; Nagase, S.; Nishimoto, K. *J. Comput. Chem.* **2007**, *28* (4), 727.
- (54) Sikorska, E.; Khmelinskii, I. V.; Bednarek, A.; Williams, S. L.; Worrall, D. R.; Herance, J. R.; Bourdelande, J. L.; Nowacka, G.; Koput, J.; Sikorski, M. *J. Fluoresc.* **2004**, *14* (1), 57.
- (55) Sun, M.; Moore, T. A.; Song, P.-S. *J. Am. Chem. Soc.* **1972**, *94* (5), 1730.
- (56) Eweg, J. K.; Müller, F.; Visser, A. J. W. G.; Veeger, C.; Bebelaar, D.; Voorst, J. D. W. van. *Photochem. Photobiol.* **1979**, *30* (4), 463.
- (57) Visser, A. J. W. G.; Müller, F. *Helv. Chim. Acta* **1979**, *62* (2), 593.
- (58) Weigel, A.; Dobryakov, A. L.; Veiga, M.; Pérez Lustres, J. L. *J. Phys. Chem. A* **2008**, *112* (47), 12054.
- (59) Tollin, G. *Biochemistry* **1968**, *7* (5), 1720.
- (60) Sun, M.; Moore, T. A.; Song, P.-S. *J. Am. Chem. Soc.* **1972**, *94* (5), 1730.
- (61) Bowd, A.; Byrom, P.; Hudson, J. B.; Turnbull, J. H. *Photochem. Photobiol.* **1968**, *8* (1), 1.
- (62) Weber, G. *Biochem. J.* **1950**, *47* (1), 114.
- (63) Barrio, J. R.; Tolman, G. L.; Leonard, N. J.; Spencer, R. D.; Weber, G. *Proc Natl Acad Sci U S A.* **1973**, *70* (3), 941.
- (64) Chosrowjan, H.; Taniguchi, S.; Mataga, N.; Tanaka, F.; Visser, A. J. W. G. *Chem. Phys. Lett.* **2003**, *378* (3–4), 354.
- (65) van den Berg, P. A. W.; Feenstra, K. A.; Mark, A. E.; Berendsen, H. J. C.; Visser, A. J. W. G. *J. Phys. Chem. B* **2002**, *106* (34), 8858.
- (66) Penzkofer, A.; Endres, L.; Schiereis, T.; Hegemann, P. *Chem. Phys.* **2005**, *316* (1–3), 185.
- (67) Islam, S. D. M.; Penzkofer, A.; Hegemann, P. *Chem. Phys.* **2003**, *291* (1), 97.
- (68) Grodowski, M. S.; Veyret, B.; Weiss, K. *Photochem. Photobiol.* **1977**, *26* (4), 341.
- (69) Kennis, J. T. M.; Crosson, S.; Gauden, M.; Van Stokkum, I. H. M.; Moffat, K.; Van Grondelle, R. *Biochemistry* **2003**, *42* (12), 3385.
- (70) Sikorska, E.; Khmelinskii, I.; Hoffmann, M.; Machado, I. F.; Ferreira, L. F. V.; Dobek, K.; Karolczak, J.; Krawczyk, A.; Insińska-Rak, M.; Sikorski, M. *J. Phys. Chem. A* **2005**, *109* (51), 11707.
- (71) Salzmann, S.; Marian, C. M. *Photochem. Photobiol. Sci.* **2009**, *8* (12), 1655.
- (72) Sikorska, E.; Khmelinskii, I. V.; Williams, S. L.; Worrall, D. R.; Herance, J. R.; Bourdelande, J. L.; Koput, J.; Sikorski, M. *J. Mol. Struct.* **2004**, *697* (1–3), 199.
- (73) Chang, X. P.; Xie, X. Y.; Lin, S. Y.; Cui, G. *J. Phys. Chem. A* **2016**, *120* (31), 6129.
- (74) Moyon, N. S.; Mitra, S. *J. Phys. Chem. A* **2011**, *115* (12), 2456.
- (75) Koziolowa, A. *Photochem. Photobiol.* **1979**, *29* (3), 459.
- (76) Sikorski, M.; Sikorska, E.; Koziolowa, A.; Gonzalez Moreno, R.; Bourdelande, J. L.; Steer, R. P.; Wilkinson, F. *J. Photochem. Photobiol. B Biol.* **2001**, *60* (2–3), 114.
- (77) Sikorski, M.; Prukała, D.; Insińska-Rak, M.; Khmelinskii, I.; Worrall, D. R.; Williams, S. L.; Hernando, J.; Bourdelande, J. L.; Koput, J.; Sikorska, E. *J. Photochem. Photobiol. A Chem.* **2008**, *200* (2–3), 148.
- (78) Hellingwerf, K. J. *J. Photochem. Photobiol. B Biol.* **2000**, *54* (2–3), 94.
- (79) Alexandre, M. T. A.; Domratcheva, T.; Bonetti, C.; Van Wilderen, L. J. G. W.; Van Grondelle, R.; Groot, M. L.;

- Hellingwerf, K. J.; Kennis, J. T. M. *Biophys. J.* **2009**, *97* (1), 227.
- (80) Ataka, K.; Hegemann, P.; Heberle, J. *Biophys. J.* **2003**, *84* (1), 466.
- (81) Thöing, C.; Pfeifer, A.; Kakorin, S.; Kottke, T. *Phys. Chem. Chem. Phys.* **2013**, *15* (16), 5916.
- (82) Iwata, T.; Nozaki, D.; Yamamoto, A.; Koyama, T.; Nishina, Y.; Shiga, K.; Tokutomi, S.; Unno, M.; Kandori, H. *Biochemistry* **2017**, *56* (24), 3099.
- (83) Kottke, T.; Hegemann, P.; Dick, B.; Heberle, J. *Biopolymers* **2006**, *82* (4), 373.
- (84) Bonetti, C.; Mathes, T.; van Stokkum, I. H. M.; Mullen, K. M.; Groot, M.-L.; van Grondelle, R.; Hegemann, P.; Kennis, J. T. M. *Biophys. J.* **2008**, *95* (10), 4790.
- (85) Mathes, T.; Van Stokkum, I. H. M.; Bonetti, C.; Hegemann, P.; Kennis, J. T. M. *J. Phys. Chem. B* **2011**, *115* (24), 7963.
- (86) Iwata, T.; Watanabe, A.; Iseki, M.; Watanabe, M.; Kandori, H. *J. Phys. Chem. Lett.* **2011**, *2* (9), 1015.
- (87) Masuda, S.; Hasegawa, K.; Ishii, A.; Ono, T. A. *Biochemistry* **2004**, *43* (18), 5304.
- (88) Hall, C. R.; Heisler, I. A.; Jones, G. A.; Frost, J. E.; Gil, A. A.; Tonge, P. J.; Meech, S. R. *Chem. Phys. Lett.* **2017**, *683*, 365.
- (89) Takahashi, R.; Okajima, K.; Suzuki, H.; Nakamura, H.; Ikeuchi, M.; Noguchi, T. *Biochemistry* **2007**, *46* (22), 6459.
- (90) Zirak, P.; Penzkofer, A.; Lehmpfuhl, C.; Mathes, T.; Hegemann, P. *J. Photochem. Photobiol. B Biol.* **2007**, *86* (1), 22.
- (91) Unno, M.; Sano, R.; Masuda, S.; Ono, T.; Yamauchi, S. *J. Phys. Chem. B* **2005**, *109* (25), 12620.
- (92) Hasegawa, K.; Masuda, S.; Ono, T. A. *Biochemistry* **2004**, *43* (47), 14979.
- (93) Götze, J. P.; Greco, C.; Mitrić, R.; Bonačić-Koutecký, V.; Saalfrank, P. *J. Comput. Chem.* **2012**, *33* (28), 2233.
- (94) Bouly, J.-P.; Schleicher, E.; Dionisio-Sese, M.; Vandenbussche, F.; Van Der Straeten, D.; Bakrim, N.; Meier, S.; Batschauer, A.; Galland, P.; Bittl, R.; Ahmad, M. *J. Biol. Chem.* **2007**, *282* (13), 9383.
- (95) Zeugner, A.; Byrdin, M.; Bouly, J. P.; Bakrim, N.; Giovani, B.; Brettel, H.; Ahmad, M. *J. Biol. Chem.* **2005**, *280* (20), 19437.
- (96) Insińska-Rak, M.; Sikorska, E.; Bourdelande, J. L.; Khmelinskii, I. V.; Prukała, W.; Dobek, K.; Karolczak, J.; Machado, I. F.; Ferreira, L. F. V.; Komasa, A.; Worrall, D. R.; Sikorski, M. *J. Mol. Struct.* **2006**, *783* (1–3), 184.
- (97) Li, G.; Glusac, K. D. *J. Phys. Chem. B* **2009**, *113* (27), 9059.
- (98) Brazard, J.; Usman, A.; Lacombe, F.; Ley, C.; Martin, M. M.; Plaza, P. *J. Phys. Chem. A* **2011**, *115* (15), 3251.
- (99) Weigel, A.; Dobryakov, A.; Klaumünzer, B.; Sajadi, M.; Saalfrank, P.; Ernsting, N. P. *J. Phys. Chem. B* **2011**, *115*, 3656.
- (100) Wolf, M. M. N.; Schumann, C.; Gross, R.; Domratcheva, T.; Diller, R. *J. Phys. Chem. B* **2008**, *112* (42), 13424.
- (101) Wolf, M. M. N.; Zimmermann, H.; Diller, R.; Domratcheva, T. *J. Phys. Chem. B* **2011**, *115* (23), 7621.
- (102) Lukacs, A.; Zhao, R.-K.; Haigney, A.; Brust, R.; Greetham, G. M.; Towrie, M.; Tonge, P. J.; Meech, S. R. *J. Phys. Chem. B* **2012**, *116* (20), 5810.
- (103) Klaumünzer, B.; Kröner, D.; Saalfrank, P. *J. Phys. Chem. B* **2010**, *114* (33), 10826.
- (104) Salzmann, S.; Marian, C. M. *Photochem. Photobiol. Sci.* **2009**, *8* (12), 1655.
- (105) Copeland, R. A.; Spiro, T. G. *J. Phys. Chem.* **1986**, *90* (25), 6648.
- (106) Goodsell, D. S. *Oncologist* **2001**, *6* (3), 298.

- (107) Toon, O. B.; Turco, R. P. *Sci. Am.* **1991**, 264 (6), 68.
- (108) Rowland, F. S. *Angew. Chemie Int. Ed. English* **1996**, 35, 1786.
- (109) Jung, A.; Domratcheva, T.; Tarutina, M.; Wu, Q.; Ko, W.; Shoeman, R. L.; Gomelsky, M.; Gardner, K. H.; Schlichting, I. *Proc. Natl. Acad. Sci. U. S. A.* **2005**, 102 (35), 12350.
- (110) Ingelman, M.; Ramaswamy, S.; Nivière, V.; Fontecave, M.; Eklund, H. *Biochemistry* **1999**, 38 (22), 7040.
- (111) Choi, J. Do; McCormick, D. B. *Arch. Biochem. Biophys.* **1980**, 204 (1), 41.
- (112) Murthy, Y. V. S. N.; Massey, V. *J. Biol. Chem.* **1995**, 270 (48), 28586.
- (113) Roberts, D. L.; Frerman, F. E.; Kim, J.-J. P. *Proc. Natl. Acad. Sci.* **1996**, 93 (25), 14355.
- (114) Myers, A. B., and R. A. M. *Wiley, New York.* **1987**, 2, 1.
- (115) Billinghamurst, B. E.; Yeung, R.; Loppnow, G. R. *J. Phys. Chem. A* **2006**, 110 (19), 6185.
- (116) Yarasi, S.; Brost, P.; Loppnow, G. R. *J. Phys. Chem. A* **2007**, 111 (24), 5130.
- (117) Loppnow, G. R.; Mathies, R. A. *Biophys. J.* **1988**, 54 (1), 35.
- (118) El-Yazbi, A. F.; Palech, A.; Loppnow, G. R. *J. Phys. Chem. A* **2011**, 115 (38), 10445.
- (119) Oladepo, S. A.; Loppnow, G. R. *J. Phys. Chem. B* **2011**, 115 (19), 6149.
- (120) Billinghamurst, B. E.; Loppnow, G. R. *J. Phys. Chem. A* **2006**, 110 (7), 2353.
- (121) Billinghamurst, B. E.; Yeung, R.; Loppnow, G. R. *J. Phys. Chem. A* **2006**, 110 (19), 6185.
- (122) Ng, S. S.; Teimoory, F.; Loppnow, G. R. *J. Phys. Chem. Lett.* **2011**, 2 (18), 2362.
- (123) Sasidharanpillai, S.; Loppnow, G. R. *J. Phys. Chem. A* **2014**, 118 (26), 4680.

Chapter 2: Experimental and Theoretical Methods

The Raman effect is a scattering phenomena of light, which was first discovered by Sir C. V. Raman and K. S. Krishnan in 1928.^{1,2} It is a two photon process in which a photon with energy of $\hbar\omega_0$ interacts with a molecule to produce a scattered photon of higher or lower in energy relative to the incident radiation. The difference in energy between the incident and scattered photons exhibits the energy gap between the two vibrational energy levels, $\hbar\omega_v$, in the ground electronic state (shown in Fig. 2. 1). In scattering process, upon interaction with a photon, the molecule excites to a virtual energy level and then returns back to the same or different vibrational energy level in the ground state. As such there can be three outcomes: (i) when there is no difference between the incident and scattered photon energies, i.e.; elastic scattering, the process is known as Rayleigh scattering (Fig. 2.1 (a)), (ii) if the scattered photon is lower in energy than the incident photon, the process is known as Stokes scattering ($\hbar\omega_s = \hbar\omega_0 - \hbar\omega_v$) (Fig. 2.1 (b)), and (iii) when the scattered photon is higher in energy than the incident one, it is known as anti-Stokes scattering ($\hbar\omega_{as} = \hbar\omega_0 + \hbar\omega_v$) (Fig. 2.1 (c)). The last two inelastic scattering processes (Stokes and anti-Stokes scattering) constitute Raman spectroscopy. So, the fact that the energy difference between the incident and scattered photons corresponds to the energy gap between the ground vibrational levels allows the use of Raman spectroscopy to monitor the vibrational modes of a molecule.

If the energy of the incident photon is such that it can excite the molecule to an electronic excited state, then the process is called resonance Raman effect and it was initially discovered by Shorygin on 1947.³ A schematic for the case of the Stokes resonance Raman scattering is depicted in Fig. 2.1 (d). Under resonance conditions, the Raman intensity can usually be enhanced by a factor of 10^2 - 10^6 as compared to the normal Raman intensity, and in some cases, even by a factor of 10^8 .⁴ Thus, by tuning the energy of the incident photon to match the electronic excitation of a molecule, RR spectroscopy can be used to selectively study a particular molecule in an environment of several other molecules. So, we can study the structure of a chromophore when it is in the protein core without the interference from surrounding residues. The other advantage of Raman spectroscopy in the study of biological systems is that the Raman

scattering of water is quite weak as compared to using infrared spectroscopy. This feature makes it convenient to study the vibrational modes of biomolecules in their native, aqueous environment. RR spectroscopy has been successfully applied to study the structure and hydrogen bonding environment of different flavin derivatives in solution and inside the protein core.⁵⁻¹⁶

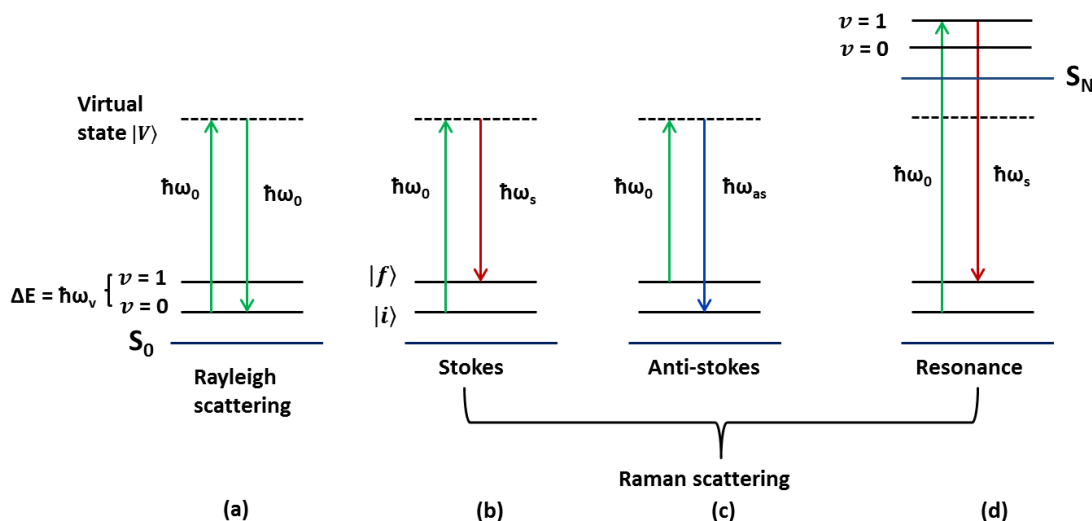


Fig. 2.1 Jablonski diagram of (a) Rayleigh scattering, (b) Stokes Raman, (c) anti-Stokes Raman and (d) resonance Raman scattering (Stokes). S_0 and S_N correspond to the ground and N^{th} excited electronic states respectively. The dash lines represent virtual states. $|i\rangle$ and $|f\rangle$ are the initial and final vibrational energy levels (v) respectively. ΔE is the energy difference between two vibrational energy levels.

When the wavelength of the incident radiation (i.e., the excitation wavelength) falls into the UV region of the electromagnetic spectrum, the technique is known as ultraviolet RR spectroscopy. The advantage of using the excitation wavelength in the UV region is the absence of interference from strong fluorescence emission which can mask the Raman spectrum. For example, aromatic amino acids such as Trp, Tyr, Phe and the amide backbone exhibit enhancement of the Raman signal if the excitation wavelength is in the deep-UV region (< 230 nm) rather than the 260 nm excitation.^{17,18} Flavin possesses strong fluorescence emission by excitations within its first two absorption bands at 450 and 375 nm. So, by tuning the excitation wavelength in the UV region of absorption, we can obtain fluorescence background free Raman spectrum of flavin.

Spiro and coworkers have pioneered RR spectroscopy with ultraviolet excitation (Ultraviolet resonance Raman or UVRR) to study structure and conformations of nucleobases,¹⁹⁻

²² heme chromophores present in hemoglobin and cytochrome,^{23–26} and aromatic amino acids.^{27,28} In the year 1986, they have reported the UVRR spectra of FAD and FMN using UV excitation wavelengths at 266, 240, 218 and 200 nm and observed the significant difference in relative Raman intensity by varying excitations.⁷ At the same time, Asher and coworkers have also demonstrated the applicability of UVRR spectroscopy to study nucleobases, proteins and their constituents.^{29,30} Since then, the number of studies that use UVRR spectroscopy on biomolecules has increased tremendously and several reviews have been published which describe the advances in this field, over time.^{31–41} The versatility of resonance Raman spectroscopy has allowed for the development of several Raman-related techniques to study the structure and dynamics of biomolecules, spanning timescales in the range of femtoseconds to several hundreds of nanoseconds.^{41–57}

One of such methodologies is the analysis of modulation of RR intensity with respect to the change of excitation energies. The band positions of the normal Raman spectrum of a molecule provide structural details of the ground electronic state. However, the intensity of the RR spectrum carries information on the initial excited state structural dynamics upon photoexcitation of the molecule.^{50,58–66} The plot of RR cross sections of a Raman mode as a function of excitation wavelengths is known as Raman excitation profile (REP). REPs are sensitive to the change in structure of the molecule upon electronic excitation. Similarly than to the absorption spectrum the REP lineshape are also influenced by the homogeneous and inhomogeneous broadening mechanism. However, by analyzing only the absorption spectrum it is not possible in general to differentiate the contribution of the homogeneous and inhomogeneous broadening mechanisms as both mechanisms have a similar effect.^{50,60,67} On the other hand, the two broadening mechanisms have different effects on the REP.⁶⁰ The amplitude of the REP strongly decreases with the increase in the homogeneous broadening linewidth, while the inhomogeneous broadening mechanism affects the REP similar to its effect on the absorption spectrum while keeping its integrated intensity unchanged. Thus, the analysis of the REPs provides a convenient approach to quantitatively determine the contribution of the homogeneous and inhomogeneous broadening mechanisms to the absorption spectrum linewidth.

Though qualitative details of the excited state structural dynamics can be obtained directly from the analysis of the experimental REP, more quantitative information requires the use of

theories which predict the RR intensity. These theories include parameters that describe the difference in structure of the ground and excited state as well as the contribution of broadening mechanisms. Different approaches have been successfully developed to achieve this goal. The introduction of models that describe the interactions between solute and its local environment has made it possible to characterize quantitatively, the response of the local environment to the change in the charge distribution of the solute upon excitation.^{66,68-73} In the next section, two of the theories which have been applied to simulate the RR intensity of molecules are described.

2.1 Theoretical methods

2.1.1 Quantum mechanical description of the resonance Raman intensity

A theoretical description of RR intensity can be obtained from the general expression of the cartesian transition polarizability tensor derived first by Kramers, Heisenberg⁷⁴ in 1925, and later modified by Dirac⁷⁵ in 1927 by using second order time dependent perturbation theory. For a Raman transition from initial state $|I\rangle$ to final state $|F\rangle$, the expression for the $\rho\sigma^{\text{th}}$ component of the transition polarizability tensor is given by,

$$(\alpha_{\rho\sigma})_{I\rightarrow F} = \sum_V \frac{\langle F|m_\rho|V\rangle\langle V|m_\sigma|I\rangle}{E_V-E_I-E_L-i\Gamma} + \frac{\langle F|m_\sigma|V\rangle\langle V|m_\rho|I\rangle}{E_V-E_F+E_L-i\Gamma} \quad (2.1)$$

Here $|I\rangle$, $|V\rangle$ and $|F\rangle$ are the initial, intermediate and final vibronic states and E_I , E_V and E_F are their energies. E_L and E_S are the incident and scattered photon energies. m_ρ is the dipole moment operator and Γ is the homogeneous linewidth. The Eq. 2.1 is known as KHD equation of transition polarizability tensor.

Now, under resonance condition with a strongly allowed electronic state, we can simplify the Eq. 2.1 by applying Born-Oppenheimer approximation to write vibronic states as a product of electronic and vibrational states. According to Born-Oppenheimer approximation, the vibronic states become,

$$|I\rangle = |g(r; Q)\rangle|i(Q)\rangle \quad (2.2a)$$

$$|V\rangle = |e(r; Q)\rangle|v(Q)\rangle \quad (2.2b)$$

$$|F\rangle = |g(r; Q)\rangle |f(Q)\rangle \quad (2.2c)$$

where, $|g\rangle$ and $|e\rangle$ are the ground and excited electronic states and $|i\rangle$, $|v\rangle$, $|f\rangle$ are the vibrational states. r and Q denote the electronic and nuclear coordinates respectively. Electronic wavefunctions depend parametrically on the nuclear coordinates. Thus, the elements of the transition dipole moment can be evaluated first with respect to the electronic part. So, the transition dipole length matrix element becomes,

$$\langle F | m_\rho | V \rangle = \langle f | \langle g | m_\rho | e \rangle | v \rangle = \langle f | M_\rho(Q) | v \rangle \quad (2.3)$$

The electronic transition length matrix element, $M_\rho(Q)$ is a function of nuclear coordinates according to Born-Oppenheimer approximation. We can expand the transition length matrix element by Taylor series expansion around ground state equilibrium geometry Q_0 .

$$M_\rho(Q) = M_\rho(Q_0) + \sum_k \frac{\partial M_\rho}{\partial Q_k} Q_k + \dots \dots \dots \quad (2.4)$$

Now using Condon approximation, only the first term $M_\rho(Q_0)$ is considerable and the other terms with explicit nuclear coordinate dependence can be ignored. Assuming the resonance condition with a single excited electronic state, we can choose a set of vector so that only one of the transition length vector is nonzero and sum over the ρ and σ indices can be eliminated.

Finally, considering the vibrational levels of the resonant electronic state contribute significantly to the sum over virtual states and dropping the non-resonant term (second term of Eq. 2.1), the transition polarizability tensor becomes,

$$\alpha_{i \rightarrow f} = M^2 \sum_v \frac{\langle f | v \rangle \langle v | i \rangle}{\epsilon_v - \epsilon_i + E_0 - E_L - i\Gamma} \quad (2.5)$$

Here, M is the transition dipole moment length. ϵ_v and ϵ_i are the energies of the vibrational states v and i . E_0 is the energy difference between two vibrational states of the resonant electronic states. The Eq. 2.5 is the Albrecht's A term⁷⁶ expression between two allowed electronic states.

Substituting Eq. 2.5 in the expression for the Raman cross-section⁷⁶ we obtain,

$$\begin{aligned}\sigma_{i \rightarrow f} &= \frac{8\pi e^4 M^4 E_S^3 E_L}{9\hbar^4 c^4} \left| \sum_v (\alpha_{\rho\sigma})_{I \rightarrow F} \right|^2 \\ &= \frac{8\pi e^4 M^4 E_S^3 E_L}{9\hbar^4 c^4} \left| \sum_v \frac{\langle f|v\rangle\langle v|i\rangle}{\epsilon_v - \epsilon_i + E_0 - E_L - i\Gamma} \right|^2\end{aligned}\quad (2.6)$$

This is known as the sum-over-state expression for the Raman cross-section. In the same way, the expression for absorption cross section can be obtained and is given by,

$$\sigma_A = \frac{4\pi^2 e^2 M^2 E_L}{3\hbar c n} \sum_v \frac{\Gamma}{\pi} \frac{|\langle v|i\rangle|^2}{\epsilon_v - \epsilon_i + E_0 - E_L + \Gamma^2}\quad (2.7)$$

where n is the refractive index of solution.

The Eqs. 2.6 and 2.7 have the disadvantage that for the convergence of the expression, the sum has to be evaluated for a very large number of vibrational levels of the electronic excited state. This becomes particularly challenging for large polyatomic molecules. In this next section, the sum-over-states approach will be used as a starting point to derive the theoretical approach that has been employed in this thesis, namely, the time-dependent wave packet propagation (TDWP) theory of the RR intensity.

2.1.2 Time-dependent wave packet propagation (TDWP) theory

There are other methods also, such as transform theory,^{62,77-79} which can describe the RR intensity, but our focus in this chapter will be on TDWP theory.^{59,71} The time-dependent picture of Resonance Raman cross section was first developed by Lee and Heller⁵⁹ using time-dependent perturbation theory and since then it has been used to determine the RR intensity and initial excited state structural dynamics of molecules.^{80,45,50,51,58,60,61,63-65,81-97} By applying time-dependent approach, we can interpret the Raman excitation profile and also the absorption and emission spectra.

The expressions obtained for the Raman and absorption cross-sections using the sum-over-state approach can be converted into the time domain by writing the denominator of the

Raman polarizability expression from Eq. 2.6 as a half-Fourier transform.^{60,66,98} The polarizability tensor now transforms into the following expression,

$$\alpha_{i \rightarrow f} = \frac{iM^2}{\hbar} \int_0^\infty \sum_v \langle f|v\rangle \langle v|i\rangle \cdot \exp\left[\frac{-i(\varepsilon_v - \varepsilon_i + E_0 - E_L - i\Gamma)t}{\hbar}\right] dt \quad (2.8)$$

Since, $|v\rangle$ is an eigenket of the excited electronic state, we can get the following expression,

$$\langle v|e^{-i(\varepsilon_v + E_0)t/\hbar} = \langle v|e^{-i\mathbf{H}t/\hbar} \quad (2.9)$$

where \mathbf{H} is vibrational Hamiltonian of the excited state. Now, combining the Eq. 2.8 and Eq. 2.9, the expression becomes,

$$\alpha_{i \rightarrow f} = \frac{iM^2}{\hbar} \int_0^\infty \sum_v \langle f|v\rangle \langle v|e^{-i\mathbf{H}t/\hbar}|i\rangle \cdot \exp\left[\frac{i(\varepsilon_i + E_L + i\Gamma)t}{\hbar}\right] dt \quad (2.10)$$

By using the advantage of the identity and the time evolution of operators we can get,

$$\sum_v \langle f|v\rangle \langle v|e^{-i\mathbf{H}t/\hbar}|i\rangle = \langle f|i(t)\rangle \quad (2.11)$$

The Eq. 2.10 now changes into the following expression by using closure theorem,

$$\alpha_{i \rightarrow f} = \frac{iM^2}{\hbar} \int_0^\infty \langle f|i(t)\rangle \cdot \exp\left[\frac{i(\varepsilon_i + E_L)t}{\hbar}\right] e^{-\Gamma t/\hbar} dt \quad (2.12)$$

The expression for Raman cross section (Eq. 2.6) transforms into the following,

$$\sigma_{i \rightarrow f} = \frac{8\pi e^4 M^4 E_s^3 E_L}{9\hbar^4 c^4} \left| \int_0^\infty \langle f|i(t)\rangle \cdot \exp\left[\frac{i(\varepsilon_i + E_L)t}{\hbar}\right] e^{-\Gamma t/\hbar} dt \right|^2 \quad (2.13a)$$

Similarly, we can also get the absorption cross section by taking the full-Fourier transform of the denominator of Eq. 2.7.

$$\sigma_A = \frac{4\pi^2 e^2 M^2 E_L}{3\hbar c n} \int_{-\infty}^\infty \langle i|i(t)\rangle \cdot \exp\left[\frac{i(\varepsilon_i + E_L)t}{\hbar}\right] e^{-\frac{\Gamma t}{\hbar}} dt \quad (2.13b)$$

Now we can interpret the Eq. 2.13a and 2.13b as depicted in Fig. 2.2. As, the electronic transition moment, $e\mathbf{M}$ interacts with the incident electric field, the vertical excitation of the ground vibrational wave function, $|i\rangle$ places itself to the Franck Condon region of the excited state potential surface of S_1 . There, it associates with a different Hamiltonian \mathbf{H} of the excited electronic state and evolves in time as $|i(t)\rangle$. It goes back and forth along the vibrational state of the excited potential energy surface of S_1 . The absorption cross section can be determined by taking the overlap between this propagating wave-packet⁹⁹, $|i(t)\rangle$, with the ground vibrational wave function $|i\rangle$ multiplied by a damping factor $\exp(-\Gamma t/\hbar)$ at time zero ($t = 0$) and taking the full-Fourier transform of it. Upon electronic transition at time, $t = 0$, the ground vibrational state does not get chance to evolve with time and the overlap $\langle i|i(t)\rangle$ is unity. As time proceeds, $|i(t)\rangle$ moves away from the ground vibrational function $|i\rangle$ and the overlap between these two states decreases. It again increases when $|i(t)\rangle$ completes its one full cycle of harmonic motion and comes back to the previous position to again start the propagation. The time dependence of the overlap $\langle i|i(t)\rangle$ determines the shape of the absorption spectra. The absorption spectrum becomes broad for short timescale of the event.

Raman cross section is determined by the half-Fourier transform of the overlap between the final ground vibrational wave function, $|f\rangle$, and the propagating wave-packet $|i(t)\rangle$. At time zero, there is no overlap between those two states. As time progresses, $|i(t)\rangle$ moves to the right and makes a significant overlap with the one lobe of vibrational state $|f\rangle$ and Raman overlap rapidly increases. The band shape of Raman excitation profile also was determined from the time dependence of $\langle f|i(t)\rangle$ overlap. Now, if the excited electronic state is not displaced from the ground electronic state, $|i(t)\rangle$ does not get chance to move far for a significant overlap with $|f\rangle$, the Raman amplitude falls off. So the enhancement of the Albrecht A-term results for those vibrations for which the large electronic distortion happens following excitation.

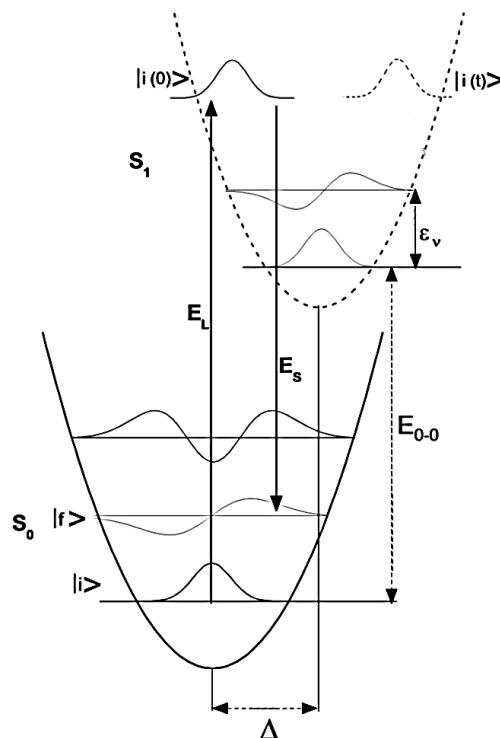


Fig. 2.2 The pictorial representation of time-dependent wave-packet propagation theory of Resonance Raman scattering. E_L and E_S are the excitation and scattered energies respectively. E_{0-0} is the energy between two zero vibrational states of ground (S_0) and excited (S_1) electronic states. Δ is the dimensionless displacement between S_0 and S_1 state along nuclear coordinate. $|i(\mathbf{0})\rangle$ is the vibrational wave function of S_0 state. $|i(\mathbf{0})\rangle$ is independent of time, but goes to excited electronic state after excitation and evolves in time, $|i(\mathbf{t})\rangle$, and propagates on the vibrational state of S_1 state.

To determine the Raman and absorption cross-section, it is necessary to compute the multidimensional overlaps $\langle i|i(t)\rangle$ and $\langle f|i(t)\rangle$. This is a difficult task especially for polyatomic molecules. However, it is possible to obtain a simplified expression for these overlaps by using different approximations. By considering the harmonicity and equality of the potential energy surfaces of ground and excited electronic states, and by neglecting Duschinsky rotation,⁹⁸ the multidimensional overlaps can be calculated as products of N one-dimensional overlaps:

$$\langle f|i(t)\rangle = \langle f_1|i_1(t)\rangle \langle f_2|i_2(t)\rangle \dots \langle f_N|i_N(t)\rangle \quad (2.14)$$

With the assumption that, only one of the mode undergoes a vibronic transition from the ground vibrational state to the first vibrational state Eq. 2.14 becomes,

$$\langle f|i(t)\rangle = \langle 1_k|0_k(t)\rangle \prod_{j \neq k}^N \langle 0_j|0_j(t)\rangle \quad (2.15a)$$

and

$$\langle i|i(t)\rangle = \prod_{j=1}^N \langle 0_j|0_j(t)\rangle \quad (2.15b)$$

Considering equalities of ground and excited states vibrational frequencies, the one-dimensional overlaps can be explicitly written as following analytic expressions,⁹⁸⁶⁰¹⁰⁰

$$\langle 0_j|0_j(t)\rangle = \exp\left[-\frac{\Delta_j^2}{2}\left(1 - \exp^{-i\omega_j t} - \frac{i\omega_j t}{2}\right)\right] \quad (2.16a)$$

and using the recursion formulae,

$$\langle 1_j|0_j(t)\rangle = \frac{\Delta_j}{\sqrt{2}} [\exp^{-i\omega_j t} - 1] \langle 0_j|0_j(t)\rangle \quad (2.16b)$$

$$\langle 2_j|0_j(t)\rangle = 2^{-\frac{1}{2}} \frac{\Delta_j}{\sqrt{2}} [\exp^{-i\omega_j t} - 1]^2 \langle 0_j|0_j(t)\rangle \quad (2.16c)$$

where Δ_j is the dimensionless displacement of the j^{th} normal mode. The time-dependent Raman overlap is linearly dependent on the dimensionless displacement Δ .

Now, inserting the products of the one-dimensional overlaps into Eq. 2.13a and 2.13b, the cross-sections can be written as explicitly multidimensional forms,

$$\begin{aligned} \sigma_{0 \rightarrow 1}(E_L) = & \frac{8\pi^4 E_S^3 E_L M^4}{9\hbar^6 c^4} \left| \int_0^\infty \exp\left[\frac{i(E_L - E_0)t}{\hbar} - \frac{\Gamma t}{\hbar}\right] \times \frac{\Delta_k}{\sqrt{2}} (\exp^{-i\omega_k t} - 1) \right. \\ & \left. \times \prod_{j \neq k}^N \exp\left(-\frac{\Delta_j^2}{2} [1 - \exp^{-i\omega_j t}]\right) dt \right|^2 \end{aligned} \quad (2.17a)$$

and

$$\begin{aligned} \sigma_A(E_L) = & \frac{4\pi^4 E_L M^2}{6\hbar^2 n c} \int_{-\infty}^\infty \exp\left[\frac{i(E_L - E_0)t}{\hbar} - \frac{\Gamma t}{\hbar}\right] \\ & \times \prod_{j=1}^N \exp\left(-\frac{\Delta_j^2}{2} [1 - \exp^{-i\omega_j t}]\right) dt \end{aligned} \quad (2.17b)$$

Comparison of Eqs. 2.17a and 2.17b, it is readily observed that, the magnitude of RR cross-section is independent of the sign of Δ , unlike the one-dimensional overlap itself.

2.1.3 Contribution of homogeneous and inhomogeneous broadenings to the total spectral linewidth

Here, the above equations assume only isolated molecules. In this case, there is only one way that the excited molecule can relax is radiatively. The homogeneous linewidth Γ then exhibits the natural radiative width, which is a fraction of a wavenumber. But, there are also environmental molecules (solvent) which are not in resonance with the incident light but they perturb the chromophore system upon excitation. In solution environments, a faster radiationless decay is possible due to the interactions with the solvent molecules.

To see the effect of the homogeneous broadening linewidth on the absorption and Raman overlaps and cross-sections, a hypothetical example has been considered. Let us assume that there is a single resonance enhanced mode with the following parameters: $E_0=44000\text{ cm}^{-1}$; $M=1\text{ \AA}$; $\Delta=1$; $\omega=1000\text{ cm}^{-1}$. Fig. 2.3 (a) and (b) show the damped absorption and Raman overlaps for two values of the homogeneous broadening linewidth. An increase in the homogeneous linewidth from 50 cm^{-1} to 100 cm^{-1} decreases the amplitude of both overlaps with time. However, the effects on the cross-sections are different: in the case of absorption (c), increasing the homogeneous linewidth produces a broadening in the spectra but no prominent changes in the integrated intensity. On the other hand, in the case of the Raman cross-section (d) it broadens the REP but also decreases the integrated intensity.

Inhomogeneous broadening can occur due to the different local environments or conformations of the molecule, or also from dynamics that take place on time scales longer than the Raman scattering processes. Here, the inhomogeneous broadening has been considered as “static” and its contribution to the absorption spectrum and REP has been introduced by using a normalized Gaussian distribution of the ground-state energy (E_0) energies with θ standard deviation. In this thesis, the effect of the inhomogeneous broadening on the absorption and RR cross-sections has been introduced by using a normalized Gaussian distribution of the zero-zero energies (E_0) with θ as its standard deviation or 2θ being the full line width, and the eqns. 2.17a and 2.17b become,

$$\begin{aligned} \sigma_{0 \rightarrow 1}(E_L) = & \frac{8\pi^4 E_S^3 E_L M^4}{9\hbar^6 c^4 \theta \sqrt{2\pi}} \int_0^\infty dE \exp\left[-\frac{(E - E_0)^2}{2\theta^2}\right] \\ & \times \left| \int_0^\infty \exp\left[\frac{i(E_L - E_0)t}{\hbar} - \frac{\Gamma t}{\hbar}\right] \times \frac{\Delta_k}{\sqrt{2}} (\exp^{-i\omega_k t} - 1) \right. \\ & \left. \times \prod_{j \neq k}^N \exp\left(-\frac{\Delta_j^2}{2} [1 - \exp^{-i\omega_j t}]\right) dt \right|^2 \end{aligned} \quad (2.18a)$$

and

$$\begin{aligned} \sigma_A(E_L) = & \frac{4\pi^4 E_L M^2}{6\hbar^2 n c \theta \sqrt{2\pi}} \int_0^\infty dE \exp\left[-\frac{(E - E_0)^2}{2\theta^2}\right] \times \int_{-\infty}^\infty \exp\left[\frac{i(E_L - E_0)t}{\hbar} - \frac{\Gamma t}{\hbar}\right] \\ & \times \prod_{j=1}^N \exp\left(-\frac{\Delta_j^2}{2} [1 - \exp^{-i\omega_j t}]\right) dt \end{aligned} \quad (2.18b)$$

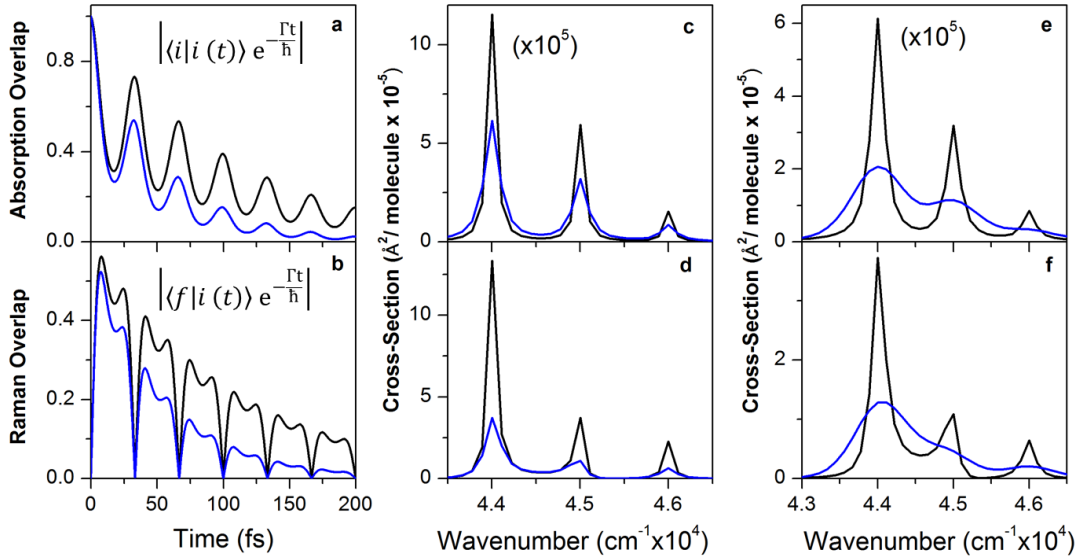


Fig. 2.3 (a) and (b): Single-mode time-dependent damped absorption and Raman overlaps for two different values of the homogeneous broadening linewidth respectively: $\Gamma = 50 \text{ cm}^{-1}$ (black) and $\Gamma = 100 \text{ cm}^{-1}$ (blue). (c) and (d): Effect of the homogeneous broadening linewidth in the absorption and Raman cross-section without contribution from inhomogeneous broadening. (e) and (f): Effect of the inhomogeneous broadening linewidth in the absorption and Raman cross-section: $\Gamma = 100 \text{ cm}^{-1}$; $\theta = 0 \text{ cm}^{-1}$ (black) and $\theta = 300 \text{ cm}^{-1}$ (blue). Other parameters used in the calculation: $E_0 = 44000 \text{ cm}^{-1}$, $M = 1 \text{ \AA}$, $\omega = 1000 \text{ cm}^{-1}$, $\Delta = 1$.

Fig. 2.3 (e) and (f) show the dependence of the absorption and Raman cross-section for two different values of the inhomogeneous broadening linewidth. Increasing the inhomogeneous broadening linewidth broaden the absorption spectrum as well as the REP, but does not affect the integrated intensity to a significant extent.

The differences between the effects of the two broadening mechanisms on the absorption and REP were discussed above. These differences reveal (and because of the sensitivity of the Raman intensity to the homogenous broadening) that the analysis of the REPs along with the absorption spectrum, can help to quantify the contribution of the homogeneous and inhomogeneous broadening mechanisms to the absorption spectrum.^{50,61,67,101} This is important because both types of broadening produce similar effects on the absorption spectrum and thus, the contributions from mechanisms cannot be determined by analyzing the absorption spectrum alone.

2.1.4 Model for solute-solvent bath interaction

A more general expression is obtained by adding the solute-solvent bath interaction in the damping term because in solution this term has dominating contribution to the line-shape function. This can be done by introducing a line-shape function, $g_{solv}(t)$ in the damping terms of Eqs. 2.18a and 2.18b and after using them Raman and absorption cross sections become,^{66,68,72,102,103}

$$\begin{aligned} \sigma_R(E_L) = & \frac{8\pi^4 E_S^3 E_L M^4}{9\hbar^6 c^4 \theta \sqrt{2\pi}} \int_0^\infty dE \exp\left[-\frac{(E - E_0)^2}{2\theta^2}\right] \\ & \times \left| \int_0^\infty \exp\left[\frac{i(E_L - E_0)t}{\hbar} - g_{solv}(t)\right] \frac{\Delta_k}{\sqrt{2}} (\exp(-i\omega_k t) - 1) \right. \\ & \times \left. \prod_{j=1}^N \exp\left(-\frac{\Delta_j^2}{2} [1 - \exp(-i\omega_j t)]\right) dt \right|^2 \end{aligned} \quad (2.19a)$$

and

$$\sigma_{\Lambda}(E_L) = \frac{4\pi^4 E_L M^2}{6\hbar^2 n c \theta \sqrt{2\pi}} \int_0^{\infty} dE \exp\left[-\frac{(E - E_0)^2}{2\theta^2}\right] \times \int_{-\infty}^{\infty} \exp\left[\frac{i(E_L - E_0)t}{\hbar} - g_{\text{solv}}(t)\right] \times \prod_{j=1}^N \exp\left(-\frac{\Delta_j^2}{2} [1 - \exp(-i\omega_j t)]\right) dt \quad (2.19b)$$

Different models have been developed to account for solute and solvent bath interactions. Here we have used a general expression for the term, $g_{\text{solv}}(t)$, which was developed by Mukamel and co-workers using stochastic theory and Brownian oscillator model.^{68,70,72,102} Unlike stochastic theory which only takes the effect of solvent on solute into account, a more general Brownian oscillator model considers effect of a change in solute dipole moment upon optical excitation on solvent degrees of freedoms.^{68,70,102} In the Brownian oscillator model, the solvent coordinates are considered as vibrational modes coupled to the electronic excitation of solute. If the collective movements of all the solvent molecules are considered as a single-mode strongly overdamped Brownian oscillator, the line shape function can be written as,^{68,70}

$$g_{\text{solv}}(t) = g'(t) + i g''(t) \quad (2.20a)$$

where the real and imaginary parts are given by the following Eqs.,

$$g'(t) = \frac{\lambda_s}{\Lambda} \cos\left(\frac{\hbar\Lambda}{2k_B T}\right) [\exp(-\Lambda t) + \Lambda t - 1] + \left(\frac{4\lambda_s \Lambda k_B T}{\hbar}\right) \sum_{m=1}^{\infty} \frac{\exp(-\nu_m t) + \nu_m t - 1}{\nu_m (\nu_m^2 - \Lambda^2)} \quad (2.20b)$$

$$g''(t) = -\frac{\lambda_s}{\Lambda} [\exp(-\Lambda t) + \Lambda t - 1] \quad (2.20c)$$

$$\nu_m = 2\pi m / \hbar \beta, \quad (2.20d)$$

where λ_s and Λ are the solvent reorganization energy and inverse solvent correlation time scale ($\Lambda = 1/2\pi c\tau$) respectively. $\beta = 1/k_B t$, where k_B is the Boltzmann's constant. ν_m is known as Matsubara frequencies and m is a positive integer. By incorporating these terms into time dependent formulas provide us to probe the solvation dynamics within few tens of femtoseconds

upon photoexcitation.⁶⁹ This model has been successfully applied to extract the quantitative information of solvation dynamics for a number of photoexcited chromophores in solution and inside the protein core.^{50,51,66,82,86,88–91,95–97,104–106}

2.1.5 Total reorganization energy

The total reorganization energy of the system has contribution from the solvent response as well as from the excess of vibrational energy of the solute upon optical excitation:

$$\lambda_{\text{total}} = \lambda_{\text{S}} + \lambda_{\text{int}} \quad (2.21a)$$

where λ_{int} is the total internal reorganization energy summed over all vibrational degrees of freedom. In the case of the harmonic approximation for potential energy surfaces, it can be estimated from:

$$\lambda_{\text{int}} = \sum_{j=1}^{3N-6} \frac{(\Delta_j^2 \hbar \omega_j)}{2}, \quad (2.21b)$$

here ω_j is the mode frequency in the ground and excited state and Δ_j is the corresponding “dimensionless” displacement.

2.1.6 Conversion from normal mode to internal coordinates

To determine the changes in the internal coordinates upon optical excitation, it is necessary to relate the “dimensionless” coordinates with the normal mode coordinates. If the matrix that relates the internal coordinates with the normal mode coordinates is known, then it is possible to estimate the changes in the internal coordinates upon optical excitation. The internal (r) and normal mode (Q) coordinates are related by,

$$r_i = \sum_j A_{ji} Q_j \quad (2.22)$$

where, A_{ji} is the j^{th} element of the pseudo inverse of the matrix S which transforms internal coordinates to the normal mode coordinates. The matrix S was determined from the frequency calculation using GAUSSIAN09 described in later section.

Normal mode coordinates (Q) are related to dimensionless coordinate (q) through the transformation,

$$Q_j = \left(\frac{\hbar}{\omega_j} \right)^{-\frac{1}{2}} q_j = 5.8065 \omega_j^{-\frac{1}{2}} q_j \quad (2.23)$$

where ω_j is the frequency of the j^{th} normal mode in cm^{-1} .

Combining Eqs. 2.22 and 2.23 the internal and dimensionless coordinates can be related as,

$$r_i = 5.8065 \sum_j A_{ji} \omega_j^{-\frac{1}{2}} q_j \quad (2.24)$$

Eqn. 2.24 clearly shows that internal coordinate r (expressed in \AA) is linearly dependent on q (dimensionless), and therefore, changes in these two coordinates can be related,

$$\begin{aligned} r_i - r'_i = \delta_i &= 5.8065 \sum_j A_{ji} \omega_j^{-\frac{1}{2}} (q_j - q'_j) \\ &= 5.8065 \sum_j A_{ji} \omega_j^{-\frac{1}{2}} \Delta_j \end{aligned} \quad (2.25)$$

2.2 Experimental Methods

2.2.1 Experimental set-up for UVRR experiments

The excitation source was a ns pulsed Ti:Sapphire laser of 1 kHz repetition rate pumped by a frequency doubled output (527 nm) of a ns pulsed Nd: YLF laser (Evolution, Coherent Inc.). The IR light from a Ti:Sapphire crystal was doubled in frequency with a beta Barium borate (BBO) crystal to produce the second-harmonic frequency that is in the visible region. Further, the IR and visible frequencies were mixed in another BBO crystal to obtain third-harmonic UV light at 257-280 nm.

Samples (300 μL) held in NMR tubes were illuminated by the UV light of power less than 500 μW . The sample tubes were attached with device for rotation of the tube along its axis during recording to minimize the photodamage to samples. Self-absorption of scattered light was

reduced by employing backscattering collection configuration. The scattered light was collected with a 135° backscattering geometry and focused using a pair of fused-silica lenses into a single grating (3600 grooves/mm) monochromator (JobinYvon) which is assembled with a liquid nitrogen-cooled charge-coupled device (CCD) detector containing 1024×256 pixels. The optical diagram of experimental set-up is shown in Fig. 2.4.

The Raman spectra obtained were calibrated using known standard solvent bands (dimethyl formamide (DMF), dimethyl sulphoxide (DMSO), cyclohexane, indene, isopropanol and acetonitrile (ACN)). Spectra were fitted by Lorentzian functions using Synergy software (JobinYvon). Area under the curve was taken as a measure of the intensity of the bands. Flavin molecules are very prone to photodegradation. Thus, spectra were recorded in less than $500 \mu\text{W}$ power exposure and the absence of any photodamage is ensured by comparing the first and last cycles recorded and ensuring that there was no loss of Raman intensity.

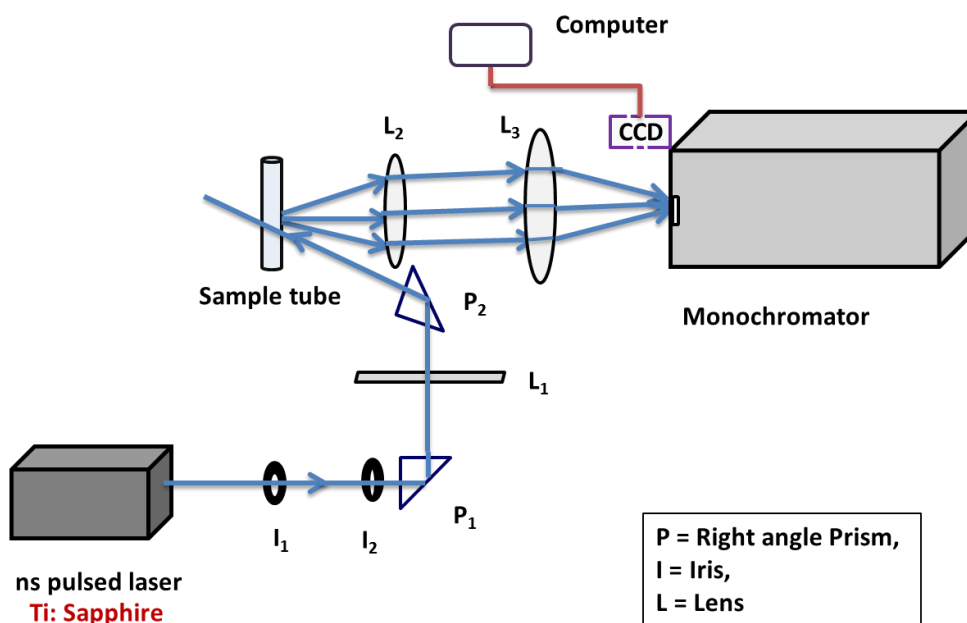


Fig.2.4 Optical diagram for UVRF experimental set-up

2.2.2 Depolarization ratio measurement

Raman depolarization ratio is given by,

$$\rho = \frac{I_{\perp}}{I_{\parallel}} \quad (2.26)$$

where I_{\perp} and I_{\parallel} are the intensity of scattered radiation perpendicular and parallel to the direction of incident light. Spectra were recorded at 266 nm excitation for flavin molecules by using a Glan-laser α -BBO polarizer (ThorLabs, Newton, NJ) and placed in front of the slit. A scrambler was introduced behind the polarizer to avoid the loss of intensity for the polarization dependence of the detector. The scattered radiation parallel to the direction of polarization of incident light and scattered radiation perpendicular to the direction of the polarization to the incident light was recorded by changing the angle of the polarizer. The ratios of these two intensities give the depolarization ratio of Raman modes of the sample.

In order to verify the Raman depolarization ratios of flavin molecules, the depolarization ratios of Raman bands of cyclohexane and carbon tetrachloride solvents were measured and compared with the literature values (Table 2.1)^{107,108} and they were found to agree well the within the experimental error value.

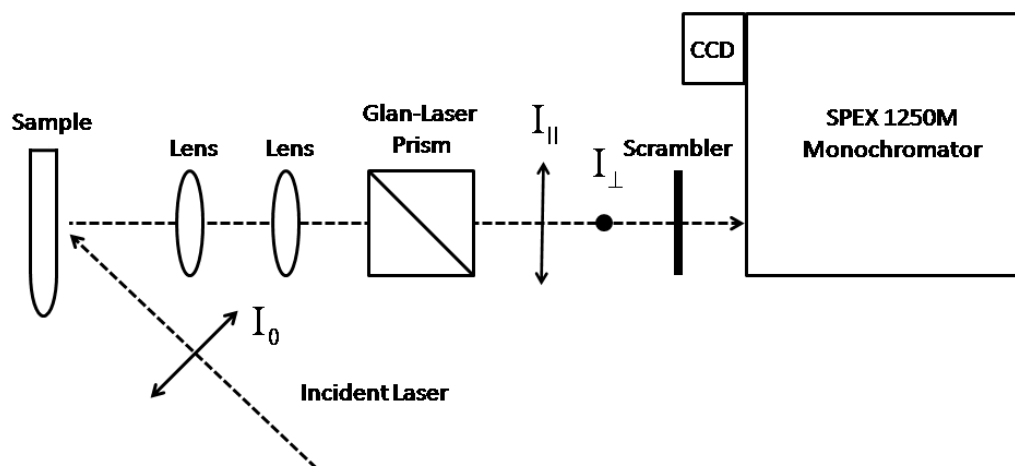


Fig. 2.5 Diagram of the experimental setup used for the measurement of the depolarization ratio. The scattered light is passed through a two collecting lenses and is incident in a Glan-laser prism to filter out the parallel and perpendicular components of the scattered light. A scrambler placed between the prism and the spectrometer slit reduce the polarization dependence of the spectrometer.

Table 2.1 Depolarization ratios of solvent Raman bands

Solvent	Raman Band (cm ⁻¹)	^a Depolarization Ratio	^b Excitation at 251 nm
Cyclohexane	802	0.098	0.1 ± 0.02
	1026	0.83	0.71 ± 0.07
	1265	0.79	0.74 ± 0.07
	1445	0.74	0.74 ± 0.09
			^c Excitation at 632.8 nm
Carbon tetrachloride	218	0.77	0.758±0.006
	314	0.78	0.751±0.005

^aIn this work; ^bfrom ref. 107; ^cfrom ref. 108.

2.2.3 Spectrometer and detector efficiency

The spectrometer can't detect scattered light intensity in all wavelengths with same efficiency. To overcome the wavelength dependence of the spectrometer, we have corrected the scattered spectra by using the spectral correction factor $S(\lambda)$ which is given by,

$$S(\lambda) = \frac{D(\lambda)}{T(\lambda)} \quad (2.27)$$

where, $D(\lambda)$ is the spectrum from a calibrated D₂O lamp (Ocean Optics Inc, Dunedin, FL) and $T(\lambda)$ is the calibrated output of the lamp. $D(\lambda)$ has been recorded at the same grating position as the actual spectrum for each excitation wavelength. We have to multiply the whole spectra by this factor $S(\lambda)$ for intensity correction. The calibrated output of the lamp was not available for all values of wavelengths in the region of interest. Thus, a linear extrapolation procedure was used to determine these values and was carried out as shown in Fig. 2.6. A representative example of $S(\lambda)$ used to correct the spectrum obtained at 262.9 nm excitation wavelength, is shown in Fig. 2.7.

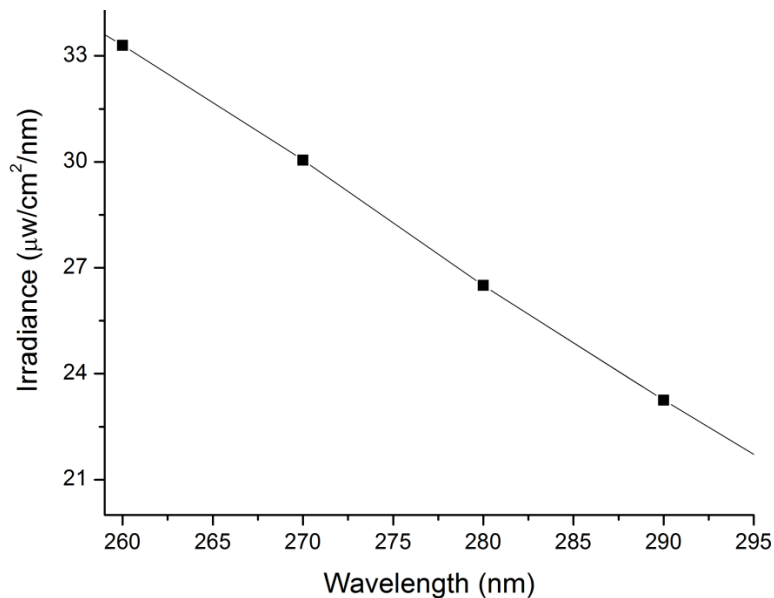


Fig 2.6 (*points*) Calibrated output of the D₂O lamp. (*line*) Linear extrapolation to the calibrated output to estimate the values in the wavelength range of interest.

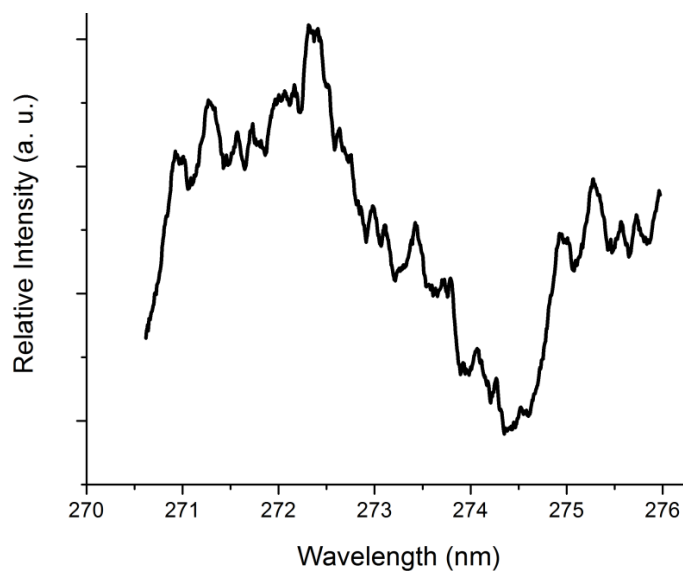


Fig. 2.7 Spectral sensitivity $S(\lambda)$ of the spectrometer recorded using the standard D₂O lamp. This function was used to correct the spectrum of flavins obtained at 262.9 nm excitation.

2.2.4 Self-absorption correction

The intensity of Raman bands are corrected from the self-absorption of sample by introducing the term $K(\lambda_N, \lambda_S)$, and it is calculated using the formula¹⁰⁹ given below,

$$K(\lambda_N, \lambda_S) = \frac{\varepsilon_N \chi + \varepsilon_0}{\varepsilon_S \chi + \varepsilon_0} \quad (2.28)$$

where ε_N and ε_S are the extinction coefficients at the wavelength position of the Raman band of the sample and internal standard respectively. ε_0 is the extinction coefficient at the excitation wavelength. χ is given by the following formula,

$$\chi = \sin \left[\cos^{-1} \left(\frac{n_1}{n_2} \cos \varphi \right) \right] \quad (2.29)$$

where, n_1 and n_2 are the values of the refractive index corresponding to air and the sample solution, assumed here to be 1.0 and 1.33 respectively. $\varphi=45^\circ$ is the angle between the direction of the excitation light and the tube. To minimize the intensity loss from self-absorption, the NMR tube was placed such that the laser beam was focused near the surface of the tube which allows minimizing the path length of the scattering light inside the sample and then maximizes the intensity of the Raman spectrum.

2.2.5 UVRR cross section determination

The experimental absolute Raman cross section of each Raman band was estimated from the known Raman cross sections of the internal standard sodium sulfate¹¹⁰ using the formula⁶¹ given below,

$$\sigma_N = \frac{8\pi}{3} \left(\frac{1+2\rho}{1+\rho} \right)_N \left(\frac{I_N}{I_S} \right) \left(\frac{C_S}{C_N} \right) \left(\frac{\partial \sigma_S}{\partial \Omega} \right)_{\perp+\parallel} \frac{S(\lambda_S)}{S(\lambda_N)} K(\lambda_N, \lambda_S), \quad (2.30)$$

where N and S stand for sample and internal standard respectively. The intensities (I_N) of the N th mode of the sample and the intensity (I_S) of the internal standard were determined from the area of the Lorentzian fit of that particular Raman band. C_S and C_N are the concentrations of internal standard and sample solutions respectively. $\left(\frac{\partial \sigma_S}{\partial \Omega} \right)_{\perp+\parallel}$ is the total differential cross section of the internal standard. ρ is the depolarization ratio of the Raman band of the solute.

2.2.6 Total differential Raman cross-section of the internal standard

The values of the absolute Raman differential cross sections of internal standard at different excitation wavelengths is given by the Albrecht A term expression¹¹⁰ as written below,

$$\left(\frac{\partial\sigma_S}{\partial\Omega}\right)_{\perp+\parallel} = K_2 \nu_0 (\nu_0 - \nu_{mn})^3 \left[\frac{\nu_e^2 + \nu_0^2}{\nu_e^2 - \nu_0^2}\right]^2 \quad (2.31)$$

where K_2 is a constant. ν_0 is the excitation frequency and ν_e is the frequency of transition to the resonant excited state.¹¹⁰ For SO_4^{2-} (981 cm^{-1} band), $K_2 = 2.75 \times 10^{-26} \text{ cm}^2/\text{molecule}$ and $\nu_e = 137000 \text{ cm}^{-1}$. The Raman cross section of internal standard (SO_4^{2-}) for 981 cm^{-1} band at 260 nm excitation calculated using Albrecht A term to be $255.4 \times 10^{-30} \text{ cm}^2/\text{molecule}$.

2.2.7 Experimental absorption cross-section

The absolute absorption cross-sections ($\text{\AA}^2/\text{molecule}$) were determined from,

$$\sigma_A = \frac{2.303 \times 10^{19} \varepsilon}{N_A} \quad (2.32)$$

where ε is the extinction coefficient of the solute in $\text{cm}^{-1} \text{ M}^{-1}$ and N_A is the Avogadro's number.

2.3 Quantum chemical calculations

Since its discovery in 1964, density functional theory (DFT) has been extensively used by physicists and chemists to determine the properties of isolated molecule and their clusters, solids, and mechanism of chemical reactions. DFT method derives properties of the molecule based on a determination of the electron density of the molecule. While the wavefunction (which is basis of traditional quantum chemistry methods), is not a physical reality but a mathematical construct, electron density is a physical characteristic of all molecules.

In this thesis, quantum chemical calculations were done using DFT as implemented in the Gaussian09 program suite. To optimize the ground state structure and frequency calculations for flavin molecules, we employed B3LYP functional^{111,112} in combination with 6-31G(d), 6-31G(d,p) and TZVP¹¹³ basis sets. But we have observed that the agreement between theoretical and experimental frequencies is better by using TZVP basis set, compared to the other basis sets. Quantum chemical calculations on flavin derivatives using various methods applied previously using TZVP basis set.^{55,114–116} So in all of our DFT calculations, we have used this basis set.

Solvent environment was included using polarizable continuum model (PCM).¹¹⁷ Dielectric constant of $\epsilon = 80.35$ for water was chosen.

To calculate the properties of singlet excited states such as electronic absorption spectrum, gradient on excited PES, time-dependent density functional theory (TDDFT) was applied. This method has been a popular choice for small molecules, such as, aromatic amino acids^{118–120}, and DNA bases^{121–126} to very large molecular systems, such as, chromophore embedded in a protein,^{127–129} aromatic^{130–132} and polymethine¹³³ dye and organic molecules.¹³⁴ I have employed this method in conjunction with B3LYP functional to compute electronic excitation spectra and nature of molecular orbitals involved in electronic transitions.

References

- (1) Raman, C. V. *Nature* **1928**, *121* (3051), 619.
- (2) Raman, C. V. *Proc. Indian Acad. Sci. - Sect. A* **1928**, *2*, 387.
- (3) P. P. Shorygin. *Zhurnal Fiz. Khimii* **1947**, *21*, 1125.
- (4) Asher, S. A. *Ultrav. Raman Spectrom. Handb. Vib. Spectrosc. Sons Ltd., Chichester UK.* **2002**, 557.
- (5) Schelvis, J. P. M.; Ramsey, M.; Sokolova, O.; Tavares, C.; Cecala, C.; Connell, K.; Wagner, S.; Gindt, Y. M. *J. Phys. Chem. B* **2003**, *107* (44), 12352.
- (6) Eisenberg, A. S.; Schelvis, J. P. M. *J. Phys. Chem. A* **2008**, *112* (27), 6179.
- (7) Copeland, R. A.; Spiro, T. G. *J. Phys. Chem.* **1986**, *90* (25), 6648.
- (8) Sokolova, O.; Cecala, C.; Gopal, A.; Cortazar, F.; McDowell-Buchanan, C.; Sancar, A.; Gindt, Y. M.; Schelvis, J. P. M. *Biochemistry* **2007**, *46* (12), 3673.
- (9) Schmidt, J.; Coudron, P.; Thompson, a W.; Watters, K. L.; McFarland, J. T. *Biochemistry* **1983**, *22* (1), 76.
- (10) Schopfer, L. M.; Haushalter, J. P.; Smith, M.; Milad, M.; Morris, M. D. *Biochemistry* **1981**, *20* (23), 6734.
- (11) NISHINA, Y.; SHIGA, K.; HORIIKE, K.; TOJO, H.; KASAI, S.; YANASE, K.; MATSUI, K.; WATARI, H.; YAMANO, T. *J. Biochem.* **1980**, *88* (2), 403.
- (12) Li, J.; Uchida, T.; Todo, T.; Kitagawa, T. *J. Biol. Chem.* **2006**, *281* (35), 25551.
- (13) Li, J.; Uchida, T.; Ohta, T.; Todo, T.; Kitagawa, T. *J. Phys. Chem. B* **2006**, *110* (33), 16724.
- (14) Nishina, Y.; Sato, K.; Miura, R.; Matsui, K.; Shiga, K. *J. Biochem.* **1998**, *124* (1), 200.
- (15) Murgida, D. H.; Schleicher, E.; Bacher, A.; Richter, G.; Hildebrandt, P. *J. Raman Spectrosc.* **2001**, *32* (6–7), 551.
- (16) Dutta, P. K.; Spiro, T. G. *Biochemistry* **1980**, *19* (8), 1590.
- (17) Rava, R. P.; Spiro, T. G. *J. Phys. Chem.* **1985**, *89* (10), 1856.
- (18) Asher, S. A.; Ludwig, M.; Johnson, C. R. *J. Am. Chem. Soc.* **1986**, *108* (12), 3186.
- (19) Fodor, S. P. A.; Rava, R. P.; Hays, T. R.; Spiro, T. G. *J. Am. Chem. Soc.* **1985**, *107* (26), 1520.

- (20) Fodor, S. P. A.; Spiro, T. G. *J. Am. Chem. Soc.* **1986**, *108* (12), 3198.
- (21) Perno, J. R.; Cwikel, D.; Spiro, T. G. *Inorg. Chem.* **1987**, *26* (3), 400.
- (22) Perno, J. R.; Grygon, C. A.; Spiro, T. G. *J. Phys. Chem.* **1989**, *93* (15), 5672.
- (23) Strekas, T. C.; Spiro, T. G. *Biochim. Biophys. Acta* **1972**, *278* (1), 188.
- (24) Strekas, T. C.; Spiro, T. G. *Biochim. Biophys. Acta* **1972**, *263* (3), 830.
- (25) Spiro, T. G.; Strekas, T. C. *Proc. Natl. Acad. Sci. U. S. A.* **1972**, *69* (9), 2622.
- (26) Spiro, T. G.; Strekas, T. C. *J. Am. Chem. Soc.* **1974**, *96* (2), 338.
- (27) Rava, R. P.; Spiro, T. G. *J. Am. Chem. Soc.* **1984**, *106* (14), 4062.
- (28) Caswell, D. S.; Spiro, T. G. *J. Am. Chem. Soc.* **1986**, *108* (21), 6470.
- (29) Johnson, C. R.; Ludwig, M.; O'Donnell, S.; Asher, S. A. *J. Am. Chem. Soc.* **1984**, *106* (17), 5008.
- (30) Johnson, C. R.; Ludwig, M.; Asher, S. A. *J. Am. Chem. Soc.* **1986**, *108* (5), 905.
- (31) Sanford, A. A. *Ann. Rev. Phys. Chem.* **1988**, *39*, 537.
- (32) Wen, Z. Q.; Thomas, G. J. *Biopolymers* **1998**, *45* (3), 247.
- (33) Efremov, E. V.; Ariese, F.; Gooijer, C. *Anal. Chim. Acta* **2008**, *606* (2), 119.
- (34) Benevides, J. M.; Overman, S. A.; Thomas, G. J. *J. Raman Spectrosc.* **2005**, *36* (4), 279.
- (35) Tuma, R.; Thomas, G. J. In *Handbook of Vibrational Spectroscopy*; Griffiths, P. R., Ed.; John Wiley & Sons, Ltd: Chichester, UK, 2006.
- (36) Thomas, G. J. *Annu. Rev. Biophys. Biomol. Struct.* **1999**, *28* (1), 1.
- (37) Carey, P. R.; Storer, A. C. *Annu. Rev. Biophys. Bioeng.* **1984**, *13* (1), 25.
- (38) Peticolas, W. L. *Method. Enzym.* **1995**, *246*, 389.
- (39) Kincaid, J. R. *Methods Enzymol.* **1995**, *246* (C), 460.
- (40) Spiro, T. G.; Czernuszewicz, R. S. *Methods Enzymol.* **1995**, *246* (C), 416.
- (41) Oladepo, S. A.; Xiong, K.; Hong, Z.; Asher, S. A. *J. Phys. Chem. Lett.* **2011**, *2* (4), 334.
- (42) Kim, J. E.; Pan, D.; Mathies, R. A. *Biochemistry* **2003**, *42* (18), 5169.
- (43) Mizuno, M.; Shibata, M.; Yamada, J.; Kandori, H.; Mizutani, Y. *J. Phys. Chem. B* **2009**, *113* (35), 12121.
- (44) Sato, A.; Mizutani, Y. *Biochemistry* **2005**, *44* (45), 14709.
- (45) Webb, M. A.; Kwong, C. M.; Loppnow, G. R. *J. Phys. Chem. B* **1997**, *101* (25), 5062.
- (46) Lednev, I. K.; Karnoup, A. S.; Sparrow, M. C.; Asher, S. A. *J. Am. Chem. Soc.* **2001**, *123* (10), 2388.
- (47) Lednev, I. K.; Karnoup, A. S.; Sparrow, M. C.; Asher, S. A. *J. Am. Chem. Soc.* **1999**, *121* (16), 4076.
- (48) Balakrishnan, G.; Weeks, C. L.; Ibrahim, M.; Soldatova, A. V.; Spiro, T. G. *Current Opinion in Structural Biology.* 2008, pp 623–629.
- (49) Oladepo, S. A.; Xiong, K.; Hong, Z.; Asher, S. A. In *J Phys Chem Lett*; 2011; Vol. 2, pp 334–344.
- (50) Loppnow, G. R.; Mathies, R. A. *Biophys. J.* **1988**, *54* (1), 35.

- (51) Billinghamurst, B. E.; Loppnow, G. R. *J. Phys. Chem. A* **2006**, *110* (7), 2353.
- (52) Kukura, P.; McCamant, D. W.; Mathies, R. A. *Annu Rev Phys Chem* **2007**, *58*, 461.
- (53) Lee, S. Y.; Zhang, D.; McCamant, D. W.; Kukura, P.; Mathies, R. A. *J. Chem. Phys.* **2004**, *121* (8), 3632.
- (54) Hall, C. R.; Heisler, I. A.; Jones, G. A.; Frost, J. E.; Gil, A. A.; Tonge, P. J.; Meech, S. R. *Chem. Phys. Lett.* **2017**, *683*, 365.
- (55) Weigel, A.; Dobryakov, A.; Klaumünzer, B.; Sajadi, M.; Saalfrank, P.; Ernsting, N. P. *J. Phys. Chem. B* **2011**, *115*, 3656.
- (56) Frontiera, R. R.; Mathies, R. a. *Laser Photon. Rev.* **2011**, *5* (1), 102.
- (57) Zhu, L. Y.; Kim, J.; Mathies, R. A. *J. Raman Spectrosc.* **1999**, *30* (9), 777.
- (58) Cao, X.; McHale, J. L. *J. Chem. Phys.* **1998**, *109* (5), 1901.
- (59) Lee, S.-Y.; Heller, E. J. *J. Chem. Phys.* **1979**, *71* (12), 4777.
- (60) Myers, A. B., and R. A. M. Wiley, New York. **1987**, 2, 1.
- (61) Myers, A. B. *Excited Electronic State Properties from Ground-State Resonance Raman Intensities*; Wiley, New York, 1995.
- (62) Stallard, B. R.; Champion; Patrik; Albrecht, A. C. *J. Chem. Phys.* **1983**, *78* (2), 712.
- (63) Stuart, C. M.; Frontiera, R. R.; Mathies, R. A. *J. Phys. Chem. A* **2007**, *111* (48), 12072.
- (64) Waterland, M. R.; Howell, S. L.; Gordon, K. C. *J. Phys. Chem. A* **2007**, *111* (21), 4604.
- (65) Zhao, X.; Burt, J. A.; McHale, J. L. *J. Chem. Phys.* **2004**, *121* (22), 11195.
- (66) Myers, A. B. *Chem. Rev.* **1996**, *96* (3), 911.
- (67) Myers, A. B.; Trulson, M. O.; Mathies, R. A. *J. Chem. Phys.* **1985**, *83* (10), 5000.
- (68) Bosma, W. B.; Yan, Y. J.; Mukamel, S. *Phys. Rev. A* **1990**, *42* (11), 6920.
- (69) Li, B. L.; Johnson, A. E.; Mukamel, S.; Myers, A. B. *J. Am. Chem. Soc.* **1994**, *116* (24), 11039.
- (70) Mukamel, S. *Principles of Nonlinear Optical Spectroscopy*, Oxford University Press, New York; 1995.
- (71) Myers, A. B. *J. Raman Spectrosc.* **1997**, *28* (6), 389.
- (72) Sue, J.; Yan, Y. J.; Mukamel, S. *J. Chem. Phys.* **1986**, *85* (1), 462.
- (73) Watanabe, J.; Kinoshita, S.; Kushida, T. *Chem. Phys. Lett.* **1986**, *126* (2), 197.
- (74) Kramers, H. A.; Heisenberg, W. *Zeitschrift für Phys. A Hadron. Nucl.* **1925**, *31* (1), 681.
- (75) Dirac, P. a. M. *Proc. R. Soc. A Math. Phys. Eng. Sci.* **1927**, *114* (769), 710.
- (76) Albrecht, A. C. *J. Chem. Phys.* **1961**, *34* (5), 1476.
- (77) Blazej, D. C.; Peticolas, W. L. *J. Chem. Phys.* **1980**, *72* (5), 3134.
- (78) Hassing, S.; Mortensen, O. S. *J. Chem. Phys.* **1980**, *73* (3), 1078.
- (79) Lu, H. M.; Page, J. B. *Chem. Phys. Lett.* **1986**, *131* (1–2), 87.
- (80) Loppnow, G. R. *J. Am. Chem.* 1997, *119* (5), 896.

- (81) Mondal, S.; Puranik, M. *Phys. Chem. Chem. Phys.* **2017**, *19*, 20224.
- (82) Mondal, S.; Puranik, M. *J. Phys. Chem. B* **2017**.
- (83) Puranik, M.; Chandrasekhar, J.; Umapathy, S. *Chem. Phys. Lett.* **2001**, *337* (1–3), 224.
- (84) Mondal, S.; Puranik, M. *Phys. Chem. Chem. Phys.* **2016**.
- (85) Milán-Garcés, E. A.; Kaptan, S.; Puranik, M. *Biophys. J.* **2013**, *105* (1), 211.
- (86) Yarasi, S.; Brost, P.; Loppnow, G. R. *J. Phys. Chem. A* **2007**, *111* (24), 5130.
- (87) El-Yazbi, A. F.; Palech, A.; Loppnow, G. R. *J. Phys. Chem. A* **2011**, *115* (38), 10445.
- (88) Shoute, L. C. T.; Loppnow, G. R. *J. Chem. Phys.* **2002**, *117* (2), 842.
- (89) Loppnow, G. R.; Mathies, R. A. *Biophys. J.* **1988**, *54* (1), 35.
- (90) Sasidharanpillai, S.; Loppnow, G. R. *J. Phys. Chem. A* **2014**, *118* (26), 4680.
- (91) Billinghamurst, B. E.; Yeung, R.; Loppnow, G. R. *J. Phys. Chem. A* **2006**, *110* (19), 6185.
- (92) Yarasi, S.; Ng, S.; Loppnow, G. R. *J. Phys. Chem. B* **2009**, *113* (43), 14336.
- (93) Billinghamurst, B. E.; Yeung, R.; Loppnow, G. R. *J. Phys. Chem. A* **2006**, *110* (19), 6185.
- (94) Oladepo, S. A.; Loppnow, G. R. *J. Phys. Chem. B* **2011**, *115* (19), 6149.
- (95) Ng, S. S.; Teimoory, F.; Loppnow, G. R. *J. Phys. Chem. Lett.* **2011**, *2* (18), 2362.
- (96) Fraga, E.; Webb, M. A.; Loppnow, G. R. *J. Phys. Chem.* **1996**, *100* (8), 3278.
- (97) Fraga, E.; Loppnow, G. R. *J. Phys. Chem. B* **1998**, *102* (39), 7659.
- (98) Tannor, D. J.; Heller, E. J. *J. Chem. Phys.* **1982**, *77* (1), 202.
- (99) Ohmori, K. *Annu. Rev. Phys. Chem.* **2009**, *60*, 487.
- (100) Myers, A. B.; Mathies, R. a.; Tannor, D. J.; Heller, E. J. *J. Chem. Phys.* **1982**, *77* (1982), 3857.
- (101) Myers, A. B.; Li, B.; Ci, X. *J. Chem. Phys.* **1988**, *89* (4), 1876.
- (102) Li, B.; Johnson, A. E.; Mukamel, S.; Myers, A. B. *J. Am. Chem. Soc.* **1994**, *116* (24), 11039.
- (103) Phillips, D. L.; Gould, I. R.; Verhoeven, J. W.; Tittelbach-Helmrich, D.; Myers, A. B. *Chem. Phys. Lett.* **1996**, *258* (1–2), 87.
- (104) Loppnow, G. R.; Fraga, E. *J. Am. Chem. Soc.* **1997**, *119* (5), 896.
- (105) Loppnow, G. R.; Billinghamurst, B. E.; Oladepo, S. A. In *Radiation Induced Molecular Phenomena in Nucleic Acids*; Springer Netherlands: Dordrecht, 2008; pp 237–263.
- (106) Billinghamurst, B. E.; Oladepo, S. A.; Loppnow, G. R. *J. Phys. Chem. B* **2012**, *116* (35), 10496.
- (107) DeVito, V. L.; Cai, M. Z.; Asher, S. A.; Kehres, L. A.; Smith, K. M. *J. Phys. Chem.* **1992**, *96* (17), 6917.
- (108) Murphy, W. F.; Evans, M. V.; Bender, P. *J. Chem. Phys.* **1967**, *47* (5), 1836.
- (109) Su, C.; Wang, Y.; Spiro, T. G. *J. Raman Spectrosc.* **1990**, *21* (7), 435.
- (110) Dudik, J. M.; Johnson, C. R.; Asher, S. a. *J. Chem. Phys.* **1985**, *82* (4), 1732.
- (111) Lee, C.; Yang, W.; Parr, R. G. *Phys. Rev. B* **1988**, *37* (2), 785.

- (112) Becke, A. D. *J. Chem. Phys.* **1993**, 98 (7), 5648.
- (113) Godbout, N.; Salahub, D. R.; Andzelm, J.; Wimmer, E. *Can. J. Chem.* **1992**, 70 (2), 560.
- (114) Klaumünzer, B.; Kröner, D.; Saalfrank, P. *J. Phys. Chem. B* **2010**, 114 (33), 10826.
- (115) Klaumünzer, B.; Kröner, D.; Lischka, H.; Saalfrank, P. *Phys. Chem. Chem. Phys.* **2012**, 14 (24), 8693.
- (116) Salzmann, S.; Marian, C. M. *Photochem. Photobiol. Sci.* **2009**, 8 (12), 1655.
- (117) Miertuš, S.; Scrocco, E.; Tomasi, J. *Chem. Phys.* **1981**, 55 (1), 117.
- (118) Rogers, D. M.; Besley, N. A.; O'Shea, P.; Hirst, J. D. *J. Phys. Chem. B* **2005**, 109 (48), 23061.
- (119) Clavaguéra, C.; Piuze, F.; Dognon, J.-P. *J. Phys. Chem. B* **2009**, 113 (51), 16443.
- (120) Štěpánek, P.; Bouř, P. *Phys. Chem. Chem. Phys.* **2014**, 16 (38), 20639.
- (121) Tsolakidis, A.; Kaxiras, E. *J. Phys. Chem. A* **2005**, 109 (10), 2373.
- (122) Shukla, M. K.; Leszczynski, J. *J. Phys. Chem. A* **2005**, 109 (34), 7775.
- (123) Varsano, D.; Di Felice, R.; Marques, M. A. L.; Rubio, A. *J. Phys. Chem. B* **2006**, 110 (14), 7129.
- (124) Karunakaran, V.; Kleiner, K.; Imbrota, R.; Kovalenko, S. A. *J. Am. Chem. Soc.* **2009**, 131 (16), 5839.
- (125) Imbrota, R.; Lami, A.; Barone, V.; Santoro, F. *Int. J. Quantum Chem.* **2010**, 110 (3), 624.
- (126) Zhao, Y.; Cao, Z. *J. Theor. Comput. Chem.* **2013**, 12 (8), 1341013.
- (127) Marques, M. A. L.; López, X.; Varsano, D.; Castro, A.; Rubio, A. *Phys. Rev. Lett.* **2003**, 90 (25), 258101.
- (128) Lopez, X.; Marques, M. A. L.; Castro, A.; Rubio, A. *J. Am. Chem. Soc.* **2005**, 127 (35), 12329.
- (129) Cannuccia, E.; Pulci, O.; Sole, R. Del; Cascella, M. *Chem. Phys.* **2011**, 389 (1–3), 35.
- (130) Jacquemin, D.; Preat, J.; Wathelot, V.; Fontaine, M.; Perpète, E. A. *J. Am. Chem. Soc.* **2006**, 128 (6), 2072.
- (131) Perpète, E. A.; Jacquemin, D. *J. Mol. Struct. THEOCHEM* **2009**, 914 (1–3), 100.
- (132) Fabian, J. *Dye. Pigment.* **2010**, 84 (1), 36.
- (133) Jacquemin, D.; Zhao, Y.; Valero, R.; Adamo, C.; Ciofini, I.; Truhlar, D. G. *J. Chem. Theory Comput.* **2012**, 8 (4), 1255.
- (134) Jacquemin, D.; Wathelot, V.; Perpète, E. A.; Adamo, C. *J. Chem. Theory Comput.* **2009**, 5 (9), 2420.

Chapter 3: Initial Excited State Structural Dynamics of Lumiflavin upon Ultraviolet Excitation

3.1 Introduction

Flavins, being blue-light photoreceptors are known to play key role in the redox cofactors in photoreceptor enzymes.¹⁻³ Lumiflavin (LF) is the parent molecule of the huge class of flavin family that includes the important biological chromophores such as riboflavin (RF), flavin mononucleotide (FMN) and flavin adenine dinucleotide (FAD).⁴ LF is the dominant photoproduct obtained from UV-Vis photolysis of RF, FMN and FAD in alkaline solution (pH > 9).⁵⁻⁷ It acts as a photosensitizer of organic and biological molecules by producing radical intermediates and reactive oxygen species.⁸⁻¹³ The central component of flavin structure is the 7, 8-dimethylisalloxazine ring (or isalloxazine ring) which displays the electron transfer capability (Fig. 3.1(a)). Flavin compounds differ by the respective substituents at N10 position.

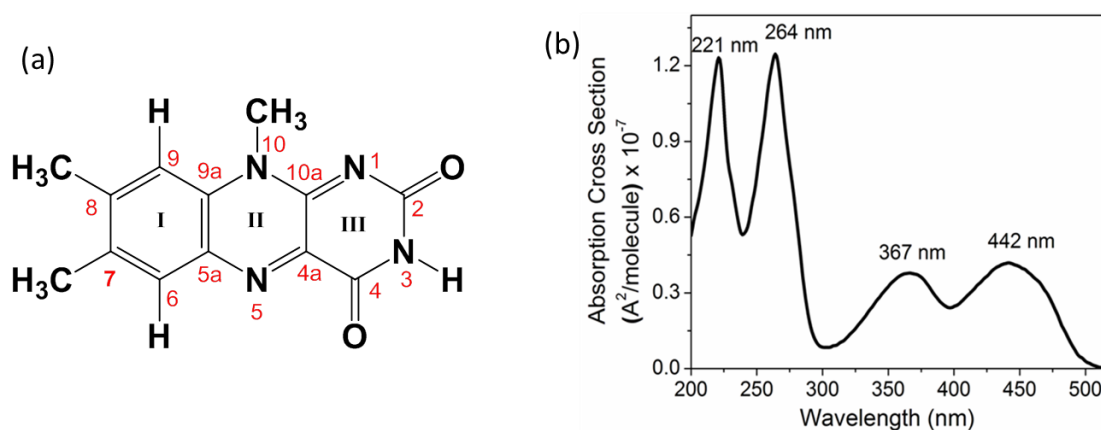


Fig. 3.1 (a) Structure of lumiflavin (LF) with conventional atom numbering. (b) Experimental absorption spectrum of LF in pH7 phosphate buffer labeled with the λ_{\max} values.

Since photoexcitation of flavin molecules initiates the biological processes in blue light photoreceptors, the study of the excited state photophysics of flavins is of utmost importance from various point of view. The photophysics and photochemistry of flavin molecules is mainly dependent on the isalloxazine core ring. So, LF being the simplest one has been studied both in vitro experiments and in theoretical calculations as a representative of other flavin molecules. Flavins have four electronic absorption bands centered at around 445, 373, 266 and 222 nm

which are theoretically proven due to $\pi\pi^*$ transitions.^{14,15} Several studies have been done on the excited state photophysics of flavins involving both experimental spectroscopy research and theoretical calculations following excitation within their first singlet excited state at around 445 nm. The photophysical behavior of LF is documented in several reports.^{4-6,9,16-21} The characterization of the first singlet and triplet excited states of LF was done using absorption spectroscopy,^{5,6,12,16,19} fluorescence spectroscopy^{9,18,19} and laser flash photolysis studies.^{9,18,19,22} Fluorescence behavior of LF upon the change of pH of solution was also carried out extensively.^{23,24} The investigation on the photostability of LF was done in aqueous solutions,^{5,6,16} organic solvents^{5,16,25} and in biological environments.^{8,9} LF was found to be thermally unstable in alkaline solution at elevated temperatures through hydrolysis reaction.²⁶

Quantum chemical calculations were also performed on LF using various methods and basis sets to determine the electronic structure, molecular properties and spectroscopic parameters.^{14,27-32} Upon excitation to the lowest energy S1 state, the geometry of LF and isoalloxazine ring was observed to show small changes using SAC-CI³¹, CASPT2³³ and TDDFT¹⁴ calculations. The change in bond lengths was found a maximum of ~ 0.05 Å along the isoalloxazine ring system in the S1 state. In S1 state, C=O and some of the C=N stretching modes show elongation in the bond length by losing their double bond characters. Non-adiabatic molecular dynamics simulations³⁴ and TDDFT³⁵ calculation on RF molecule also predicted the similar structural changes in S1 state. Wolf et al.²⁹ directly determined the vibrational response of RF in DMSO following photoexcitation to S1 state using fs time-resolved infrared (IR) spectroscopy. A vibrational cooling time of about 4 ps corroborating the downshift of vibrational modes by $10-15$ cm^{-1} in the S1 state was reported. The major change upon photoexcitation was observed in the loss of double bond character between C4a and N5 atoms.

Though there was an overwhelming research report about the excited state dynamics in the S1 state, the study regarding that in ultraviolet (UV) region of absorption of flavins is scarcely reported. Herein, we have employed Ultraviolet Resonance Raman (UVR) spectroscopy to measure the excited state structural dynamics of LF following excitation within their most intense absorption band centered at around 265 nm. RR spectroscopy can probe the vibrational mode specific excited state structural distortions after photoexcitation. At these

shorter excitation wavelengths, light induced damage of the flavin molecules is possible and the work is therefore potentially useful for understanding radiation damage in biological systems.

In RR spectroscopy, the intensity of a Raman band increases to a manifold by choosing the excitation wavelength within the absorption band. Raman frequencies determine the ground state structure of the molecule, whereas Raman intensities have the information of the resonant excited state. RR intensities are proportional to the slope at the potential energy surface (PES) of excited state along the normal mode coordinates which are coupled through the resonant electronic excitation. So, the RR intensity is proportional to the extent of structural distortions happening in the resonant excited state. The excited state structural distortions determined along normal mode coordinates are expressed as dimensionless displacements (Δ) which is the displacements between the minima of the PES's of resonant excited state and the ground electronic state. RR intensities are proportional to the square of the dimensionless displacements. Moreover, the lineshape analysis of Raman excitation profile (REP), i.e. excitation wavelength dependence of RR cross sections, can extract the information on the dynamical response of the environment. Now, through a comprehensive measurement and modeling of experimental Raman excitation profile (REP), it is possible to measure the excited state structural distortions take place within tens of femtoseconds (Raman process timescale) following photoexcitation.

In this work, we have measured the short time excited state structural dynamics of LF within the most intense absorption band at 264 nm. Self-consistent simulation of the experimental REPs and absorption spectrum was done by employing Lee and Heller's time-dependent wave packet theory.³⁶ We have determined excited state structural distortions in terms of change in internal coordinates of the ground state. Internal reorganization energies obtained in short time scale was partitioned into each specific vibrational modes. In condensed phase, the surrounding solvent molecules determine line shape of the REP on the ultrafast timescale. Brownian oscillator model³⁷ was applied to account for the effect of the solvent dynamics (homogeneous broadening) and a simple Gaussian broadening function for inhomogeneous broadening originates from static microenvironments of the solute. Simultaneous modeling of the line shape of REP and the absorption spectrum allows us to separate the solvent contribution into homogeneous and inhomogeneous broadening.

3.2 Experimental and Theoretical Methods

3.2.1 Sample Preparation

LF ($\geq 97\%$ HPLC pure) was purchased from Sigma Chemicals Co. and used as supplied. The sample solution which was used for Raman experiments contained $100 \mu\text{M}$ LF in 50 mM phosphate buffer at pH7. Concentrations of LF sample solutions were determined spectrophotometrically from the published molar extinction coefficients.¹⁶ 250 mM sodium sulfate (Na_2SO_4) was added in the sample solution as internal standard. UV/Vis absorption spectra were measured using Perkin-Elmer (lambda 45) absorption spectrometer at pH 7 in phosphate buffer.

3.2.2 UVRR Spectroscopy

UVRR Spectra of LF were obtained by using a tunable Ti: sapphire laser with Raman excitations between 257 to 275 nm . The details of UVRR experimental set up for measuring REP have been given in chapter 2.

3.2.3 UVRR Cross-section Determination

The detailed method of UVRR cross section determination has been described in experimental and theoretical method chapter. The depolarization ratio of Raman bands of LF was measured using the same method as shown in the previous chapter. The value of depolarization ratios of Raman bands of LF are depicted in Table 3.1.

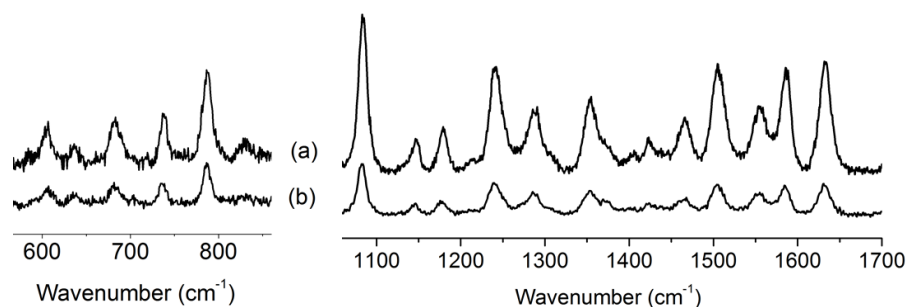


Fig. 3.2 (a) Polarized and (b) depolarized spectra of $100 \mu\text{M}$ LF in low (left) and high (right) frequency regions obtained at 260 nm excitation wavelength.

The depolarization ratio of all the Raman bands was obtained to be one-third (0.33). The depolarization ratios for low intense modes of LF are difficult to measure due to the weak signal

of the depolarized spectrum. So, it was assumed that the depolarization ratios for these bands are also one third.

Table 3.1 Depolarization Ratios of UVRR bands of LF obtained at 260 nm excitation

Raman Band (cm^{-1})	Depolarization ratio
607	0.37
684	0.41
739	0.40
1086	0.33
1149	0.32
1182	0.41
1243	0.31
1288	0.31
1355	0.34
1374	0.33
1466	0.31
1504	0.25
1555	0.33
1585	0.27
1632	0.30

3.2.4 Computational Method - Simulation of Experimental REP and Absorption Spectrum

We have used time-dependent wave propagation theory^{36,38} to simulate the experimental REP and absorption spectrum in a self-consistent manner and detailed method is described in the previous chapter. The initial relative Δ 's for simulation were calculated from the intensity of the UVRR bands relative to the that of the band at 1585 cm^{-1} band in the spectrum recorded with 271.1 nm excitation assuming that the intensity of a RR band is proportional to Δ^2 . E_0 was estimated so that the red edge of simulated absorption spectrum matches well with the experimental spectrum. The transition dipole moment (M) was taken 1.12 \AA and derived from the constrained deconvolution of the experimental absorption spectrum. An initial guess for the ultrafast solvent relaxation time scale (50 fs) was taken from the fluorescence up-conversion measurement on coumarin by Jimenez et al.³⁹ These initial guess parameters were iteratively optimized in a self-consistent manner using MATLAB software (The MathWorks, Natick, MA) until a best agreement was achieved between the calculated and experimental REPs and

absorption spectrum. Then the best fit parameter values were allowed to change after increasing and decreasing the best fit Δ values by 20% to check the robustness of the fit.

3.2.5 Deconvolution of Absorption Spectrum

Theoretical calculations (TDDFT¹⁵, SAC-CI³¹, CASPT2/CASSCF,³³ PPP-CI¹⁹) and circular dichroism (CD) experiments⁴⁰ revealed that the absorption band of isoalloxazine derivatives centered at around 266 nm is composed of more than one $\pi\pi^*$ transitions. CD spectra of RF and FMN and PPP-CI calculations predicted a weak $\pi\pi^*$ transition at around 245 nm which is at the red-energy site of the strong $\pi\pi^*$ transition at 265 nm. SAC-CI³¹ and DFT/MRCI¹⁴ calculations on LF indicated that two strong $\pi\pi^*$ transition can contribute to the 265 nm absorption band, whereas other methods using CASPT2³³ and TDDFT¹⁵ computed three $\pi\pi^*$ transitions within this absorption band. So, we deconvoluted the absorption band centered at 264 nm with three Gaussians. The unconstrained fit of the absorption band yields a transition dipole of 0.91 Å for the band centered at 264 nm. This value was further refined with simultaneous, self-consistent fit to the REP and the absorption cross section to a transition dipole length of 1.12 Å. Consistent with this, our TDDFT calculations also show the existence of weak $\pi\pi^*$ transitions to the both sides of the strong central $\pi\pi^*$ electronic state inside the broad experimental absorption band at 264 nm.

3.2.6 DFT Calculations

All quantum chemical calculations on LF molecule were carried out using density functional theory (DFT) using the software Gaussian09. The ground state structure of the molecule was optimized using B3LYP hybrid functional^{41,42} and TZVP⁴³ basis set. Polarizable continuum model (PCM)⁴⁴ was applied to take into account the dielectric environment of bulk water. The frequency calculation was done on the optimized structure. The coordinates of optimized structure in the ground state are given in Table 3.2. To assign the experimental UVRR modes the deuterium exchange calculation was also performed after replacing the N3-H proton by the mass of deuterium (D). No scaling factor was used for the calculated frequencies.

To calculate the excitation energies and molecular orbitals (MOs) involved in electronic transitions, TD-B3LYP calculation was done on the previously optimized structure using the same basis set and in PCM solvent model. The absorption spectrum was calculated from the vertical excitation energies obtained from TDDFT calculation and by taking the fixed Gaussian

band width of 2500 cm^{-1} . The visualization of the optimized structure, molecular orbitals (MOs) and vibrational modes were performed using Chemcraft v 1.6 software.

Table 3.2 Coordinates of the ground state optimized structure of LF

Atom number		X	Y	Z	Atom number		X	Y	Z
1	C	-3.746468000	-0.629317000	0.000031000	16	N	4.697537000	-1.315193000	0.000107000
2	C	-1.430349000	-0.622493000	0.000047000	17	C	5.296649000	-1.057407000	-0.877188000
3	C	-1.337446000	0.825160000	-0.000019000	18	H	5.296799000	-1.057018000	0.877181000
4	C	-2.616891000	1.589076000	0.000124000	19	H	4.538555000	-2.392271000	0.000352000
5	C	0.947197000	0.794279000	-0.000074000	20	H	4.666081000	1.638005000	-0.000062000
6	C	0.966795000	-0.623909000	-0.000019000	21	C	5.273976000	1.406560000	0.878305000
7	C	2.203051000	-1.281476000	0.000044000	22	H	5.274152000	1.406259000	-0.878226000
8	H	2.245087000	-2.360008000	0.000133000	23	H	4.467044000	2.708852000	-0.000261000
9	C	3.393253000	-0.570447000	0.000038000	24	H	-0.242717000	-2.773151000	-0.000093000
10	C	3.381170000	0.855581000	-0.000050000	25	C	0.265529000	-3.138680000	-0.891120000
11	C	2.166411000	1.501204000	-0.000094000	26	H	0.264684000	-3.138786000	0.891382000
12	H	2.109938000	2.582448000	-0.000143000	27	H	-1.272570000	-3.104886000	-0.000585000
13	N	-2.558324000	-1.297675000	0.000118000	28	H	-4.834333000	-1.192550000	0.000170000
14	N	-3.725300000	0.780108000	0.000084000	29	O	-4.628870000	1.237694000	0.000010000
15	N	-0.239214000	-1.301865000	-0.000032000	30	H	-2.693065000	2.806003000	-0.000206000
16	N	-0.219668000	1.487387000	-0.000088000					

3.3 Results and Discussion

3.3.1 Electronic Structure

The experimental absorption spectrum of LF shows four strong absorption bands similar to other flavin molecules having maxima at around 221, 264, 368 and 442 nm (Fig 3.1(b)). The absorption band at 264 nm is the most intense one amongst all. We have applied TD-B3LYP/TZVP calculations with continuum PCM solvent model to determine the excitation energies and the MOs involved in electronic transitions. The vertical transition energies, nature of the electronic transitions involved and corresponding MO contributions with the published literature values are compiled in Table 3.3. The MOs involved at around 264 nm transition confirms that it is a $\pi\pi^*$ transition (see Fig 3.3(a)).

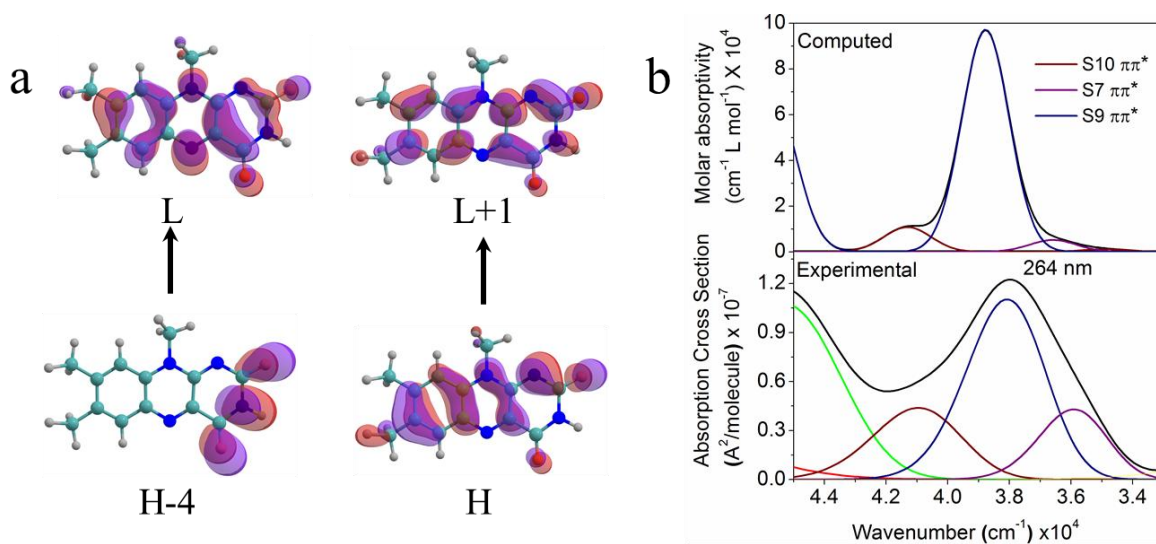


Fig. 3.3 (a) Computed orbitals of LF involved in the electronic transition observed in excitation within the 264 nm excited state. H and L stand for HOMO and LUMO respectively; (b) theoretical absorption spectrum (above) was computed using TD-B3LYP/TZVP//PCM method on LF molecule. Computed band positions are depicted with a Gaussian line shape of fixed line width (2500 cm^{-1}) and deconvoluted experimental absorption (below) of LF labeled with the λ_{max} .

The first $\pi\pi^*$ electronic transition was found to be at 2.93 eV with an oscillator strength of 0.234. This transition can be assigned with the first experimentally observed band in LF absorption spectrum. The calculated transition energy is very similar to the reported transition energy (2.94 eV) using DFT/MRCI(TZVP).¹⁴ Our finding also matches with other TDDFT calculations by Zenichowski et al.³² In contrast; the vertical SAC-CI transition energy³¹ for the lowest energy absorption band of LF is lower by 0.51 eV. The second visible band in the absorption spectrum can be assigned with the second $\pi\pi^*$ transition (S3) in our calculation with an excitation energy of 3.57 eV. The oscillator strength for this transition is 0.26. The calculated vertical transition energy for this transition agrees well with the vertical SAC-CI and TDDFT energies. The DFT/MRCI calculations on LF in gas phase show a lower energy by 0.27 eV for the above transition.

Between the energy regime of 4.5 to 5.2 eV, three $\pi\pi^*$ electronic transitions at 4.53 (S7), 4.81 (S9) and 5.12 eV (S10) are observed with oscillator strengths of 0.04, 0.80 and 0.09 respectively. The third experimentally observed absorption band of LF can be assigned to the second one (S9 state) with an excitation energy of 4.807 eV, because this is the strongest transition with an oscillator strength of 0.803 which is much higher than the oscillator strengths of other two transitions. The M. O. picture in Fig 3.3 (a) shows that the transition is dominated

by one electron transition from H to L+1 (83%). Circular dichroism spectra⁴⁰ and PPP/CI¹⁹ calculations suggested that this absorption band is composed by two electronic transitions. A weak $\pi\pi^*$ transition is predicted to the red energy site of the strong $\pi\pi^*$ transition at around 265 nm. DFT/MRCI¹⁴ and SAC-CI³¹ calculations for LF molecule found two $\pi\pi^*$ transitions of similar oscillator strengths in that region, both of which can contribute to this experimental band. Choe et al.¹⁵ using the TD-B3LYP method with aug-cc-pVDZ basis function have reported that this band is composed by three $\pi\pi^*$ transitions computed at 4.52, 4.79 and 5.02 eV. The oscillator strength is computed to be 0.79 for the transition at 4.79 eV, whereas other two are found to be weak transitions. CASPT2³³ results also show that three $\pi\pi^*$ transitions can contribute to the absorption band at around 266 nm (see Table 3.3). So, we can suggest that the other two weak $\pi\pi^*$ transitions obtained in our calculation can also contribute to that experimental band.

The absorption band at around 222 nm can be compared with the $\pi\pi^*$ transition found at 5.66 eV (S13) with an oscillator strength of 0.546. This state arises from a combination of two electronic transitions from H-1→L+1 (44%) and H→L+2 (39%). TDDFT calculations by Choe et al.¹⁵ predicted that the corresponding transition comes at 5.71 eV.

3.3.2 UVRR Spectra and Experimental Raman Excitation Profile

The UVRR spectrum of LF obtained with a laser excitation of 262 nm is shown in Fig. 3.4. The spectrum shows 22 UVRR bands of LF (607, 637, 684, 739, 787, 832, 1086, 1149, 1182, 1243, 1288, 1355, 1374, 1423, 1438, 1466, 1504, 1555, 1585, 1632 and 1714 cm^{-1}) between the spectral region of 600 to 1750 cm^{-1} . The observed UVRR band positions show good agreement within the experimental error with the RR and SERS spectrum of LF excited at 488 nm.⁴⁵⁻⁴⁷ Here at 262 nm excitation, we have observed two new bands at 1182 and 684 cm^{-1} . The UVRR band at 1182 cm^{-1} was seen at 1190 cm^{-1} in SERS spectrum⁴⁷ and at 1169 cm^{-1} in IR spectrum of LF⁴⁸, whereas 684 cm^{-1} band was observed in the IR spectrum of LF and also in the RR spectra of RF and FMN at UV and visible excitations (see Table 3.4).^{49,50}

Normal mode assignments of the observed UVRR bands of LF are described in Table 3.4. All flavin compounds (LF, RF, FMN and FAD) exhibit similar Raman bands between the 1300 to 1750 cm^{-1} region of spectrum.^{45,46,49-53} These bands do not show significant isotopic

Table 3.3 Vertical singlet excitation energies ΔE_{vert} in nm (in eV in parenthesis), oscillator strengths (f) and major orbital contribution to each transition of oxidized LF molecule computed using TD-B3LYP/TZVP//PCM method and comparison with published computed and experimental transition energies are given in the table.

state order	Type	Major orbital contribution (%) ^a	Computed			Published		Experimental	
			ΔE_{vert} ^b in nm (eV)	f	ΔE_{vert} in eV	LF	IA ^g	$\Delta E_{\text{expt}}^{\text{h}}$ (λ_{max}) in nm	ϵ^{h} (M ⁻¹ cm ⁻¹)
S1	($\pi\pi^*$)	H→L (96%)	422.7 (2.93)	0.2338	2.91(0.23) ^c , 2.40 ^d , 2.97 (0.219) ^e , 2.94 ^f	3.09 (0.239)	444	10930	
S2	($n\pi^*$)	H-2→L (55%) H-3→L (43%)	363.1 (3.41)	0.0008					
S3	($\pi\pi^*$)	H-1→L (92%)	347.3 (3.56)	0.2602	3.50 (0.28) ^c , 3.54 ^d , 3.64 (0.242) ^e , 3.84 ^f	4.28 (0.158)	369	8540	
S4	($n\pi^*$)	H-3→L (53%) H-2→L (41%)	342.4 (3.62)	0.0000					
S5	($n\pi^*$)	H-6→L (92%)	288.7 (4.29)	0.0000					
S6	($\pi\pi^*$)	H-4→L (82%)	286.7 (4.32)	0.0096					
S7	($\pi\pi^*$)	H-5→L (84%)	273.3 (4.53)	0.0429					
S8	($n\pi^*$)	H-7→L (94%)	263.4 (4.70)	0.0004					
S9	($\pi\pi^*$)	H→L+1 (83%) H-4→L (11%)	257.9 (4.81)	0.8033	4.79 (0.79)^c, 4.56^d, 4.95^d, 4.86 (0.775)^e, 4.77^f, 4.91^f	4.69 (0.104), 5.00 (0.337), 5.37 (0.641)	265.5	32400	
S10	($\pi\pi^*$)	H→L+2 (51%) H-1→L+1 (44%)	242.1 (5.12)	0.0897					
S11	($n\pi^*$)	H-3→L+1 (54%) H-2→L+1 (41%)	235.6 (5.26)	0.0003					
S12	($n\pi^*$)	H-2→L+1 (53%) H-3→L+1 (40%)	228.1 (5.43)	0.0000					
S13	($\pi\pi^*$)	H-1→L+1 (44%) H→L+2 (39%)	219.0 (5.66)	0.5460	5.54 (0.56) ^c		222.5	30300	

^aPercentages are calculated as 100x twice the squares of the coefficients in the CI expansion of TDDFT wave functions. H and L stand for highest occupied molecular orbital (HOMO) and lowest unoccupied molecular orbital (LUMO) respectively. ^bIn this work; ^cTD-B3LYP/aug-cc-pVDZ in PCM solvent model to account for medium polarizations effect of water, oscillator strengths in parentheses, see ref. 15; ^dSAC-CI method with D95V (d) basis functions and solvation effect included through PCM model along with five explicit water molecules, see ref. 31; ^eTD-B3LYP/6-31G (d)/PCM, see ref. 32; ^fDFT/MRCI (TZVP) in gas phase, see ref.14; ^gCASPT2 method with 6-31G(d) basis functions on isoalloxazine structure (IA), oscillator strengths in parentheses, see ref. 33; ^hfrom ref. 16.

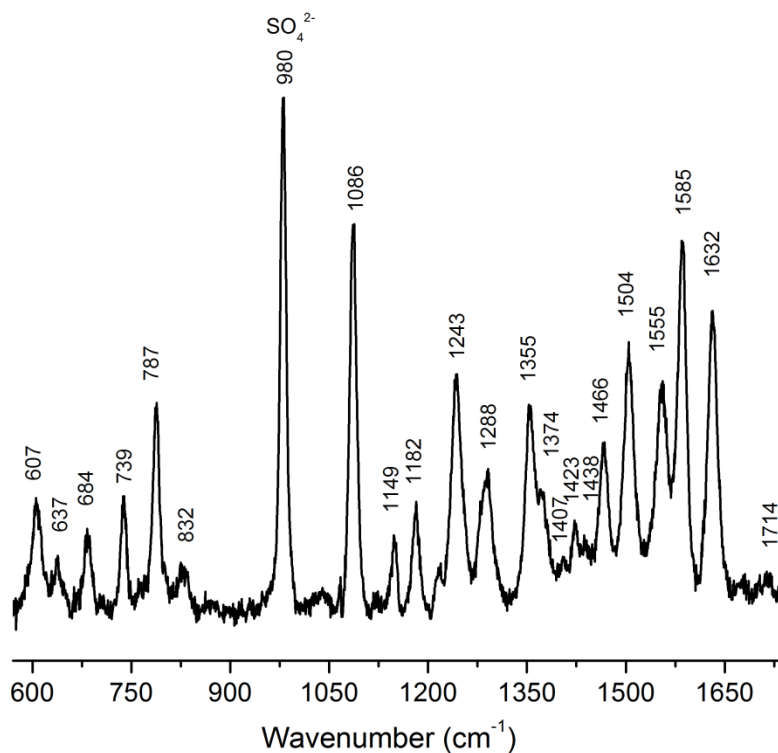


Fig. 3.4 UVRR spectrum of LF of 100 μM concentration obtained at 262 nm excitation in phosphate buffer at pH7. 980 cm^{-1} is the internal standard (sulfate) band which is added to the sample solution.

shifts upon N3-H/D exchange^{45,46,49,52} and we have followed the assignments suggested for RF using the same level of theory as we have used here, except the addition of four explicit water molecules.⁵⁴ However, N3-H/D exchange in flavins largely affects the Raman bands within the 1300 to 1000 cm^{-1} region and it has been assigned to uncoupling of N3-H bending vibration from these normal modes.^{45,46,49,55,56} For these bands and also for the bands below 1000 cm^{-1} , the assignments are done according to the literature.^{49,53} Our assignments are also consistent with other DFT calculations.⁵⁷⁻⁶⁰

Variation of the UVRR band intensities by tuning the excitation wavelength across the 266 nm absorption band is shown in Fig. 3.5. The Raman band intensities in each spectrum are normalized against that of the sulfate band at 980 cm^{-1} which was added as an internal standard in the sample solution. The substantial changes are observed in intensities for the bands at 1632, 1585 and 1555 cm^{-1} with increasing the excitation wavelengths. The intensities of the bands at 1632 and 1555 cm^{-1} decreases by going towards 274.8 nm excitation, whereas the intensity of the band at 1585 cm^{-1} at first increases with increasing the excitation wavelength and it shows

Table 3.4 Assignments of experimental UVRR bands of LF using B3LYP/TZVP//PCM level of theory, computed potential energy distributions (PED) and comparison with published experimental and computational results.

Exp. UVRR in H ₂ O (cm ⁻¹)	Comp. in H ₂ O ^a (cm ⁻¹)	RR (cm ⁻¹) ^c	RR (cm ⁻¹) ^d	SERS (cm ⁻¹) ^e	IR (cm ⁻¹) ^f	Comp. in gas phase ^g (cm ⁻¹)	PED in H ₂ O (%) ^b	Comp. after N3-H/D exchange (cm ⁻¹) ^a	Comp. shift (cm ⁻¹)	PED in D ₂ O (%) ^b
1714	1736	no	no	no	1708 (+2)	1745 (-1)	str C4=O (68)	1733	-3	str C4=O (64) + str C2=O (13)
no	1692	no	no	no	1662 (-14)	1735 (-11)	str C2=O (62)	1677	-15	- str C4=O (17) + str C2=O (56)
1632	1662	1630 (0)	1628 (+1)	1630 (+1)	no	1617 (0)	str C6-C7 (31) - str C8-C9 (14)	1661	-1	str C6-C7 (30) - str C8-C9 (13)
1585	1599	1585 (-2)	1584 (-1)	1578 (+1)	1583 (-3)	1574 (0)	str N5-C4a (21) - str C8-C9 (13) + str C5a-C9a (21)	1599	0	- str N5-C4a (21) - str C8-C9 (13) + str C5a-C9a (21)
1555	1559	1553 (+2)	1551 (+5)	1540 (+4)	1552 (0)	1537 (0)	- str N5-C4a (21) + str N10-C10a (12)	1559	0	str N5-C4a (21) - str N10-C10a (12)
1504	1525	1503 (0)	1503 (0)	1508 (0)	1513 (+7)	1478 (0)	- be C6-H (10) + be C9-H (19)	1525	0	be C9-H (19)
1466	1493	1465 (-3)	1465 (-3)	1469 (+1)	1461 (0)	1457 (0)	- be (H-C-H) 8-CH3 (10)	1493	0	be (H-C-H) 8-CH3 (11)
1438	1458	no	no	no	no		be (H-C-H) 10-CH ₃ (21)	1457	-1	- str C8-C9 (10) + be (H-C-H) 10-CH ₃ (21)
1423	1445	weak	sh	sh	1425 (0)		- str C6-C7 (14) + be (H-C-H) 10-CH ₃ (22)	1445	0	- str C6-C7 (14) + be (H-C-H) 10-CH ₃ (22)
1407	1410	1406 (-)	1405 (0)	1406 (+2)	1396 (-5)		- str N3-C4 (10) + be N3-H (30)	-	-	-
1374	1376	sh	no	1370sh (0)	no		- str C8-C9 (15) + str N3-C4 (12)	1373	-3	str C8-C9 (14) - str N3-C4 (12)
1355	1352	1354 (-2)	1353 (0)	1349 (0)	1346 (+3)	1328 (-1)	- str C9-C9a (20) + str N10-C10a (21)	1352	0	- str C9-C9a (20) + str N10-C10a (20)
1288	1309	no	1278 (+4)	1280sh (+2)	1272 (+20)	1288 (0)	str N10-C9a (12)	1309	0	str N10-C9a (13)
1243	1237	1243 (+19)	1240 (no)	1264 (+2)	1238		- str N3-C4 (10) + str C8-CH3 (16) + str C7-CH3 (10) + be C6-H (17)	1229	-8	str C8-CH3 (18) + be C6-H (21)
1182	1191			1190 (0)	1169 (+21)	1174 (-)	str N5-C5a (14)	1146	-45	str N1-C2(10) - str N10-C9a(10) + be N3H (16) - be C4=O (11)
1149	1164	1150 (-10)	1147 (-5)	1152 (0)	no	1119 (+1)	- str C8-CH ₃ (15) + str C7-CH ₃ (21) + be C6-H (11)	1164	0	- str C8-CH ₃ (14) + str C7-CH ₃ (20) + be C6-H (13)
1086	1091	1085 (-1)	1084 (-4)	1096 (0)	1081 (-7)	1056(-7)	tors 10-CH ₃ (22)	1085	-6	tors 10-CH ₃ (24)
832	839	835 (-2)		838 (0)	824 (-1)	837(-4)	- be C9a-N10-C10a (12)	836	-3	be C9a-N10-C10a (11)
787	793	790 (-20)			785 (-15)	758(-22)	be C4a-N5-C5a (10) + be N1-C10a-C4a (14)	772	-21	- str C7-CH ₃ (11) + be D3-N3-C4 (10) + be N1-C10a-C4a (11)
739	750	741 (-3)		744 (0)	735 (+1)	725(0)	str C9a-C5a (16) - be C5a-C6-C7 (13) - be C8-C9-C9a (13) + be C9-C9a-C5a (12) + be C9a-C5a-C6 (10)	749	-1	str C9a-C5a (15) - be C5a-C6-C7 (12) - be C8-C9-C9a (12) + be C9-C9a-C5a (11) + be C9a-C5a-C6 (11)
684	682				676 (-16)	647(-23)	be C4-O (20) + be C2-O (28)	661	-21	be C4-O (19) - be C2-O (26) + be N5-C5a-C6 (10)
637	641	638 (-2)		646 (0)	627	614(-1)	- be CH ₃ -C7-C6 (11)	639	-2	- be CH ₃ -C7-C6 (10)
607	605	608 (-2)		621 (+1)	604 (-4)	579(-4)	be N5-C5a-C6 (12)	602	-3	be N3-C2-N1 (11)

^aall frequency calculations are done using B3LYP/TZVP//PCM level of theory and no scaling factor for theoretical frequencies are used; no - not observed; sh - shoulder; str - stretching; be - bending; tors - torsional vibrations; ^bPEDs are computed using the VEDA 4.0 program; ^cRR spectrum of LF bound to riboflavin binding protein (RBP) excited at 488 nm, from ref. 45; ^d RR spectrum of LF in H₂O and 10% Me₂SO solution mixture excited at 488 nm, from ref 46; ^efrom ref 47; ^ffrom ref 48; ^gComputed frequencies of LF structure using B3LYP/6-31G(d,p) level of theory, from ref 49; the numbers in the parenthesis for all literature values are the isotope shifts of the N3-H/D exchange.

Table 3.5 Normal mode descriptions of UVRR bands of LF by B3LYP/TZVP level of theory using PCM as solvent model, PED, dimensionless displacements and mode specific internal reorganization energies.

Experimental wavenumber (cm ⁻¹)	Computed wavenumber (cm ⁻¹)	PED (%) ^a	Dimensionless displacements Δ	Mode specific reorganization energy (cm ⁻¹)
1714	1736	str C4=O (68)	0.085	6
1632	1662	str C6-C7 (31) - str C8-C9 (14)	0.195	31
1585	1599	str N5-C4a (21) - str C8-C9 (13) + str C5a-C9a (21)	0.385	117
1555	1559	- str N5-C4a (21) + str N10-C10a (12)	0.185	26
1504	1525	- be C6-H (10) + be C9-H (19)	0.195	28
1466	1493	- be (H-C-H) 8-CH ₃ (10)	0.145	15
1438	1458	be (H-C-H) 10-CH ₃ (21)	0.08	5
1423	1445	- str C6-C7 (14) + be (H-C-H) 10-CH ₃ (22)	0.085	5
1408	1410	- str N3-C4 (10) + be N3-H (30)	0.05	2
1374	1376	- str C8-C9 (15) + str N3-C4 (12)	0.175	22
1355	1352	- str C9-C9a (20) + str N10-C10a (21)	0.165	19
1288	1309	str N10-C9a (12)	0.175	20
1243	1237	- str N3-C4 (10) + str C8-CH ₃ (16) + str C7-CH ₃ (10) + be C6-H (17)	0.23	34
1182	1191	str N5-C5a (14)	0.12	8
1149	1164	- str C8-CH ₃ (15) + str C7-CH ₃ (21) + be C6-H (11)	0.08	6
1086	1091	tors 10-CH ₃ (22)	0.27	40
832	839	- be C9a-N10-C10a (12)	0.11	5
787	793	be C4a-N5-C5a (10) + be N1-C10a-C4a (14)	0.22	19
739	750	str C9a-C5a (16) - be C5a-C6-C7 (13) - be C8-C9-C9a (13) + be C9-C9a-C5a (12) + be C9a-C5a-C6 (10)	0.189	12
684	682	be C4-O (20) + be C2-O (28)	0.189	12
637	641	- be CH ₃ -C7-C6 (11)	0.168	9
607	605	be N5-C5a-C6 (12)	0.24	18

^aPEDs are computed using the VEDA 4.0 program; str.-stretching, be-bending

maximum at 272.7, then it starts decreasing. Those three bands may be enhanced by more than one electronic transition. The two Raman modes at 1355 and 1374 cm⁻¹ is observed to have reversed relative intensity on increasing the excitation wavelengths from 259.9 to 274.8 nm. We

have observed a new band at 1280 cm^{-1} at 265.9 nm excitation and onwards. This band was seen in the RR spectrum of LF excited at 488 nm . This band may be enhanced by the lower energy electronic transitions placed right to the resonant electronic state (see Fig. 3.3(b)) within the 265 nm absorption band. Raman band positions show no appreciable changes with changing the excitation wavelengths. Most of the UVRR bands show their highest Raman cross sections at 259.1 nm and 262 nm excitations.

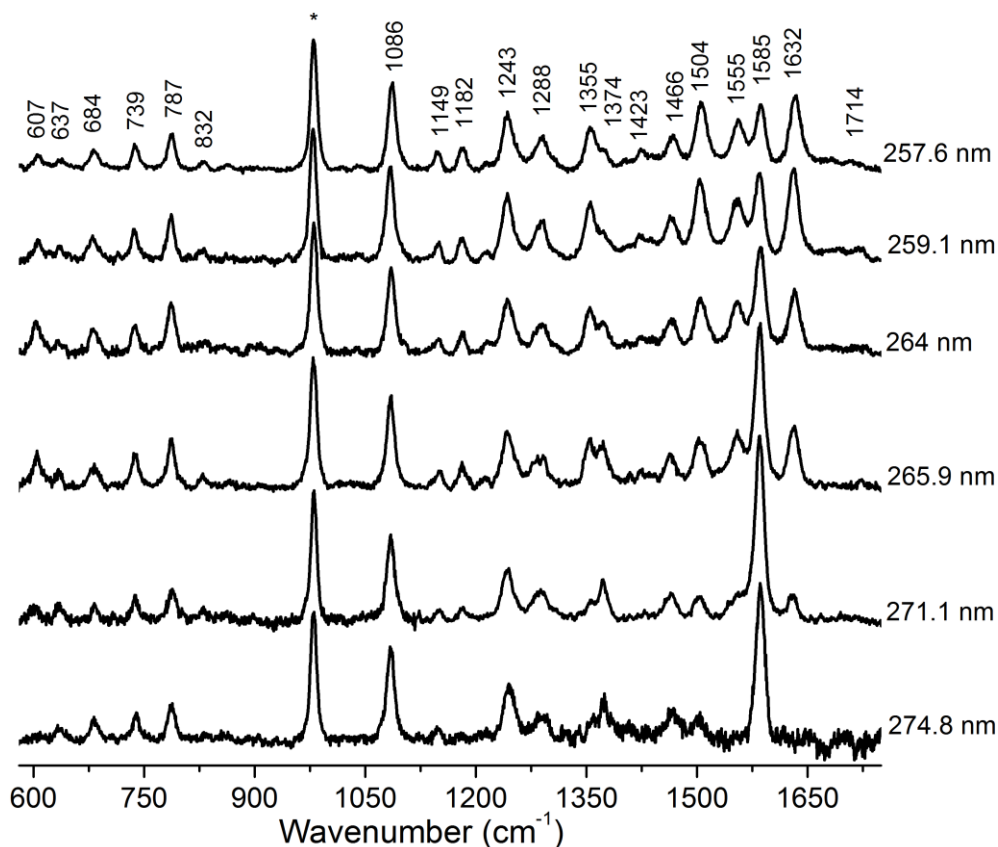


Fig. 3.5 UVRR spectra of $100\text{ }\mu\text{M}$ LF in pH7 sodium phosphate buffer obtained at 6 different excitation wavelengths. Variation in the UVRR band intensity can be seen as the excitation wavelength is tuned across the absorption band at 264 nm . All spectra are normalized with respect to the internal standard band at 980 cm^{-1} marked by an asterisk (*).

The maximum of REPs of the bands at 1084 , 1149 , 1181 , 1243 , 1289 , 1355 , 1465 , 1505 , 1554 and 1631 cm^{-1} are blueshifted with respect to the absorption band maximum at 264 nm (Fig. 3.6 and Fig. 3.7). This kind of shift was observed earlier in the REPs of 6-ClGua nucleobase⁶¹ and tryptophan⁶², and it can be characterized as a vibronic coupling of these Raman modes with nearby electronic states. We have already mentioned in the preceding section that the

published experimental results and theoretical calculations predicted the existence of other two weak electronic states to both sides of the strong electronic state centered around 264 nm. **The depolarization ratios of the UVRR bands of LF measured at 260 nm are close to 0.33 which indicates that the major contributions to the UVRR intensity result from a single electronic transition centered at 264 nm.** So, the blueshift of the maxima of REPs arises due to the coupling of those UVRR modes with the higher energy electronic state placed left to the electronic state positioned at around 264 nm (see Fig. 3.3(b)). The experimental REPs of the bands at 1374 and 1585 cm^{-1} show their maxima at 265.9 and 272.7 nm excitations respectively (Fig 3.7). This is due to the strong coupling of those modes with the lower energy electronic state placed at the red edge of the 264 nm electronic state.

3.3.3 Simulation of Absorption and Experimental REPs

Self-consistent simulation of experimental REPs made with the normalized UVRR intensities and the absorption spectrum of LF was done by using a common set of parameters. Fig. 3.6 and Fig. 3.7 show the experimental and simulated REPs for the observed Raman bands and the deconvoluted absorption band of LF centered around 264 nm. The parameters corresponding to the best fit are shown in Table 3.6. The dimensionless displacements (Δ) obtained from the best fit simulation and the internal reorganization energies for each Raman bands were depicted in Table 3.5. Overall, a good agreement is achieved between the experimental and simulated REPs.

We have observed a deviation in simulated and experimental REPs for the bands at 1373 and 1585 cm^{-1} . The UVRR cross sections at lower excitation wavelengths for those bands do not match with the simulated REPs. This is because of the method of simulation which is used here, is applicable only for single electronic excitation and does not take into account the interferences from other nearby electronic transitions. **The electronic state at around 264 nm is coupled with the higher energy electronic state through the UVRR modes at 1373 and 1583 cm^{-1} and these modes may assist the internal conversion between the above two electronic states.** Experimental REPs of the bands at 1355, 1554 and 1631 cm^{-1} show small deviation with the simulated REPs at higher excitation wavelengths. This is due to the interference from the nearby lower energy electronic state located at the red edge of the resonant electronic state.

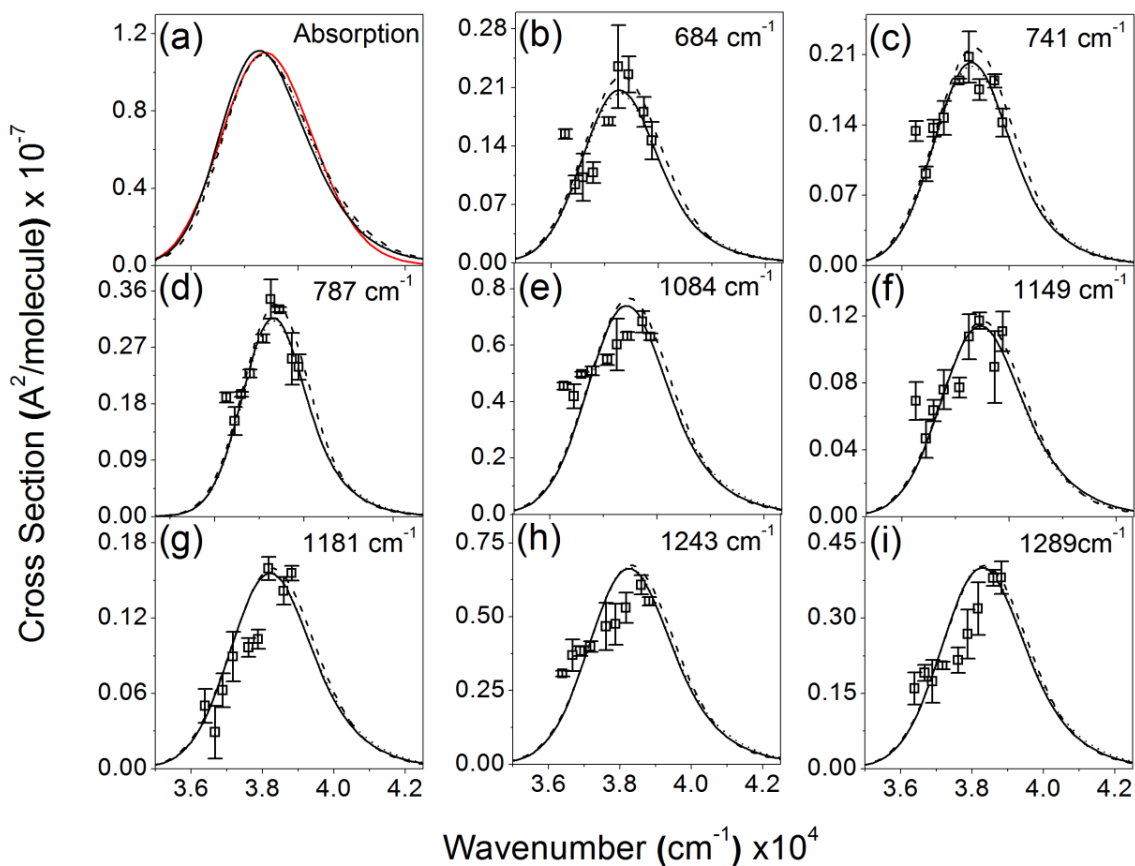


Fig. 3.6 Experimental and simulated Raman excitation profiles and absorption cross section of LF for the transition at 264 nm. (a) Experimental (solid), deconvoluted (red) and simulated absorption (dash) spectrum. (b-i) Raman excitation profiles of eight UVRR modes of LF at 9 different excitation wavelengths. The best fit (solid) was obtained by using the parameters of Table 3.2. Set 1 (dash) and Set 2 (dot) parameters are obtained by decreasing and increasing the best fit delta values by 10% respectively

The structural changes in the excited state upon photoexcitation with respect to the ground state are determined from the dimensionless displacements, Δs , obtained from the best fit simulation. These Δs are converted into geometrical changes in terms of internal coordinates using normal mode calculations of LF by B3LYP/TZVP//PCM level of theory and applying eq. 2.25. The major changes along the bond lengths of LF upon photoexcitation are listed in Table 3.7. **The structural changes in excited state occur along all over the isoalloxazine ring bonds.** The initial dynamics following excitation to the 264 nm excited state results in a contraction of ring II and III through C4a-N5 (-0.031), C9a-N10 (-0.127), N1-C10a (-0.013), C4-N3 (-0.082), N10-C10a (-0.017), N5-C5a (-0.016) bonds. Elongation in the bond of C2-N3 (0.03), N1-C2 (0.023) and C4-C4a (0.018) are observed in Ring III. The distortion is seen in

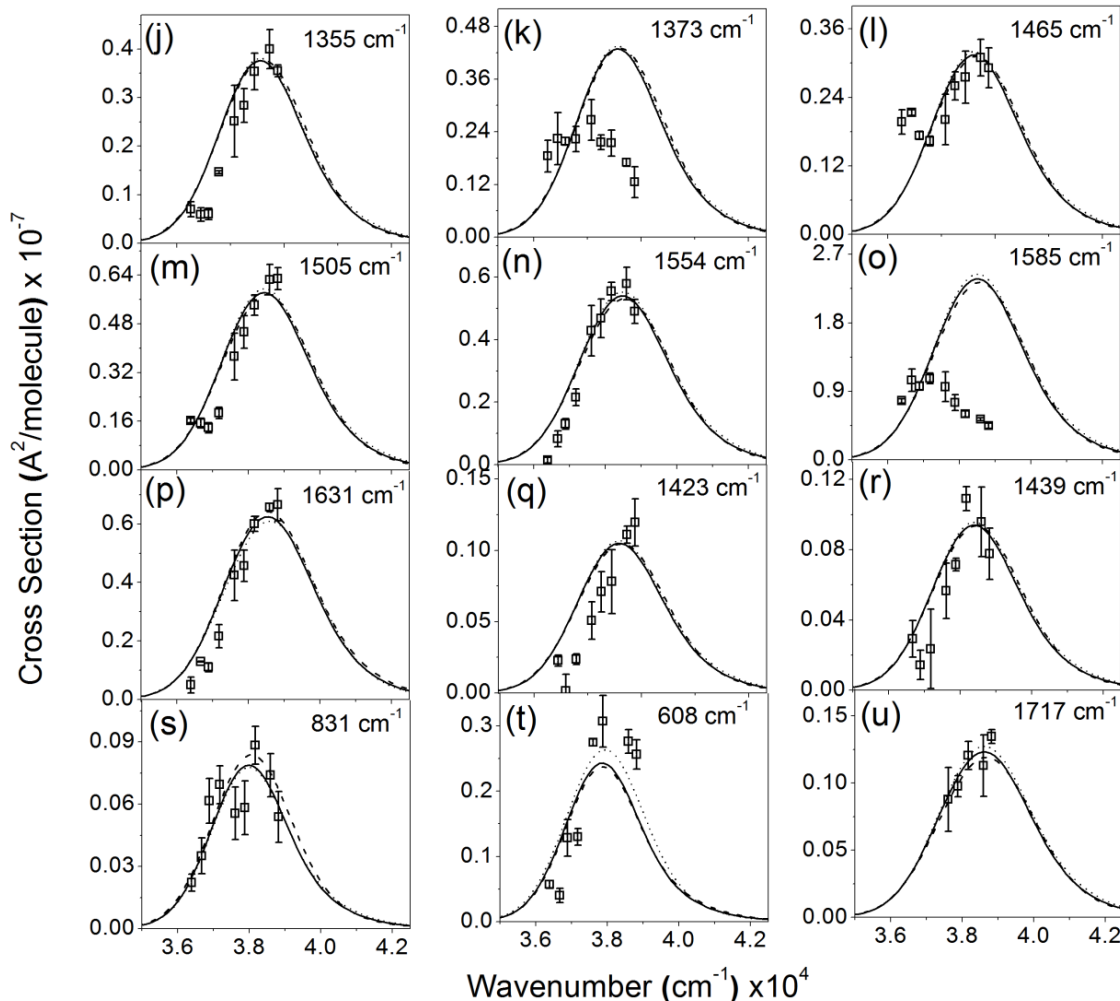


Fig. 3.7 Experimental and simulated Raman excitation profiles (j-u) of other 12 UVRR modes of LF obtained by using the same set of parameters as in Fig. 3.6.

Table 3.6 Parameters used in self-consistent fit of REP and absorption spectra for LF

	E_0 (cm^{-1})	Λ (cm^{-1})	τ (fs)	θ (cm^{-1})	M (\AA)	λ_{int} (cm^{-1})	λ_S (cm^{-1})	λ (cm^{-1})
Best Fit	37719	140	37.9	750	1.12	472	1070	1542
Set 1	37830	180	29.5	930	1.12	368	870	1238
Set 2	37720	100	53.1	710	1.12	549	1130	1679

Ring I by elongation in the C7-C8 (0.032), C9-C9a (0.01), C5a-C9a (0.024) bonds and contraction in the C5a-C6 (-0.057), C8-C9 (-0.036) bonds. So, upon photoexcitation to the 264 nm excited state the maximum change along the ring coordinates of LF was observed in the contraction of C9a-N10 (-0.127) and C4-N3 (-0.082) bonds. Between the carbonyl (C=O) stretching modes, there is an elongation in the bond of C2=O (0.05), whereas a small contraction

is observed in the C4=O bond. All of the outer ring stretching coordinates show contraction in the bond lengths following photoexcitation.

Table 3.7 Internal coordinate changes in LF upon excitation to 264 nm excited state.

Internal Coordinates (bond length)	Internal coordinates in ground state (Å)	Internal coordinate change (Å)	First singlet $\pi\pi^*$ transition at 445 nm
N1-C2	1.3632	0.023	0.016
C2-N3	1.4096	0.03	-0.027
C2=O	1.225	0.05	0.003
C4a-C10a	1.4506	0.003	-0.052
N1=C10a	1.3146	-0.013	0.014
N10-C10a	1.3713	-0.017	0.031
C4-C4a	1.4902	0.018	-0.038
C4a-N5	1.2992	-0.031	0.067
C4-N3	1.3722	-0.082	0.019
C4=O	1.2193	-0.008	0.007
C5a-C9a	1.4183	0.024	0.049
C5a-C6	1.4093	-0.057	0.006
N5-C5a	1.3572	-0.016	-0.04
C9-C9a	1.4003	0.01	0.005
C9a-N10	1.3835	-0.127	-0.025
C9-H9	1.0794	0.004	0
C8-C9	1.3864	-0.036	-0.005
C7-C8	1.4261	0.032	0.017
C8-CH3	1.5019	-0.009	-0.002
C6-C7	1.3757	-0.04	0
C7-CH3	1.5044	-0.037	-0.004
C6-H6	1.0827	0.001	0
N3-H3	1.0128	-0.004	-0.001
N10-CH3	1.4713	-0.044	-0.002

^ataken from ref. 15, calculated using SAC-CI method.

The geometry changes in the excited state can be understood from the nature of the MOs involved in the $\pi\pi^*$ transition at 264 nm. Here the major contribution for this transition comes from H (π) to L+1 (π^*) transition (see Fig 3.3(b)). The changes in the bond lengths follow the character of those orbitals. For example, H shows bonding character for C7-C8 bond while, it changes to anti-bonding in L+1, thus appears in an elongation of this bond. The contraction in the bond of C9a-N10 in excited state is a result of the more bonding character of this bond in

L+1 compare to H. The C4a-N5, C9a-N10, N1-C10a, C4-N3, C5a-C6 and C8-C9 bonds show contraction in excited state because they have more bonding character in L+1 with respect to H, whereas the bonds C7-C8, C9-C9a and C5a-C9a change the nature from bonding in H to anti-bonding in L+1 and as a result these bonds elongate in the excited state.

The structural changes detected in the S1 state using TDDFT³⁵, SAC-CI calculations⁶³ and ultrafast infrared (IR) spectroscopy²⁹ on LF and RF molecules are different from the excited state at 264 nm (shown in Table 3.7). The major change was observed in the elongation of C4a-N5 bond in S1 state. Here we have found contraction in the bond of C4a-N5 in the excited state at 264 nm. The first $\pi\pi^*$ transition happens from H to L. The H for this bond is bonding character while it changes to anti-bonding in L of S1. In S1 state, both the carbonyl stretching bonds show elongation in the bond length, but our finding at 264 nm excited state predicts that contraction happens in C4=O bond. So, these changes are because of the nature of different excited state MOs involved for those different electronic transitions as mentioned in preceding section. The angle of transition dipole moment^{63,64} for those transitions also changes which in turn results in the distinct geometry changes for the two excited states.

The signs of dimensionless displacements are very important quantities that need to be computed for determination of the excited state geometry in terms of changes in internal coordinates. These signs are determined from the excited state gradients computed at the Franck-Condon region on the PES of the relevant electronic state with TDDFT calculations. Now depending upon the specific functional and basis sets used in DFT calculations, the normal mode compositions may also vary slightly which can change the computed excited state geometry. Thus, mode specific reorganization energies are more accurately obtained from REP simulations because they do not rely on the signs of displacements. The mode specific internal reorganization energies can be determined from the best fitted Δs using Eq. 2.21b. **The total internal reorganization energy (λ_{int}) measured over all the UVRR modes of LF is 472 cm⁻¹. The maximum contribution (24%) to the total internal reorganization energy comes from the UVRR band at 1585 cm⁻¹. All of the other intense UVRR modes also contribute significantly to the total λ_{int} . The mode compositions obtained from PED for those modes demonstrate that the initial excited state dynamics lie over all the isalloxazine ring structure in LF.**

Solvent dynamics plays a significant role in condensed phase through line broadening of REPs and absorption spectrum. The spectral breadth of the absorption spectrum and REPs appear from two types of broadening mechanisms, homogeneous and inhomogeneous broadening. However, these two types of broadening affect the absorption spectrum and REPs differently. Analysis of absorption spectrum only cannot differentiate the two mechanisms, because they both broaden the absorption spectrum in a similar way. The homogeneous broadening arises due to the coupling of solute with solvent bath, and it affects the RR intensity at the amplitude level on the ultrafast timescale. Whereas the existence of different microsolvated structures of solute is the cause to appear the inhomogeneous broadening that produces a distribution of cross sections. These microsolvated structures are static in nature in Raman process timescale. So, the self-consistent simulation of absorption spectrum and RR cross sections can separate the two types of broadening. Here we have applied the Brownian oscillator model of Mukamel and Coworkers^{37,65} which incorporates physical parameters, solvent reorganization energy (λ_S) and dynamic solvent response timescale (τ) to account for the solute–solvent interaction on the ultrafast timescale. **Using this model our simulation extracts a solvent reorganization energy of 1070 cm⁻¹ with a dynamic solvent response timescale of 37.9 fs for LF within the 264 nm excited state.**

We compare the solvation characteristics obtained here from our simulation with the previous literature reports. The solvent reorganization energies measured for several natural and substituted nucleobases in the S1 state^{61,66–68} are in the same range with that obtained for LF. The amplitude of solvent response depends on the instantaneous charge reorientation in effect to electronic excitation of the solute (LF). So, this quantity is the inherent characteristic of the resonant excited state of that solute. As Raman is a scattering process, it happens within tens of femtoseconds. The excited state do not get populated significantly within this fast timescale. Thus the solvent reorganization energy obtained here is entirely due to the inertial response of solvent (water) which is found to occur in <100 fs.

The fastest solvation response of water is observed to happen within 50 fs timescale by using ultrafast time-resolved experimental techniques^{39,69,70} and molecular dynamics simulations^{39,71–73} using different probe molecules. Jimenez et al.³⁹ have found the solvation response time of water surrounding coumarin probe is bimodal with an initial ultrafast response

of 55 fs resulting from the inertial motions of water molecules, followed by a slower component corresponding to diffusive motions. Molecular dynamics study of 3-methylindole also showed that fastest response of water relaxation is a Gaussian in nature with a ~ 15 fs time constant, following a slower exponential decay of 400 fs.⁷¹ Time dependent Stokes shift measurements on tryptophan and organic dyes have reported a significant amount of Stokes shift always happens in tens of femtoseconds, much before the fluorescence measurement.^{70,74,75} Explicit measurement of the inertial component of solvent relaxation is beyond the time resolution of any fluorescence based techniques because of the slow internal relaxation processes in fluorescence emission spectroscopy. Our simulated result for the timescale of solvent response (37.9 fs) is in the same order as that obtained for chloro-Guanine⁶¹ and tryptophan⁶² molecules.

Although it was reported earlier^{62,76} that simulated REPs are not much affected by the variation of Λ in the range of 50 cm^{-1} , our simulation indicates an ultrafast timescale of solvent response within 50 fs. Effect of the solvent response timescale on the global fit to the REPs is shown in Fig. 3.8 and 3.9. If we decrease the Λ value by 50% (70 cm^{-1} corresponding to $\tau = 75.7$ fs), the simulated absorption shows better agreement with the experimental absorption spectrum while the simulated REPs are much broader than the experimental ones. On the contrary, if Λ is increased by 50% (210 cm^{-1} corresponding to $\tau = 25.2$ fs), the simulated REPs compress a little bit compared to the optimum values, whereas practically no change is observed in the simulated absorption spectrum. Therefore, for the best fit between simulated and experimental REPs, a solvent reorganization energy of 1070 cm^{-1} and a solvent response timescale of 37.9 fs are desired for our simulation.

The inhomogeneous broadening (θ) requires to be large in our simulation to get the best agreement between simulated and experimental REPs. Our simulation results in a θ value of 750 cm^{-1} which arises due to the ensemble site effect of different microsolvated structures of solute. High θ value ($900\text{-}1300\text{ cm}^{-1}$) for a number of natural and substituted nucleobases was reported using wave-packet dynamics simulations.^{66-68,77-79} All of those nucleobases contain amino ($-\text{NH}_2$) and carbonyl groups ($\text{C}=\text{O}$) which can form hydrogen bonds with the surrounding water molecules and thus facilitates the formation of several microsolvated structures. LF also can form hydrogen bonds with the surrounding water molecules through the free electrons on nitrogen (N) and oxygen (O) atoms (see the structure of LF). DFT calculations

on LF molecule with the addition of explicit water molecules also reported the formation of extensive hydrogen bonding between LF and those water molecules.⁶³ Apart from the microsolvated structures, other slower components of solvation within 100 fs also contribute to the inhomogeneous broadening derived from our simulation.

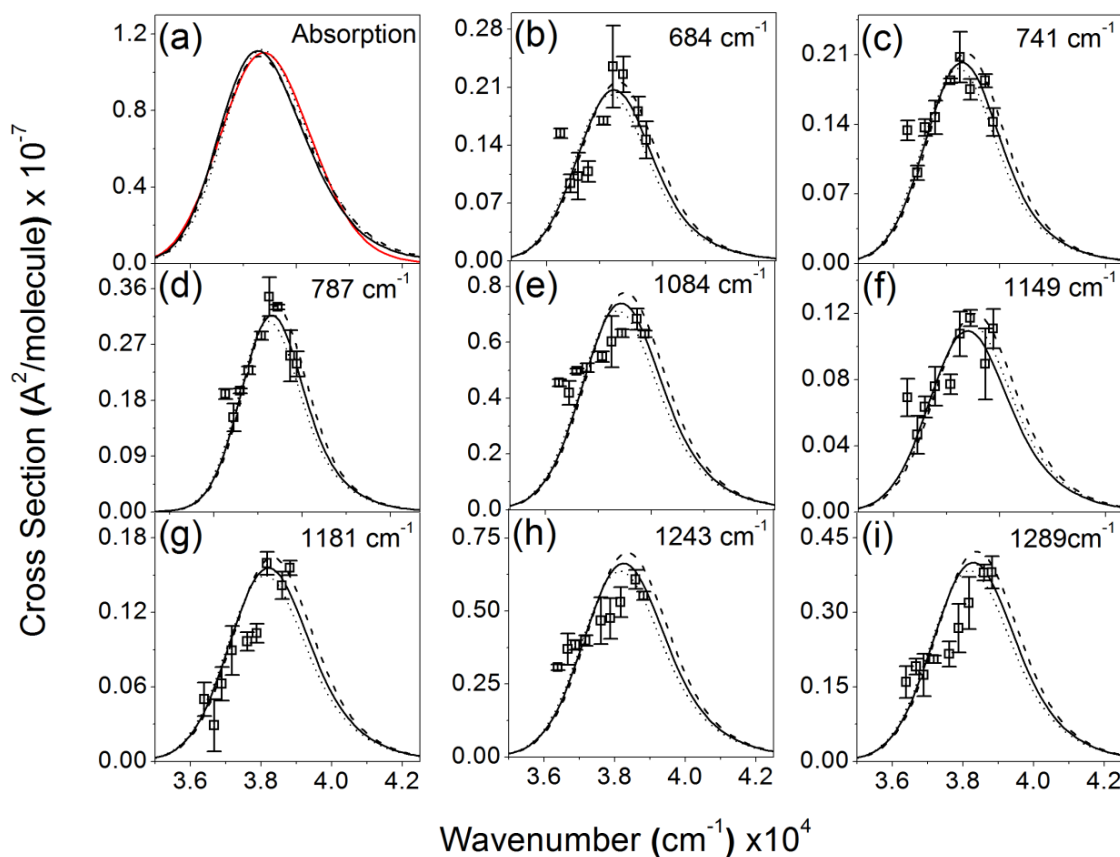


Fig. 3. 8 Experimental and simulated Raman excitation profiles and absorption cross section of LF for the transition at 264 nm. (a) Experimental (solid), deconvoluted (red) and simulated absorption by decreasing Λ value by 50% (dash), simulated absorption by increasing Λ value by 50% (dot) spectrum. (b-i) Raman excitation profiles of eight UVRR modes of LF at 9 different excitation wavelengths by decreasing (dash) and increasing (dot) the Λ value by 50%.

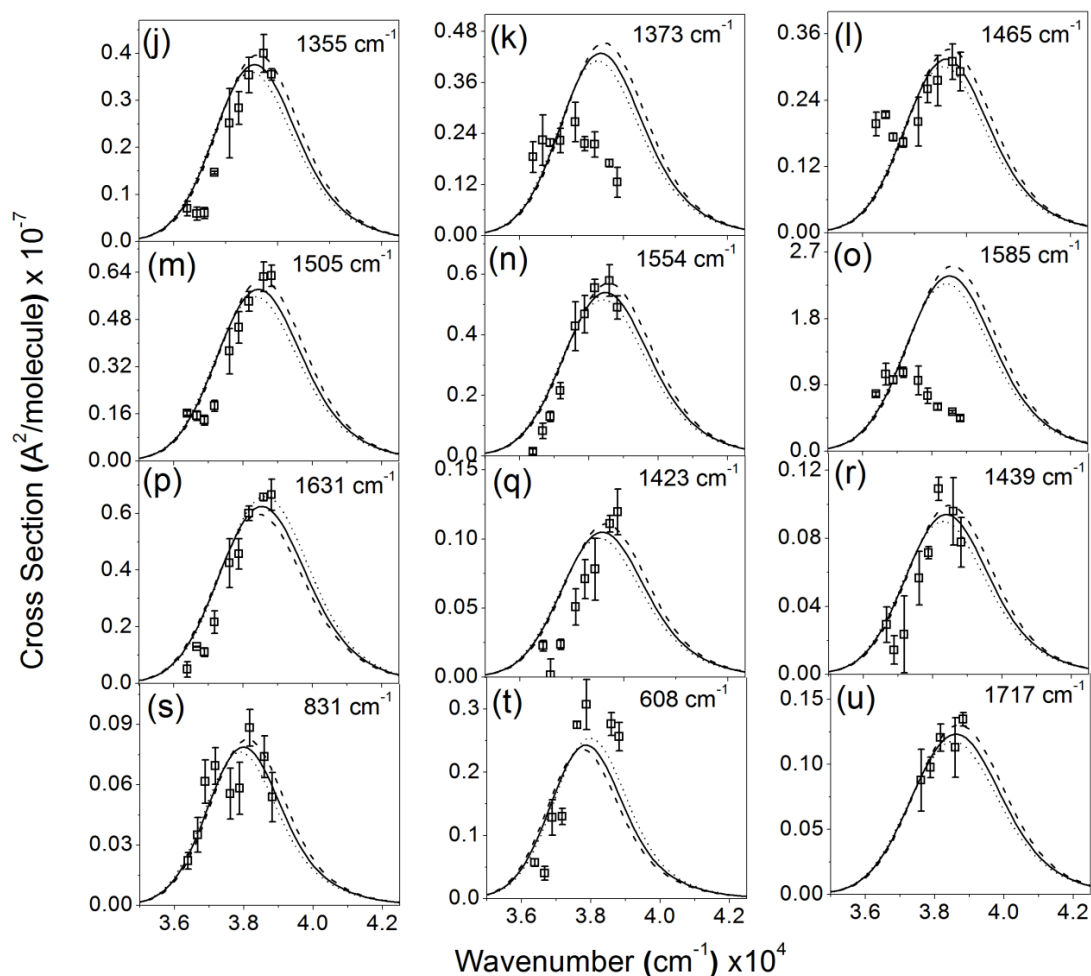


Fig. 3.9 Raman excitation profiles of other UVRR modes of LF at 9 different excitation wavelengths by decreasing (dash) and increasing (dot) the Λ value by 50%.

It is possible to fit the absorption and REP simultaneously by a different set of parameters. Therefore, it is important to check the limits of variability of the parameters used in self-consistent simulation. In this effect, we have used two sets of deltas determined by decreasing and increasing 10% to the best fitted deltas, and then the zero-zero energy, the homogeneous and inhomogeneous linewidths were optimized iteratively to obtain the best possible fit. For the smaller set of deltas (Set1), we were able to obtain a good fit to the absorption spectrum but not in the REPs. The solvent reorganization energy had to be decreased to 930 cm^{-1} whereas the inhomogeneous broadening was required to be 870 cm^{-1} . For the higher set of deltas (Set2), it was not possible to get a good fit either in the absorption spectrum or in the REPs. Here, solvent reorganization energy was required to be 1130 cm^{-1} and we had to decrease the inhomogeneous broadening (710 cm^{-1}) to get an adequate fit for both. However, as our

simulation examines the Raman intensity analysis through modeling of the lineshape function, the resultant parameters depend on the choice of the model used. Here we have applied the simplest model that can partition the total spectral breadth into homogeneous and inhomogeneous broadening components. The simultaneous fit to the absorption and the REPs of several modes restricts the variability in the choice of the parameters used.

3.4 Conclusion

RR intensity analysis using wave-packet dynamics simulations can render insight into the initial excited state structural dynamics of LF within 50 fs of excitation in UV region of the absorption spectrum. **Structural distortion was observed along all over the isoalloxazine ring system following excitation within 264 nm absorption band. Primarily contraction in the bond lengths was observed in Ring II and Ring III with major contractions in the stretching mode of C9a-N10 and C4-N3 bonds. Upon excitation to the 264 nm excited state, the structural distortions are found to be different from that in the first $\pi\pi^*$ excited state. Partitioning of the total spectral breadth into homogeneous and inhomogeneous broadening acquaints that a 71% contribution to the total reorganization energy (1498 cm^{-1}) originates from the inertial response of water. The fastest component of water solvation response was found in ~ 30 fs timescale for LF.** This work has been extended into other flavins (RF, FMN and FAD) to understand the role of different substituents in the dynamics of flavin molecules.

References

- (1) Sancar, A. *Chem. Rev.* **2003**, *103* (6), 2203.
- (2) Losi, A.; Gärtner, W. *Photochem. Photobiol. Sci.* **2008**, *7* (10), 1168.
- (3) Nakasako, M.; Zikihara, K.; Matsuoka, D.; Katsura, H.; Tokutomi, S. *J. Mol. Biol.* **2008**, *381* (3), 718.
- (4) Heelis, P. F. *Chem. Soc. Rev.* **1982**, *11* (1), 15.
- (5) Koziol, J.; Knobloch, E. *Biochim. Biophys. Acta - Biophys. Incl. Photosynth.* **1965**, *102* (1), 289.
- (6) Holzer, W.; Shirdel, J.; Zirak, P.; Penzkofer, A.; Hegemann, P.; Deutzmann, R.; Hochmuth, E. *Chem. Phys.* **2005**, *308* (1–2), 69.
- (7) Ahmad, I.; Fasihullah, Q.; Vaid, F. H. M. *J. Photochem. Photobiol. B.* **2005**, *78* (3), 229.
- (8) Choe, E.; Huang, R.; Min, D. B. *J. Food Sci.* **2005**, *70* (1), R28.
- (9) Grodowski, M. S.; Veyret, B.; Weiss, K. *Photochem. Photobiol.* **1977**, *26* (4), 341.

- (10) Yoshimura, A.; Ohno, T. *Photochem. Photobiol.* **1988**, *48* (5), 561.
- (11) Jung, M. Y.; Min, D. B. *J. Food Sci.* **2009**, *74* (6).
- (12) KNOWLES, A.; ROE, E. M. F. *Photochem. Photobiol.* **1968**, *7* (5), 421.
- (13) Huang, R.; Hyun, J. K.; Min, D. B. *J. Agric. Food Chem.* **2006**, *54* (6), 2359.
- (14) Salzmänn, S.; Tatchen, J.; Marian, C. M. *J. Photochem. Photobiol. A Chem.* **2008**, *198* (2–3), 221.
- (15) Choe, Y.-K.; Nagase, S.; Nishimoto, K. *J. Comput. Chem.* **2007**, *28* (4), 727.
- (16) Koziół, J. *Photochem. Photobiol.* **1969**, *9* (1), 45.
- (17) Schreiner, S.; Steiner, U.; Kramer, H. E. A. *Photochem. Photobiol.* **1975**, *21* (2), 81.
- (18) Bowd, A.; Byrom, P.; Hudson, J. B.; Turnbull, J. H. *Photochem. Photobiol.* **1968**, *8* (1), 1.
- (19) Sun, M.; Moore, T. A.; Song, P.-S. *J. Am. Chem. Soc.* **1972**, *94* (5), 1730.
- (20) Penzkofer, a. *Chem. Phys.* **2012**, *400*, 142.
- (21) Sikorska, E.; Khmelinskii, I. V.; Koput, J.; Sikorski, M. *J. Mol. Struct. THEOCHEM* **2004**, *676* (1–3), 155.
- (22) Vaish, S. P.; Tollin, G. *J. Bioenerg.* **1970**, *1* (2), 181.
- (23) Weller, A. *Naturwissenschaften* **1955**, *42* (7), 175.
- (24) Lothrop, W. C.; Richard Handrick, G. *Chem. Rev.* **1949**, *44* (3), 419.
- (25) GREEN, M.; TOLLIN, G. *Photochem. Photobiol.* **1968**, *7* (2), 145.
- (26) Surrey, A. R.; Nachod, F. C. *J. Am. Chem. Soc.* **1951**, *73* (5), 2336.
- (27) Sikorska, E.; Khmelinskii, I. V.; Pruka??a, W.; Williams, S. L.; Patel, M.; Worrall, D. R.; Bourdelande, J. L.; Koput, J.; Sikorski, M. *J. Phys. Chem. A* **2004**, *108* (9), 1501.
- (28) Kondo, M.; Nappa, J.; Ronayne, K. L.; Stelling, A. L.; Tonge, P. J.; Meech, S. R. *J. Phys. Chem. B* **2006**, *110* (41), 20107.
- (29) Wolf, M. M. N.; Schumann, C.; Gross, R.; Domratcheva, T.; Diller, R. *J. Phys. Chem. B* **2008**, *112* (42), 13424.
- (30) Salzmänn, S.; Marian, C. M. *Chem. Phys. Lett.* **2008**, *463* (4–6), 400.
- (31) Hasegawa, J. y.; Bureekaew, S.; Nakatsuji, H. *J. Photochem. Photobiol. A Chem.* **2007**, *189* (2–3), 205.
- (32) Zenichowski, K.; Gothe, M.; Saalfrank, P. *J. Photochem. Photobiol. A Chem.* **2007**, *190* (2–3), 290.
- (33) Climent, T.; González-Luque, R.; Merchán, M.; Serrano-Andrés, L. *J. Phys. Chem. A* **2006**, *110* (50), 13584.
- (34) Klaumünzer, B.; Kröner, D.; Lischka, H.; Saalfrank, P. *Phys. Chem. Chem. Phys.* **2012**, *14* (24), 8693.
- (35) Klaumünzer, B.; Kröner, D.; Saalfrank, P. *J. Phys. Chem. B* **2010**, *114* (33), 10826.
- (36) Lee, S.; Heller, E. J. *J. Chem. Phys.* **1979**, *71* (12), 4777.
- (37) Li, B.; Johnson, A. E.; Mukamel, S.; Myers, A. B. *J. Am. Chem. Soc.* **1994**, *116* (24), 11039.
- (38) Myers, A. B. *Chem. Rev.* **1996**, *96* (3), 911.
- (39) Jimenez, R.; Fleming, G. R.; Kumar, P. V.; Maroncelli, M. *Nature* **1994**, *369* (6480), 471.
- (40) Tollin, G. *Biochemistry* **1968**, *7* (5), 1720.

- (41) Lee, C.; Yang, W.; Parr, R. G. *Phys. Rev. B* **1988**, *37* (2), 785.
- (42) Becke, A. D. *J. Chem. Phys.* **1993**, *98* (7), 5648.
- (43) Godbout, N.; Salahub, D. R.; Andzelm, J.; Wimmer, E. *Can. J. Chem.* **1992**, *70* (2), 560.
- (44) Miertuš, S.; Scrocco, E.; Tomasi, J. *J. Chem. Phys.* **1981**, *55* (1), 117.
- (45) NISHINA, Y.; SHIGA, K.; HORIIKE, K.; TOJO, H.; KASAI, S.; YANASE, K.; MATSUI, K.; WATARI, H.; YAMANO, T. *J. Biochem.* **1980**, *88* (2), 403.
- (46) Schmidt, J.; Coudron, P.; Thompson, A. W.; Watters, K. L.; McFarland, J. T. *Biochemistry* **1983**, *22* (1970), 76.
- (47) Lee, N. S.; Sheng, R. S.; Morris, M. D.; Schopfer, L. M. *J. Am. Chem. Soc.* **1986**, *108* (20), 6179.
- (48) Abe, M.; Kyogoku, Y.; Kitagawa, T.; Kawano, K.; Ohishi, N.; Takai-Suzuki, A.; Yagi, K. *Spectrochim. Acta Part A Mol. Spectrosc.* **1986**, *42* (9), 1059.
- (49) Eisenberg, A. S.; Schelvis, J. P. M. *J. Phys. Chem. A* **2008**, *112* (27), 6179.
- (50) Copeland, R. A.; Spiro, T. G. *J. Phys. Chem.* **1986**, *90* (25), 6648.
- (51) Weigel, a; Dobryakov, a; Klaumünzer, B.; Sajadi, M.; Saalfrank, P.; Ernsting, N. P. *J. Phys. Chem. B* **2011**, *115* (13), 3656.
- (52) Kim, M.; Carey, P. R. *J. Am. Chem. Soc.* **1993**, *115* (15), 7015.
- (53) Lively, C. R.; McFarland, J. T. *J. Phys. Chem.* **1990**, *94* (10), 3980.
- (54) Weigel, A.; Dobryakov, A.; Klaumünzer, B.; Sajadi, M.; Saalfrank, P.; Ernsting, N. P. *J. Phys. Chem. B* **2011**, *115*, 3656.
- (55) Abe, M.; Kyogoku, Y. *Spectrochim. Acta Part A Mol. Spectrosc.* **1987**, *43* (8), 1027.
- (56) Nishina, Y.; Sato, K.; Miura, R.; Matsui, K.; Shiga, K. *J. Biochem.* **1998**, *124* (1), 200.
- (57) Wolf, M. M. N.; Zimmermann, H.; Diller, R.; Domratcheva, T. *J. Phys. Chem. B* **2011**, *115* (23), 7621.
- (58) Zheng, Y.; Dong, J.; Palfey, B. A.; Carey, P. R. *Biochemistry* **1999**, *38* (51), 16727.
- (59) Swartz, T. E.; Corchnoy, S. B.; Christie, J. M.; Lewis, J. W.; Szundi, I.; Briggs, W. R.; Bogomolni, R. A. *J. Biol. Chem.* **2001**, *276* (39), 36493.
- (60) Unno, M.; Sano, R.; Masuda, S.; Ono, T.-A.; Yamauchi, S. *J. Phys. Chem. B* **2005**, *109* (25), 12620.
- (61) Mondal, S.; Puranik, M. *Phys. Chem. Chem. Phys.* **2016**.
- (62) Milán-Garcés, E. A.; Kaptan, S.; Puranik, M. *Biophys. J.* **2013**, *105* (1), 211.
- (63) Hasegawa, J. ya; Bureekaew, S.; Nakatsuji, H. *J. Photochem. Photobiol. A Chem.* **2007**, *189* (2–3), 205.
- (64) Johansson, L. B.; Davidsson, a; Lindblom, G.; Naqvi, K. R. *Biochemistry* **1979**, *18* (19), 4249.
- (65) Mukamel, S. *Principles of Nonlinear Optical Spectroscopy*, Oxford University Press, New York; 1995.
- (66) El-Yazbi, A. F.; Palech, A.; Loppnow, G. R. *J. Phys. Chem. A* **2011**, *115* (38), 10445.
- (67) Oladepo, S. A.; Loppnow, G. R. *J. Phys. Chem. B* **2011**, *115* (19), 6149.
- (68) Billingham, B. E.; Oladepo, S. A.; Loppnow, G. R. *J. Phys. Chem. B* **2012**, *116* (35), 10496.
- (69) Jarzba, W.; Walker, G. C.; Johnson, A. E.; Kahlow, M. A.; Barbara, P. F. *J. Phys. Chem.* **1988**, *92* (20), 7039.

- (70) Vajda, S.; Jimenez, R.; Rosenthal, S. J.; Fidler, V.; Fleming, G. R.; Castner, E. W. *J. Chem. Soc. Trans.* **1995**, 91 (5), 867.
- (71) Muino, P. L.; Callis, P. R. *J. Chem. Phys.* **1994**, 100 (6), 4093.
- (72) Barnett, R. B.; Landman, U.; Nitzan, A. *J. Chem. Phys.* **1989**, 90 (8), 4413.
- (73) Maroncelli, M.; Fleming, G. R. *J. Chem. Phys.* **1988**, 89 (8), 5044.
- (74) Bräm, O.; Oskouei, A. A.; Tortschanoff, A.; Van Mourik, F.; Madrid, M.; Echave, J.; Cannizzo, A.; Chergui, M. *J. Phys. Chem. A* **2010**, 114 (34), 9034.
- (75) Shen, X.; Knutson, J. R. *J. Phys. Chem. B* **2001**, 105 (26), 6260.
- (76) Cao, X.; McHale, J. L. *J. Chem. Phys.* **1998**, 109 (5), 1901.
- (77) Billinghamurst, B. E.; Yeung, R.; Loppnow, G. R. *J. Phys. Chem. A* **2006**, 110 (19), 6185.
- (78) Yarasi, S.; Ng, S.; Loppnow, G. R. *J. Phys. Chem. B* **2009**, 113 (43), 14336.
- (79) Yarasi, S.; Brost, P.; Loppnow, G. R. *J. Phys. Chem. A* **2007**, 111 (24), 5130.

Chapter 4: Deep UV Initiated Excited State Dynamics of Riboflavin (RF) and Flavin mononucleotide (FMN)

4.1 Introduction

Flavins are the chromophores in blue-light photoreceptors and henceforth play pivotal role in various photobiological processes. These compounds are redox active coenzymes which consist of a heterocyclic isoalloxazine ring (7,8-dimethylisoalloxazine) with substitution at nitrogen 10 (Fig 4.1). flavin adenine dinucleotide (FAD) and flavin mononucleotide (FMN) are the two main light harvesting chromophores present in several enzymes such as DNA photolyase, cryptochromes, blue-light-sensing -using-FAD (BLUF) and light-oxygen-voltage domains (LOV), phototropins etc.¹⁻³ In these photoreceptors, FAD and FMN can undergo both one electron and two electron redox processes to carry out a number of key biological processes. Riboflavin (RF) known as vitamin B2, is the precursor of biologically important cofactors, FAD and FMN. RF is commonly present in our everyday diet, such as vegetables, milk, meat products and acts as an effective photosensitizer in food and biological systems.⁴⁻⁷ The deficiency of RF causes skin disease and growth retardation.

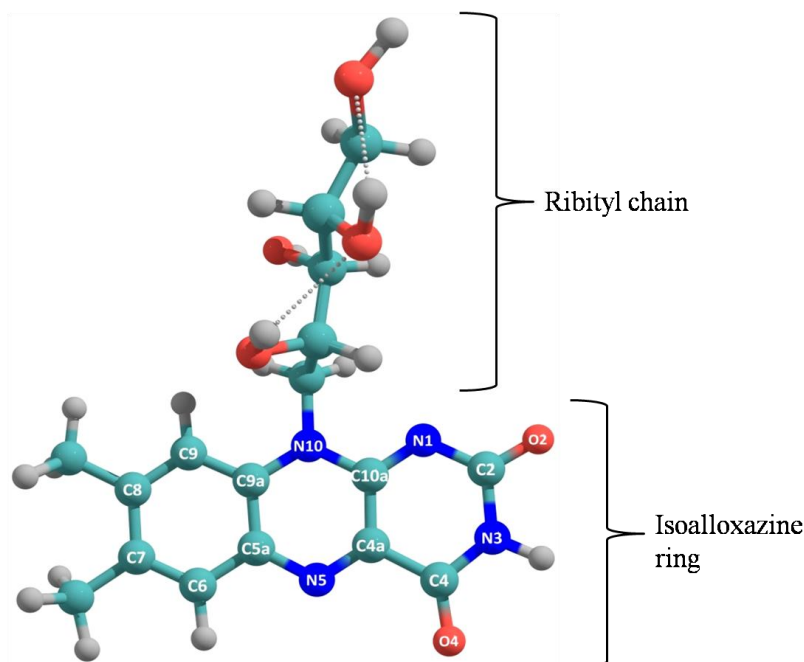


Fig. 4.1. Optimized structure of riboflavin using B3LYP/TZVP basis set with PCM solvent model. The conventional atomic numbering for flavins is used in the above structure. The colors of the atoms are chosen as, O (red), N (blue), C (cyan) and H (grey).

Flavins get excited following light absorption and initiate the signal processing in the blue light photoreceptors which are abundant in plants and microorganisms. Understanding the photo-induced phenomenon in flavin family is fundamentally important to elucidate the role of these molecules in the context of their biological functions. Several groups have provided significant insight to both experimental⁸⁻²¹ and theoretical research²²⁻²⁶ in the area of flavin excited state photophysics. Flavins have four electronic excitations at ~ 220, 266, 375 and 445 nm, which are of $\pi\pi^*$ character (Fig. 4.2 (c)). Time-resolved spectroscopic techniques having time resolution from femtoseconds (fs) to nanoseconds (ns) are routinely applied to examine excited state properties of flavins in solution^{8,10,12,14,16,18,20,21,27} and inside the protein core²⁸⁻³⁶ in the lowest energy singlet (S_1) excited state at ~ 445 nm. The S_1 state in all flavins has excited state lifetime of several ns, except FAD which exhibits a faster decay in picoseconds (ps) time scale. This is attributed to the stacked conformation between the adenine and flavin ring in FAD.^{37,38} Femtosecond-infrared (fs-IR) spectroscopy of RF has probed vibrational cooling which is associated with downshifting to vibrational modes by 10-15 cm^{-1} within 4 ps of photoexcitation in S_1 state.¹⁰ Weigel et al.²⁰ studied the fs dynamics of RF in polar solvents (DMSO) after photoexcitation to S_1 state using fs stimulated Raman, transient optical absorption and fluorescence spectroscopies. Their studies showed 10 fs lifetime for the Franck-Condon $\pi\pi^*$ state. They also observed that the vibrational fine structure formed following photoexcitation, vanishes with a very fast time constant of 20 fs using transient absorption spectra. Weigel et al also noticed the characteristic feature of non-adiabatic coupling between the S_1 state and nearby $n\pi^*$ state and this coupling was found to depend on solvent polarity and temperature.

Short-time dynamics of RF in the S_1 state was studied employing mixed quantum classical non-adiabatic molecular dynamics simulation.²² The decay time of the Franck-Condon state was found to be 10 fs, in excellent agreement with experimental report. They found a longer time scale of 80-100 fs compare to the above experimental report for the Intramolecular Vibrational energy Redistribution (IVR). The vibrational energy first spreads to the C-C stretching modes and then over the entire isoalloxazine ring vibrations include the low frequency in-plane modes. Time dependent density functional (TDDFT) calculations using TD-B3LYP/TZVP/PCM method revealed that a red shift occurs in the C2=O and C4=O stretching vibrations upon photoexcitation to the S_1 state.²⁵ They also observed the loss of double bond character of the C=N stretching vibrational modes above 1500 cm^{-1} frequency upon photoexcitation.

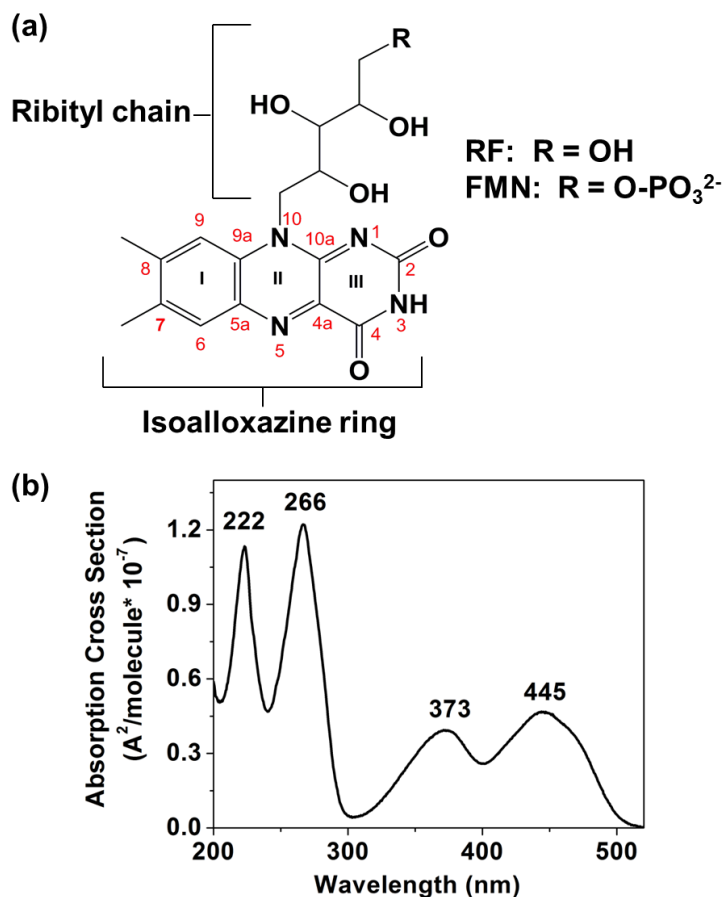


Fig. 4.2 Structures of (a) riboflavin (RF) and (b) flavin mononucleotide (FMN). (c) Experimental absorption spectrum of RF and FMN in pH7 phosphate buffer labeled with the λ_{\max} values.

Other than the S1 state (~ 445 nm), flavins have strong $\pi\pi^*$ transitions in the ultraviolet (UV) region of the absorption spectrum. A number of reports investigating photophysics of these heavily absorbing electronic states are limited. In this work, we employed Ultraviolet Resonance Raman (UVR) spectroscopy to explore the initial excited state dynamics of RF and FMN within the 266 nm absorption band. Resonance enhancement of vibrational modes happens when the excitation wavelengths are chosen to lie within an allowed electronic absorption band of the molecule, and is known as resonance Raman (RR) effect. Strong fluorescence emission of a molecule masks the Raman spectra in visible excitations and to get rid of this, excitations near UV is preferred. Copeland and Spiro have reported the UVR spectra of FMN and FAD with excitation wavelengths at 200, 218, 240, 266, 355 and 488 nm.³⁹ Unique patterns of relative intensities of RR bands at the aforementioned Raman excitations suggest very different FC activity in each of the singlet excited states of these molecules.

The positions of the RR bands of a molecule reflect its ground state molecular structure, while the RR intensities encode information of the resonant vibronic state. Specifically, RR

intensity of a band is directly proportional to the slope on the potential energy surface (PES) of the resonant electronic state along that vibrational coordinate. Thus, greater the molecular distortion in the electronic excited state compared to that in the ground state along the vibrational coordinate, higher the intensity of the resulting RR band. Therefore, RR vibrational band intensity is precisely indicative of the change in the molecular structure along each vibrational coordinate upon excitation to an electronic excited state. UVRR spectroscopy has been successfully applied to explore the excited state structural dynamics for a number of nucleic acid bases⁴⁰⁻⁴⁶ and bacteriorhodopsins⁴⁷. In order to characterize the excited state centered at 266 nm, we have measured UVRR spectra of both the molecules throughout this absorption band at ten different Raman excitations. Now, distortions taking place within Raman scattering timescale (tens of femtoseconds) upon photoexcitation can be extracted from UVRR intensity analysis along each vibrational coordinate. Through comprehensive measurement and modeling of experimental Raman intensities, a number of parameters describing initial solvation process and excited state dynamics of RF and FMN molecule can be extracted.

Lee and Heller's time dependent wave packet theory (TDWP)⁴⁸ was applied to simulate the Raman excitation profiles *i.e.* excitation wavelength dependence of RR cross-sections of all resonant modes and absorption cross-section of RF and FMN molecule in a self-consistent manner. We have determined the changes in the internal coordinates of both the molecules from respective ground state values following photoexcitation to the 266 nm centered excited state. Total reorganization energy determined on the fs timescale was partitioned into inter (vibrational) and intramolecular (solvent) reorganization energies. We have applied Brownian oscillator model to simulate the line shape of REPs accounting for fast solvent induced dephasing.⁴⁹ The total linewidth broadening contributions to both REPs and absorption spectrum is partitioned into two components; (i) homogeneous broadening arising from the coupling of solute and surrounding solvent bath, and (ii) the inhomogeneous part resulting from the existence of numbers of distinct microsolvated structures of solute formed by the solvent molecules. Time dependent density functional theory (TDDFT) was employed to compute excitation energies and other properties of the resonant electronic states.

4.2 Experimental and Computational Methods

4.2.1 Sample Preparation

RF and FMN were purchased from Sigma Chemicals Co. with greater than 95% HPLC purity and were used without further purification. Sample solutions were prepared in 50 mM sodium phosphate buffer of pH 7. Concentrations of sample solutions were determined from the known molar extinction coefficients of RF.⁵⁰ 300 μ L of 100 μ M RF and 250 μ M of FMN sample solutions were used for UVRR experiments. In all the samples 250 mM sodium sulphate (Na_2SO_4) solutions were added as internal standard. Acetonitrile, Dimethyl sulphoxide (DMSO), Dimethyl formamide (DMF), Cyclohexane, Isopropanol, Trichloroethylene and Indene solvents were purchased from Ranchem Chemicals and Sigma Co. and used for calibration of spectra obtained. UV/Vis absorption spectra were recorded using Perkin-Elmer (lambda 45) absorption spectrometer at pH 7 in phosphate buffer.

4.2.2 UVRR Spectroscopy

UVRR Spectra were recorded at 10 excitation wavelengths throughout the 266 nm absorption band of RF. The detailed experimental set-up for UVRR experiments has been given in method chapter.

4.2.3 UVRR Cross-section Determination

The detailed process of UVRR cross section determination has been given in method chapter. The depolarization ratio of RF and FMN (Table 4.1) are measured using the similar experimental technique as described earlier.

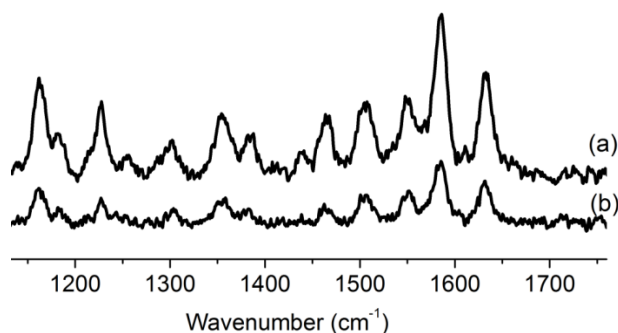


Fig. 4.3 (a) Polarized and (b) depolarized spectra of 300 μ M FMN in higher frequency region obtained at 266 nm excitation wavelength.

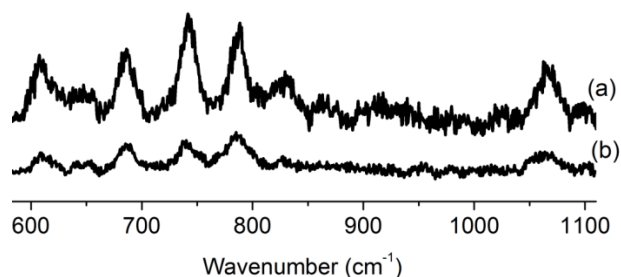


Fig. 4.4 (a) Polarized and (b) depolarized spectra of 300 μM FMN in lower frequency region obtained at 266 nm excitation.

Table 4.1 Depolarization ratios of UVRR bands of RF at 266 nm excitation

Raman Band (cm^{-1})	Depolarization Ratio
609	0.42
685	0.34
742	0.21
787	0.63
828	0.41
1065	0.27
1163	0.44
1228	0.21
1302	0.28
1356	0.35
1382	0.32
1464	0.33
1505	0.47
1549	0.33
1583	0.38
1632	0.36

4.2.4 Computational Method - Simulation of Experimental REP and Absorption Spectrum

The simulation of experimental REP and absorption cross sections was done using time dependent wave packet propagation theory and described in detail in method section. Initial parameters for starting the simulation were determined in the same way as described for LF.

4.2.5 Deconvolution of the Absorption Spectrum

Deconvolution of absorption spectrum for simulation was done in the similar way as done for LF in the previous chapter

4.2.6 Quantum Chemical Computations

RF and FMN are structurally different in only a phosphate group. Thus, RF structure serves as a good comparison for FMN as well. All quantum chemical calculations were done using density functional theory on the B3LYP/TZVP level of theory using the program Gaussian 09 software. Structure of RF molecule was optimized using B3LYP^{51,52} exchange correlation functional along with TZVP⁵³ basis set. Polarizable continuum model (PCM)⁵⁴ was employed to simulate the bulk dielectric environment of water. For the assignment of experimental vibrational modes, we also computed the spectra of the deuterium labeled molecule. Isotopic shifts on deuterium exchange were calculated after replacement of the mass of N₃-H proton by the mass of deuterium (D). Normal mode analysis was carried out on theoretical spectra and matched with the observed experimental frequencies in H₂O and in D₂O. No scaling factor was used for computed frequencies. TDDFT^{55,56} calculation was done using the same level of theory on the previously optimized structures. The absorption spectra were calculated from the vertical excitation energies at TD-B3LYP level of theory and by considering the fixed Gaussian band width of 2500 cm⁻¹. Optimized structures, vibrational modes and molecular orbitals are visualized using the software Chemcraft v 1.6.

4.3 Results and Discussion

4.3.1 Electronic Structure

RF and FMN, like other flavins have four strong experimental absorption peaks at around 222, 266, 373 and 445 nm (Fig. 4.2 (c)). Among them, 266 nm peak is the most intense one. We excited both the molecules within this 266 nm absorption band using 10 different UV excitations at 257.6, 259.9, 263, 265.9, 268, 270.4, 272.9, 274.8, 277.4 and 280.1 nm. Theoretical calculations using various quantum chemical calculations^{22,25,26,57-62} have reported the molecular orbital's (MO) involved following excitation to the visible and UV excited states for different isoalloxazine derivatives. TDDFT calculations were done using B3LYP/TZVP/PCM method in DMSO on RF molecule to compute the vibrational spectra and excitation energies in S₁ state.^{20,22,25} Here, we have also applied this method in water (using PCM solvent model) on RF to identify the nature of MO's involved upon photoexcitation to the excited state inside the 266 nm absorption band.

Table 4.2 Coordinates of ground state optimized structure of RF

Atom no.	Atom	X	Y	Z	Atom no.	Atom	X	Y	Z
1	C	-3.634474000	-2.636017000	-0.224375000	25	H	5.878431000	-0.918629000	1.010259000
2	C	-3.848617000	-1.291216000	-0.409037000	26	O	1.476342000	-1.394846000	-0.827329000
3	C	-2.840878000	-0.334458000	-0.167759000	27	H	2.023721000	-1.316266000	-1.621553000
4	C	-1.561346000	-0.763169000	0.277844000	28	O	3.246069000	-1.375000000	1.676416000
5	C	-1.341991000	-2.136467000	0.449469000	29	H	3.153788000	-0.941013000	2.531266000
6	C	-2.344572000	-3.061847000	0.211177000	30	O	3.946700000	-0.194343000	-1.649148000
7	C	-0.865869000	1.533341000	0.317230000	31	H	4.707548000	-0.352561000	-2.224978000
8	C	-2.196863000	1.857546000	-0.148727000	32	O	6.540961000	-0.948426000	-0.975586000
9	C	-2.507871000	3.296814000	-0.371763000	33	H	7.408241000	-0.544211000	-0.861519000
10	C	-0.173176000	3.742218000	0.369702000	34	N	-0.599277000	0.203966000	0.530073000
11	H	-4.807741000	-0.919602000	-0.747106000	35	N	-3.124986000	0.976200000	-0.372084000
12	H	-0.369193000	-2.499326000	0.738382000	36	N	0.080355000	2.414810000	0.556407000
13	H	-1.595842000	5.117960000	-0.219576000	37	N	-1.448430000	4.123942000	-0.093065000
14	C	0.728616000	-0.147429000	1.073684000	38	C	-2.060267000	-4.523952000	0.407515000
15	H	1.003532000	0.651266000	1.757357000	39	H	-2.220536000	-5.082620000	-0.518283000
16	H	0.636772000	-1.069002000	1.637163000	40	H	-1.034257000	-4.688203000	0.732756000
17	C	1.799711000	-0.273977000	-0.004721000	41	H	-2.730134000	-4.956068000	1.155616000
18	H	1.797949000	0.637756000	-0.605368000	42	C	-4.729627000	-3.633753000	-0.484684000
19	C	3.198085000	-0.389970000	0.635769000	43	H	-4.439786000	-4.351686000	-1.256215000
20	H	3.451907000	0.595289000	1.040747000	44	H	-4.964867000	-4.210080000	0.413774000
21	C	4.252691000	-0.813443000	-0.392848000	45	H	-5.639699000	-3.133525000	-0.813191000
22	H	4.185878000	-1.902669000	-0.497090000	46	O	0.654329000	4.620199000	0.581108000
23	C	5.661195000	-0.455743000	0.043750000	47	O	-3.584366000	3.718488000	-0.759455000
24	H	5.751898000	0.631311000	0.136841000					

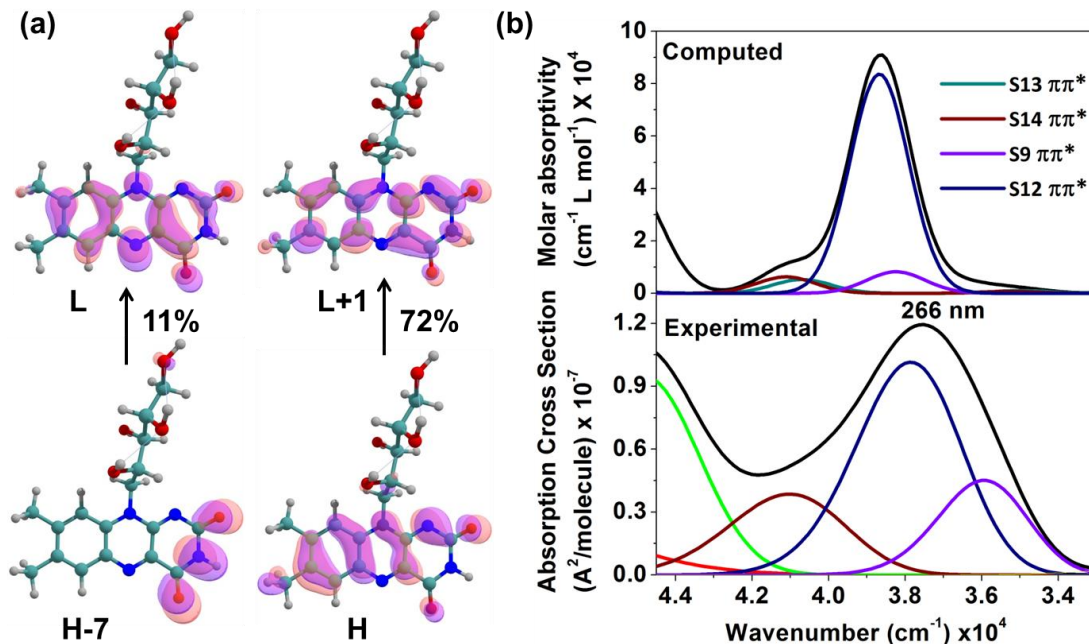


Fig. 4.5 (a) Computed orbitals of RF involved in the electronic transition observed in experiments at 266 nm; H and L stands for highest occupied molecular orbital (HOMO) and lowest unoccupied molecular orbital (LUMO) respectively; (b) theoretical absorption spectra (above) was computed using TD-B3LYP/TZVP//PCM method on RF molecule. Computed band positions are depicted with a Gaussian line shape of fixed line width (2500 cm^{-1}) and deconvoluted experimental absorption (below) of RF labeled with the λ_{max} .

We assign the lowest energy experimental band at 445 nm to the computed $\pi\pi^*$ transition at 2.93 eV with oscillator strength 0.2042 (Table 4.3). Previously reported excitation energies for the lowest energy absorption band using various quantum chemical methods agree well with our results (see Table 4.3). Saalfrank et al. have found the excitation energy at 2.94 eV of oscillator strength 0.2091 for this transition by using the same basis set in gas phase with four explicit water molecules placed near the polar atoms.²² Climent et al. computed the CASPT2 energy at 3.09 eV for isoalloxazine ring.⁵⁸ The vertical SAC-CI energy calculated for the transition at 2.40 eV for LF molecule, which is a slightly lower than our results.⁵⁹ The absorption band at 373 nm is assigned to the $\pi\pi^*$ transition obtained at 3.51 eV of oscillator strength 0.2667. TDDFT calculation using the same basis set (B3LYP/TZVP) in the gas phase for this transition was found at 3.54 eV with oscillator strength 0.2687²². For LF and isoalloxazine ring using DFT/MRCI⁶⁰ and SAC-CI⁵⁹ also show similar results whereas CASPT2⁵⁸ results show higher vertical excitation energy for the same transition.

Table 4.3 Vertical singlet excitation energies ΔE_{vert} in nm (in eV in parenthesis), oscillator strengths (f) and major orbital contribution for electronic transitions of oxidized RF molecule by TD-B3LYP/TZVP/PCM method and comparison with published computed and experimental transition energies were given in the table.

State order	Type	Major orbital contribution (%) ^a	Computed				Experimental		
			ΔE_{vert} ^b in nm (eV)	f	Published ΔE_{vert} in eV			ΔE_{expt} ⁱ (λ_{max}) in nm	ϵ^i ($\text{M}^{-1} \text{cm}^{-1}$)
					RF	IA ^c	LF	RF	
S1	($\pi\pi^*$)	H→L (95%) H-1→L (5%)	423.0 (2.93)	0.2042	3.04(0.1749)/ 2.94(0.2091) ^c , 3.04 ^d	3.09 (0.239)	2.40 ^f , 2.94 ^g , 2.91(0.23) ^h ,	449	12100
S2	($n\pi^*$)	H-4→L (32%) H-2→L (39%)	365.4 (3.39)	0.0109					
S3	($\pi\pi^*$)	H-1→L (84%)	352.9 (3.51)	0.2667	3.76(0.1620)/ 3.54(0.2687) ^c	4.28 (0.158)	3.54 ^f , 3.84 ^g , 3.50(0.28) ^h ,	374	10300
S9	($\pi\pi^*$)	H-8→L (62%) H-6→L (19%)* (Ribityl chain)*	274.2 (4.52)	0.0289					
S10	($\pi\pi^*$)	H-6→L (75%)* (Ribityl chain)*	269.7 (4.59)	0.0051					
S11	($n\pi^*$)	H-11→L (83%)	261.5 (4.74)	0.0681					
S12	($\pi\pi^*$)	H→L+1 (72%) H-7→L (11%)	258.6 (4.79)	0.6925		4.69 (0.104), 5.00 (0.337), 5.37 (0.641)	4.56^f, 4.95^f, 4.77^g, 4.91^g 4.79(0.79)^h,	268	31600
S13	($\pi\pi^*$)	H-10→L (76%) H-1→L (15%)	245.8 (5.04)	0.0436					
S14	($\pi\pi^*$)	H→L+2 (41%) H-1→L+1 (34%) H-10→L (20%)	243.2 (5.10)	0.0519					

^aPercentages are calculated as 100x twice the squares of the coefficients in the CI expansion of TDDFT wave functions. H and L stands for highest occupied molecular orbital (HOMO) and lowest unoccupied molecular orbital (LUMO) respectively. *Electronic distributions involve within Ribityl chains. ^bIn this work; ^cVertical excitation energy of RF molecule calculated using TDB3LYP/TZVP method in gas phase/in addition with four explicit water molecules, oscillator strengths in parentheses, see ref. 22; ^dTDB3LYP/TZVP method with PCM model taking the dielectric constant of $\epsilon=46.68$ for DMSO, see ref. 25; ^eCASPT2 method with 6-31G(d) basis functions on isoalloxazine structure (IA), oscillator strengths in parentheses, see ref. 58; ^fSAC-CI method with D95V(d) basis functions and solvation effect included through PCM model along with five explicit water molecules see ref. 59; ^gDFT/MRCI(TZVP) in gas phase, see ref. 60; ^hTD-B3LYP/aug-cc-pVDZ method in PCM model to account for the solvent effect, see ref. 57; ⁱAbsorption maxima (λ_{max}) and molar extinction coefficients (ϵ) are taken from ref. 50.

Our TDDFT calculations determined four $\pi\pi^*$ transitions of considerable oscillator strengths at 4.52 (f = 0.0289), 4.79 (f = 0.6925), 5.04 (f = 0.0436) and 5.10 eV (f = 0.0519) within the energy regime of 4.5 to 5.1 eV (Table 4.3). The third experimentally observed band at around 266 nm can be assigned to the $\pi\pi^*$ transition computed at 4.79 eV, because this is the

most intense transition with an oscillator strength of 0.6925 relative to the other weak transitions. The molecular orbitals (MO) involved (see Fig. 4.5(a)) in this transition clearly assign it as a $\pi\pi^*$ transition. The largest contribution (72%) for the above transition is a one electron transition from H to L+1 orbital. However, we have discussed earlier for LF that this absorption band is composed by more than one $\pi\pi^*$ electronic transitions, predicted by several experimental measurements and theoretical computations. For example, Circular dichroism spectra⁶³ and theoretical computations using PPP/CI⁶⁴, DFT/MRCI⁶⁰ and SAC-CI⁵⁹ methods suggested that two $\pi\pi^*$ electronic transitions exist within this absorption band, whereas TDDFT⁵⁷ and CASPT2⁵⁸ computed results show that three electronic transitions can contribute to this absorption band (see Table 4.3). So, the other weak electronic transitions obtained from our calculation also contribute to the absorption band centered at 266 nm.

4.3.2 UVRR Spectra and Experimental Raman Excitation Profile

The UVRR spectra of RF and FMN obtained with 262.9 nm laser excitation are shown in Fig. 4.6. Both the molecules show very similar UVRR enhancement patterns having twenty UVRR bands (608, 685, 741, 787, 831, 1065, 1161, 1183, 1226, 1255, 1300, 1354, 1385, 1439, 1465, 1505, 1550, 1583, 1632 and 1715 cm^{-1}) in the 600 to 1750 cm^{-1} spectral region. These band positions are in good agreement with reported 266 nm excited UVRR spectra of FMN³⁹ within the experimental error. **The UVRR spectra of RF and FMN in the range from 1000 to 1300 cm^{-1} are very different from that of LF obtained at a laser excitation wavelength of 262 nm.** This may be due to the substitution of methyl ($-\text{CH}_3$) group at the N10 position of LF by a ribityl chain (present in RF and FMN) which can form hydrogen bonds with the isoalloxazine ring atoms.⁸

The variation in resonance Raman band intensities of RF as a function of excitation wavelengths is shown in Fig. 4.7 and Fig. 4.8. The intensities of RR bands in all spectra are normalized to the intensity of sulfate band at 980 cm^{-1} that was used as an internal intensity standard. No substantial change in the band positions are observed across the excitation wavelength values. We observed that the relative intensity of the bands at 1550, 1583 and 1632 cm^{-1} bands change from 259.9 nm to 280.07 nm excitation. The intensity of 1550 and 1632 cm^{-1} bands are drastically decreased on moving towards longer excitation wavelengths. The intensity of 1583 cm^{-1} band increases from 259.9 to 272.9 nm excitation and then slightly decreases upto

280.07 nm excitation. The Raman band at 1550 cm^{-1} almost disappeared at 280.07 nm excitation. This kind of feature for intensity changes of those bands with increasing the excitation wavelengths was seen in the UVRR spectra of LF following excitations within the absorption band at around 264 nm. It is supposed that these three bands at 1550 , 1583 and 1631 cm^{-1} may be enhanced by more than one electronic transition.

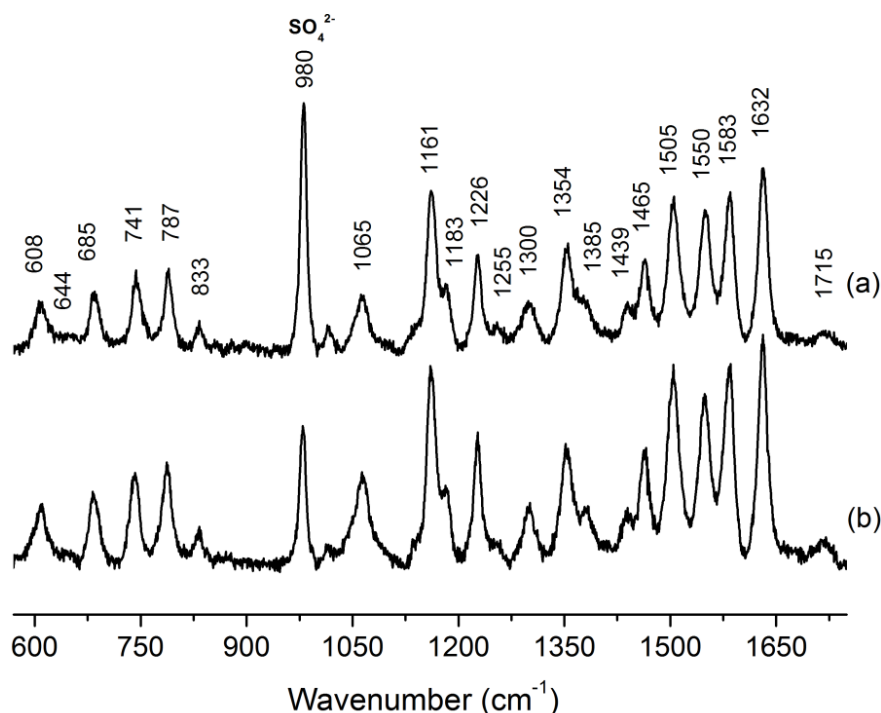


Fig. 4.6 UVRR spectra of (a) RF and (b) FMN of 100 and 300 μM concentrations respectively obtained at 262.9 nm excitation in phosphate buffer at pH7. 980 cm^{-1} is the internal standard sulfate band which is added to the aqueous sample.

The Raman bands at 1354 and 1383 cm^{-1} show similar intensity change like the bands at 1355 and 1374 cm^{-1} in the UVRR spectra of LF with increasing excitation wavelengths. The relative intensity ratio of those bands becomes reverse by going towards higher excitation wavelengths. A new band appears at 1281 cm^{-1} with 270.43 nm and other higher excitation wavelengths. The Raman band at 1281 cm^{-1} for flavins was previously reported with UV and Visible excitations.^{20,39,65,66} So, this band is resonance enhanced by low energy electronic transitions centered around 280 nm within the examining absorption band.

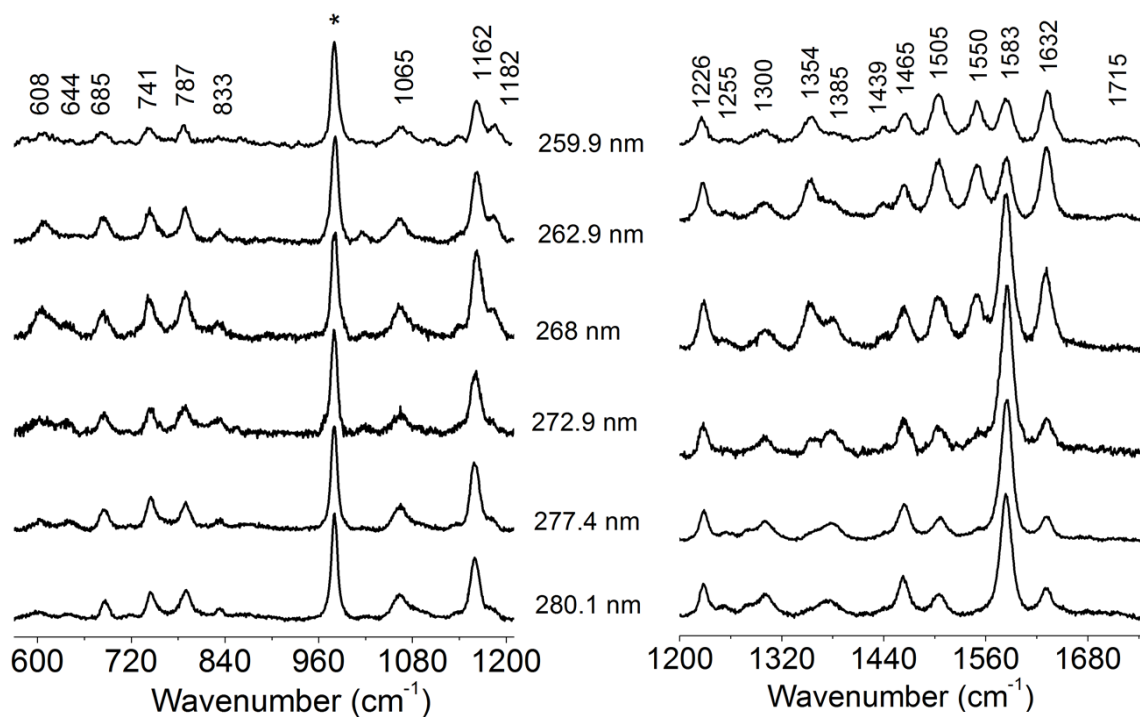


Fig. 4.7 UVRR spectra of 100 μM RF in pH7 sodium phosphate buffer obtained at 6 different excitation wavelengths. Internal standard sulfate band at 980 cm^{-1} is marked by an asterisk (*). Variation in the UVRR band intensity with changing excitation wavelengths can be seen. All spectra are normalized with respect to the internal standard band at 980 cm^{-1} .

Normal mode assignments of the observed UVRR bands of RF and the potential energy distributions (PED) of UVRR bands obtained using VEDA software have been shown in Table 4.4. A. Weigel et al.²⁰ have done the assignment of RR bands of RF and FAD using the same B3LYP/TZVP/PCM model with the addition of four water molecules around the electronegative atoms. Our assignments of UVRR bands of RF are consistent with their assignment and also with other calculations.^{8,10,25,65} The vibrations which have less than 10% contribution have not been included in the assignment table. Hence, the assignments for the UVRR bands positioned at 1437 , 1381 and 829 cm^{-1} are not given in the PED table. The proper theoretical frequency for the 1227 cm^{-1} band has not been found in our calculation and both the bands at 1253 cm^{-1} and 1227 cm^{-1} were assigned with the same theoretical frequency.²⁰ The experimental Raman cross sections of each band were estimated using Eq. 2.30. Full table of assignments is given in Appendix I.

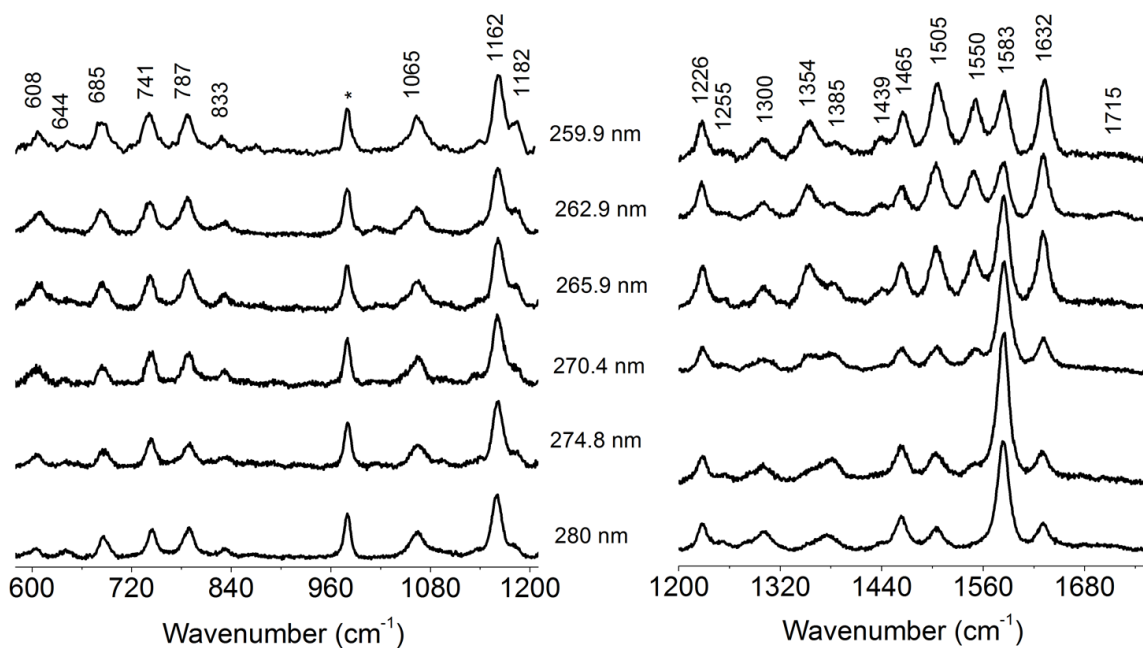


Fig. 4.8 UVRR spectra of 300 μM FMN in pH7 sodium phosphate buffer obtained at 6 different excitation wavelengths. Internal standard sulfate band at 980 cm^{-1} is marked by an asterisk. Variation in the UVRR band intensity with changing excitation wavelengths can be seen. All spectra are normalized with respect to the internal standard band at 980 cm^{-1} .

4.3.3 Simulation of Absorption and Experimental REPs

Experimental and simulated REPs and absorption band of RF centered at 266 nm are shown in Fig 4.9, and Fig 4.10. These plots for FMN are depicted in Fig. 4.11 and Fig. 4.12. A good agreement between the experimental and simulated REP's and absorption cross sections is observed for both the molecules. The parameters corresponding to the best fit are listed in Table 4.5 (for RF) and Table 4.6 (for FMN). Table 4.4 shows the dimensionless displacements, Δ , and the internal reorganization energies for each UVRR bands. We have observed that most of the bands show their REP maximum between 266 and 268 nm.

Table 4.4. UVRR band assignments of RF using B3LYP/TZVP level of theory with PCM as solvent model, PED, dimensionless displacements and mode specific internal reorganization energies of 19 UVRR modes.

Experimental wavenumber (cm ⁻¹)	Computed wavenumber (cm ⁻¹)	PED (%) ^a	Δ (Dimensionless)		Mode specific internal reorganization energy λ _k (cm ⁻¹)	
			RF	FMN	RF	FMN
608	594	be Ribityl chain(10)	0.26	0.24	20	17
644	643	-	0.12	0.1	4	3
685	682	be C4-O (19) + be C2-O (27) + be N5-C5a-C9a (12)	0.23	0.21	18	15
741	748	str C9a-C5a(11) - be C8-C9-C9a(10) - be C5a-C6-C7(10) + be C9a-C5a-C6(15)	0.24	0.22	20	18
787	794	be N1-C10a-C4a (10)	0.26	0.24	27	23
833	868	be N3-C2-N1 (13)	0.13	0.12	6	6
1065	1095	Ribityl chain def.	0.22	0.21	26	24
1160	1167	str C7-CH ₃ (11)	0.28	0.25	44	36
1182	1192	str N5-C5a (15) - str N3-C4 (14)	0.11	0.1	6	6
1226	1232*	str N1-C2 (11) + str N3-C4 (15) - str N3-C2 (12)	0.19	0.16	21	15
1256	1232	str N1-C2 (11) + str N3-C4 (15) - str N3-C2 (12)	0.1	0.09	6	5
1300	1320	tors Ribityl chain (16)	0.15	0.13	15	11
1353	1363	str N10-C10a (10) + be H-C-H (Ribityl chain) (24)	0.19	0.17	24	19
1381	1376	- str C8-C9 (18) + str N3-C4 (12)	0.21	0.2	30	28
1438	1457	-	0.12	0.09	10	6
1463	1491	be H-C-H (8-CH ₃)(46)	0.18	0.17	22	22
1504	1520	- be C6-H(13) + be C9-H(24)	0.24	0.22	43	35
1548	1555	- str N5-C4a (17) + str N10-C10a (11)	0.21	0.19	34	28
1584	1597	- str N5-C4a (24) - str C8-C9 (15) + str C9a-C5a (19)	0.46	0.5	167	195
1630	1663	str C6-C7 (34) - str C8-C9 (15)	0.23	0.21	41	34
1717	1736	str C4-O (67)	0.1	0.08	9	5

^astr, be and tors are for stretching, bending and torsional vibrations respectively. *1227 and 1253 cm⁻¹ modes were assigned with the same theoretical frequency. ^aPEDs are computed using the VEDA 4.0 program; the vibrations which have less than 10% contribution have not been included in the assignment table.

Table 4.5 Parameters used in self-consistent fit of REP and absorption spectra for RF

	E ₀ (cm ⁻¹)	Λ (cm ⁻¹)	τ (fs)	θ (cm ⁻¹)	M (Å)	λ _{int} (cm ⁻¹)	λ _S (cm ⁻¹)	λ (cm ⁻¹)
Best Fit	37500	200	26.5	880	1.14	594	1110	1704
Set 1	37615	240	21.1	970	1.14	481	1000	1481
Set 2	37450	140	37.9	760	1.14	691	1180	1871

Table 4.6 Parameters used in self-consistent fit of REP and absorption spectra for FMN

	E_0 (cm^{-1})	Λ (cm^{-1})	τ (fs)	θ (cm^{-1})	M (\AA)	λ_{int} (cm^{-1})	λ_S (cm^{-1})	λ (cm^{-1})
Best Fit	37495	200	26.5	890	1.14	550	1080	1630
Set 1	37590	245	21.7	960	1.14	453	990	1443
Set 2	37450	140	37.9	770	1.14	657	1170	1827

The maximum of experimental REPs of the UVRR bands at 1437, 1463, 1505, 1549 and 1631 cm^{-1} are blueshifted with respect to the absorption band maxima at 266 nm for both the flavins. It is attributed to the vibronic coupling of these UVRR modes with nearby higher energy electronic states which are not involved in resonance enhancement of UVRR bands. We have shown that there are two electronic transitions (one higher and one lower in energy) close to the electronic state centered around 266 nm (see Fig. 4.5(b)). Resonance enhancements of most UVRR bands appear by tuning the excitation wavelength along this most intense deconvoluted band centered around 266 nm. **The depolarization ratios of UVRR bands (Table 4.1) measured close to 0.33 are also indicative for resonance enhancement arising from a single electronic state excitation except the UVRR band at 787 cm^{-1} whose depolarization ratio obtained to be 0.59.** So, the blueshifts of the REPs of above UVRR modes are due to the vibronic coupling of these modes with high energy electronic state which is at the left of the most intense one.

We also observe here like in LF that the REP of the band at 1583 cm^{-1} shows maxima at 272.9 nm excitation wavelength (Fig. 4.10 and Fig. 4.12). The redshift of the REP maxima of this band was previously explained that the Raman band is coupled with the low energy electronic states located right side to the electronic state at 266 nm. These type of shifts in experimental REP's with respect to the absorption maxima are previously reported in Tryptophan⁶⁷ and 6-chloroguanine⁴⁶ molecules upon deep UV excitations.

We observed a good match between the simulated and experimental REP's for 684, 741 cm^{-1} , 787 cm^{-1} , 1065 cm^{-1} , 1162 cm^{-1} , 1353 cm^{-1} , 1504 cm^{-1} and 1632 cm^{-1} bands. Our model of simulation of REPs applies for single excited state and omits the interference from nearby electronic states. We have seen a deviation in simulated and experimental REPs at the high frequency regions for 1300 cm^{-1} and 1463 cm^{-1} bands and to some extent for the band at 1227 cm^{-1} (for RF only). This is likely due to the coupling of these modes with high energy electronic

states. We can see a complete disagreement between Experimental and simulated REPs at the high frequency region of REP's at 1383 cm^{-1} and 1583 cm^{-1} bands for both RF and FMN (Fig. 4.10 and Fig. 4.12). These two modes may be coupled with the high energy electronic state which is at the blue edge of the 266 nm centered electronic state. The simulated REP of the Raman band at 1549 cm^{-1} also shows a little deviation from the experimental Raman cross sections at low frequency region. This deviation indicates a possible coupling of the Raman band at 1549 cm^{-1} with the lower energy electronic state existing at the red edge of the resonant electronic state at 266 nm.

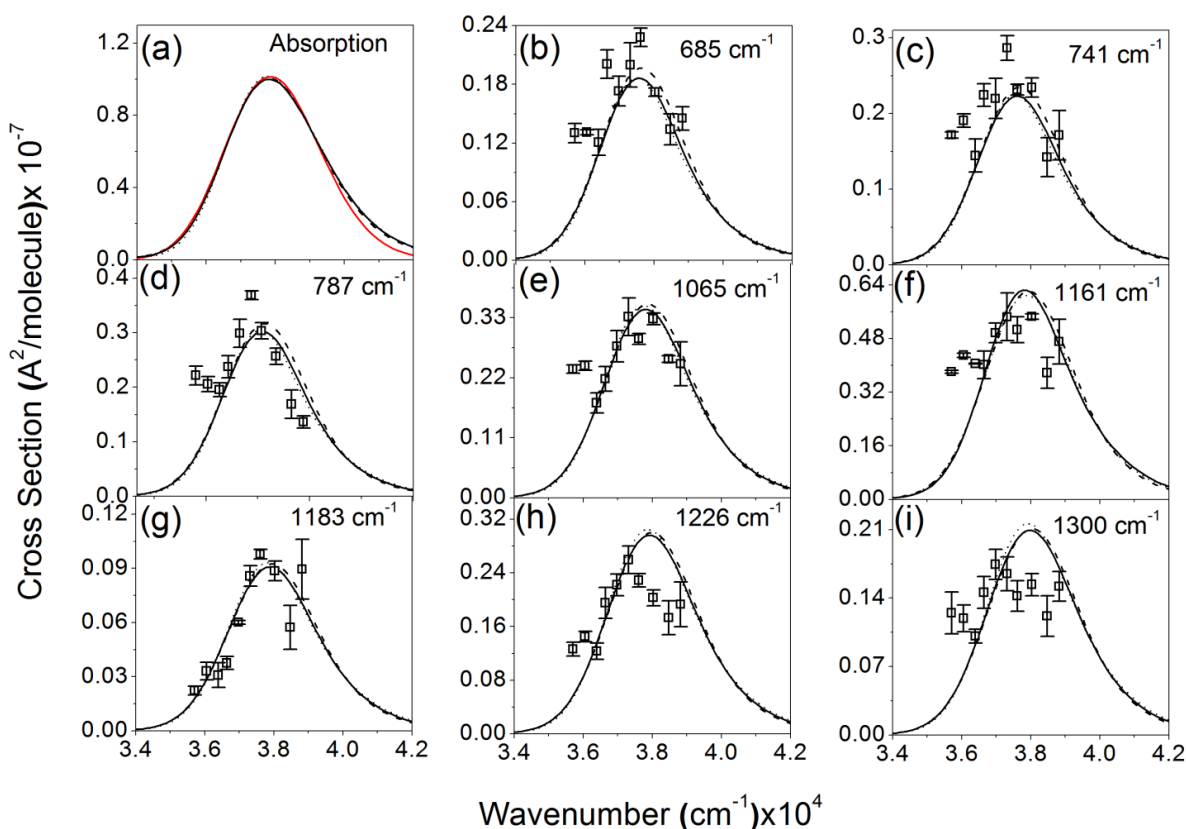


Fig. 4.9. Experimental and simulated Raman excitation profiles and absorption cross section of RF for the transition at 266 nm. (a) Experimental (solid) and simulated absorption (dash) spectrum. (b-i) Raman excitation profiles of eight UVRR modes of RF at 10 different excitation wavelengths. The best fit (solid) was obtained by using the parameters of Table 4.5. Set 1 (dot) and Set 2 (dash dot) parameters are obtained by decreasing and increasing the best fit delta values by 10% respectively.

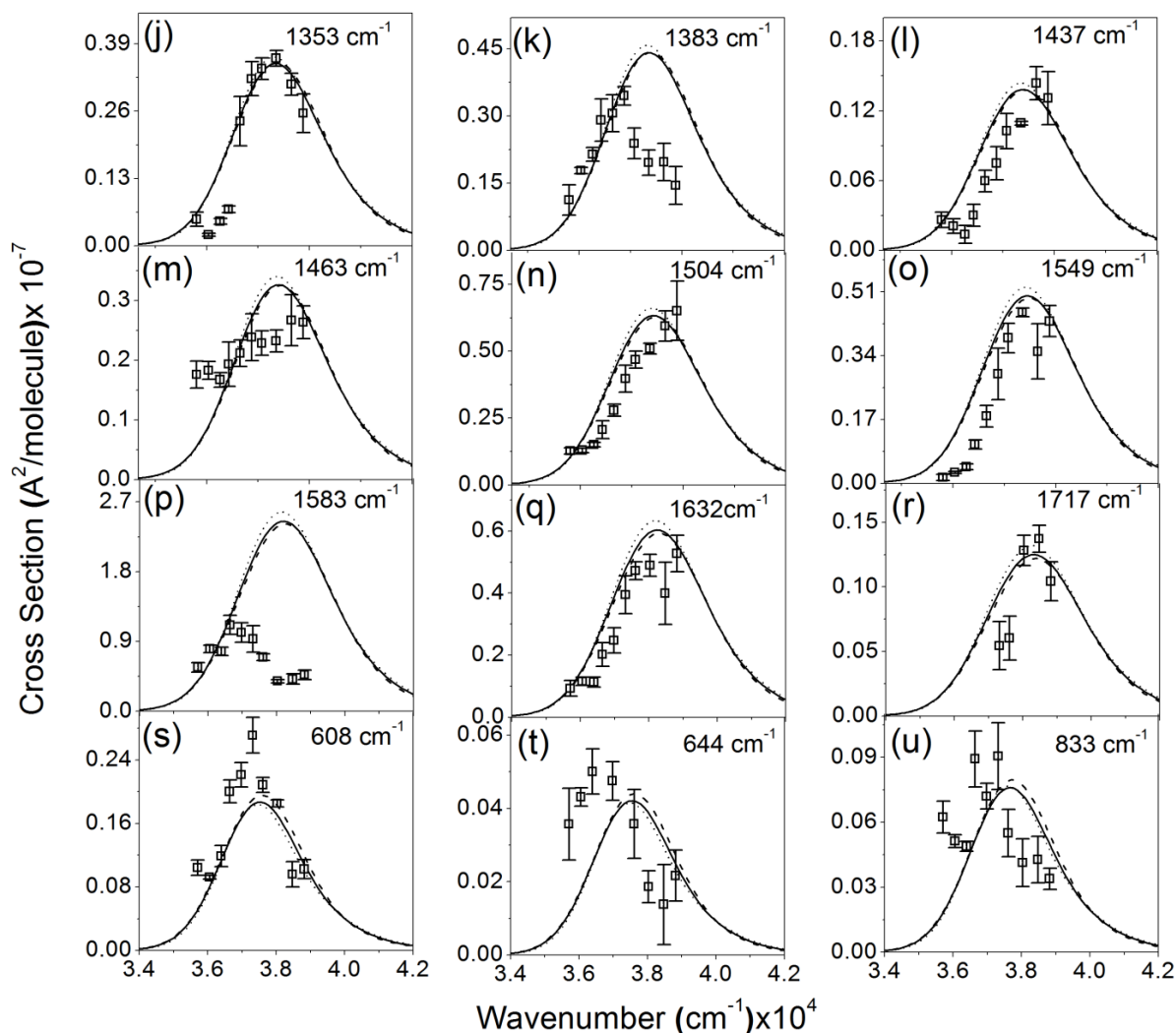


Fig. 4.10. Experimental and simulated Raman excitation profiles (j-u) of other 12 UVRR modes of RF obtained by using the same set of parameters as in Fig. 4.9.

The excited state structural distortions are governed by the dimensionless displacements; Δ . Δ 's obtained from best fit REPs are converted into geometrical changes in terms of changes in internal coordinates by using Eq. 2.25. Table 4.7 shows the internal coordinates enduring the major distortions in the bond lengths of RF molecule. **Major changes in the bond lengths are found in all over the isoalloxazine ring system. We can consider the excited state structural changes for both RF and FMN are similar.** The contraction in the bond length was observed in C6-C7 (-0.019), C5a-C6 (-0.086), N5-C5a (-0.073), C9-C9a (-0.088), C9a-N10 (-0.073), C8-C9 (-0.071), C4a-C10a (-0.029), C10a-N1 (-0.082), C4-C4a (-0.055), C10a-N10 (-0.06) and C4a-N5 (-0.052) bonds. There was an elongation in the C2-N3 bond (0.063) following 266 nm excitations. Photoexcitation to the first singlet excited state using

ultrafast Infrared,^{8,10} Raman difference spectroscopy⁶⁸ and TDDFT calculations^{22,25} was reported that the major changes happen in the loss of double bond character of C=N, C=C and C=O bonds.

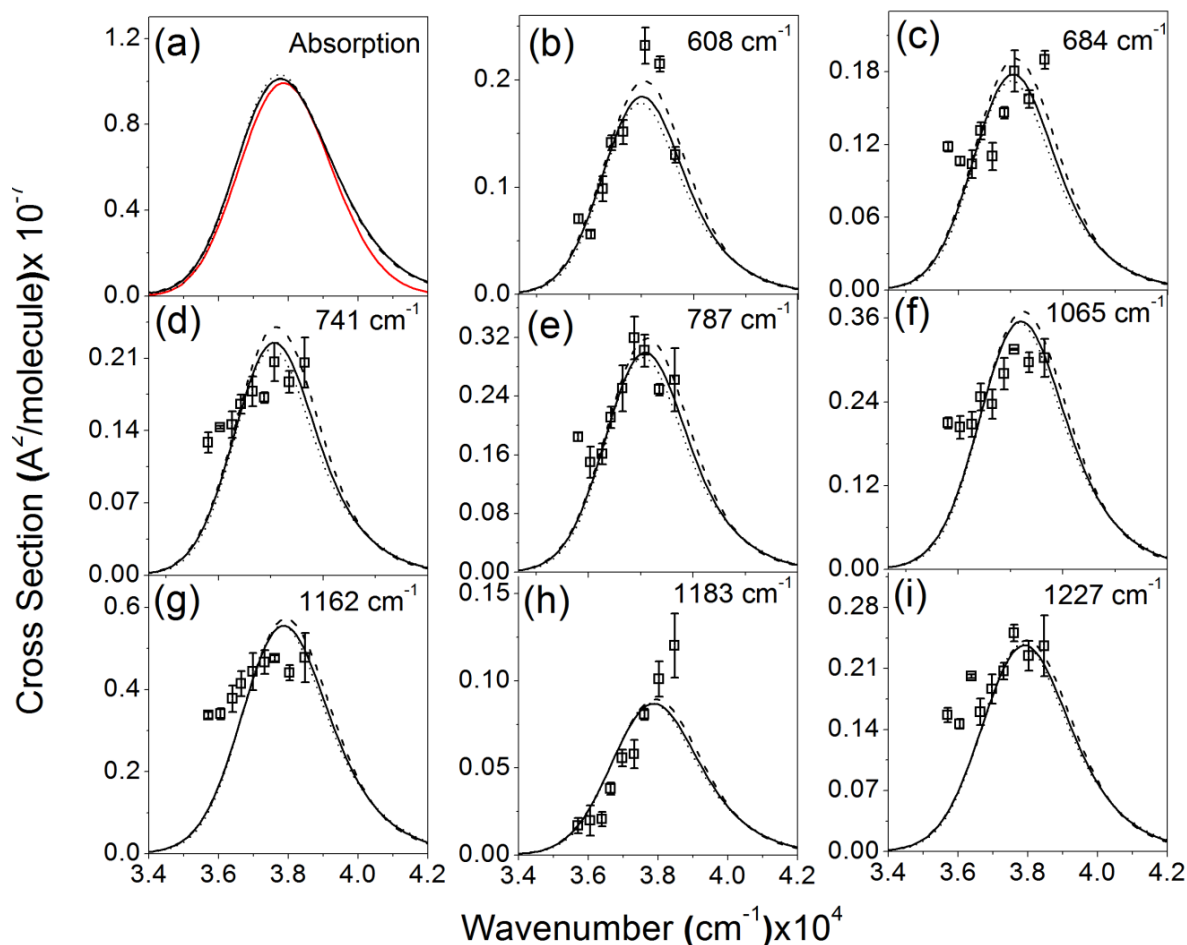


Fig 4.11 Experimental and simulated Raman excitation profiles and absorption cross section of FMN for the transition at 266 nm. (a) Experimental (solid) and simulated absorption (dash) spectrum. (b-i) Raman excitation profiles of eight UVRR modes of FMN at 10 different excitation wavelengths. The best fit (solid) was obtained by using the parameters of Table 4.6. Set 1 (dash) and Set 2 (dot) parameters are obtained by decreasing and increasing the best fit delta values by 10% respectively.

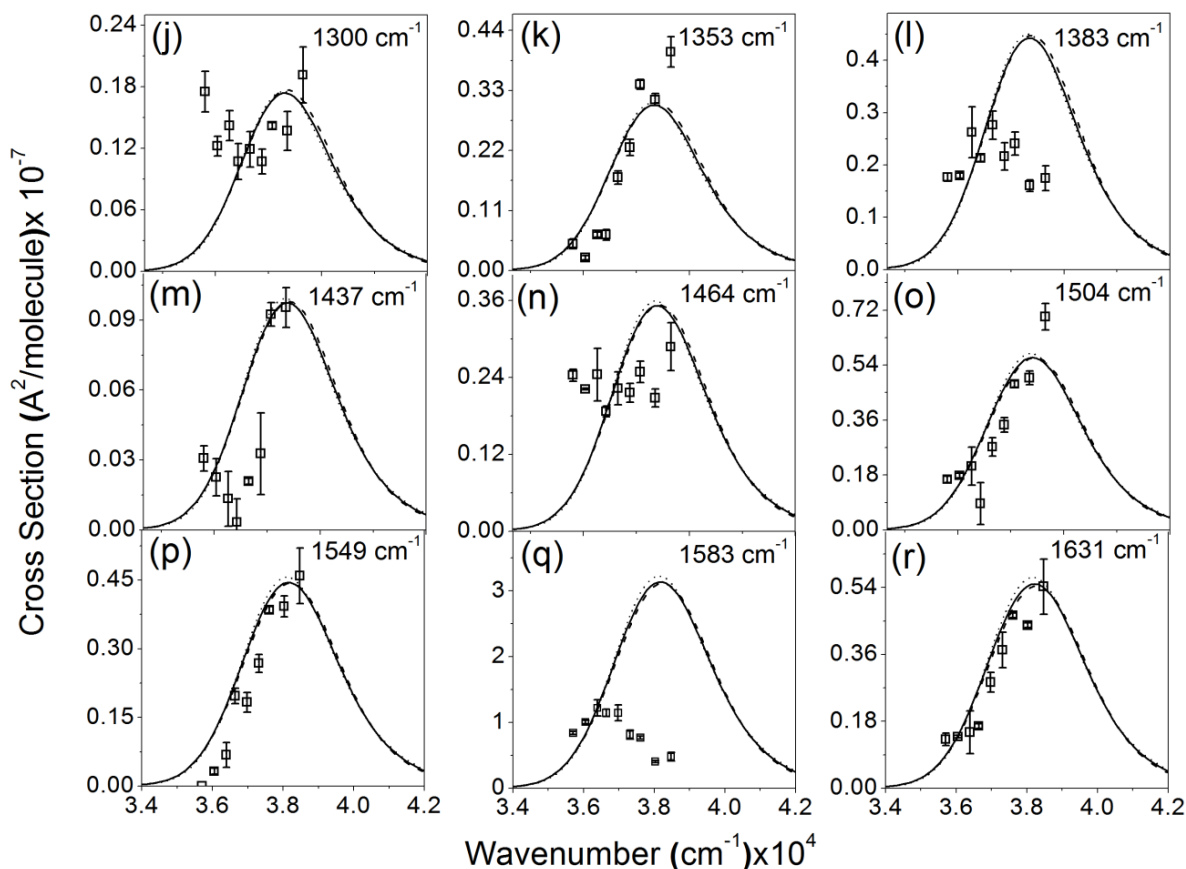


Fig. 4.11 Experimental and simulated Raman excitation profiles (j-r) of other nine UVRR modes of FMN obtained by using the same set of parameters as in Fig. 4.11.

Bastian Klaumüller et al²⁵ have been shown the excited state structural changes in the first singlet excited state (S_1) using (TD)-B3LYP/TZVP basis set. According to them, C4-N5 and C10a-N1 and C2=O bonds elongate which is opposite to our findings in UV excitations. This is due to the different orientations of transition dipole for the two different electronic transitions. The angle of the transition dipole moment for the two electronic states at 450 and 266 nm are 75° and 120° respectively with respect to the short molecular axis.⁶⁹⁻⁷¹

The internal coordinate changes determined for RF and LF following photoexcitation within the absorption band at around 266 nm are compared in Table 4.7. Although most of the similar isoalloxazine ring bonds show changes in bond lengths in the same directions for these two photoexcited molecules, we found that the changes for some of the bonds are in opposite directions. For example, the contraction was seen in the C7-C8, C9-C9a, C4-C4a, and C5a-C9a bonds for RF, whereas an elongation in those bond lengths was

observed for LF. The C4-N3 bond shows almost no change for photoexcited RF, but this bond shows a major contraction (-0.082) in case of LF. Therefore, we suggest that upon photoexcitation to the 266 nm $\pi\pi^*$ excited state, different structural distortions occur for RF and FMN in comparison to LF. It can be explained from the UVRR spectra of LF and RF. **We have seen that RF and LF show RR spectra with different enhancement patterns within the spectral region of 1000 to 1300 cm^{-1} , reflecting to the differing molecular distortions at the Franck-Condon regions in the excited states of those two flavins.**

Table 4.7 Internal coordinate changes in RF and LF

RF			LF
Internal Coordinates (bond length)	Internal coordinates in ground state (Å)	Internal coordinate change (Å)	Internal coordinate change (Å)
C6-C7	1.3742	-0.019	-0.04
C7-C8	1.4265	-0.008	0.032
C7-CH3	1.5042	-0.019	-0.037
C5a-C6	1.4104	-0.086	-0.057
C6-H6	1.0827	0.001	0.001
C5a-C9a	1.4211	-0.003	0.024
N5-C5a	1.3566	-0.073	-0.016
C9-C9a	1.4013	-0.088	0.01
C9a-N10	1.3873	-0.073	-0.127
C8-C9	1.385	-0.071	-0.036
C9-H9	1.0777	0.002	0.004
C8-CH3	1.5024	-0.034	-0.009
C4a-C10a	1.447	-0.029	0.003
C10a-N10	1.3724	-0.06	-0.017
C10a-N1	1.3151	-0.082	-0.013
C4-C4a	1.4893	-0.055	0.018
C4a-N5	1.2993	-0.052	-0.031
C4-N3	1.3727	0	-0.082
C4=O	1.2194	0	-0.008
N1-C2	1.3642	-0.011	0.023
C2-N3	1.4093	0.063	0.03
C2=O	1.2249	-0.029	0.05
N3-H3	1.0128	0.003	-0.004

We have already discussed in the previous chapter that the mode specific reorganization energies are more accurate to determine the structural changes upon photoexcitation, because they do not depend on the sign of Δs . **The total internal reorganization energies over all the modes is obtained to be 594 cm⁻¹ and 550 cm⁻¹ for RF and FMN respectively (Table 4.5 & 4.6). The Raman mode at 1584 cm⁻¹ contributes 30% (36%) to the total reorganization energy obtained for RF (FMN). For LF, we also have observed that the major contribution arises from this band.** So, we can suggest that major structural distortion happens along this mode for all of these three flavins following photoexcitation to the 266 nm excited state. The other modes which contributes significantly to the total reorganization energy are 741, 787, 1065, 1162, 1223, 1353, 1381, 1461, 1504, 1548 and 1630 cm⁻¹. Thus initial photochemistry of the photoexcited RF and FMN are expected to occur along these vibrational coordinates and maximum distortion can happen along the Raman mode at 1584 cm⁻¹.

In condensed phase, solvent dynamics plays a crucial role to broaden the absorption and Raman line shapes through either homogeneous or inhomogeneous broadening mechanisms. We can separate the overall broadening into these two contributing components through self-consistent simulation of absorption and REPs because these two types of broadening affect the absorption and Raman line shapes in distinct ways. The homogeneous broadening comes from ultrafast solute-solvent coupling which damps the RR scattering intensity. On another hand, inhomogeneous broadening results due to the existence of distinct micro-solvated structures of solutes. These solvated structures are static in nature in the time scale of Raman scattering process and lead to a Gaussian distribution of electronic transition energies. By using Brownian oscillator spectral density model of Mukamel and coworkers,^{49,72} our simulation yields two parameters τ , which is the dynamic solvent response timescale of 26.5 fs (for both RF and FMN) and λ_S , which is the solvent reorganization energy of 1110 cm⁻¹ for RF and 1080 cm⁻¹ for FMN.

The solvent reorganization energy of RF and FMN is comparable to the same obtained for several natural and substituted nucleobases.^{40,42,45,73,74} The solvent reorganization energy obtained for LF (1070 cm⁻¹) is also within the same range as obtained here for RF and FMN. As Raman is a scattering phenomenon, happening within tens of femtoseconds after photoexcitation, the obtained solvent reorganization energy is solely due to the inertial response of water. So the

main contribution to the total reorganization energy (1704 cm^{-1} and 1630 cm^{-1} for RF and FMN respectively) from our simulation arises from the pure electronic dephasing between solute and surrounding solvent bath (water). The amplitude of the solvent response corresponds to the instantaneous change in the charge distribution of the solute following photoexcitation to an electronic excited state. Thus this quantity is expected to be a sole characteristic of the resonant excited state. Very similar solvent reorganization energy for RF and FMN reinforces the fact that their electronic structure is very much identical in the excited state studied.

The fastest component of the water solvation is associated with the instantaneous electronic rearrangement of solute molecules following photoexcitation. This ultrafast component of water dynamics was found to occur within 50 fs of photoexcitation by using numerous spectroscopic techniques⁷⁵⁻⁷⁷ as well as molecular dynamics simulations⁷⁸⁻⁸¹ with different chromophores being used as probe molecules. **The inertial solvent response time obtained in our simulation (26.5 fs) for RF and FMN is in the same order as obtained for LF (37.9 fs) and in earlier reports for 6-chloroguanine (~15 fs)⁴⁶ and tryptophan (~8 fs).⁶⁷** We have used same solvent correlation time (26.5 fs) for both the molecules, as we have shown in earlier reports that our model is not very sensitive to the timescale of dynamic solvent response.^{46,67}

The homogeneous and inhomogeneous broadenings required to be relatively large to accurately model the experimental absorption spectrum and REPs in our simulation. **Our simulation yield almost same inhomogeneous broadening value (θ) for both RF (900 cm^{-1}) and FMN (910 cm^{-1}).** The inhomogeneous broadening originates due to the different solvation structures of solute (RF and FMN) molecules which remain static on the resonance Raman timescale. The similar θ value indicates that although FMN might have in a distinct solvation shell around the anionic phosphate group which does not have any effect on the enhanced RR modes of the isoalloxazine ring. The inhomogeneous linewidth contribution to the total solvent reorganization energy was reported to lie between $900\text{-}1300\text{ cm}^{-1}$ for several purines and pyrimidine Nucleobases.^{40-43,45,73} All of these nucleobases can form hydrogen bonds through their amino and carbonyl groups present outside the ring structure. These strong hydrogen bonding groups can thus assist the formation of several micro-solvated structures with surrounding water molecules leading to large inhomogeneous linewidths. RF also has carbonyl

group, nitrogen atoms which can form strong hydrogen bonds with the neighboring water molecules^{22,82,83} and hence support to the high value of θ . Although RF and FMN contain a ribityl chain substituent which also can form hydrogen bonds with the neighboring water molecules, we did not find a significant change in the value of θ determined for RF and LF molecules (750 cm^{-1}).

4.4 Conclusion

UVRR intensity analysis with time dependent wave packet theory can reveal the excited state structural dynamics of RF and FMN within 50 fs of photoexcitation to the UV region of absorption. **We have observed that the excited state structural distortions following UV excitations are not similar to that of S_0 to S_1 transitions. The excited state distortions occur along all over the isoalloxazine ring modes through contraction in most of the bond lengths with an elongation along C2-N3 bond. We also observed that upon excitation to the 266 nm excited state, RF and LF show different molecular distortions.** Partitioning of the total spectral breadth into homogeneous and inhomogeneous broadening explored the contribution of the inertial response of water to the total reorganization energy and strong hydrogen bonding interactions of flavins with surrounding water molecules. The homogeneous and inhomogeneous linewidths obtained here for RF and FMN are similar. **We have also measured an ultrafast inertial water response timescale at ~ 30 fs for both the molecules.**

Determination of initial excited state parameters can be extended into FAD (which has a Ribityl chain with an adenosine 5'-monophosphate moiety). Therefore we may be able to extract the contribution of ribityl chain and adenine group to the excited state dynamics of isoalloxazine ring. Protein dynamics and hydration also play an important role during photoexcitation of the flavin chromophores in response to the biological processes. The excited state parameters obtained might change a little bit when flavin will be inside the protein core. So, flavin will be a good probe to study the dynamics and heterogeneity of proteins in UV excitations.

References

- (1) Losi, A. *Photochem. Photobiol.* **2007**, 83 (6), 1283.
- (2) Sancar, A. *Chem. Rev.* **2003**, 103 (6), 2203.
- (3) Nakasako, M.; Zikihara, K.; Matsuoka, D.; Katsura, H.; Tokutomi, S. *J. Mol. Biol.* **2008**, 381 (3), 718.

- (4) BARTON-WRIGHT, E. C.; MORAN, T.; SARSON, H. S. *Nature* **1943**, 152 (3853), 273.
- (5) Powers, H. J. *Am. J. Clin. Nutr.* **2003**, 77 (6), 1352.
- (6) Choe, E.; Huang, R.; Min, D. B. *J. Food Sci.* **2005**, 70 (1), R28.
- (7) Haggi, E.; Blasich, N.; Gutiérrez, L.; Vázquez, G.; Criado, S.; Miskoski, S.; Ferrari, G.; Paulina Montaña, M.; García, N. *A. J. Photochem. Photobiol. B Biol.* **2012**, 113, 22.
- (8) Wolf, M. M. N.; Zimmermann, H.; Diller, R.; Domratcheva, T. *J. Phys. Chem. B* **2011**, 115 (23), 7621.
- (9) Salzmann, S.; Martinez-junza, V.; Zorn, B.; Braslavsky, S. E.; Marian, C. M.; Gärtner, W. **2009**, 145, 9365.
- (10) Wolf, M. M. N.; Schumann, C.; Gross, R.; Domratcheva, T.; Diller, R. *J. Phys. Chem. B* **2008**, 112 (42), 13424.
- (11) Staudt, H.; Oesterheld, D.; Grininger, M.; Wachtveitl, J. *J. Biol. Chem.* **2012**, 287 (21), 17637.
- (12) Radoszkowicz, L.; Presiado, I.; Erez, Y.; Nachliel, E.; Huppert, D.; Gutman, M. *Phys. Chem. Chem. Phys.* **2011**, 13 (25), 12058.
- (13) Kowalczyk, R. M.; Schleicher, E.; Bittl, R.; Weber, S. *J. Am. Chem. Soc.* **2004**, 126 (36), 11393.
- (14) Lukacs, A.; Zhao, R. K.; Haigney, A.; Brust, R.; Greetham, G. M.; Towrie, M.; Tonge, P. J.; Meech, S. R. *J. Phys. Chem. B* **2012**, 116 (20), 5810.
- (15) Stanley, R. J.; MacFarlane, A. W. I. *J. Phys. Chem. A* **2000**, 104 (30), 6899.
- (16) Kondo, M.; Nappa, J.; Ronayne, K. L.; Stelling, A. L.; Tonge, P. J.; Meech, S. R. *J. Phys. Chem. B* **2006**, 110 (41), 20107.
- (17) Gil, M.; Wang, Y.; Douhal, A. *J. Photochem. Photobiol. A Chem.* **2012**, 234, 146.
- (18) Kao, Y.; Saxena, C.; He, T.; Guo, L.; Wang, L.; Sancar, A.; Zhong, D. *J. Am. Chem. Soc.* **2008**, 130 (39), 13132.
- (19) Weigel, A.; Dobryakov, A. L.; Veiga, M.; Pérez Lustres, J. L. *J. Phys. Chem. A* **2008**, 112 (47), 12054.
- (20) Weigel, A.; Dobryakov, A.; Klaumünzer, B.; Sajadi, M.; Saalfrank, P.; Ernsting, N. P. *J. Phys. Chem. B* **2011**, 115, 3656.
- (21) Zhao, R.-K.; Lukacs, A.; Haigney, A.; Brust, R.; Greetham, G. M.; Towrie, M.; Tonge, P. J.; Meech, S. R. *Phys. Chem. Chem. Phys.* **2011**, 13 (39), 17642.
- (22) Klaumünzer, B.; Kröner, D.; Lischka, H.; Saalfrank, P. *Phys. Chem. Chem. Phys.* **2012**, 14 (24), 8693.
- (23) Hasegawa, J. ya; Bureekaew, S.; Nakatsuji, H. *J. Photochem. Photobiol. A Chem.* **2007**, 189 (2–3), 205.
- (24) Van den Berg, P. A. W.; Feenstra, K. A.; Mark, A. E.; Berendsen, H. J. C.; Visser, A. J. W. G. *J. Phys. Chem. B* **2002**, 106 (34), 8858.
- (25) Klaumünzer, B.; Kröner, D.; Saalfrank, P. *J. Phys. Chem. B* **2010**, 114 (33), 10826.
- (26) Neiss, C.; Saalfrank, P.; Parac, M.; Grimme, S. *J. Phys. Chem. A* **2003**, 107 (1), 140.
- (27) Li, G.; Glusac, K. D. *J. Phys. Chem. B* **2009**, 113 (27), 9059.
- (28) Wang, H.; Saxena, C.; Quan, D.; Sancar, A.; Zhong, D. *J. Phys. Chem. B* **2005**, 109 (4), 1329.
- (29) Stelling, A. L.; Ronayne, K. L.; Nappa, J.; Tonge, P. J.; Meech, S. R. *J. Am. Chem. Soc.* **2007**, 129 (50), 15556.
- (30) Kao, Y. T.; Tan, C.; Song, S. H.; Öztürk, N.; Li, J.; Wang, L.; Sancar, A.; Zhong, D. *J. Am. Chem. Soc.* **2008**, 130 (24), 7695.
- (31) Mataga, N.; Chosrowjan, H.; Shibata, Y.; Imamoto, Y.; Tokunaga, F.; Tanaka, F. *J. Lumin.* **2000**, 87, 821.
- (32) Zhong, D.; Zewail, a H. *Proc. Natl. Acad. Sci. U. S. A.* **2001**, 98 (21), 11867.
- (33) Bonetti, C.; Mathes, T.; van Stokkum, I. H.; Mullen, K. M.; Groot, M. L.; van Grondelle, R.; Hegemann, P.; Kennis, J. T. *Biophys. J.* **2008**, 95 (10), 4790.
- (34) Saxena, C.; Wang, H.; Kavakli, I. H.; Sancar, A.; Zhong, D. *J. Am. Chem. Soc.* **2005**, 127 (22), 7984.
- (35) Brust, R.; Lukacs, A.; Haigney, A.; Addison, K.; Gil, A.; Towrie, M.; Clark, I. P.; Greetham, G. M.; Tonge, P. J.;

- Meech, S. R. *J. Am. Chem. Soc.* **2013**, *135* (43), 16168.
- (36) Chang, C. W.; He, T. F.; Guo, L.; Stevens, J. A.; Li, T.; Wang, L.; Zhong, D. *J. Am. Chem. Soc.* **2010**, *132* (36), 12741.
- (37) Raszka, M.; Kaplan, N. O. *Proc. Natl. Acad. Sci. U. S. A.* **1974**, *71* (11), 4546.
- (38) Chosrowjan, H.; Taniguchi, S.; Mataga, N.; Tanaka, F.; Visser, A. J. W. G. *Chem. Phys. Lett.* **2003**, *378* (3–4), 354.
- (39) Copeland, R. A.; Spiro, T. G. *J. Phys. Chem.* **1986**, *90* (25), 6648.
- (40) El-Yazbi, A. F.; Palech, A.; Loppnow, G. R. *J. Phys. Chem. A* **2011**, *115* (38), 10445.
- (41) Billinghamurst, B. E.; Yeung, R.; Loppnow, G. R. *J. Phys. Chem. A* **2006**, *110* (19), 6185.
- (42) Yarasi, S.; Brost, P.; Loppnow, G. R. *J. Phys. Chem. A* **2007**, *111* (24), 5130.
- (43) Yarasi, S.; Ng, S.; Loppnow, G. R. *J. Phys. Chem. B* **2009**, *113* (43), 14336.
- (44) Ng, S. S.; Teemoory, F.; Loppnow, G. R. *J. Phys. Chem. Lett.* **2011**, *2* (18), 2362.
- (45) Oladepo, S. A.; Loppnow, G. R. *J. Phys. Chem. B* **2011**, *115* (19), 6149.
- (46) Mondal, S.; Puranik, M. *Phys. Chem. Chem. Phys.* **2016**.
- (47) Loppnow, G. R.; Mathies, R. A. *Biophys. J.* **1988**, *54* (1), 35.
- (48) Lee, S.; Heller, E. J. *J. Chem. Phys.* **1979**, *71* (12), 4777.
- (49) Li, B.; Johnson, A. E.; Mukamel, S.; Myers, A. B. *J. Am. Chem. Soc.* **1994**, *116* (24), 11039.
- (50) Koziol, J. *Photochem. Photobiol.* **1966**, *5* (1), 41.
- (51) Lee, C.; Yang, W.; Parr, R. G. *Phys. Rev. B* **1988**, *37* (2), 785.
- (52) Becke, A. D. *J. Chem. Phys.* **1993**, *98* (7), 5648.
- (53) Godbout, N.; Salahub, D. R.; Andzelm, J.; Wimmer, E. *Can. J. Chem.* **1992**, *70* (2), 560.
- (54) Miertuš, S.; Scrocco, E.; Tomasi, J. *Chem. Phys.* **1981**, *55* (1), 117.
- (55) Bauernschmitt, R.; Ahlrichs, R. *Chem. Phys. Lett.* **1996**, *256* (4–5), 454.
- (56) Casida, M. E.; Jamorski, C.; Casida, K. C.; Salahub, D. R. *J. Chem. Phys.* **1998**, *108* (11), 4439.
- (57) Choe, Y.-K.; Nagase, S.; Nishimoto, K. *J. Comput. Chem.* **2007**, *28* (4), 727.
- (58) Climent, T.; González-Luque, R.; Merchán, M.; Serrano-Andrés, L. *J. Phys. Chem. A* **2006**, *110* (50), 13584.
- (59) Hasegawa, J. y.; Bureekaew, S.; Nakatsuji, H. *J. Photochem. Photobiol. A Chem.* **2007**, *189* (2–3), 205.
- (60) Salzmann, S.; Tatchen, J.; Marian, C. M. *J. Photochem. Photobiol. A Chem.* **2008**, *198* (2–3), 221.
- (61) Zenichowski, K.; Gothe, M.; Saalfrank, P. *J. Photochem. Photobiol. A Chem.* **2007**, *190* (2–3), 290.
- (62) Sikorska, E.; Khmelinskii, I. V.; Prukala, W.; Williams, S. L.; Patel, M.; Worrall, D. R.; Bourdelande, J. L.; Koput, J.; Sikorski, M. *J. Phys. Chem. A* **2004**, *108* (9), 1501.
- (63) Tollin, G. *Biochemistry* **1968**, *7* (5), 1720.
- (64) Sun, M.; Moore, T. A.; Song, P.-S. *J. Am. Chem. Soc.* **1972**, *94* (5), 1730.
- (65) Eisenberg, A. S.; Schelvis, J. P. M. *J. Phys. Chem. A* **2008**, *112* (27), 6179.
- (66) Kim, M.; Carey, P. R. *J. Am. Chem. Soc.* **1993**, *115* (15), 7015.
- (67) Milán-Garcés, E. A.; Kaptan, S.; Puranik, M. *Biophys. J.* **2013**, *105* (1), 211.
- (68) Unno, M.; Sano, R.; Masuda, S.; Ono, T.-A.; Yamauchi, S. *J. Phys. Chem. B* **2005**, *109* (25), 12620.
- (69) Climent, T.; González-Luque, R.; Merchán, M.; Serrano-Andrés, L. *J. Phys. Chem. A* **2006**, *110* (50), 13584.
- (70) Johansson, L. B.; Davidsson, a; Lindblom, G.; Naqvi, K. R. *Biochemistry* **1979**, *18* (19), 4249.
- (71) Eaton, W. a; Hofrichter, J.; Makinen, M. W.; Andersen, R. D.; Ludwig, M. L. *Biochemistry* **1975**, *14* (10), 2146.

- (72) Mukamel, S. *Principles of Nonlinear Optical Spectroscopy*, Oxford University Press, New York; 1995.
- (73) Billinghamurst, B. E.; Oladepo, S. A.; Loppnow, G. R. *J. Phys. Chem. B* **2012**, *116* (35), 10496.
- (74) Sasidharanpillai, S.; Loppnow, G. R. *J. Phys. Chem. A* **2014**, *118* (26), 4680.
- (75) Vajda, S.; Jimenez, R.; Rosenthal, S. J.; Fidler, V.; Fleming, G. R.; Castner, E. W. *J. Chem. Soc. Trans.* **1995**, *91* (5), 867.
- (76) Jarzba, W.; Walker, G. C.; Johnson, A. E.; Kahlow, M. A.; Barbara, P. F. *J. Phys. Chem.* **1988**, *92* (20), 7039.
- (77) Jimenez, R.; Case, D. A.; Romesberg, F. E. *J. Phys. Chem. B* **2002**, *106* (5), 1090.
- (78) Jimenez, R.; Fleming, G. R.; Kumar, P. V.; Maroncelli, M. *Nature* **1994**, *369* (6480), 471.
- (79) Muino, P. L.; Callis, P. R. *J. Chem. Phys.* **1994**, *100* (6), 4093.
- (80) Barnett, R. B.; Landman, U.; Nitzan, A. *J. Chem. Phys.* **1989**, *90* (8), 4413.
- (81) Maroncelli, M.; Fleming, G. R. *J. Chem. Phys.* **1988**, *89* (8), 5044.
- (82) Valle, L.; Morán Vieyra, F. E.; Borsarelli, C. D. *Photochem. Photobiol. Sci.* **2012**, *11* (6), 1051.
- (83) Schmidt, J.; Coudron, P.; Thompson, a W.; Watters, K. L.; McFarland, J. T. *Biochemistry* **1983**, *22* (1), 76.

Chapter 5: Is the photophysics of Flavin and Adenine Rings of FAD Coupled?

5.1 Introduction

Flavin adenine dinucleotide (FAD) is a photoactive chromophore found in all of the blue-light activated proteins of photolyase¹ and cryptochrome² family. Photolyases are enzymes which repair the pyrimidine dimers in damaged DNA, while cryptochromes regulate the circadian rhythms in plants and higher animals. Flavins can exist in three different redox states: oxidized, one-electron and two electron reduced states.³ These versatile redox active properties help them to participate in a variety of biological redox-processes in blue-light photoreceptors. For example, in DNA-photolyase, upon blue-light activation the fully reduced FAD molecule transfers an electron to the cyclobutane pyrimidine dimer (CPD) to break the bond between two pyrimidine Nucleobases.^{1,4} In cryptochromes, the photoexcitation of the semi reduced form of FAD triggers an intra or inter protein electron transfer to initiate a primary signaling state.^{2,5} Another class of prominent blue light sensing FAD containing protein are blue light using FAD (BLUF) domain family.⁶ The BLUF proteins participate in light induced phototaxis and gene expression in bacteria.⁷ The decisive role of photoexcited FAD in these processes of light-gated proteins has instigated a considerable interest in elucidating the excited state properties and dynamics of FAD in solution.

Photophysics of FAD molecule in its oxidized and reduced forms in solution and inside the protein core has been extensively studied. Oxidized FAD (Fig 5.1. (a)) has four absorption bands similar to other flavin molecules (FMN, RF, LF) centered at around 212, 265, 375 and 450 nm (Fig 5.1 (b)) which result due to $\pi\pi^*$ electronic transitions.^{8,9} The excited state lifetime of first singlet excited state (S1) for FAD in solution measured are in picosecond (ps) timescale compare to the slower nanosecond (ns) lifetime for other flavins.¹⁰⁻¹³ This is because, in aqueous solution, the oxidized FAD can remain in two conformers: a closed conformer in which the adenine and isoalloxazine rings are stacked, and another one is the open conformer where those two moieties stay separated from each other.¹⁴ In solution at neutral pH range (4-8), the oxidized FAD molecule contains 80% of the closed conformer and 20% of the open conformer.^{14,15} The lifetime in S1 state was measured to be about 2.5 ns for the open conformer,

whereas the reported lifetime for the closed conformer lies between 1 and 20 ps.^{10-13,16-18} This fast excited state deactivation of the closed conformer has been attributed to an intramolecular photoinduced electron transfer from adenine to the excited isoalloxazine ring.^{10,12} Although some of the experimental studies^{11,13,16-18} proposed the evidence of electron transfer process but, the distinct spectroscopic signature for the intermediates (adenine cation and isoalloxazine anion) formed in this process has been lacking.

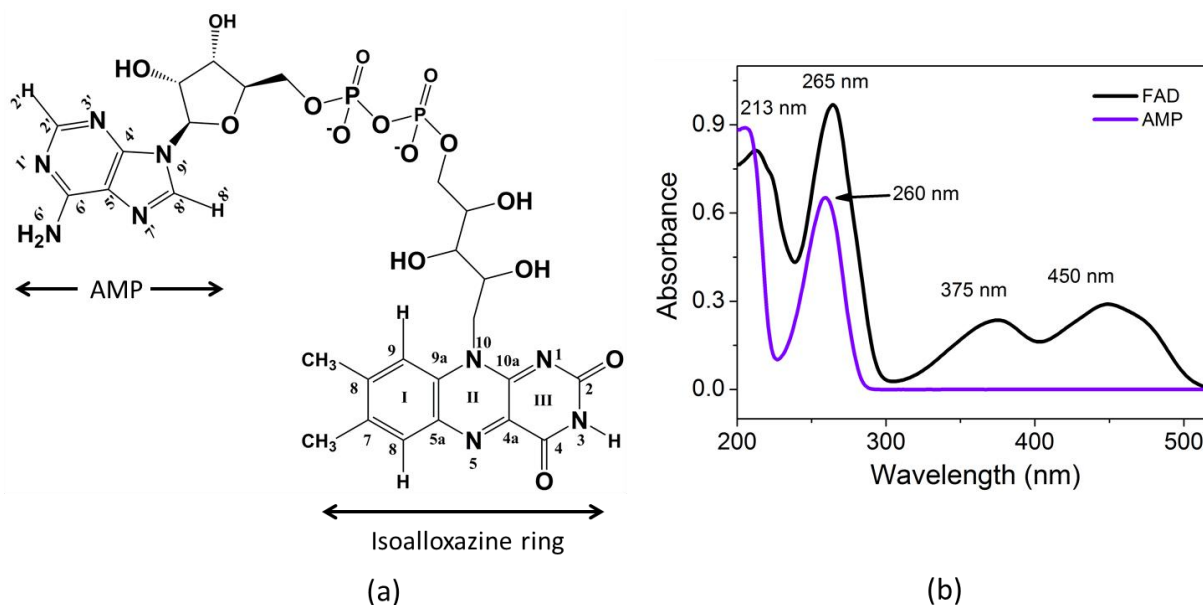


Fig. 5.1 (a) Structure of FAD with the atom numbering of isoalloxazine ring and adenine 5'-monophosphate (AMP). (b) Absorption spectra of 2.5×10^{-5} M FAD (black) and 4.4×10^{-5} M AMP (violet) in pH7 phosphate buffer with absorption maxima values in nm.

Time-resolved vibrational spectroscopies, such as femtosecond mid-IR and stimulated Raman spectroscopy (FSRS) has been employed to deduce structural changes in flavins following photoexcitation to S1 excited state in solution,^{16,17,19,20} and inside blue-light photoreceptors.^{21,22} The solvation dynamics in S1 excited state is detected as a dynamic Stokes shift of the emission band.²⁰ Apart from the S1 excited state, no such studies have been done within the ultraviolet (UV) region of absorption where flavins have strong $\pi\pi^*$ transitions. Copeland and Spiro²³ reported the Resonance Raman (RR) spectroscopy of FAD molecule with UV excitations at 266, 240, 218 and 200 nm. UVRR spectra of FAD contain contributions from both flavin and adenine moieties because both can absorb UV light. RR excitation within the

absorption band centered at 265 nm can selectively enhance the bands of FAD over the amino acid bands and thus make it as a useful probe to study the protein dynamics.

The excess vibrational energy of a molecule in solution upon photoexcitation to the electronic excited state dissipates via the specific vibrational modes and through the intermolecular interaction with the surrounding solvent molecules. To understand the relaxation pathways of an electronically excited molecule, it is important to deduce this energy dissipation mechanism. The determination of instantaneous structural distortions in the Franck-Condon region upon photoexcitation is also very critical to know because these quantities affect the excited state photophysics in later timescales. RR spectroscopy is the only technique which can measure the vibrational mode-specific reorganization energies following photoexcitation to the electronic excited state. Here we have measured the short time excited state dynamics of oxidized FAD molecule within its 265 nm absorption band using RR spectroscopy.

Vibrational frequencies of FAD are sensitive to the changes of hydrogen bonding, π - π stacking and ionic interactions with the neighboring amino acids and ligands in proteins. In addition to the Raman band positions, RR intensities contain information about dynamics of the resonant excited state. When Raman excitation is in resonance with an electronic excited state, the observed Raman band intensity is proportional to the square of structural distortions in the resonant excited state along that vibrational normal coordinate. So, greater the structural distortions in the excited state with respect to the ground state along the vibrational coordinate means higher the RR intensity of that vibrational mode. The structural distortions in the excited state determined along each vibrational coordinate are defined as dimensionless displacements (Δ). These Δ 's are proportional to the slope at the potential energy surface (PES) of the excited state along the vibrational coordinate. Moreover, the line shape analysis of the Raman excitation profile (REP), i.e., the excitation wavelength dependence of RR cross sections can reveal the response of the effect of solvent environments through line broadening. Through measurement and modeling of experimental REP, we can extract the parameters corresponding to the initial excited state structural dynamics of FAD molecule within tens of femtoseconds of excitation.

Lee and Heller's time dependent wave-packet propagation (TDWP) theory²⁴ was used to simulate the experimental REPs and absorption spectrum of FAD. Through modeling of experimental REP, we have extracted the parameters describing the initial excited state structural

and solvation dynamics of FAD. Structural distortions upon photoexcitation to the excited state at 265 nm were obtained in terms of changes in internal coordinates of ground electronic state structure. Total internal reorganization energies along all RR active modes are partitioned in a mode-specific manner. We used Brownian oscillator model²⁵ to account for fast solvent induced dephasing that originate from interaction of FAD with surrounding solvents. We have been able to partition total line-width contribution to both REPs and absorption process in fast homogeneous, and static inhomogeneous components. A detailed comparison of thus excited state parameters of FAD with those obtained for FMN and AMP brings out the nature of electronic coupling between the ring.

5.2. Experimental and Computational Methods

5.2.1 Sample Preparation

FAD was purchased from Sigma Chemicals Co. with greater than 95% HPLC purity and used as supplied. Sample solutions were prepared in 50 mM sodium phosphate buffer of pH 7. The concentration of sample solution was determined using the extinction coefficient (ϵ) value of $11500 \text{ M}^{-1} \text{ cm}^{-1}$ at 450 nm.²⁶ 300 μL of 450 μM FAD sample solutions were used for UVRR experiments. In all the samples 250 mM sodium sulphate (Na_2SO_4) solutions were added as internal standard. UV/Vis absorption spectra were recorded using Perkin-Elmer (lambda 45) absorption spectrometer at pH 7 in phosphate buffer.

5.2.2 UVRR Spectroscopy

UVRR Spectra of FAD were recorded at 10 excitation wavelengths throughout the 265 nm absorption band of FAD. The detailed experimental set-up was described in chapter 2.

5.2.3 UVRR Cross-section Determination

The methods of UVRR cross section determination have been described in chapter 2. Depolarization ratios of the observed UVRR bands were measured using a similar experimental set-up as used for other flavins. Table 5.1 shows the depolarization ratios for intense Raman bands of FAD. For the weak Raman bands, it is difficult to determine the ratios due to the very low signal to noise ratio of perpendicular polarized spectrum and we have taken the value of 0.33 for those bands.

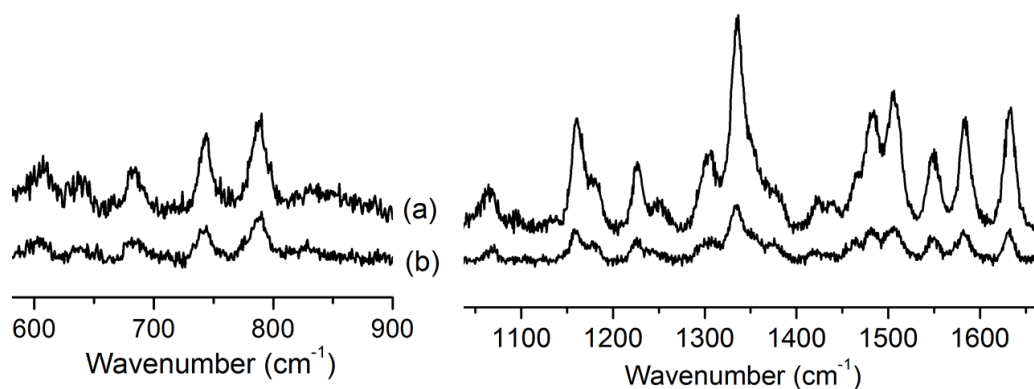


Fig. 5.2 (a) Polarized and (b) depolarized spectra of 450 μM FAD in high (left) and low (right) frequency regions obtained at 260 nm excitation wavelength.

Table 5.1. Depolarization ratios of UVRR bands of FAD

Raman band (cm^{-1})	Depolarization ratio
609	0.32
685	0.32
742	0.32
787	0.64
1065	0.23
1163	0.27
1182	0.37
1228	0.30
1300	0.34
1336	0.30
1356	0.29
1482	0.21
1505	0.32
1549	0.31
1583	0.34
1632	0.23

5.2.4 Computational Method - Simulation of Experimental REP and Absorption Spectrum

Self-consistent simulation of absorption and experimental REPs were done using Lee and Heller's time-dependent wave-packet theory of RR cross sections^{24,27} which was described in method chapter in detail.

5.2.5 Quantum Chemical Computations

All quantum chemical calculations were done using density functional theory on the B3LYP/TZVP level of theory using the program Gaussian 09 software. FAD molecule was optimized using B3LYP^{28,29} exchange correlation functional along with TZVP³⁰ basis set. Polarizable continuum model (PCM)³¹ was employed to simulate the bulk dielectric environment of water. For the assignment of experimental vibrational modes deuterium exchange calculation was also done. The isotopic shifts on deuterium exchange were calculated after replacement of the mass of protons associated with nitrogen (N) atoms by the mass of deuterium (D). Normal mode analysis was carried out on the theoretical frequencies and matched with the observed experimental frequencies in H₂O and in D₂O. No scaling factor was used for theoretical frequencies. TDDFT^{32,33} calculation was done using the same level of theory on the previously optimized structures. The absorption spectra were calculated from the vertical excitation energies at TD-B3LYP level of theory and by considering the fixed Gaussian band width of 2500 cm⁻¹. Optimized structures, vibrational modes and molecular orbitals (MOs) are visualized using the software Chemcraft v 1.6.

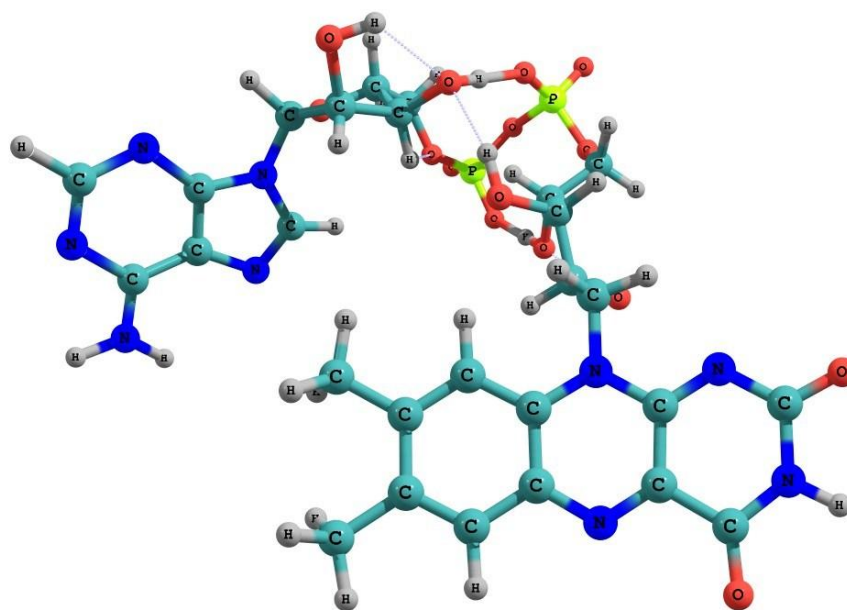


Fig. 5.3 Optimized structure of FAD applying B3LYP/TZVP//PCM level of theory. Extensive hydrogen bonding can be seen between the phosphate groups and sugar moiety.

5.3 Results and Discussion

5.3.1 Electronic Structure

The experimental absorption spectrum of FAD shows four absorption bands at around 212, 265, 375 and 450 nm (Fig 5.1 (b)). The absorption band centered at 265 nm is the most intense one among the four bands. FAD contains adenine moiety which strongly absorbs 260 nm. Thus, the electronic transition of FAD at 265 nm arises from combination of both flavin and adenine. We have applied TD-B3LYP method in conjunction with TZVP basis set and PCM solvent model to determine the vertical transition energies for the electronic transitions involved in both visible and UV regions of FAD absorption spectrum. Table 5.2 describes the computed vertical transition energies, oscillator strengths and MOs involved in those transitions together with other reported theoretical and experimental results.

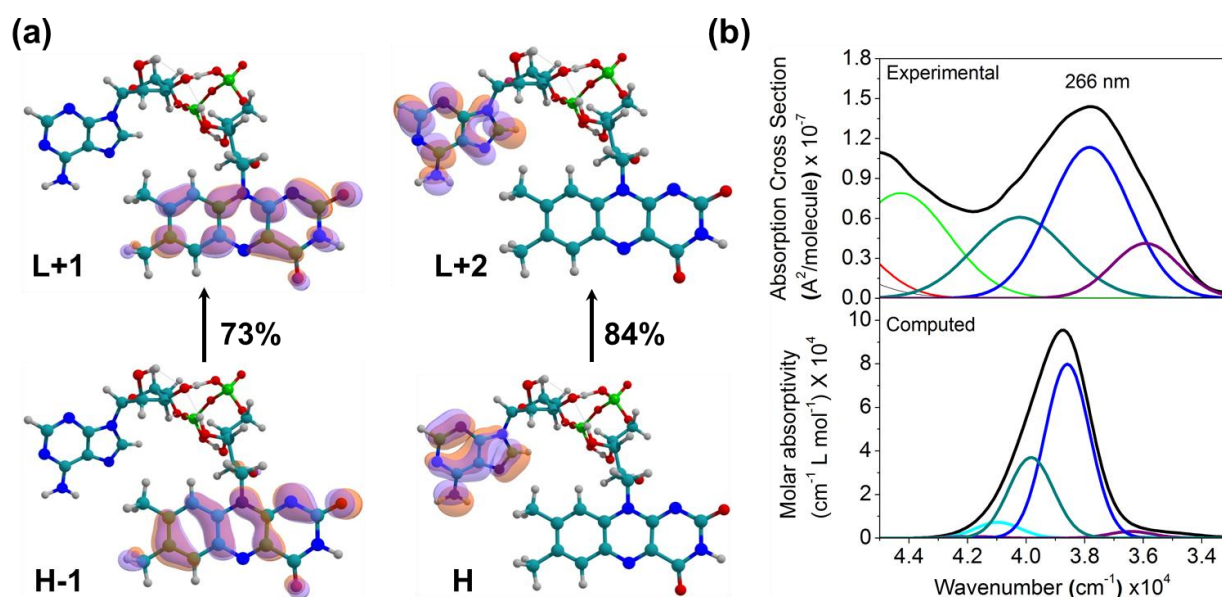


Fig. 5.4 (a) Computed orbitals of FAD involved in the electronic transition following excitation within the 265 nm absorption band of FAD, H and L stands for HOMO and LUMO respectively; (b) deconvoluted experimental absorption spectrum (above) of FAD and theoretical absorption spectra (below) was computed using TD-B3LYP/TZVP//PCM method on FAD molecule. Computed band positions are depicted with a Gaussian line shape of fixed line width (2500 cm^{-1}) and

The experimental absorption bands at 450 and 375 nm are assigned to the $\pi\pi^*$ transitions computed at 2.90 and 3.54 eV respectively. The oscillator strengths calculated for those electronic transitions are 0.2273 and 0.2228. The calculated vertical transition energies for these

Table 5.2 Vertical singlet excitation energies ΔE_{vert} in nm (in eV in parenthesis), oscillator strengths (f) and major orbital contribution for electronic transitions of oxidized FAD molecule by TD-B3LYP/TZVP//PCM method and comparison with published computed and experimental transition energies are given in the table.

Computed					Experimental ^l			
Computed state order	Type	Major orbital contribution (%) ^c	ΔE_{vert} in nm (eV) ^d	f	Published ΔE_{vert} in (eV)		λ_{max} (nm)	ϵ ($M^{-1} \text{cm}^{-1}$)
FAD					RF ^e	LF	Adenine	FAD
S1	($\pi\pi^*$)	H-1 \rightarrow L (95%)	427.1 (2.90)	0.2273	3.04 (0.1749)/ 2.94 (0.2091)	2.40 ^f , 2.94 ^g , 2.91 ^h		450 11500
S3	($n\pi^*$)	H-10 \rightarrow L (56%) H-13 \rightarrow L (13%)	368.2 (3.37)	0.0131				
S4	($\pi\pi^*$)	H-2 \rightarrow L (86%)	359 (3.45)	0.0115				
S5	($\pi\pi^*$)	H-5 \rightarrow L (+43%) H-4 \rightarrow L (40%)	350.3 (3.54)	0.2228	3.76 (0.1620)/ 3.54 (0.2687)	3.54 ^f , 3.84 ^g , 3.50 ^h		375 9300
S19	($\pi\pi^*$)	H-21 \rightarrow L (+36%) H-22 \rightarrow L (+34%)	274.6 (4.52)	0.0250				
S20	($\pi\pi^*$)	H-16 \rightarrow L (+82%)	272.2 (4.55)	0.0001				
S21	($\pi\pi^*$) ^a	H-17 \rightarrow L (+56%)	267.4 (4.64)	0.0138				
S22	($\pi\pi^*$) ^a	H-17 \rightarrow L (+39%) H-19 \rightarrow L (28%)	265.8 (4.66)	0.0153				
S23	($n\pi^*$)	H-19 \rightarrow L (+48%) H-28 \rightarrow L (+24%)	264.2 (4.69)	0.0280				
S24	($n\pi^*$) ^b	H-20 \rightarrow L (+97%)	260.2 (4.77)	0.0015				
S25	($\pi\pi^*$) ^b	H \rightarrow L+1 (+99%)	259.8 (4.77)	0.0062				
S26	($\pi\pi^*$)	H-1\rightarrowL+1(+73%)	259.1 (4.79)	0.6618		4.56^f, 4.95^f, 4.77^g, 4.91^g 4.79^h		
S27	($\pi\pi^*$)	H-21 \rightarrow L (+52%) H-22 \rightarrow L (42%)	256.8 (4.83)	0.0008				
S28	($\pi\pi^*$)^b	H\rightarrowL+2(+84%)	251.0 (4.94)	0.3065			5.18^l, 5.20^l, 4.88^k	
S29	($\pi\pi^*$) ^a	H-24 \rightarrow L (+89%)	250.5 (4.95)	0.0015				
S30	($\pi\pi^*$) ^a	H-25 \rightarrow L (+86%)	247.6 (5.01)	0.0031				
S31	($\pi\pi^*$)	H-1 \rightarrow L+3 (+48%) H-5 \rightarrow L+1 (+24%) H-4 \rightarrow L+1 (20%)	244.0 (5.08)	0.0604				

Electronic transitions involved within the ^aribityl chain, ^badenine moiety and rest are between isoalloxazine ring. ^cPercentages are calculated as 100x twice the squares of the coefficients in the CI expansion of TDDFT wave functions. H and L stands for highest occupied molecular orbital (HOMO)

and lowest unoccupied molecular orbital (LUMO) respectively. ^dVertical excitation energy in this work. ^eTDB3LYP/TZVP method in gas phase/in addition with four explicit water molecules, oscillator strengths in parentheses, see ref. 20. ^fSAC-CI(D95V(d)) method with PCM model along with five explicit water molecules see ref. 35. ^gDFT/MRCI(TZVP), see ref. 36. ^hTD-B3LYP/aug-cc-pVDZ//PCM, see ref. 38. ⁱTD-CAM-B3LYP/6-311+G(2d,p)//PCM, see ref 39. ^jCASPT2, see ref 47. ^kTD-B3LYP/6-31++G(d,p) see ref. 40, ^lAbsorption maxima (λ_{max}) and molar extinction coefficients (ϵ) are taken from ref. 26.

transitions are close to that calculated for RF and LF in our calculations (shown in previous chapters) and also with the reported transition energies (see Table 5.2).^{9,34-37}

We find two adjacent strong electronic transitions at 4.79 and 4.94 eV with oscillator strengths of 0.6618 and 0.3065 respectively. MO representations in Fig. 5.4.(a) show that the orbitals involved in these transitions are π orbitals in nature. The lower energy transition between them is dominated by a $\pi\pi^*$ transition between H-1 to L+1. Fig. 5.4.(a) indicates that these two MOs are localized in isoalloxazine ring of FAD and so the electronic transition happens within isoalloxazine ring. On the other hand, the $\pi\pi^*$ transition at 4.94 eV is dominated by a transition from H to L+2 (84%). The electronic transition from H to L+2 is shown to involve within the adenine moiety. The excitation energy computed for this transition of adenine are close to the that computed using TDDFT^{38,39} and CASPT2⁴⁰ methods for N9-H tautomer. The experimentally observed absorption band at 265 nm of FAD is composed with the two above $\pi\pi^*$ transitions. Along with these two strong transitions, we also find other weak $\pi\pi^*$ transitions within the range of the experimental band at 265 nm as observed in TDDFT calculations of LF and RF.^{9,35,41}

5.3.2 UVRR Spectra of FAD and Adenine

The absorption spectra of FAD and adenine (Fig. 5.1 (b)) suggest that flavin and adenine both absorb at UV-excitations. Therefore, the Raman bands of flavin and adenine both get enhanced by excitation within the 265 nm absorption band of FAD. UVRR spectra of FAD, FMN and adenosine 5'-monophosphate (AMP) obtained at an excitation wavelength of 263 nm are shown in Fig. 5.5. The UVRR band positions of FAD and AMP are in good agreement within the experimental error with the reported spectrum of both the compounds at 266 nm excitation.^{23,42} Copeland and Spiro²³ reported that adenine contributions are dominant at 266 nm excitation wavelength. They have marked the UVRR bands of FAD by F (flavin) or A (adenine) or F+A according to the enhancements originating from purely flavin or adenine or a combination of

both. As we can see in Fig. 5.5 that Raman bands of FAD at 1251, 1304, 1335, 1423 and 1482 cm^{-1} arise due to the enhancement of adenine Raman modes. Flavin and adenine both contribute to the Raman bands at 1377, 1505 and 1582 cm^{-1} .

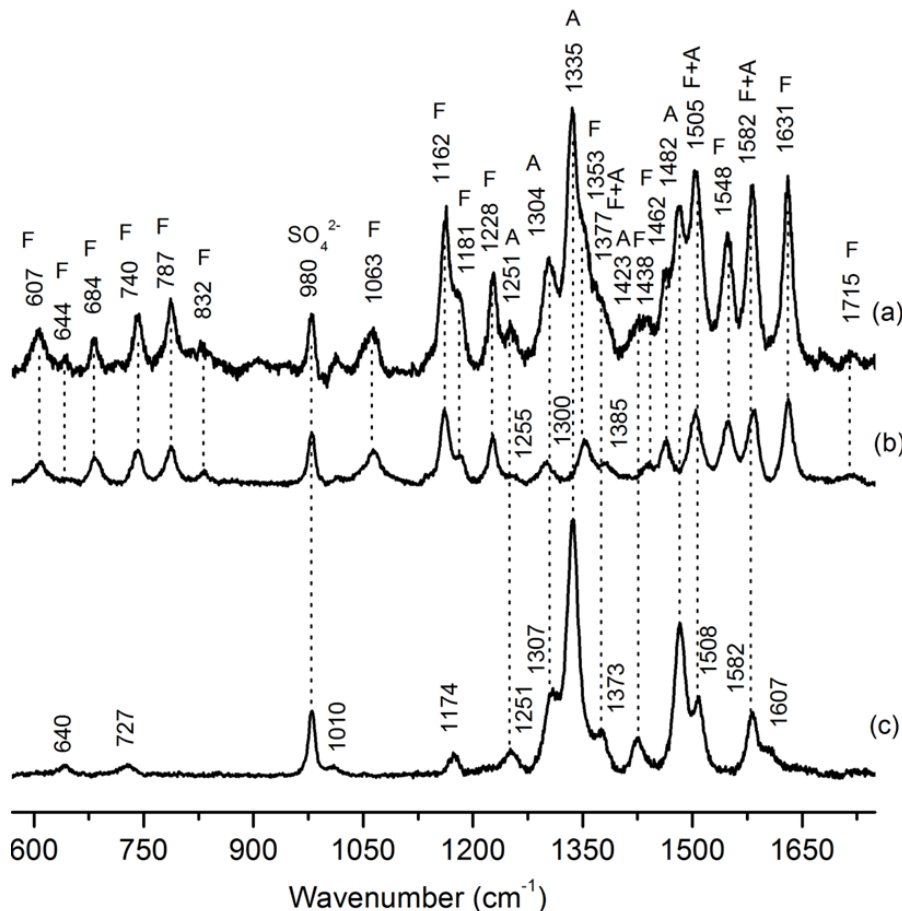


Fig. 5.5 UVRR spectra of (a) FAD (concentration - 450 μM), (b) FMN (concentration - 300 μM) and (c) AMP (concentration - 250 μM) obtained at an excitation wavelength of 263 nm. All spectra are normalized with respect to the intensity of Raman band of sulfate at 980 cm^{-1} which was added as an internal standard. Each Raman band of FAD was marked as F (flavin), A (adenine) or F+A by comparing all three spectra and also from Ref. 31.

However, the cross sections of FAD RR bands that have contribution from both the adenine and isoalloxazine rings are not the sum of that of the bands from AMP and FMN. We have calculated the ratios of the cross sections, $\text{RR}_{\text{FAD}} / \text{RR}_{(\text{FMN}+\text{AMP})}$ for the combined bands, and the ratios, $\text{RR}_{\text{FAD}} / \text{RR}_{\text{FMN}}$ for the pure flavin bands. Table 5.3 indicates that the ratios vary from 1.41 to 0.48, most being less than unity. This variation of cross section ratios is a clear evidence for the electronic interaction between flavin and adenine rings in FAD. Similar effect of Raman hypochromism was observed for nucleobases in stacked duplex

structure.^{43,44} It was also found that the absorption band of FAD is not those summing the absorption bands of FMN and adenine.^{45,46} Stacking interaction between flavin and adenine rings was also proved through the excited state electron transfer from adenine to flavin ring which eventually quenches the FAD fluorescence.^{10,14,47}

Table 5.3. UVRR cross section ratios of FAD with respect to FMN plus AMP

UVRR bands (cm^{-1})	Excitation wavelengths	
	263 nm	266 nm
683 (F)	0.61	0.67
741 (F)	0.86	0.71
787 (F)	0.78	0.59
1062 (F)	0.84	0.67
1162 (F)	0.96	0.65
1228 (F)	0.91	0.63
1307 (A)	0.91	0.99
1335 (A)	0.62	0.57
1353 (F)	1.06	1.03
1376 (F+A)	0.56	0.48
1422 (A)	0.86	1.19
1438 (F)	0.84	0.66
1462 (F)	0.73	0.76
1482(A)	0.72	0.69
1505 (F+A)	0.79	0.74
1548 (F)	0.83	0.63
1582 (F+A)	0.75	0.60
1630 (F)	0.94	0.77
1715 (F)	0.77	1.41

Fig. 5.6 and Fig. 5.7 show the UVRR spectra of FAD obtained at six different excitation wavelengths across the absorption band at 265 nm. Each spectrum was normalized against the intensity of internal standard sulfate band at 980 cm^{-1} . We can observe the variation of Raman

band intensity by moving towards higher excitation wavelength. The intensity changes of UVRR bands of FAD are similar to that seen previously in the UVRR spectra of RF and LF. The intensity of Raman bands at 1548 and 1632 cm^{-1} show maxima at 262.9 nm excitation and then the intensity of those bands decrease rapidly on moving towards higher excitation wavelengths. The intensity change of the band at 1582 cm^{-1} on moving towards higher excitation wavelength is similar to that band of RF and LF and it shows a maximum at an excitation wavelength of 274.7 nm. The intensity change of the bands at 1377 and 1353 cm^{-1} resembles the intensity changes of the Raman bands at 1354 and 1385 cm^{-1} of RF. On going towards higher excitation wavelengths, the intensity ratio of the bands at 1377 and 1355 cm^{-1} becomes reverse. Similar to the UVRR spectra of RF here also we have found a new band at 1281 cm^{-1} at higher excitation wavelengths.

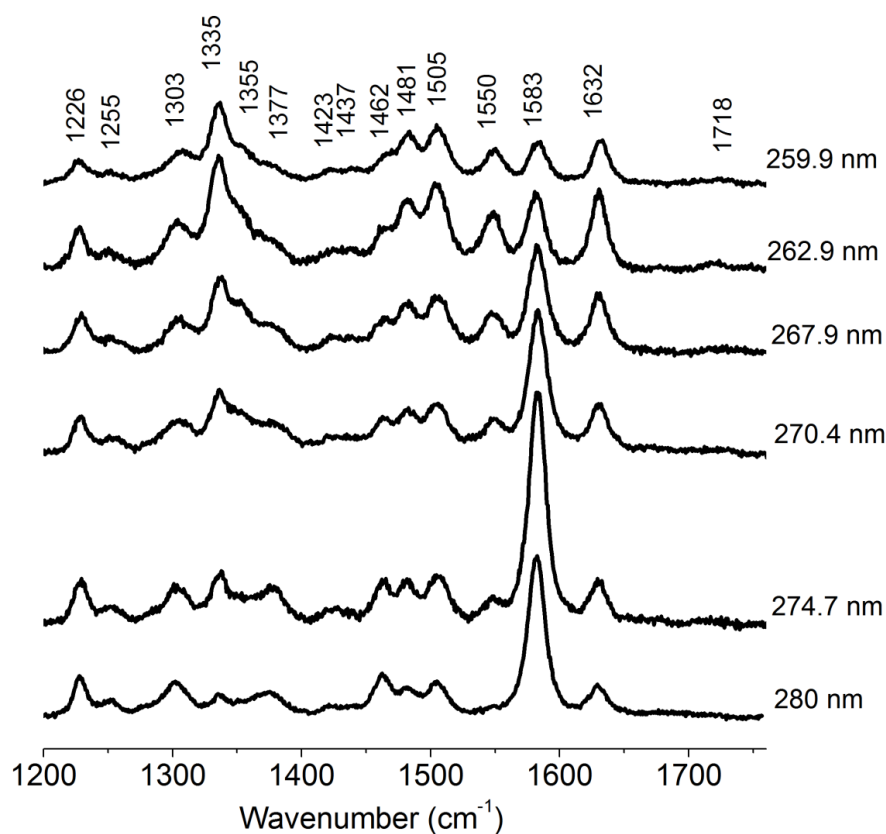


Fig. 5.6 UVRR spectra of 450 μM FAD in pH7 sodium phosphate buffer obtained at 6 different excitation wavelengths at high frequency regions. Variation in the UVRR band intensity with changing excitation wavelengths can be seen. All spectra are normalized with respect to the internal standard band at 980 cm^{-1} .

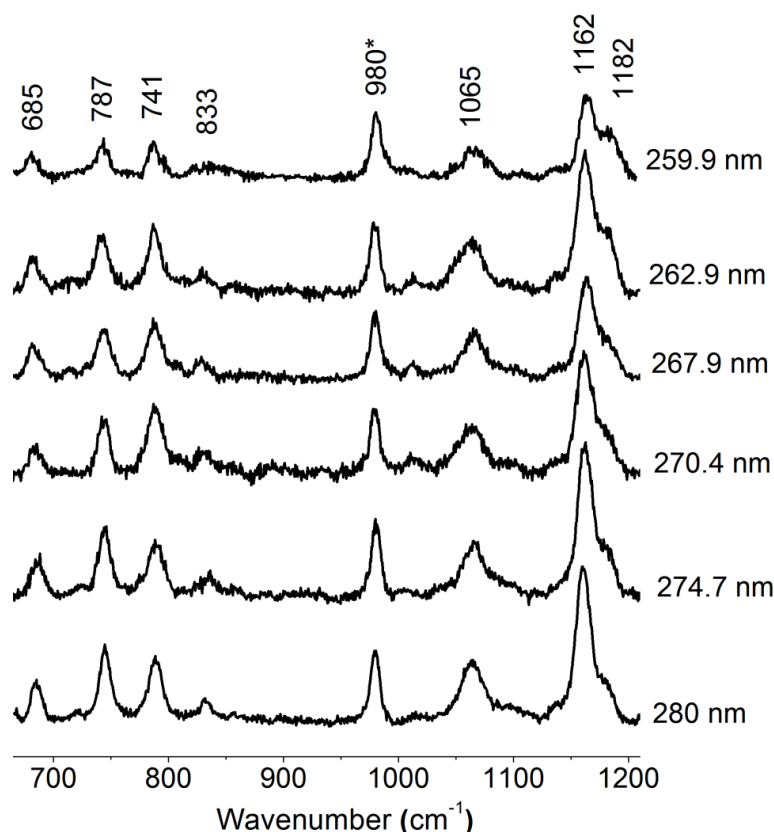


Fig. 5.7 UVRR spectra of 450 μM FAD in pH7 sodium phosphate buffer obtained at 6 different excitation wavelengths at low frequency regions. Internal standard sulfate band at 980 cm^{-1} is marked by an asterisk. All spectra are normalized with respect to the internal standard band at 980 cm^{-1} .

Normal mode assignments of the observed UVRR bands of FAD using B3LYP/TZVP/PCM method have been shown in Table 5.4. A. Weigel et al.²⁰ have done the assignment of RR bands of FAD using the same method with the addition of four water molecules around the electronegative atoms. Our assignments of UVRR bands of FAD are consistent with their assignments and with other reported assignments^{48,49}. The assignments of adenine Raman modes in UVRR spectra of FAD agree with the reported assignments of adenine nucleobase.⁵⁰⁻⁵² It was already discussed that three Raman modes of FAD at 1582 , 1505 and 1377 cm^{-1} appear because of Franck-Condon active transitions from both adenine and flavin ring coordinates. We find two adjacent computed frequencies associated with adenine and flavin ring vibrations respectively for each of those three modes of FAD from our DFT calculation. Thus

Table 5.4 Experimental and computed wavenumbers of FAD calculated using B3LYP/TZVP//PCM level of theory, dimensionless displacements (Δ) and mode specific internal reorganization energies of 23 UVRR modes.

Experimental wavenumber (cm ⁻¹)	Computed wavenumber (cm ⁻¹)	Mode type ^a	Δ	Mode specific internal reorganization energy λ_k (cm ⁻¹)
607 (F)	596	be C9a-N10-C10a, be C2-N3-C4, be H-C-H (Ribityl chain)	0.23	15
683 (F)	684	be O4-C4-N3, be O2-C2-N1, be N5-C5a-C9a	0.18	11
741 (F)	750	str C9a-C5a, be C8-C9-C9a, be C5a-C6-C7	0.2	15
787 (F)	791	be C4a-N5-C5a, be N1-C10a-C4a, be N3-H	0.22	19
831 (F)	866/840*	be N3-C2-N1, be C4-C4a-C10a, be C6-H	0.13	7
1062 (F)	1054	be H-C-H (Ribityl chain)	0.19	19
1162 (F)	1166	str C7-Me, str C8-Me, str. N1-C2, str. C4-C4a, str. N10-C10a, be C6-H, str. N10-C1*	0.24	32
1181 (F)	1190	str N5-C5a, str N3-C4, be N3-H, be C6-H, be C9-H	0.12	9
1228 (F)	1235	str N3-C4, str N3-C2, str N1-C2, be C6-H, be C9-H	0.16	15
1251 (A)	1263 (A)	be H8'-C8'-N7', str C5'-N7', be C4'-N9'-C8', be H2'-C2'-N1', 6'-NH2 (wag)	0.11	7
1307 (A)	1329 (A)	str N1'-C2', str C2'-N3', str C5'-N7', be N3'-C2'-H2'	0.2	26
1335 (A)	1356 (A)	str N1'-C2', str C5'-N7', be N7'-C8'-H8', be N1'-C2'-H2'	0.25	40
1353 (F)	1362 (F)	str. N10-C10a, Ribityl chain vibration	0.18	22
1377 (F+A)	1376 (F)	str C8-C9, str N3-C4, str C-C(I, II, III), str C-N(II, III), be H-C-H (10-CH2)	0.17	19
	1387 (A)	str N1'-C6', be H2'-C2'-N3', str C4'-N9', be C4'-N9'-C8'		
1422 (A)	1436 (A)	str N9'-C4', str. N7'-C8', be C5'-N7'-C8', str C6'-N6', be C4'-N9'-C8', be H2'-C2'-N3'	0.09	6
1438 (F)	1455	7, 8-Methyl def., be C4a-N5-C5a	0.08	5
1462 (F)	1491	str N1-C10a, str C5a-C6, 7,8-Methyl def., be H-C-H (10-CH2)	0.15	16
1482(A)	1495 (A)	str N1'-C6', str C2'-N3', be H2'-C2'-N3', be 6'-NH2, be H8'-C8'-N9'	0.18	24
1505 (F+A)	1521 (F)	str C7-C8, str C9-C9a, str N5-C5a, str N10-C10a, 7, 8-Methyl def., be C6-H, be C9-H	0.22	37
	1521 (A)	str N7'-C8', str C6-N10, be H8'-C8'-N7' (A), be 6'-NH2, be C4'-N9'-C8'		
1548 (F)	1553 (F)	str N5-C4a, str N10-C10a, str C7-C8, str. C9-C9a, str C5a-C9a, 7,8-Methyl def., be H-C-H (10-CH2)	0.15	18
1582 (F+A)	1598 (F)	str N5-C4a, str C8-C9, str C5a-C9a, be C9-H, 8-Methyl def.	0.43	144
	1599 (A)	str N3'-C4', str C4'-C5', str N1'-C6', be 6'-NH2, be N9'-C4'-C5'		

1630 (F)	1662 (F)	str C6-C7, str. C8-C9, be C9a-N10-C10a, str N5-C4a, be C6-H, be C9-H	0.18	27
1715 (F)	1735 (F)	str C4-O, str C2-O, be N3-H	0.07	5

^astr - stretching, be - bending, def – deformation. F, A and F+A represent flavin, adenine and combination normal modes respectively.

both the computed frequencies can contribute to each of those combined Raman modes (Table 5.4).

5.3.3 Simulation of Absorption and Experimental REPs

The cross sections of each Raman band of FAD were determined by experimental measurements described in chapter 2. Experimental and simulated REPs and the absorption band of FAD centered at 265 nm are shown in Fig 5.8, and Fig 5.9. Simulation of experimental REPs using time-dependent wave-packet theory was carried out by iterating a set of parameters until a good agreement between the simulated and experimental REPs was attained. The parameters corresponding to the final best fit are reported in Table 5.5. Table 5.4 shows the dimensionless displacements, Δ , and the internal reorganization energies for Raman bands of FAD.

We find that the maxima of most of the REPs are either blueshifted or redshifted (Fig 5.8 and Fig 5.9) compared to the absorption band maximum at 265 nm. This kind of shift of maxima was observed in the REPs of RF and LF (see previous chapters) and it is attributed to the interference coming from weak $\pi\pi^*$ electronic transitions present to both lower and higher energy sides of the strong central $\pi\pi^*$ transition within the experimental absorption band at around 265 nm. The computed vertical transition energies for FAD also suggest the existence of those weak electronic transitions to the both sides of the strong electronic state centered at around 265 nm (Fig 5.4(b)). A decrease in UVRR cross sections is observed in the REPs of most of the Raman bands at 259.9 nm. It was mentioned earlier that two strong electronic states exist for adenine and flavin rings within the absorption band at 265 nm. The decrease in cross section at that particular excitation indicates that most of the observed bands are vibronically coupled to both of these electronic states. But as we don't know how much of these two states are electronically coupled, we consider these two electronic states as a single electronic state from which the resonance enhancement of UVRR modes occurs. The depolarization ratios measured for most of the UVRR bands are close to 0.33, also indicating that the enhancement is coming

from a single electronic state despite the existence of two electronic states within the absorption band.

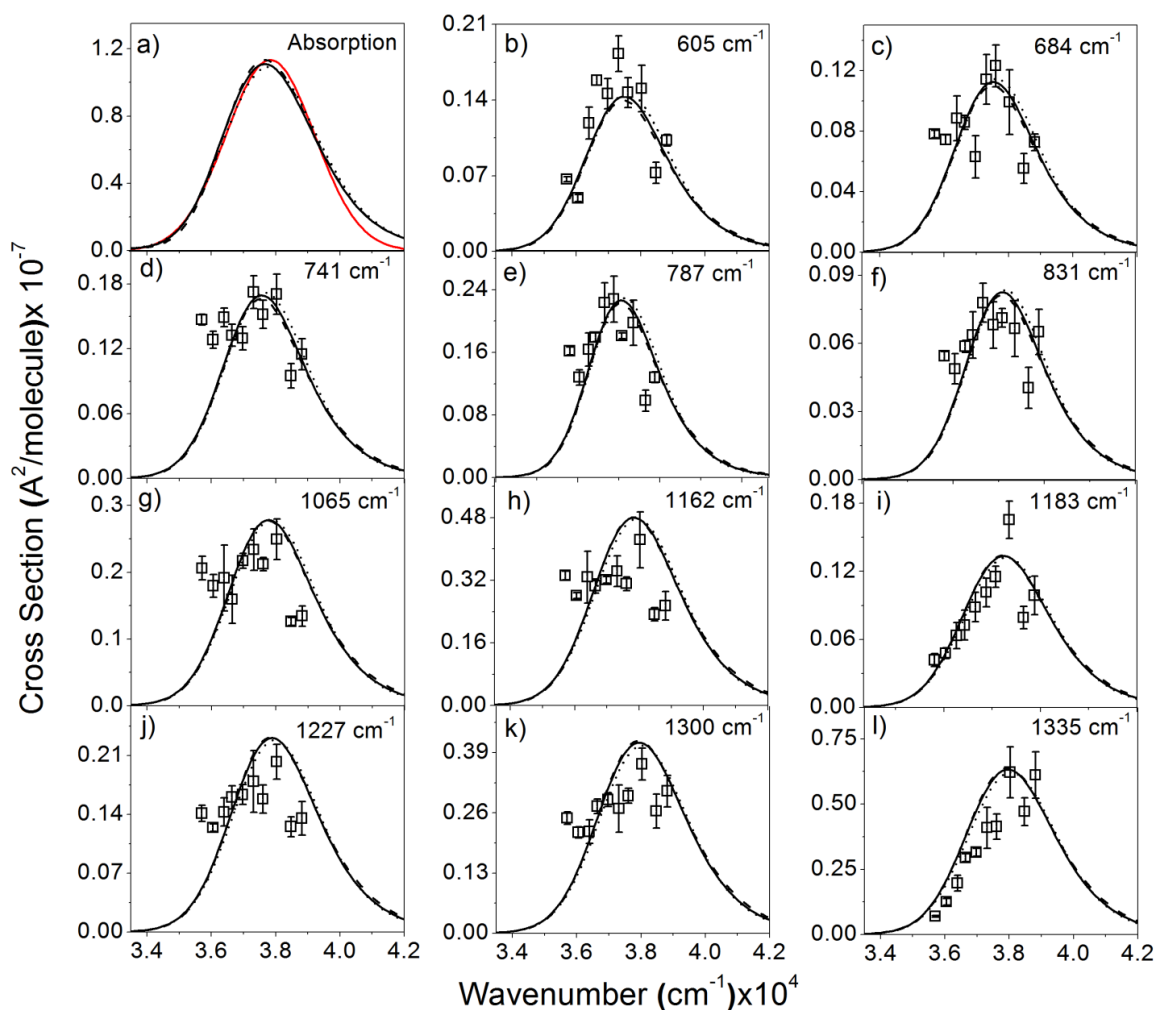


Fig. 5.8 Experimental and simulated Raman excitation profiles and absorption cross section of FAD obtained following excitations within 265 nm absorption band. (a) Experimental (solid) and simulated absorption (dash) spectrum. (b-l) Raman excitation profiles of 11 UVRR modes of FAD at 10 different excitation wavelengths. The best fit (solid) was obtained by using the parameters of Table 5.5. Set 1 (dot) and Set 2 (dash dot) parameters are obtained by decreasing and increasing the best fit delta values by 10% respectively.

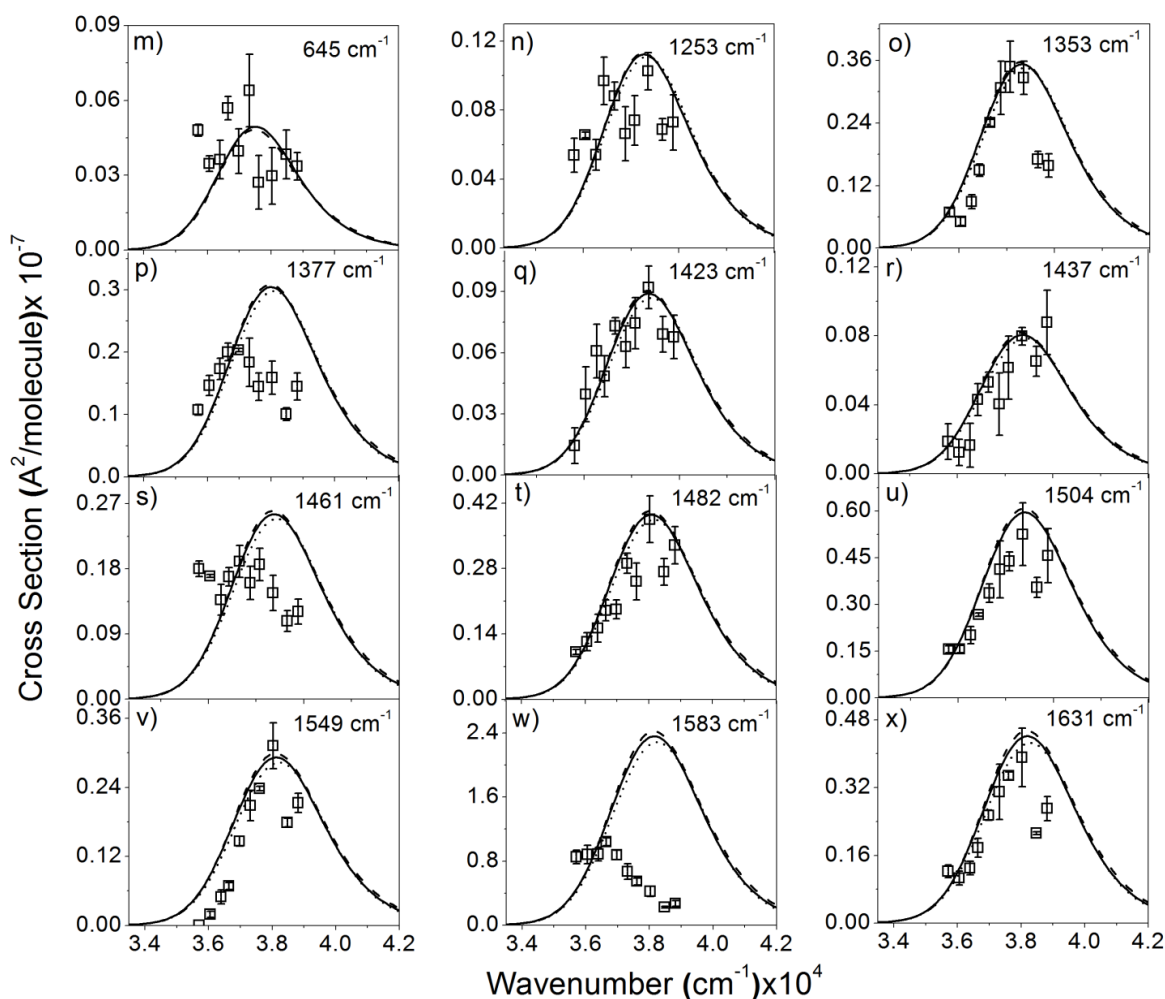


Fig. 5.9 Experimental and simulated Raman excitation profiles (m-x) of other 12 UVRR modes of FAD obtained using the same parameters as in Table 5.5.

The REPs of the UVRR bands at 1162, 1227, 1300, 1423, 1482, 1505, 1549, 1631 cm^{-1} show maxima at an excitation wavelength of 263 nm. We have seen similar shifts in the maxima of REPs for the Raman bands at 1437, 1463, 1505, 1549 and 1631 cm^{-1} for RF and FMN and this was attributed to the interference from nearby electronic states. The REPs of the Raman bands at 1377 and 1583 cm^{-1} exhibits maxima at 270.4 and 272.9 nm respectively. For all other three flavins (LF, RF and FMN), we have observed similar redshift in the maxima of REPs for these two bands and those are because of the strong vibronic coupling of these two modes with nearby lower energy electronic states.

The simulated and experimental REPs for 1377 and 1583 cm^{-1} bands do not agree at high frequency regions, observed previously for all of the flavins for these two bands. This is

likely due to the coupling of these modes with high energy electronic states. The deviation of simulated and experimental REPs of the Raman band at 1549 cm^{-1} at low frequency region was also observed for LF, RF and FMN for that band.

Table 5.5 Parameters used in self-consistent fit of REP and absorption spectra for FAD

	E_0 (cm^{-1})	Λ (cm^{-1})	τ (fs)	θ (cm^{-1})	M (\AA)	λ_{int} (cm^{-1})	λ_S (cm^{-1})	λ (cm^{-1})
Best Fit	37490	210	25.2	870	1.22	543	1370	1913
Set 1	37600	245	21.7	955	1.22	438	1275	1713
Set 2	37450	160	33.2	770	1.22	659	1480	2139

5.3.4 Structural Dynamics upon Photoexcitation

As we know that the intensity of a RR band is roughly proportional to the dimensionless displacements (Δ), the excited state structural changes upon photoexcitation to the Franck-Condon region can be explained from the best fitted Δ s. The higher value of Δ along a vibrational coordinate suggests greater distortion along that coordinate. The Δ values for each mode obtained from our simulation are depicted in Table 5.4. We find a maximum value of Δ (0.43) for the Raman mode at 1583 cm^{-1} . Since 1583 cm^{-1} band is a combined band coming from the enhancement of both flavin and adenine ring modes, major structural distortion occur in both isoalloxazine and adenine ring coordinates. Theoretical assignment (Table 5.4) of this band suggests that the N5-C4a, C8-C9, C5a-C9a bonds and H-C-H bond angles in 8-methyl group of isoalloxazine ring as well as the N3-C4, C4-C5, N1-C6 bonds and N9-C4-C5 bond angles in adenine ring show most structural changes in the 265 nm excited state. Major changes were observed previously in the isoalloxazine ring along the N5a-C4a and C8-C9 bonds for RF and LF in the same excited state. For FAD unlike other flavin molecules, we are unable to convert the Δ into the internal coordinate changes because of the crowding of atoms for such a big molecule which produces complexity in theoretical calculations.

It was found for photoexcited RF and FMN that the structural distortions occur along all over the isoalloxazine ring stretching coordinates. The UVRR bands of FAD arising from enhancements of only isoalloxazine ring and also the combination bands at 607, 684, 741, 787,

1062, 1162, 1353, 1377, 1505, 1630 cm^{-1} show relatively high value of Δ and thus the initial excited state dynamics of FAD also dominate along these internal coordinates. Mode assignments of these bands indicate that the isoalloxazine ring bonds C6-C7, C8-C9, C7-C8, N1-C2, C4-C4a, C5a-C9a, N1-C10a, N5-C4a, and N10-C10a will be more affected in the excited state. For RF and FMN, we observed higher Δ values for the same Raman modes. **So we can conclude that initial excited state structural distortion lies along the similar coordinates for all three flavins. The high values of Δ obtained for the combined bands at 1377 and 1505 cm^{-1} indicate that the distortion in adenine ring happens along the N1-C6, C4-N9, N7-C8, C6-N10 bonds and H8-C8-N7, C4-N9-C8, H2-C2-N3 bond angles.**

Along with the flavin Raman modes, we also find high Δ values for the adenine bands at 1303 (0.17), 1335 (0.20) and 1482 cm^{-1} (0.16). WPD simulations for free AMP also determine the high Δ values for these Raman bands (Table 5.6), although these values are higher as compared to that obtained for FAD. It indicates a smaller distortion of adenine in FAD in comparison to the free AMP upon excitation to the 260 nm excited state. The higher value of Δ for the three bands indicates that largest structural changes in adenine ring (FAD) in the excited state happen along the stretching coordinates of N1-C2, C2-N3, C5-N7 and N7-C8 bonds. The bond angles localized to N7, C8, N3 and C2 atoms also show strong excited state distortions according to the assignments of those three adenine bands. Mondal and Puranik³⁸ have determined the structural changes for 9-Methyladenine by using the best fitted Δ s from Lopponow and coworkers⁵³ following excitation to its L_a excited state at ~ 260 nm. They have reported that the expansion and contraction occur in the excited state along N1-C2, C2-N3, C5-C6, N3-C4, C5-N7, C8-N9, N9-C4 and N7-C8 bonds for 9-Methyladenine. So, some of our predicted excited state changes agree with their structural dynamics for the methyl substituted adenine at N9 position.

The distortions in the excited state along vibrational modes can also be explained by determining mode specific internal reorganization energies. The internal reorganization energies determined along each normal mode are shown in Table 5.4. Adding up these reorganization energies results total internal reorganization energy of 543 cm^{-1} . **The Raman mode at 1583 cm^{-1} contributes 26% to the total reorganization energy obtained and supports the strong structural distortion along this mode.** We have obtained the similar result for all other flavins

(LF, RF and FMN) along this vibrational mode in the same excited state. The other vibrational modes with significant contributions to the total reorganization energy are at 787, 1065, 1162, 1303, 1335, 1355, 1377, 1481, 1505 and 1631 cm^{-1} . These UVRR modes contribute 44% to the total reorganization energy and thus provide the influence of these vibrational modes in the excited state dynamics of FAD.

5.3.5 Linewidth Broadening

Wave-packet dynamics simulation of REPs and absorption spectrum allows us to separate the total spectral linewidth into homogeneous and inhomogeneous broadenings. Homogeneous broadening appears because of dynamic fluctuation of transition energies due to solvent induced dephasing, whereas inhomogeneous broadening originates from the site effect of distinct micro-solvated structures of solute in different local environments. Here, we have used Brownian oscillator model of Mukamel and coworkers²⁵ to account for the solute-solvent bath interaction which considers the effect of change of solute dipole moment upon excitation on the solvent coordinates. Our simulation determines homogeneous broadening component as solvent reorganization energy (λ_s) = 1370 cm^{-1} for FAD upon excitation to the 266 nm excited state. **The solvent reorganization energy obtained for FAD is little bit higher as compared to that obtained for RF and FMN (1150 cm^{-1}) in the same excited state. The higher value of solvent reorganization energy indicates an increase in coupling strength between the solute and surrounding solvent bath due to the larger dipole moment in the excited state as compared to that of RF and FMN.** Addition of adenine moiety in flavin structure can alter the structure of first solvation shell surrounding the solute which in turn changes the magnitude of inertial solvent response of water for FAD. Addition of exocyclic substitutions with a hydrophilic group can significantly alter the structure of first solvation shell, and interaction of solute with surrounding solvent. For example, a twofold increase in the solvent reorganization energy (2500 cm^{-1}) was obtained for GMP in B_b state due to the presence of exocyclic oxygen (O) and ribophosphate group.⁵⁴

As Raman is a scattering phenomena which happens within tens of femtoseconds following photoexcitation, the dynamic component of solvation obtained here is due to the inertial response of water. We have determined previously a dynamic ultrafast response of water solvation (τ) in ~ 30 fs for LF, RF and FMN in the 266 nm excited state. For FAD also, an

ultrafast solvent relaxation time of 25.3 fs is determined from our simulation associated with solvent reorganization energy of 1370 cm^{-1} . The obtained solvent relaxation timescale for FAD is in good agreement with the reported experimental^{38,55–60} and molecular dynamics simulation^{56,61–63} results that detect an ultrafast component of water solvation originating from the inertial response of water following photoexcitation. However it was shown earlier^{58,59} that the simulated REPs are not very sensitive to a change in Λ ($\Lambda = 1/2\pi c\tau$) and we estimate a lower and higher value of τ by increasing and decreasing the best fitted Δ s by 10 %.

Apart from the static microsolvated structures of solute, other processes occurring at longer timescales than RR process, such as interconversion between the rotational isomers also included in inhomogeneous broadening component (θ) obtained from our simulation. For RF and FMN, a large value of inhomogeneous broadening linewidth (900 cm^{-1}) was determined in the 266 nm excited state. For FAD, we obtain a similar inhomogeneous broadening linewidth to be 870 cm^{-1} . Although FAD has an additional AMP group as compare to the FMN, the obtained value of inhomogeneous broadening suggests the existence of an almost same number of microsolvated structures for all three flavins.

5.4 Caveats and Future Prospects

The simulation of RR intensities using the time-dependent wave packet theory of Lee and Heller²⁴ in combination with DFT calculations has some limitations. Our method of simulation is considered the resonant electronic state at around 265 nm as a single, non-degenerate state and the potential energy surface is harmonic. Although the depolarization ratios measured for each Raman band of FAD are close to 0.33, we have discussed that two strong interfering electronic states exist within 265 nm absorption band of FAD. So, it would be more appropriate to use a two state model for these two excited states as applied for L_a and L_b excited states of guanine nucleobase.⁶⁴ However, it will be a much complicated process to use this two state model here because of the involvement of a large number of parameters in the simulation. Nevertheless, these first measurements within the excited states at 265 nm of FAD, reveal the mode-specific influence of coupling between the electronic states. Our data will be of importance for developing theoretical methods and accurate physical models for more reliable informations of electronic excited states within the absorption band at 265 nm of FAD.

5.5 Conclusion

Self-consistent simulation of REP and absorption spectrum together with DFT computations reveal the sub-100 fs excited state structural dynamics of FAD upon excitation to the excited state centered at around 266 nm. **Raman hypochroism was observed for FAD, indicating electronic interactions (stacking) between flavin and adenine rings. It was found that initial excited state dynamics is dominated by 607, 684, 741, 787, 1062, 1162, 1303, 1335, 1353, 1377, 1482, 1505, 1583 and 1630 cm⁻¹ UVRR bands. The higher Δ values obtained along these bands indicate that major structural distortion happens in both flavin and adenine rings in the excited state. Here, we found a little higher solvent reorganization energy for FAD as compared to RF and FMN, suggesting existence of a stronger dipole interaction with the surrounding water molecules in FAD compared to that of RF and FMN. Despite the structural difference between FAD and FMN, inhomogeneous broadening values obtained for both the molecules are almost same. Similar to other three flavins, we also determined that the first solvation shell of FAD inertially responds with an ultrafast timescale of around ~ 30 fs.** The excited state parameters obtained for FAD will impact studies on flavin containing proteins that use FAD as a probe of protein dynamics.

Figure and Tables of Wave-packet Dynamics Simulations of AMP

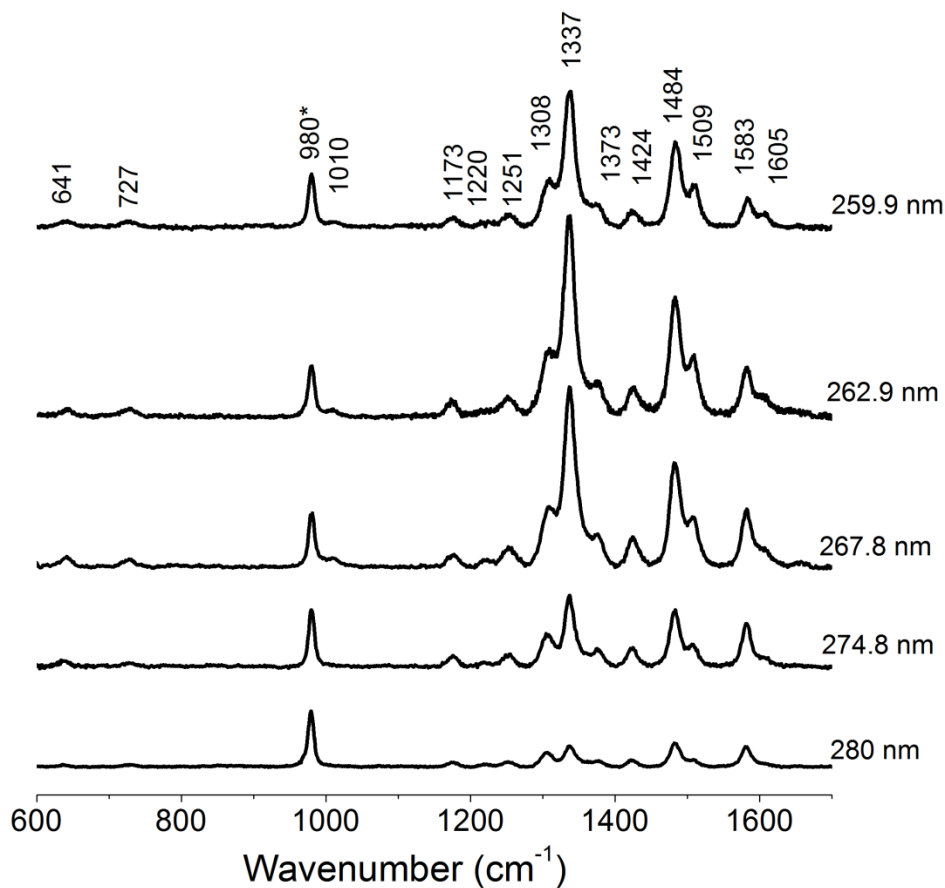


Fig. 5.10 UVRR spectra of 250 μM AMP in pH7 sodium phosphate buffer obtained at 5 different excitation wavelengths. Internal standard sulfate band at 980 cm^{-1} is marked by an asterisk. Variation in the UVRR band intensity with changing excitation wavelengths can be seen. All spectra are normalized with respect to the internal standard band at 980 cm^{-1} .

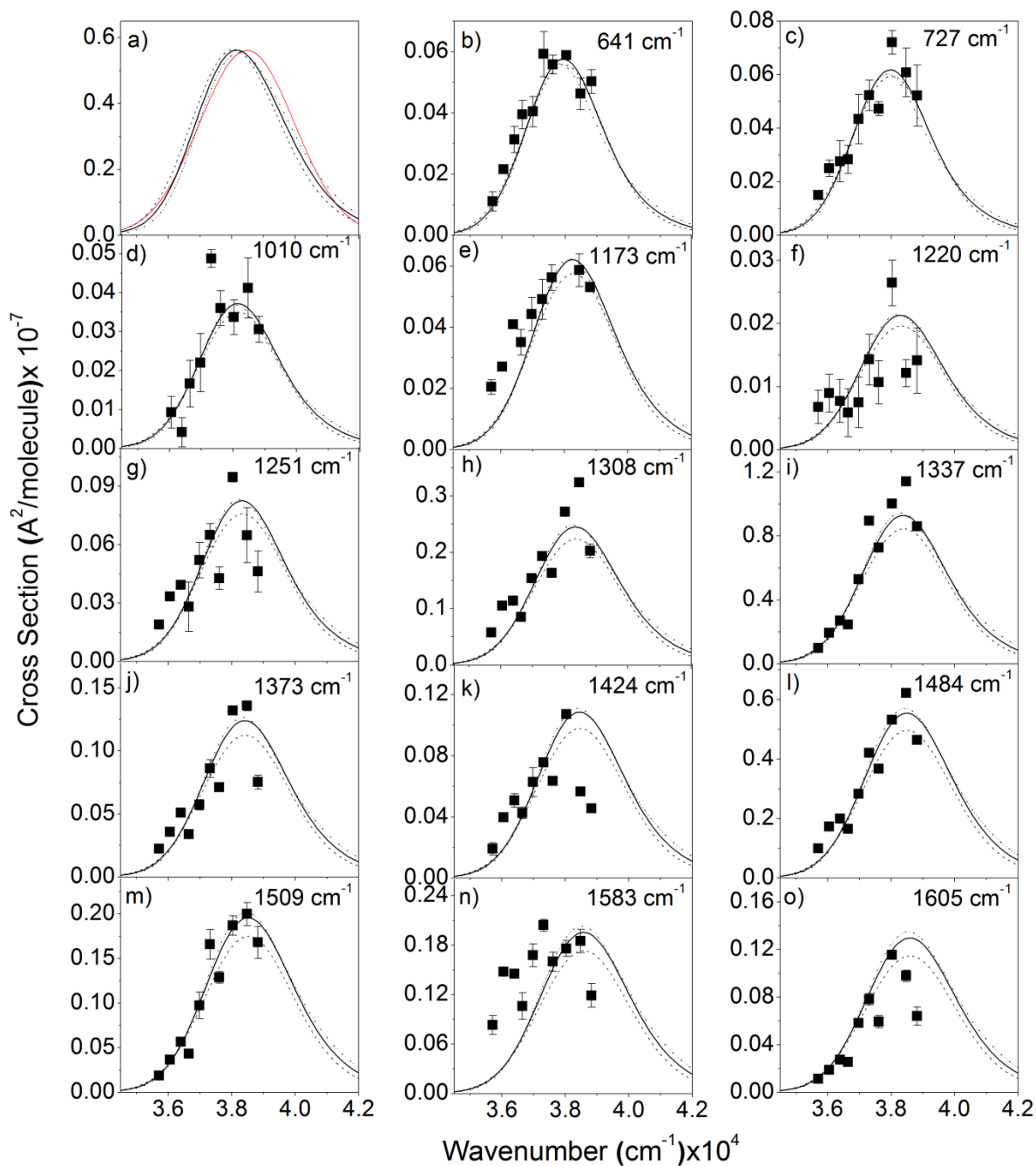


Fig. 5.11 Experimental and simulated Raman excitation profiles and absorption cross section of AMP obtained following excitations within 260 nm absorption band. (a) Experimental (red) and simulated absorption (black) spectrum. (b-o) Raman excitation profiles of 14 UVRR modes of AMP at 10 different excitation wavelengths. The best fit (solid) was obtained by using the parameters of Table 5.6. Set 1 (dash) and Set 2 (dash dot) parameters are obtained by decreasing and increasing the best fit delta values by 10% respectively.

Table 5.6. Experimental wavenumbers of AMP, dimensionless displacements (Δ) and mode specific internal reorganization energies of 14 UVRR modes

Experimental frequency (cm ⁻¹)	Δ	Mode specific reorganization energy (cm ⁻¹)
641	0.21	14
727	0.2	14
1010	0.12	7
1173	0.14	11
1220	0.08	4
1251	0.15	14
1308	0.25	42
1337	0.49	161
1373	0.18	21
1424	0.16	19
1484	0.36	95
1509	0.21	33
1583	0.21	34
1605	0.17	22

Table 5.7. Parameters used in self-consistent fit of REP and absorption spectra for AMP

	E_0 (cm ⁻¹)	Λ (cm ⁻¹)	τ (fs)	θ (cm ⁻¹)	M (Å)	λ_{int} (cm ⁻¹)	λ_S (cm ⁻¹)	λ (cm ⁻¹)
Best Fit	37830	150	35.4	930	0.85	553	1050	1603
Set 1	37890	190	27.9	1040	0.85	361	970	1331
Set 2	37800	120	44.2	800	0.85	787	1100	1887

References

- (1) Sancar, A. *Chem. Rev.* **2003**, *103* (6), 2203.
- (2) Cashmore, A. R. *Cell* **2003**, *114* (5), 537.
- (3) Massey, V. *Biochem. Soc. Trans.* **2000**, *28* (4), 283.
- (4) Weber, S. *Biochim. Biophys. Acta - Bioenerg.* **2005**, *1707* (1), 1.
- (5) Schleicher, E.; Bittl, R.; Weber, S. *FEBS J.* **2009**, *276* (16), 4290.
- (6) Losi, A. *Photochem. Photobiol.* **2007**, *83* (6), 1283.
- (7) Losi, A.; Gärtner, W. *Photochem. Photobiol.* **2011**, *87* (3), 491.
- (8) Heelis, P. F. *Chem. Soc. Rev.* **1982**, *11* (1), 15.
- (9) Choe, Y.-K.; Nagase, S.; Nishimoto, K. *J. Comput. Chem.* **2007**, *28* (4), 727.
- (10) Chosrowjan, H.; Taniguchi, S.; Mataga, N.; Tanaka, F.; Visser, A. J. W. G. *Chem. Phys. Lett.* **2003**, *378* (3–4), 354.
- (11) Stanley, R. J.; MacFarlane, A. W. I. *J. Phys. Chem. A* **2000**, *104* (30), 6899.
- (12) Van den Berg, P. A. W.; Feenstra, K. A.; Mark, A. E.; Berendsen, H. J. C.; Visser, A. J. W. G. *J. Phys. Chem. B* **2002**, *106* (34), 8858.
- (13) Kao, Y.; Saxena, C.; He, T.; Guo, L.; Wang, L.; Sancar, A.; Zhong, D. *J. Am. Chem. Soc.* **2008**, *130* (39), 13132.
- (14) Barrio, J. R.; Tolman, G. L.; Leonard, N. J.; Spencer, R. D.; Weber, G. *Proc Natl Acad Sci U S A.* **1973**, *70* (3), 941.
- (15) Islam, S. D. M.; Susdorf, T.; Penzkofer, A.; Hegemann, P. *Chem. Phys.* **2003**, *295* (2), 137.
- (16) Kondo, M.; Nappa, J.; Ronayne, K. L.; Stelling, A. L.; Tonge, P. J.; Meech, S. R. *J. Phys. Chem. B* **2006**, *110* (41), 20107.
- (17) Li, G.; Glusac, K. D. *J. Phys. Chem. B* **2009**, *113* (27), 9059.
- (18) Brazard, J.; Usman, A.; Lacombat, F.; Ley, C.; Martin, M. M.; Plaza, P. *J. Phys. Chem. A* **2011**, *115* (15), 3251.
- (19) Wolf, M. M. N.; Schumann, C.; Gross, R.; Domratcheva, T.; Diller, R. *J. Phys. Chem. B* **2008**, *112* (42), 13424.
- (20) Weigel, A.; Dobryakov, A.; Klaumünzer, B.; Sajadi, M.; Saalfrank, P.; Ernsting, N. P. *J. Phys. Chem. B* **2011**, *115*, 3656.
- (21) Alexandre, M. T. A.; Domratcheva, T.; Bonetti, C.; Van Wilderen, L. J. G. W.; Van Grondelle, R.; Groot, M. L.; Hellingwerf, K. J.; Kennis, J. T. M. *Biophys. J.* **2009**, *97* (1), 227.
- (22) Bonetti, C.; Mathes, T.; van Stokkum, I. H.; Mullen, K. M.; Groot, M. L.; van Grondelle, R.; Hegemann, P.; Kennis, J. T. *Biophys. J.* **2008**, *95* (10), 4790.
- (23) Copeland, R. A.; Spiro, T. G. *J. Phys. Chem.* **1986**, *90* (25), 6648.
- (24) Lee, S.; Heller, E. J. *J. Chem. Phys.* **1979**, *71* (12), 4777.
- (25) Li, B.; Johnson, A. E.; Mukamel, S.; Myers, A. B. *J. Am. Chem. Soc.* **1994**, *116* (24), 11039.
- (26) Walsh, C.; Fisher, J.; Spencer, R.; Graham, D. W.; Ashton, W. T.; Brown, J. E.; Brown, R. D.; Rogers, E. F. *Biochemistry* **1978**, *17* (10), 1942.
- (27) Myers, A. B.; Mathies, R. A. In *Biological Applications of Raman Spectroscopy: Vol. 2 - Resonance Raman Spectra of Polyenes and Aromatics*; Spiro, T. G., Ed.; John Wiley & Sons Inc: New York, 1987; pp 1–58.

- (28) Lee, C.; Yang, W.; Parr, R. G. *Phys. Rev. B* **1988**, *37* (2), 785.
- (29) Becke, A. D. *J. Chem. Phys.* **1993**, *98* (7), 5648.
- (30) Godbout, N.; Salahub, D. R.; Andzelm, J.; Wimmer, E. *Can. J. Chem.* **1992**, *70* (2), 560.
- (31) Miertuš, S.; Scrocco, E.; Tomasi, J. *Chem. Phys.* **1981**, *55* (1), 117.
- (32) Bauernschmitt, R.; Ahlrichs, R. *Chem. Phys. Lett.* **1996**, *256* (4–5), 454.
- (33) Casida, M. E.; Jamorski, C.; Casida, K. C.; Salahub, D. R. *J. Chem. Phys.* **1998**, *108* (11), 4439.
- (34) Klaumünzer, B.; Kröner, D.; Lischka, H.; Saalfrank, P. *Phys. Chem. Chem. Phys.* **2012**, *14* (24), 8693.
- (35) Hasegawa, J. y.; Bureekaew, S.; Nakatsuji, H. *J. Photochem. Photobiol. A Chem.* **2007**, *189* (2–3), 205.
- (36) Salzmann, S.; Tatchen, J.; Marian, C. M. *J. Photochem. Photobiol. A Chem.* **2008**, *198* (2–3), 221.
- (37) Zenichowski, K.; Gothe, M.; Saalfrank, P. *J. Photochem. Photobiol. A Chem.* **2007**, *190* (2–3), 290.
- (38) Mondal, S.; Puranik, M. *Phys. Chem. Chem. Phys.* **2017**, *19*, 20224.
- (39) Varsano, D.; Di Felice, R.; Marques, M. A. L.; Rubio, A. *J. Phys. Chem. B* **2006**, *110* (14), 7129.
- (40) Fülischer, M. P.; Serrano-Andrés, L.; Roos, B. O. *J. Am. Chem. Soc.* **1997**, *119* (26), 6168.
- (41) Climent, T.; González-Luque, R.; Merchán, M.; Serrano-Andrés, L. *J. Phys. Chem. A* **2006**, *110* (50), 13584.
- (42) Fodor, S. P. A.; Rava, R. P.; Hays, T. R.; Spiro, T. G. *J. Am. Chem. Soc.* **1985**, *107* (26), 1520.
- (43) Fodor, S. P. A.; Spiro, T. G. *J. Am. Chem. Soc.* **1986**, *108* (12), 3198.
- (44) Small, E. W.; Peticolas, W. L. *Biopolymers* **1971**, *10* (1), 69.
- (45) Warburg, O.; Christian, W. *Biochem. Z.* **1938**, *298*, 150.
- (46) Tsibris, J. C. M.; McCormick, D. B.; Wright, L. D. *Biochemistry* **1965**, *4* (3), 504.
- (47) Weber, G. *Biochem. J.* **1950**, *47* (1), 114.
- (48) Zheng, Y.; Dong, J.; Palfey, B. A.; Carey, P. R. *Biochemistry* **1999**, *38* (51), 16727.
- (49) Unno, M.; Sano, R.; Masuda, S.; Ono, T.-A.; Yamauchi, S. *J. Phys. Chem. B* **2005**, *109* (25), 12620.
- (50) Shanmugasundaram, M.; Puranik, M. *Phys. Chem. Chem. Phys.* **2011**, *13* (9), 3851.
- (51) Majoube, M. *J. Raman Spectrosc.* **1985**, *16* (2), 98.
- (52) Dhaouadi, Z.; Ghomi, M.; Mojzes, P. *J. Phys. Chem.* **1993**, *97*, 1074.
- (53) Oladepo, S. A.; Loppnow, G. R. *J. Phys. Chem. B* **2011**, *115* (19), 6149.
- (54) Mondal, S.; Puranik, M. *J. Phys. Chem. B* **2017**.
- (55) Vajda, S.; Jimenez, R.; Rosenthal, S. J.; Fidler, V.; Fleming, G. R.; Castner, E. W. *J. Chem. Soc. Trans.* **1995**, *91* (5), 867.
- (56) Jimenez, R.; Fleming, G. R.; Kumar, P. V.; Maroncelli, M. *Nature* **1994**, *369* (6480), 471.
- (57) Jarzba, W.; Walker, G. C.; Johnson, A. E.; Kahlow, M. A.; Barbara, P. F. *J. Phys. Chem.* **1988**, *92* (20), 7039.
- (58) Milán-Garcés, E. A.; Kaptan, S.; Puranik, M. *Biophys. J.* **2013**, *105* (1), 211.

- (59) Mondal, S.; Puranik, M. *Phys. Chem. Chem. Phys.* **2016**.
- (60) Jimenez, R.; Case, D. A.; Romesberg, F. E. *J. Phys. Chem. B* **2002**, *106* (5), 1090.
- (61) Barnett, R. B.; Landman, U.; Nitzan, A. *J. Chem. Phys.* **1989**, *90* (8), 4413.
- (62) Muino, P. L.; Callis, P. R. *J. Chem. Phys.* **1994**, *100* (6), 4093.
- (63) Maroncelli, M.; Fleming, G. R. *J. Chem. Phys.* **1988**, *89* (8), 5044.
- (64) El-Yazbi, A. F.; Palech, A.; Loppnow, G. R. *J. Phys. Chem. A* **2011**, *115* (38), 10445.

Chapter 6: Initial Excited State Dynamics of Lumichrome (LC) upon Ultraviolet Excitation

6.1 Introduction

Lumichrome (LC, 7,8-dimethylalloxazine, Fig. 6.1(a)), a prominent member of alloxazine family, is the product formed by photodecomposition of biologically relevant isoalloxazine molecules, specially flavins (LC, RF, FMN and FAD).¹⁻³ Although alloxazines and isoalloxazines are structurally very closely related compounds, they exhibit a distinctly altered photophysical and photochemical properties. Notably, flavins have higher fluorescence intensity and longer excited state lifetime compare to the alloxazine molecules due to their slower radiationless relaxation in the excited state.⁴ The photophysics of LC and other substituted alloxazines have drawn much attention recently because of their essential roles in several biological systems.⁵⁻⁹ the photosensitizing ability of LC to generate singlet oxygen through biochemical activity triggers the oxidation of various biological system like enzymes, proteins and nucleic acids.^{10,11} It has been reported that LC may be used to inhibit flavin reductase in living *Escherichia coli* cells, the riboflavin uptake by human-derived liver cells Hep G2, colonic epithelial NCM460 cells and Caco-2 human intestinal epithelial cells.^{5,7} LC is also known to be used in the photodegradation of polyamidehydroxyurethane polymers in aqueous solution,¹¹ polymerization of 2-hydroxyethyl methacrylate^{12,13} and as an optical transistor device¹⁴.

Photophysical properties of isoalloxazine molecules in their first singlet excited states are well characterized¹⁵⁻²¹ whereas the photophysics of LC and other alloxazine molecules are fairly understood. The experimental absorption spectrum of LC in aqueous solution is shown in Fig 6.1(b). The longest wavelength absorption band having a maximum at 353 nm along with a shoulder at 385 nm are assigned to two independent optically bright $\pi\pi^*$ transitions which are associated with two closely spaced optically dark $n\pi^*$ transitions.^{4,22-24} Experimentally, the overlap of each pair shows up as a broad band in solution. An internal conversion (IC) is expected between the first optically dark $^1n\pi^*$ state and optically bright $^1\pi\pi^*$ state, which may result a substantial radiationless decay of the $^1\pi\pi^*$ population to the ground state and results in the quenching of fluorescence.²²⁻²⁴

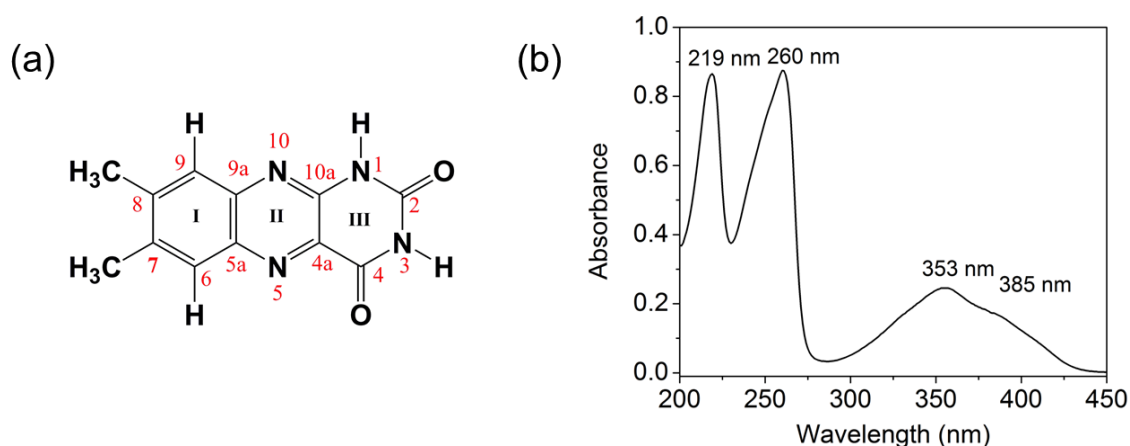


Fig. 6.1 (a) Structure of LC with conventional atom numbering. (b) Experimental absorption spectrum of 4.8×10^{-5} M LC in pH7 phosphate buffer labeled with the λ_{\max} values.

The excited state proton transfer process from N1 atom to N10 atom of LC and other alloxazine molecules to form an isoalloxazine type structure are extensively studied using experimental and theoretical methods.^{4,25–33} This phototautomerization process in the excited state was shown to be promoted by intermolecular hydrogen bonding with acetic acid and pyridine derivatives.^{4,25–27,31,32} No phototautomerization was observed in neutral aqueous solution.^{34–36} It was also reported that solvent hydrogen bonding plays a significant role in the photophysics of LC.^{4,33} In polar protic solvents, the absorption and emission band maxima of LC were found to undergo redshifts and fluorescence quantum yield increases, if compared to polar aprotic solvents.⁴

Though these studies in the lower energy excited states are exceedingly valuable, it is important to know the excited state properties within the Ultraviolet (UV) region of spectrum to understand the overall photophysics of LC. LC has strong absorption bands in the UV regions with maxima at about 260 and 220 nm (Fig 6.1 (b)). Similar to other flavin molecules, LC absorbs light more efficiently in the UV regions rather than the near-UV regions because of higher absorption cross sections in former regions. Till date, no study is being carried out on the dynamics of LC molecule upon photoexcitation to an excited state in UV-region of absorption. Herein as a series of studies on flavin molecules we have investigated the initial excited state structural dynamics of LC molecule within its 260 nm absorption band.

Resonance Raman (RR) spectroscopy is the only experimental technique which can probe the vibrational mode-specific instantaneous structural dynamics upon photoexcitation to an electronic excited state. Raman frequencies contain information of electronic ground state of a molecule. Additionally, when Raman excitation wavelength is in resonance with an electronic excited state, i.e. RR spectroscopy, Raman intensities encode information of the resonant excited state. Intensity of a RR band is proportional to the slope at the excited state potential energy surface along that vibrational normal coordinate. So, RR intensity is also proportional to the structural distortion happens in the electronic excited state with respect to the ground state structure and thus RR intensity analysis extracts the conformational distortion along each normal coordinates within tens of femtoseconds of photoexcitation. In solution, the line shape of the Raman excitation profile (REP), i.e. excitation wavelength dependence of intensities of RR vibrational bands, are also influenced by the solvation dynamics on the ultrafast timescale. Through comprehensive measurement and modeling of REPs, it is possible to extract the excited state parameters related to instantaneous structural distortions following photoexcitation.

We have applied Lee and Heller's time dependent wave-packet propagation theory³⁷ to simulate the experimental REPs and absorption spectrum of LC in a self-consistent manner. We determine the structural distortions in terms of changes in internal coordinates of the electronic ground state of LC following photoexcitation to the excited state at 260 nm. Total internal reorganization energies measured was distributed into each Raman active modes. Brownian oscillator model of Mukamel and coworkers³⁸ was used to incorporate the effect of surrounding solvent molecules on the initial excited state dynamics. Total line-width of REPs can be partitioned into two broadening components: dynamic homogeneous and static inhomogeneous effects through simultaneous modeling of REPs of multiple modes and absorption spectrum.

6.2 Experimental Methods

6.2.1 Sample Preparation

LC ($\geq 99\%$ HPLC pure) was purchased from Sigma Chemicals Co. and used as supplied. The sample concentration for Raman experiments was 350 μM . All samples were prepared in 50 mM phosphate buffer. Concentrations of LC sample solutions were determined spectrophotometrically from the published molar extinction coefficients.²⁵ 250 mM sodium

sulfate (Na_2SO_4) was used as an internal standard. UV/Vis absorption spectra were measured using Perkin-Elmer (lambda 45) absorption spectrometer at pH 7 in phosphate buffer.

6.2.2 UVRR Spectroscopy

UVRR Spectra of LC were obtained by using a tunable Ti: sapphire laser with Raman excitations between 257 to 275 nm and the experimental set-up has been described in experimental method section in chapter 2. The UVRR spectra of LC were recorded at nine excitation wavelengths of 257.6, 259.1, 262, 264, 265.9, 269, 271.1, 272.7 and 274.8 nm. For Raman experiments, 400 μL sample solutions were illuminated by a laser excitation of power less than 500 μW . The average width of each Raman band was taken and it was decided by deconvoluting the UVRR spectra using Lorentzian fit in each excitation wavelengths independently.

6.2.3 UVRR Cross-section Determination

The method of UVRR cross section determination has been described in detail in method chapter. The depolarization ratios of Raman bands of LC are determined using the same experimental technique as described earlier. The depolarization ratio of all the Raman bands was obtained to be one-third (0.33) except for the band at 617 and 1580 cm^{-1} (Table 6.1). The depolarization ratios for low intense modes of LC are difficult to measure due to the weak signal to noise ratio of the depolarized spectrum. So, it was assumed that the depolarization ratios for these bands are also one third.

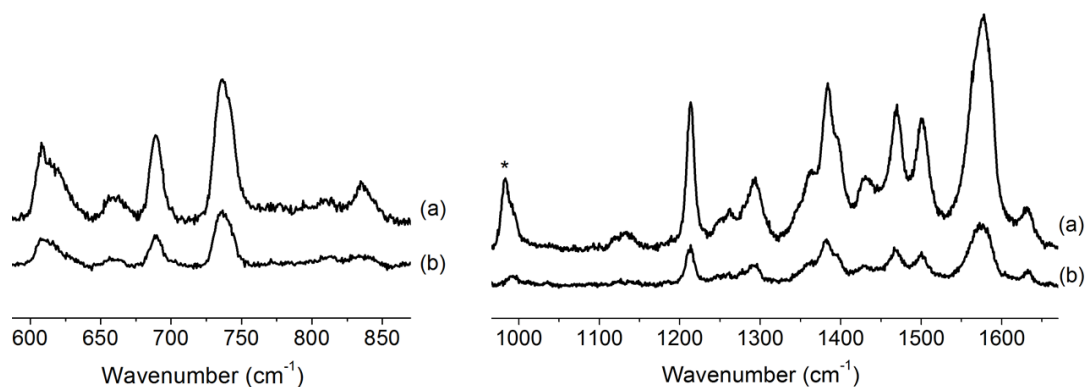


Fig. 6.2 (a) Polarized and (b) depolarized spectra of 350 μM LC in high (right) and low (left) wavenumber region obtained at 260 nm excitation wavelength. The internal standard band is marked with an asterisk (*).

Table 6.1. Depolarization ratios of UVRR bands of LC obtained at 260 nm excitation

Raman band (cm ⁻¹)	Depolarization ratio
608	0.30
617	0.43
661	0.27
689	0.38
738	0.36
810	0.28
836	0.34
991	0.32
1214	0.28
1260	0.34
1292	0.26
1361	0.26
1383	0.32
1427	0.26
1468	0.29
1500	0.23
1567	0.35
1581	0.15
1630	0.28

6.2.4 Computational Method - Simulation of Experimental REP and Absorption Spectrum

We have used time-dependent wave packet propagation theory to simulate the experimental REP and absorption spectrum in a self-consistent manner described in detail in chapter 2. Initial parameters for the simulation were obtained in the similar way as that obtained for previous studies.

6.2.5 DFT Calculations

All quantum chemical calculations on LC molecule were carried out using density functional theory (DFT) using the software Gaussian09. The ground state structure of the molecule was optimized using B3LYP hybrid functional^{39,40} and TZVP⁴¹ basis set. Polarizable continuum model (PCM)⁴² was applied to take into account the dielectric environment of bulk water. The coordinates of the optimized ground state structure are given in Table 6.2. The frequency calculation was done on the optimized structure. To assign the experimental UVRR modes, the

deuterium exchange calculation was also performed after replacing the N1-H and N3-H proton by the mass of deuterium (D). The calculated frequencies were compared with the recorded UVRR spectra of LC in H₂O and D₂O for the assignment of vibrational modes. No scaling factor was used for the calculated frequencies.

To calculate the excitation energies and molecular orbitals (MOs) involved in electronic transitions, TD-DFT calculations were done by using B3LYP method in conjunction with the same TZVP basis set and in PCM solvent model.⁴² The absorption spectrum was calculated from the vertical excitation energies obtained from TDDFT calculation and by taking the fixed Gaussian band width of 2500 cm⁻¹. The visualization of the optimized structure, molecular orbitals (MOs) and vibrational modes were performed using Chemcraft v 1.6 software.

Table 6.2. Coordinates of the optimized ground state structure of LC using B3LYP/TZVP/PCM method

Atom no.	Atom	X	Y	Z	Atom no.	Atom	X	Y	Z
1	C	-3.382035000	0.661877000	0.000053000	15	N	2.532185000	-1.436626000	-0.000179000
2	C	-2.188738000	1.339695000	-0.000038000	16	N	3.733254000	0.553310000	-0.000046000
3	C	-0.950201000	0.654813000	-0.000122000	17	C	-4.672764000	-1.535258000	0.000295000
4	C	-0.945140000	-0.776079000	-0.000144000	18	H	-5.276363000	-1.286830000	-0.876602000
5	C	-2.179634000	-1.457969000	-0.000022000	19	H	-4.497499000	-2.610041000	-0.000390000
6	C	-3.375239000	-0.776803000	0.000071000	20	H	-5.275387000	-1.287833000	0.878162000
7	C	1.325328000	-0.763053000	-0.000295000	21	C	-4.684980000	1.413650000	0.000062000
8	C	1.328552000	0.661610000	-0.000295000	22	H	-5.287318000	1.166874000	-0.878128000
9	C	2.624190000	1.388621000	-0.000732000	23	H	-5.287891000	1.165967000	0.877590000
10	C	3.766405000	-0.836839000	0.000072000	24	H	-4.512403000	2.489082000	0.000653000
11	H	-2.164922000	2.422506000	-0.000032000	25	O	4.812244000	-1.459631000	0.000517000
12	H	-2.161378000	-2.540723000	-0.000018000	26	O	2.745932000	2.598057000	0.000637000
13	N	0.219614000	-1.468583000	-0.000223000	27	H	2.513143000	-2.448128000	-0.000077000
14	N	0.207904000	1.347699000	-0.000165000	28	H	4.639449000	1.005541000	0.000473000

6.3 Results and Discussion

6.3.1 Electronic Structure

The experimental absorption spectrum of LC in aqueous solution (Fig 6.1(b)) shows two absorption bands in the UV regions having maxima at around 260 and 218 nm. These two absorption bands are more intense than the longer wavelength bands. The absorption band at 260 nm is not symmetric and a small shoulder can be seen in its high energy site. It was observed that in less polar solvents (Ethanol, Dioxane, Dioxane-cyclohexane mixture) this band splits into two with a new peak at 248-250 nm.^{4,25} Alloxazine and its methyl derivatives also exhibit similar feature for the band at around 260 nm which separates into two bands in methanol.⁴³ This kind of feature indicates that more than one electronic transition exists within the 260 nm absorption band.

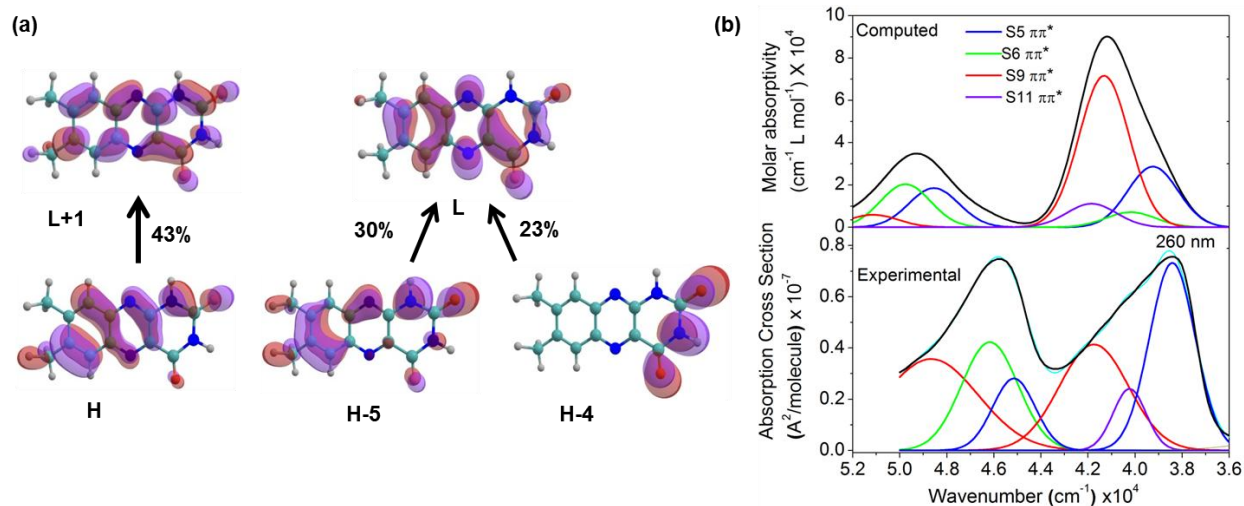


Fig. 6.3 (a) Computed orbitals of LC involved in the electronic transition observed in excitation within the third $^1\pi\pi^*$ excited state. H and L stand for HOMO and LUMO respectively; (b) theoretical absorption spectrum (above) was computed using TD-B3LYP/TZVP//PCM method on LC molecule. Computed band positions are depicted with a Gaussian line shape of fixed line width (2500 cm^{-1}) and deconvoluted experimental absorption (below) of LC labeled with the λ_{max} .

The first two experimental bands have been well reproduced using diverse theoretical methods in the gas phase and different solvents.^{4,22–24,31,33,35,44–48} However, the agreement between the theoretical and experimental transition energies is poor in the UV region. To calculate the nature of MOs involved in the transitions at around 260 nm, we have calculated the excitation spectrum using TD-B3LYP/TZVP/PCM method. Table 6.3 compiles the calculated vertical transition energies and corresponding orbital contributions compared with the recent

theoretical and experimental results. The calculated energies for the first two absorption bands are close to the reported results by DFT/MRCI/COSMO,²² TD-B3LYP/6-311++G (d, p)³³ and TD-B3LYP/6-31G*/MM computations,²³ whereas CASPT2 results²³ are little bit higher in energies.

Table 6.3. Vertical singlet excitation energies, ΔE_{vert} , in nm (eV in paranthesis), oscillator strengths (f) and major orbital contribution for each transition of oxidized LC molecule by TD-B3LYP/TZVP//PCM method and comparison with published computed and experimental transition energies are given

LC ^a					LC	Alloxazine	LC (Experimental)	
State	Type	Major orbital contribution (%) ^b	ΔE_{vert} in nm (eV)	f	ΔE_{vert} in eV	ΔE_{vert} in eV	ΔE_{exp} (λ_{max}) in nm (eV)	ϵ (l mol ⁻¹ cm ⁻¹) ^g
S1	¹ $\pi\pi^*$	H→L (+94%)	376.4 (3.29)	0.0665	3.23 ^c , 3.23 (0.0626) ^d	3.41 ^e , 3.57 ^{e''} , 3.53 ^{e'''}	385 ^f (3.22)	4400
S2	¹ $n\pi^*$	H-2→L (+97%)	350.5 (3.54)	0.0017	3.72 ^c , 3.53 (0.0019) ^d	3.48 ^e , 3.90 ^{e''} , 3.35 ^{e'''}		
S3	¹ $\pi\pi^*$	H-1→L (+89%)	329.9 (3.76)	0.3318	3.66 ^c , 3.70 (0.3398) ^d		353 ^f (3.51)	6000
S4	¹ $n\pi^*$	H-3→L (+90%)	295.4 (4.20)	0.0001	4.18 (0.0001) ^d			
S5	¹$\pi\pi^*$	H→L+1 (+43%) H-5→L (+30%) H-4→L (23%)	254.8 (4.87)	0.3302			262^g	19800
S6	¹ $\pi\pi^*$	H-4→L (+53%) H-5→L (+22%) H-1→L+1 (21%)	248.8 (4.98)	0.0821				
S7	¹ $n\pi^*$	H-2→L+1 (+78%)	246.4 (5.03)	0.0001				
S8	¹ $n\pi^*$	H-6→L (+77%)	243.3 (5.10)	0				
S9	¹$\pi\pi^*$	H→L+1 (+42%) H-5→L (40%)	242 (5.12)	0.8237			~ 252^g	17900

^aIn this work. ^bPercentages are calculated as 100x twice the squares of the coefficients in the CI expansion of TDDFT wave functions. H and L stands for highest occupied molecular orbital (HOMO) and lowest unoccupied molecular orbital (LUMO) respectively. ^cDFT/MRCI/COSMO, from ref. 22; ^dTD-B3LYP/6-311++G(d,p)/SCRF-PCM, oscillator strengths in paranthes, from ref.33; ^eTD-B3LYP/6-31G*/MM, ^{e''}MS-CASPT2/6-31G*/MM, ^{e'''}MS-CASPT2/cc-pVTZ/MM, from ref. 23; ^fFrom ref. 4; ^gFrom ref. 25.

Our TDDFT calculation determines four $\pi\pi^*$ transitions at 4.87, 4.98, 5.12 and 5.19 eV within the energy regime of 4.5 to 5.2 eV. Among them, the two transitions at 4.87 and 5.12 eV with oscillator strengths of 0.3302 and 0.8237 respectively are stronger than the other two transitions with low oscillator strengths (see Table 6.3). We have discussed in the preceding section that the 260 nm absorption band splits into two bands in less polar solvents. The

experimental band at around 260 nm can be assigned to the third ${}^1\pi\pi^*$ transition obtained at 4.87 eV (254.8 nm). The orbital contributions for this transition along with the computed absorption spectrum are shown in Fig 6.3 (a). This transition is dominated by a contribution of three mixed $\pi\pi^*$ excitations: $H\rightarrow L+1$, $H-5\rightarrow L$ and $H-4\rightarrow L$. The absorption band at around 248-250 nm is assigned to the fifth ${}^1\pi\pi^*$ transition calculated at 5.12 eV (242 nm). Two $\pi\pi^*$ transitions, $H\rightarrow L+1$ and $H-5\rightarrow L$ contribute dominantly in this transition. The other two weak transitions with low oscillator strengths may be hidden under the two neighboring strong $\pi\pi^*$ transitions in experiments. The deviation obtained here between the calculated transition energies and experimental λ_{\max} values are within the average accuracy (~ 0.2 eV) achieved in transition energy calculations using TDDFT method.⁴⁹

6.3.2 UVRR Spectra

UVRR spectrum of LC obtained with a laser excitation of 262 nm wavelength is shown in Fig. 6.4. We find 22 UVRR bands of LC between the spectral region of 600 to 1750 cm^{-1} . The Raman band positions are in good agreement within the experimental error with the FT-Raman and SERS spectra of LC (Table 6.4).^{50,51} The UVRR spectrum of LC is completely different compared to the UVRR spectrum of isoalloxazine molecules (LF, RF, FMN, FAD) obtained at an excitation wavelength of 263 nm. The most intense band observed for LC is the overlapping band of two at 1567 and 1581 cm^{-1} . We have seen another doublet in the LC spectrum at 608 and 617 cm^{-1} .

Normal mode assignments of all the observed Raman bands using B3LYP functional in conjunction with TZVP basis set in PCM solvent model are described in Table 6.5. It is difficult to assign the LC bands by comparing the experimental H_2O and D_2O spectra, because LC bands show large shifts upon deuterium (D) exchange at N1-H and N3-H positions. So, we have done the assignment based on the theoretical frequencies in H_2O and D_2O and followed the assignment done for LC in ref. 50. Full assignment table was given in Appendix II.

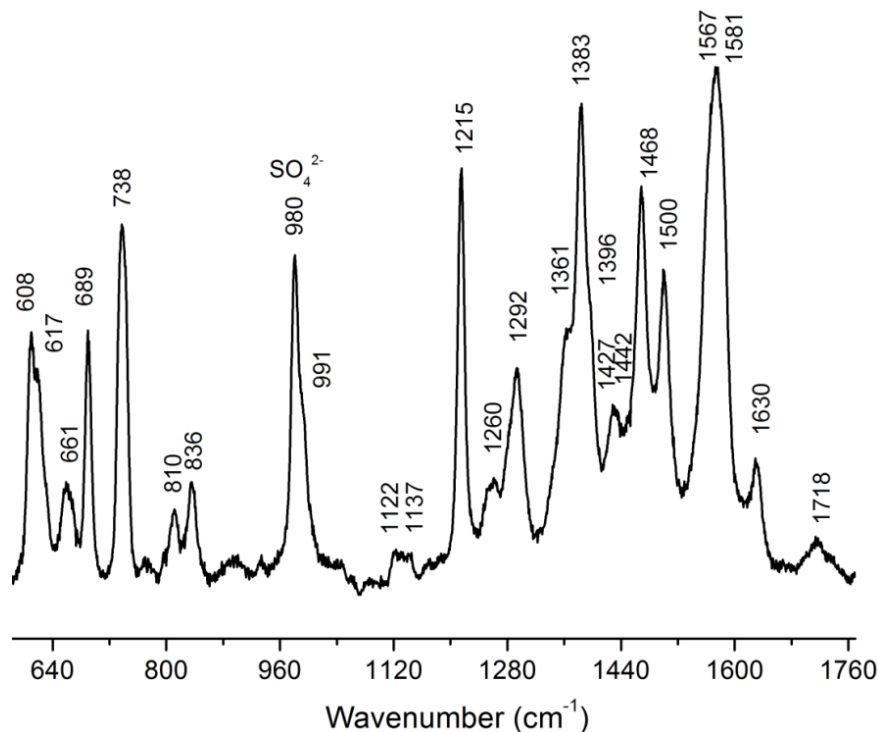


Fig. 6.4 UVRR spectrum of 350 μM LC obtained at the Raman excitation wavelength of 262 nm. 980 cm^{-1} band is the SO_4^{2-} band which was added as an internal standard.

The spectra of LC acquired using 6 different excitation wavelengths within the red energy site of the absorption band at 260 nm are compared in Fig. 6.5. The intensity of Raman bands of each spectrum was normalized against the intensity of internal standard sulfate band at 980 cm^{-1} . We observe that the intensity of vibrational bands decreases by moving towards higher excitation wavelengths. The frequency and the relative intensity of Raman bands remain unchanged as we tune the excitation wavelengths across the red energy region of 260 nm absorption band, indicating that the enhancement of the Raman bands arises from a single electronic transition, i.e., the third $^1\pi\pi^*$ transition computed using TDDFT. **The depolarization ratios measured at 260 nm excitation for the Raman modes are close to 0.33 which too supports the contribution from a single electronic transition.**

6.3.3 Simulation of Absorption and Experimental REPs

Experimental REPs of each Raman bands of LC constructed using Eq. 2.30 with the normalized UVRR spectra, simulated REPs and the absorption band at 260 nm are shown in Fig. 6.6 and Fig. 6.7. An excellent agreement between the simulated and experimental REPs was achieved

Table 6.4 Experimental UVRR bands of LC in comparison with the FT-Raman, FT-IR and SERS spectra

UVRR Bands (cm ⁻¹)	FT Raman ^a (cm ⁻¹)	FT-IR ^a (cm ⁻¹)	SERS ^b (cm ⁻¹)
no	1723	1725	no
1717	1718	sh	no
no	1697	1700	no
no	vw	1641	no
1630	1620	1623	1629
no	vw	1598	no
1580	1576	1578	1573
1567	1558	1561	1548
1500	1496	vw	1525
no	1484	1484	1481
no	sh	1471	sh
1468	1458	1461	1460
sh	1441	1447	no
1427	sh	1420	no
1396	1386	1384	1377
1383	1380	vw	1377
1361	1356	1357	1348
no	vw	1339	1322
1292	1288	vw	no
no	1279	1281	no
1260	1261	1261	no
sh	sh	1253	no
1215	1213	1214	1212
no	vw	1185	1185
1137	vw	1144	1155
no	1026	1024	no
991	vw	1006	no

^asee ref. 53; ^bsee ref. 54.

using self-consistent simulation. The parameters corresponding to the best fit to the Experimental REPs are tabulated in Table 6.6. The dimensionless displacements, Δ , obtained from the best fit and the internal reorganization energies measured using Eq. 2.21b, are listed in Table 6.5.

We find that the maxima of simulated REPs for some Raman bands are shifted with respect to the experimental REPs. The simulated absorption spectrum shows discrepancy at the blue edge of the experimental spectrum. This is because of the method used in our simulation incorporates a single electronic excited state and does not consider the interference coming from

the nearby electronic states. We have already discussed that there exists a strong electronic transition at the blue energy site of the third ${}^1\pi\pi^*$ electronic state (see Fig 6.3(b)). It is also observed that at shorter excitation wavelengths, the simulated REPs of some modes, in particular for the bands at 1630, 1360, 1291, 991, 617 and 608 cm^{-1} , do not agree well with the experimental REPs. The disagreement between the simulated and experimental REPs at shorter Raman excitations is due to the coupling of those modes with the higher energy electronic state situated at around 252 nm. The Raman band at 617 cm^{-1} is the most affected one among them from the interference of higher energy transition, consistent with the high depolarization ratio (0.43) obtained for that band. This kind of effect at shorter excitation wavelengths from nearby electronic states was previously observed in the REPs for the bands at 1585 and 1383 cm^{-1} of LF and RF molecules. However, we use a global fit to all of the observed UVRR modes using a

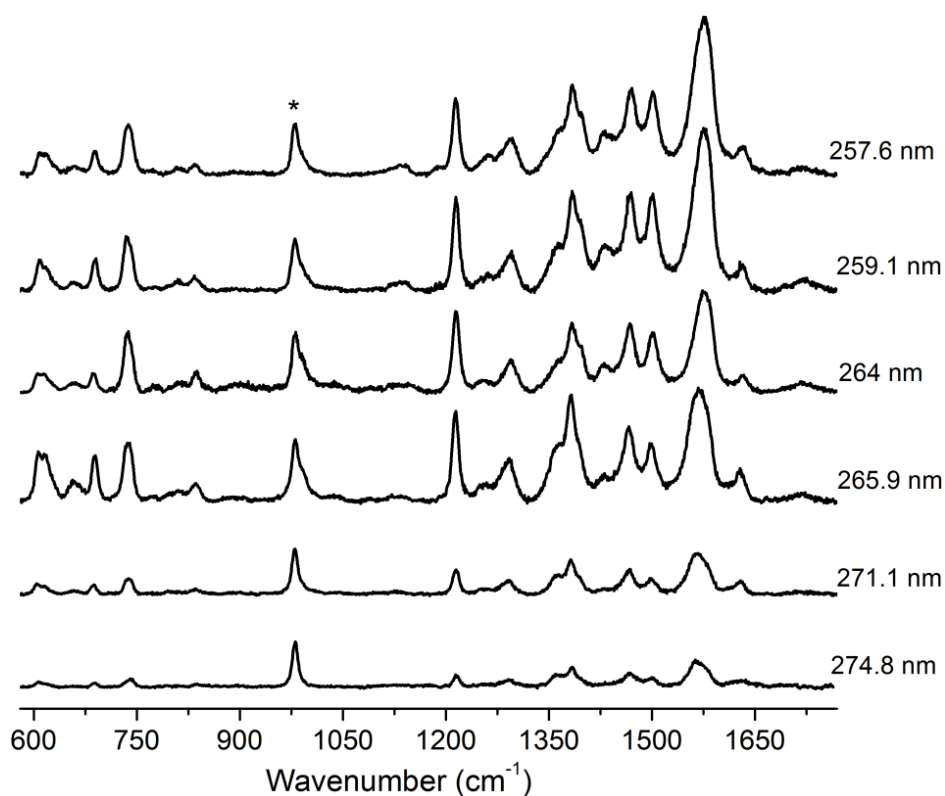


Fig. 6.5 UVRR spectra of 350 μM LC obtained at six different excitation wavelengths within the 260 nm absorption band. The Raman band of internal standard SO_4^{2-} is marked with an asterisk (*). All the spectra are normalized against the intensity of the internal standard band. Change in intensity of Raman bands is visible with increasing excitation wavelengths.

Table 6.5 Assignments of all observed UVRR bands of LC with the dimensionless displacements and mode specific internal reorganization energies.

Experimental wavenumber (cm ⁻¹)	Computed wavenumber (cm ⁻¹)	PED (%)	Dimensionless displacements (Δ)	Mode specific internal reorganization energies (cm ⁻¹)
1718	1756	str C2O2(42) + str C4O4(36)	0.117	12
1630	1666	- str C7C6(27) + str C8C9(23)	0.108	9
1580	1600	str N10C10a(21) - str C4aC10a(12)	0.21	35
1567	1583	- str N5C4a(11) - str N10C9a(11) + str C4aC10a(14)	0.285	64
1500	1523	str N10C9a(13)	0.195	29
1468	1467	str C7C6(13) + str C4aC10a(11)	0.225	37
1443	1439	- str C2OC2(10) - str N5C4a(12) + be N1H(13) + be N3H(20)	0.117	10
1428	1420	be N3H (35)	0.108	8
1397	1394	- str C8C9(14) - str N1C2(14)	0.111	9
1383	1372	- str N10C10a(15) + str C9C9a(17)	0.222	34
1361	1340	str N5C4a(15) - str N1C10a(14) + be N1H (20)	0.18	22
1293	1291	- str N5C5a(12) + str N10C9a(14) - be C8C9C9a(12)	0.177	20
1261	1283	- be C6H (27) + be C9H (32)	0.12	9
1215	1234	str N10C10a(11) + str N3C4(14) - str N3C2(10)	0.183	20
1137	1146	- str C8-Methyl(20) + str C7-Methyl(17)	0.057	2
1122	1138	- str C4aC10a(10) + str N3C4(18)	0.078	3
993	1041	- tors (H-C-H) 8-Methyl(26) - tors (H-C-H) 7-Methyl(30)	0.15	11
836	842	be C9C9aN10(10) - be C2N1C10a(10)	0.108	5
805	801	str C7Me (12) + be N1C10aN10(14)	0.102	4
739	744	be C9aN10C10a(10) - be N10C10aC4a(11) - be N5C4aC10a(11) + be C9C9aN10(10)	0.228	19
689	687	be C9aN10C10a(14) + be C5aN5C4a(11)	0.156	8
659	655	- be O2C2N3(27) + be O4C4N3(18)	0.129	5
618	611	- be C8C9C9a(12) + be C5aN5C4a(16)	0.186	11
608	601	tors N1H (19) + out N1C4aN10C10a(35)	0.135	6

^aComputed using B3LYP/TZVP/PCM level of theory; ^busing VEDA 4.0; str: stretching, be: bending, tors: torsional vibrations.

common set of parameters; it is acceptable that these effects will have a little influence on the excited state parameters derived for the absorption band at 260 nm.

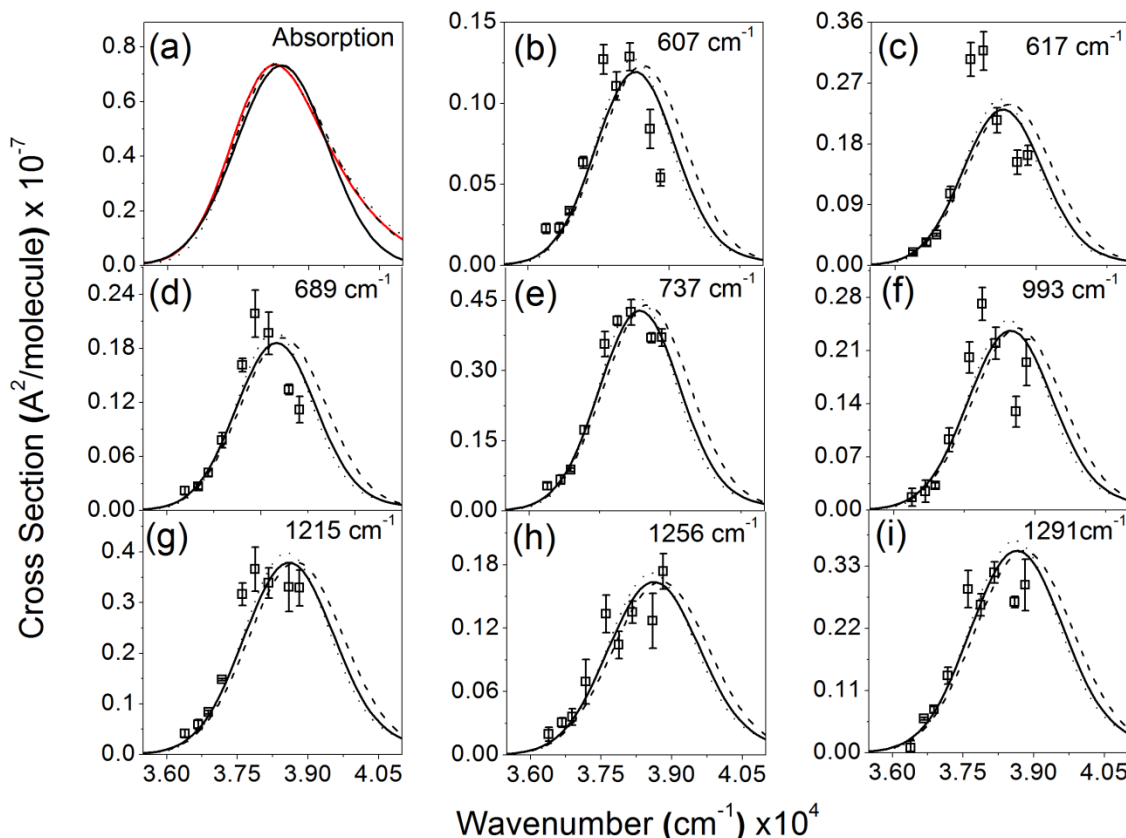


Fig. 6.6 Experimental and simulated Raman excitation profiles and absorption cross section of LC obtained using nine different excitation wavelengths within the third computationally found ${}^1\pi\pi^*$ excited state. (a) Experimental (solid), deconvoluted (red) and simulated absorption (dash) spectrum. (b-i) Raman excitation profiles of eight UVRR modes of LC at nine different excitation wavelengths. The best fit (solid) was obtained by using the parameters of Table 6.3. Set 1 (dash) and Set 2 (dot) parameters are obtained by decreasing and increasing the best fit delta values by 10% respectively.

The dimensionless displacements, Δ s, obtained from the best fit to the REPs are used to determine the structural changes in the excited state in terms of the internal coordinates of ground state using Eq. 2.25. Raman band intensity is proportional to Δ^2 , rather than Δ . That is why the simulated REP values do not depend on the sign of Δ . However, this sign is necessary as expected from Eq. 6 to calculate the change in the excited state geometry in terms of the internal coordinates of the molecule. Here the signs of the displacements were taken from the signs of the gradients computed at the Franck-Condon region of the relevant potential energy surface using TDDFT calculations. Major changes in the internal coordinates following photoexcitation to the 260 nm excited state of LC are listed in Table 6.7.

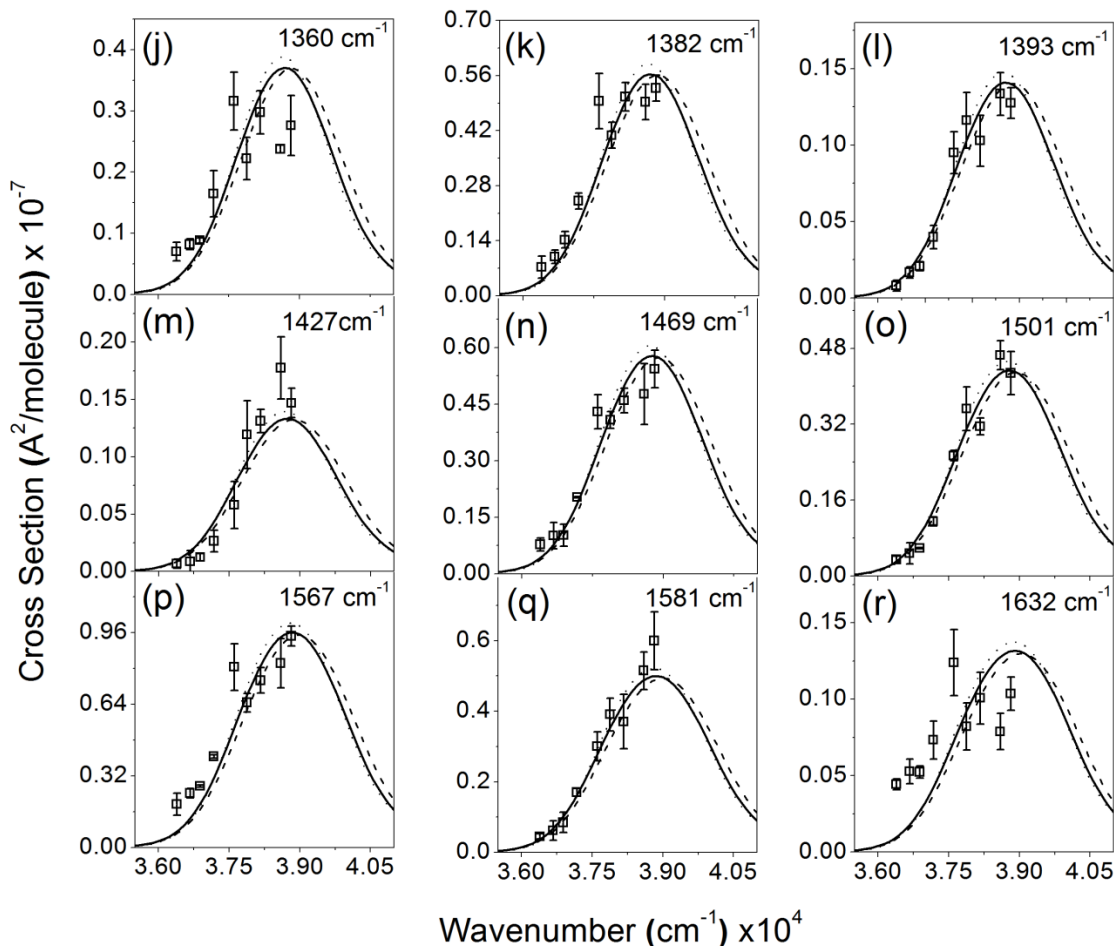


Fig. 6.7 Experimental and simulated Raman excitation profiles (j-r) of other nine UVRR modes of LC obtained by using the same set of parameters as in Fig. 6.6.

Table 6.6 Parameters used in self-consistent fit of REP and absorption spectra for LC

	E_0 (cm^{-1})	Λ (cm^{-1})	τ (fs)	θ (cm^{-1})	M (\AA)	λ_{int} (cm^{-1})	λ_s (cm^{-1})	λ (cm^{-1})
Best Fit	38210	230	23.1	730	0.84	393	470	863
Set 1	38250	190	27.9	790	0.84	318	420	738
Set 2	38160	260	20.4	655	0.84	475	490	965

The initial excited state structural changes in response to instantaneous charge redistribution upon photoexcitation were observed over all along the alloxazine ring system. **The changes in the bond lengths were found to be less than 0.05 \AA .** In ring I, the major changes were observed through elongation in the bonds of C5a-C6 (0.023), C5a-C9a (0.13) and a contraction in the bond of C9-C9a (-0.046). The outer ring coordinates, C7-Me (0.016) and C8-Me (-0.037) bonds follow elongation and contraction respectively. In Ring II, elongation in the

bonds of N5-C5a (0.017), N10-C10a (0.042) and C4a-N5 (0.009) was detected. The distortions in Ring III were found through elongation in the C4-C4a (0.015) and C2-N3 (0.011) bonds and contraction in the N1-C2 (-0.029) and N3-C4 (-0.007) bonds. Among the two carbonyl stretching frequencies, C4=O (0.04) bond gets elongated whereas contraction was seen in the C2=O (-0.029) bond.

Table 6.7 Internal coordinate changes of LC structure following excitation to the third $^1\pi\pi^*$ excited state

Internal coordinates	Internal coordinates in ground state (Å)	Internal coordinate changes (Å)
C6-C7	1.3724	0.002
C7-C8	1.4387	0.004
C7-CH3	1.5043	0.016
C5a-C6	1.4153	0.023
C6-H	1.0831	-0.001
C5a-C9a	1.4309	0.013
N5-C5a	1.3496	0.017
C9-C9a	1.4103	-0.046
C9a-N10	1.3551	-0.004
C8-C9	1.376	-0.006
C9-H	1.0829	-0.002
C8-CH3	1.5029	-0.037
C4a-C10a	1.4247	0.017
N10-C10a	1.3116	0.042
N1-C10a	1.3821	0.004
C4-C4a	1.4857	0.015
C4a-N5	1.314	0.009
N3-C4	1.3884	-0.007
C4=O	1.2155	0.04
N1-C2	1.3722	-0.029
C2-N3	1.3905	0.011
C2=O	1.2172	-0.029
N1-H	1.0117	-0.003
N3-H	1.0128	0.002

In the first singlet $^1\pi\pi^*$ excited state, the deviation for some of the bond lengths relative to the ground state structure was found to be more than 0.05 Å for alloxazine

molecules using MS-CASPT2/CASSCF²³ and DFT/MRCI²² methods in gas phase and in aqueous solutions. For example, the largest deviation was computed for the C6-C7 bond length which changes by more than 0.1 Å using CASSCF/6-31G*/MM method.²³ The C8-C9 and C9-C9a bond length also show deviation of more than 0.5 Å in the first ¹ππ* state at the same level of theory. This is may be due to the greater charge redistribution following excitation in the first ¹ππ* excited state compared to that in the third ¹ππ* excited state.

Comparing the internal coordinate changes between LF and LC, we found that LC experiences a different molecular distortion in the 260 nm excited state as compared to RF and LF in their 266 nm excited state. The C5a-C6 and N5-C5a bonds show contraction for both RF and LF, whereas for LC we find that these two bonds elongate for photoexcited LC. Similarly, lengthening in the C9-C9a and N1-C2 bonds are observed for LF, but for LC the change in these two bond lengths are found to be in opposite directions. For LF and RF, the changes in some of the bond lengths obtained within the isoalloxazine ring are more than 0.05 Å, indicating alloxazines are more photostable than isoalloxazines following UV excitations.

Another feasible way to support our results is to determine the mode specific reorganization energies along each specific mode. The total internal reorganization energy (λ_{int}) obtained over all the observed UVRR modes is 393 cm⁻¹. Nine modes corresponding to the bands at 738 cm⁻¹, 1215 cm⁻¹, 1292 cm⁻¹, 1361 cm⁻¹, 1383 cm⁻¹, 1468 cm⁻¹, 1500 cm⁻¹, 1567 cm⁻¹ and 1581 cm⁻¹ contribute 71% to the total reorganization energy. **The mode compositions obtained from PED (Table 6.5) for those Raman bands indicate that major structural distortions happen within ring stretching coordinates localized in ring II and III. A relatively low value of λ_{int} was determined for LC than that for RF, FMN (594 cm⁻¹) and LF (472 cm⁻¹) molecules at their 260 nm excited state is reasonable that a less relative distortion may happen between ground and excited states upon photoexcitation for the photoproduct LC in comparison to its parent molecules.**

In the simulation, the Δ values which are used to calculate the λ_{int} , are dependent on the width of the absorption band of the resonant electronic state and intensity of UVRR bands. A relatively low value of λ_{int} is expected with a narrow absorption band of the resonant electronic state of LC (FWHM of 2300 cm⁻¹) compared to the other flavin molecules (~ 3200 cm⁻¹) in the

same wavelength region. We have also shown that there are two closely spaced $\pi\pi^*$ excited states exist within the 260 nm absorption band of LC. So, ultrafast population transfer is possible via conical intersections within these two states. This ultrafast state crossing decreases the Resonance Raman cross sections obtained upon excitation within the third $^1\pi\pi^*$ excited state and hence a lower internal reorganization energy. For, other flavin molecules (RF, FMN and LF), there also exist two electronic states in both sides of the absorption band at 266 nm, but the ultrafast population decay might be small compared to the LC excited state. This kind of ultrafast population transfer is observed for Nucleobases, e.g., 9-methyladenine and 6-chloro-guanine.^{52,53}

Photoexcitation results in an instantaneous change in the induced dipole moment of the solute (LC). The second component of reorganization energy parameters from our simulation is the solvent reorganization energy, λ_s , which corresponds to the response of the solvent (water) to that change in the solute (LC). As Raman is a scattering phenomenon which completes within tens of femtoseconds (fs), the solvent reorganization energy determined from Raman intensity analysis corresponds to the inertial response of water. Here we employed the Brownian oscillator spectral density model of Mukamel and Co-workers³⁸ to account for the solute and solvent bath interactions on ultrafast timescale. This model introduces the dynamic solvent response timescale (τ) and solvent reorganization energy (λ_s) as the parameters to include the ultrafast water relaxation process in effect of solute charge redistributions. From our simulations, we find a solvent response timescale of 23.1 fs and solvent reorganization energy of 470 cm^{-1} following excitation to the third $^1\pi\pi^*$ excited state of LC. However, we have shown earlier^{53,54} that the model is not sensitive to the solvent response timescale.

The solvent reorganization energy obtained for LC in the third $\pi\pi^*$ excited state is lower than that obtained for parent flavin molecules (1070 cm^{-1} for LF, 1110 cm^{-1} for RF) within their 266 nm excited state. The amplitude of solvent response is dependent on the magnitude of instantaneous change in the charge distribution and consequent induced dipole moment of the solute. Hence, solvent reorganization energy is expected to be an intrinsic property of the resonant excited state. So the inertial response of water contributes 54% to the total reorganization energy (863 cm^{-1}) obtained from our simulation. The lower value of solvent reorganization energy compare to the isoalloxazine structures indicates a smaller dipole moment in the resonant excited state of LC.

The fastest component of water solvation dynamics in response to an instantaneous change in the charge redistribution is reported to be less than 50 fs by using molecular dynamics simulations,⁵⁵⁻⁵⁸ time-dependent Stokes shift measurements^{59,60} and fluorescence up-conversion experiments^{55,61,62} using different probe molecules. However, the determinations of the fastest water solvation response are beyond the time-resolution of fluorescence emission experiments because of slower vibrational relaxation in fluorescence processes. Nonetheless, time-resolved Stokes shift measurements for Tryptophan and organic dyes found that a fast inertial response of water solvation occurs within tens of femtoseconds.⁵⁹⁻⁶¹ The fastest response of water solvation dynamics derived from our simulation is in the same order as obtained for other flavin molecules. It is expected that the timescale of solvent response is characteristic of the solute molecule rather than the excited electronic state itself. So, this response time will be similar for all other electronic states of LC.

The other components of water solvation response contribute to the inhomogeneous broadening linewidth (θ) in our model. The inhomogeneous broadening arises due to the ensemble site effect of different micro-solvated configurations of solute which remain static within Raman scattering timescale. These static micro-solvated configurations contribute to the distribution of Raman cross sections. **We have required a large inhomogeneous broadening value of 730 cm⁻¹ to achieve the best agreement between simulated and experimental REPs.** The inhomogeneous broadening linewidth determined in the third $\pi\pi^*$ excited state of LC is in the same range as that obtained for RF, FMN (900 cm⁻¹) and LF (750 cm⁻¹) using similar excitation wavelengths. The alloxazine ring can also form hydrogen bonds with the surrounding water molecules through the lone pairs of ring nitrogen (N) and oxygen atoms (O), similar to the isoalloxazine ring. The ability to form hydrogen bonds with solvent molecules produces a number of micro-solvated structures and consequently a high value of inhomogeneous broadening. The other slower components within the 100 fs timescale apart from the micro-solvated structures also contribute to the inhomogeneous broadening value determined from our simulation.

6.4 Conclusion

We have successfully applied the self-consistent simulation of absorption and Resonance Raman cross sections using time-dependent wave packet theory to probe the initial excited state

structural dynamics of LC using UV excitations. **It has been found that major structural distortions happen in ring II and ring III of the alloxazine structure following photoexcitation to the third $\pi\pi^*$ excited state. The homogeneous broadening linewidth determined for LC is lower in comparison to the isoalloxazine molecules within similar excitation wavelengths, whereas the inhomogeneous broadening values obtained are comparable. The fastest response of dynamic water solvation within 23.1 fs timescale was detected due to the inertial response of water.** Our TDDFT calculation results show an existence of a strong $\pi\pi^*$ electronic state in the higher energy site of the theoretically computed third $^1\pi\pi^*$ electronic state within the 260 nm absorption band of LC. So, to get an entire picture of initial excited state dynamics within the absorption band at 260 nm, it is important to explore the dynamics within the higher energy electronic state.

References

- (1) E. Silva, A. M. E. (Eds. . *Flavins: Photochemistry and Photobiology*; Royal Society of Chemistry, London, 2006.
- (2) Holzer, W.; Shirdel, J.; Zirak, P.; Penzkofer, a.; Hegemann, P.; Deutzmann, R.; Hochmuth, E. *Chem. Phys.* **2005**, *308* (1–2), 69.
- (3) Ahmad, I.; Fasihullah, Q.; Vaid, F. H. M. *J. Photochem. Photobiol. B Biol.* **2004**, *75* (1–2), 13.
- (4) Sikorska, E.; Khmelinskii, I. V.; Prukala, W.; Williams, S. L.; Patel, M.; Worrall, D. R.; Bourdelande, J. L.; Koput, J.; Sikorski, M. *J. Phys. Chem. A* **2004**, *108* (9), 1501.
- (5) Said, H. M.; Ortiz, a; Moyer, M. P.; Yanagawa, N. *Am. J. Physiol. Cell Physiol.* **2000**, *278* (2), C270.
- (6) Grininger, M.; Zeth, K.; Oesterheld, D. *J. Mol. Biol.* **2006**, *357* (3), 842.
- (7) CUNNINGHAM, O.; GORE, M. G.; MANTLE, T. J. *Biochem. J.* **2000**, *345* (2), 393.
- (8) Tyagi, A.; Penzkofer, A.; Mathes, T.; Hegemann, P. *J. Photochem. Photobiol. B Biol.* **2010**, *101* (1), 76.
- (9) Fieschi, F.; Nivière, V.; Frier, C.; Décout, J.; Fontecave, M. *J. Biol. Chem.* **1995**, *270* (51), 30392.
- (10) Sikorska, E.; Sikorski, M.; Steer, R. P.; Wilkinson, F.; Worrall, D. R. *J. Chem. Soc. Trans.* **1998**, *94* (16), 2347.
- (11) Onu, A.; Palamaru, M.; Tutovan, E.; Ciobanu, C. *Polym. Degrad. Stab.* **1998**, *60* (2–3), 465.
- (12) Bertolotti, S. G.; Previtali, C. M.; Rufs, A. M.; Encinas, M. V. *Macromolecules* **1999**, *32* (9), 2920.
- (13) Bairi, P.; Roy, B.; Nandi, A. K. *J. Phys. Chem. B* **2010**, *114* (35), 11454.
- (14) Zen, Y. H.; Wang, C. M. *J. Chem. Soc. Chem. Commun.* **1994**, *36* (22), 2625.
- (15) Kao, Y.; Saxena, C.; He, T.; Guo, L.; Wang, L.; Sancar, A.; Zhong, D. *J. Am. Chem. Soc.* **2008**, *130* (39), 13132.
- (16) Dutta Choudhury, S.; Mohanty, J.; Bhasikuttan, A. C.; Pal, H. *J. Phys. Chem. B* **2010**, *114* (33), 10717.
- (17) Radoszkowicz, L.; Huppert, D.; Nachliel, E.; Gutman, M. *J. Phys. Chem. A* **2010**, *114* (2), 1017.
- (18) Wolf, M. M. N.; Schumann, C.; Gross, R.; Domratcheva, T.; Diller, R. *J. Phys. Chem. B* **2008**, *112* (42), 13424.

- (19) Weigel, A.; Dobryakov, A.; Klaumünzer, B.; Sajadi, M.; Saalfrank, P.; Ernsting, N. P. *J. Phys. Chem. B* **2011**, *115*, 3656.
- (20) Van den Berg, P. A. W.; Widengren, J.; Hink, M. A.; Rigler, R.; Visser, A. J. W. G. *Spectrochim. Acta - Part A Mol. Biomol. Spectrosc.* **2001**, *57* (11), 2135.
- (21) Li, G.; Glusac, K. D. *J. Phys. Chem. B* **2009**, *113* (27), 9059.
- (22) Salzmann, S.; Marian, C. M. *Photochem. Photobiol. Sci.* **2009**, *8* (12), 1655.
- (23) Chang, X. P.; Xie, X. Y.; Lin, S. Y.; Cui, G. *J. Phys. Chem. A* **2016**, *120* (31), 6129.
- (24) Sikorska, E.; Khmelinskii, I. V.; Worrall, D. R.; Koput, J.; Sikorski, M. *J. Fluoresc.* **2004**, *14* (1), 57.
- (25) Koziol, J. *Photochem. Photobiol.* **1966**, *5* (1), 41.
- (26) Song, P.; Sun, M.; Koziolowa, A.; Koziol, J. *J. Am. Chem. Soc.* **1974**, *96* (13), 4319.
- (27) Koziolowa, A.; Visser, N. V.; Koziol, J.; Szafran, M. M. *J. Photochem. Photobiol. A Chem.* **1996**, *93* (2–3), 157.
- (28) Koziolowa, A. *Photochem. Photobiol.* **1979**, *29* (3), 459.
- (29) Tyagi, A.; Penzkofer, A. *Photochem. Photobiol.* **2011**, *87* (3), 524.
- (30) Choi, J. Do; Fugate, R. D.; Song, P.-S. *J. Am. Chem. Soc.* **1980**, *102* (16), 5293.
- (31) Sikorska, E.; Khmelinskii, I.; Hoffmann, M.; Machado, I. F.; Ferreira, L. F. V.; Dobek, K.; Karolczak, J.; Krawczyk, A.; Insińska-Rak, M.; Sikorski, M. *J. Phys. Chem. A* **2005**, *109* (51), 11707.
- (32) Sikorska, E.; Khmelinskii, I.; Kubicki, M.; Prukale, W.; Hoffmann, M.; Machado, I. F.; Ferreira, L. F. V.; Karolczak, J.; Worrall, D. R.; Krawczyk, A.; Insińska-Rak, M.; Sikorski, M. *J. Phys. Chem. A* **2006**, *110* (14), 4638.
- (33) Moyon, N. S.; Mitra, S. *J. Phys. Chem. A* **2011**, *115* (12), 2456.
- (34) Sikorski, M.; Sikorska, E.; Koziolowa, A.; Gonzalez Moreno, R.; Bourdelande, J. L.; Steer, R. P.; Wilkinson, F. *J. Photochem. Photobiol. B Biol.* **2001**, *60* (2–3), 114.
- (35) Prukala, D.; Sikorska, E.; Koput, J.; Khmelinskii, I.; Karolczak, J.; Gierszewski, M.; Sikorski, M. *J. Phys. Chem. A* **2012**, *116* (28), 7474.
- (36) Marchena, M.; Gil, M.; Mart??n, C.; Organero, J. A.; Sanchez, F.; Douhal, A. *J. Phys. Chem. B* **2011**, *115* (10), 2424.
- (37) Lee, S.; Heller, E. J. *J. Chem. Phys.* **1979**, *71* (12), 4777.
- (38) Li, B.; Johnson, A. E.; Mukamel, S.; Myers, A. B. *J. Am. Chem. Soc.* **1994**, *116* (24), 11039.
- (39) Lee, C.; Yang, W.; Parr, R. G. *Phys. Rev. B* **1988**, *37* (2), 785.
- (40) Becke, A. D. *J. Chem. Phys.* **1993**, *98* (7), 5648.
- (41) Godbout, N.; Salahub, D. R.; Andzelm, J.; Wimmer, E. *Can. J. Chem.* **1992**, *70* (2), 560.
- (42) Miertuř, S.; Scrocco, E.; Tomasi, J. *J. Chem. Phys.* **1981**, *55* (1), 117.
- (43) Sun, M.; Moore, T. A.; Song, P.-S. *J. Am. Chem. Soc.* **1972**, *94* (5), 1730.
- (44) Insińska-Rak, M.; Sikorska, E.; Bourdelande, J. L.; Khmelinskii, I. V.; Prukala, W.; Dobek, K.; Karolczak, J.; Machado, I. F.; Ferreira, L. F. V.; Komasa, A.; Worrall, D. R.; Sikorski, M. *J. Mol. Struct.* **2006**, *783* (1–3), 184.
- (45) Sikorska, E.; Khmelinskii, I. V.; Williams, S. L.; Worrall, D. R.; Herance, J. R.; Bourdelande, J. L.; Koput, J.; Sikorski, M. *J. Mol. Struct.* **2004**, *697* (1–3), 199.
- (46) Sikorska, E.; Khmelinskii, I. V.; Kubicki, M.; Prukala, W.; Nowacka, G.; Siemiarczuk, A.; Koput, J.; Ferreira, L. F. V;

- Sikorski, M. *J. Phys. Chem. A* **2005**, *109* (9), 1785.
- (47) Sikorska, E.; Khmelinskii, I. V.; Prukala, W.; Williams, S. L.; Worrall, D. R.; Bourdelande, J. L.; Bednarek, A.; Koput, J.; Sikorski, M. *J. Mol. Struct.* **2004**, *689* (1–2), 121.
- (48) Sikorski, M.; Prukala, D.; Insińska-Rak, M.; Khmelinskii, I.; Worrall, D. R.; Williams, S. L.; Hernando, J.; Bourdelande, J. L.; Koput, J.; Sikorska, E. *J. Photochem. Photobiol. A Chem.* **2008**, *200* (2–3), 148.
- (49) Laurent, A. D.; Jacquemin, D. *Int. J. Quantum Chem.* **2013**, *113* (17), 2019.
- (50) Lee, N. S. *Bull. Korean Chem. Soc.* **1994**, *15* (1), 91.
- (51) Lee, N. S.; Sheng, R. S.; Morris, M. D.; Schopfer, L. M. *J. Am. Chem. Soc.* **1986**, *108* (20), 6179.
- (52) Oladepo, S. A.; Loppnow, G. R. *J. Phys. Chem. B* **2011**, *115* (19), 6149.
- (53) Mondal, S.; Puranik, M. *Phys. Chem. Chem. Phys.* **2016**.
- (54) Milán-Garcés, E. A.; Kaptan, S.; Puranik, M. *Biophys. J.* **2013**, *105* (1), 211.
- (55) Jimenez, R.; Fleming, G. R.; Kumar, P. V.; Maroncelli, M. *Nature* **1994**, *369* (6480), 471.
- (56) Barnett, R. B.; Landman, U.; Nitzan, A. *J. Chem. Phys.* **1989**, *90* (8), 4413.
- (57) Muino, P. L.; Callis, P. R. *J. Chem. Phys.* **1994**, *100* (6), 4093.
- (58) Maroncelli, M.; Fleming, G. R. *J. Chem. Phys.* **1988**, *89* (8), 5044.
- (59) Bräm, O.; Oskouei, A. A.; Tortschanoff, A.; Van Mourik, F.; Madrid, M.; Echave, J.; Cannizzo, A.; Chergui, M. *J. Phys. Chem. A* **2010**, *114* (34), 9034.
- (60) Shen, X.; Knutson, J. R. *J. Phys. Chem. B* **2001**, *105* (26), 6260.
- (61) Vajda, S.; Jimenez, R.; Rosenthal, S. J.; Fidler, V.; Fleming, G. R.; Castner, E. W. *J. Chem. Soc. Trans.* **1995**, *91* (5), 867.
- (62) Jarzba, W.; Walker, G. C.; Johnson, A. E.; Kahlow, M. A.; Barbara, P. F. *J. Phys. Chem.* **1988**, *92* (20), 7039.

7. Conclusion and Future Perspective

7.1 Conclusion

Sub-100 fs excited state structural dynamics of flavin molecules (LF, RF, FMN and FAD) including LC (alloxazine) were investigated in this thesis following photoexcitation to their absorption band centered at around 266 nm. We have used time-dependent wave packet theory to simulate the intensities of Resonance Raman bands of different flavins, Brownian oscillator model to account for the effect of ultrafast solvation dynamics, DFT and TDDFT calculations to determine the internal coordinate changes within the isoalloxazine and alloxazine rings following excitation. Total spectral breadth was partitioned into homogeneous and inhomogeneous broadenings contributing to both absorption and Raman line shapes. We found that the partitioning of internal reorganization energy among different vibrational modes is influenced by the change in the charge redistributions following photoexcitation.

We have observed that RF and FMN show similar UVRR intensity patterns following excitation within the 266 nm absorption band, whereas LF shows UVRR spectra with very different enhancement patterns within the spectral region of 1000 to 1300 cm^{-1} (see Fig. 7.1). It can be inferred to the different excited state distortions for LF in comparison to RF and FMN upon excitation to the 266 nm excited state. FAD has two absorbing chromophores at UV excitations, and thus we found both flavin and adenine Raman bands in the UVRR spectra of FAD. We have observed significant Raman hypochromism in FAD, consistent with stacking interaction between flavin and adenine rings. Although isoalloxazine and alloxazine (LC) structures are structurally very close, they show very distinct RR spectra upon UV excitations.

Upon excitation, excited state structural changes were observed along all over the isoalloxazine ring system for all of the flavins. **We found that the structural changes observed following excitation to the first singlet excited state (S_1) are different than excitation to the 266 nm excited state of flavins. Internal coordinate changes in the excited state relative to the ground state determined from best fitted Δs support the different excited state distortions for LF than that of the other flavins following photoexcitation to their 266 nm**

excited state (see Fig. 7.2). For FAD, it was found that the excited state structural changes happen in both the flavin and adenine ring coordinates. Upon excitation to the 260 nm excited state, LC shows a very different geometry change than that of flavins. Mode specific reorganization energies determined along each observed Raman modes indicate that for all of the flavins, major structural distortion occurs along the Raman band at 1583 cm^{-1} upon photoexcitation. All of the other intense Raman modes also contribute significantly to the total internal reorganization energy.

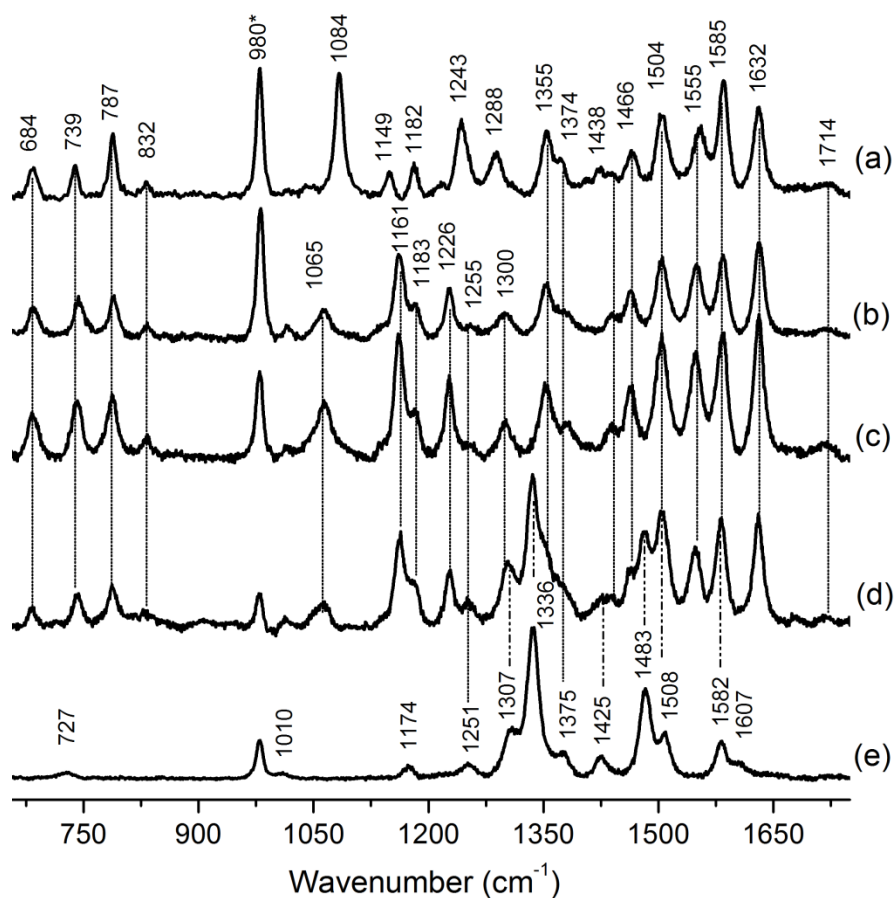


Fig. 7.1 UVRR spectra of (a) LF obtained at an excitation wavelength of 262 nm. The other spectra of (b) RF, (c) FMN, (d) FAD and (e) AMP are obtained at 263 nm excitation wavelength.

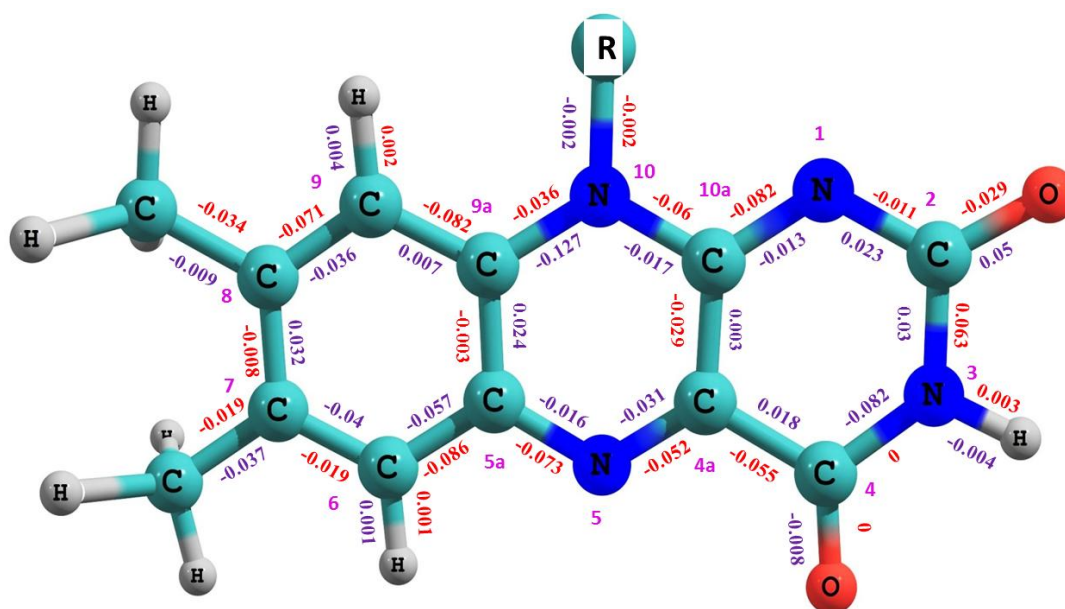


Fig. 7.2 Internal coordinate changes obtained along the isoalloxazine ring coordinates for LF (violet) and RF (red) following photoexcitation to their 266 nm excited state. R refers to the substituent at N10 position.

We found that the major contribution to the total reorganization energy comes from the inertial response of water which corresponds to the solvent reorganization energy derived from our simulation. **The solvent reorganization energy obtained for LF, RF and FMN are almost same, indicating identical coupling strength between the solute and solvent bath. A little bit higher solvent reorganization energy was obtained for FAD in comparison to the other flavins (Table 7.1) by excitation to the 266 nm excited state suggests a greater amplitude of response of solvent due to the larger dipole moment of the excited state structure of FAD. For LC, we have obtained a lower solvent reorganization energy than flavins indicates a weaker interaction between solute and solvent bath for alloxazines due to the smaller dipole moment in the $\pi\pi^*$ excited state at around 260 nm. We find upon excitation, the first solvation shell inertially responds with an ultrafast timescale of < 30 fs for all of the flavins.**

The ensemble site effect of slightly different static microsolvated structures of solute together with other processes occurring longer than 100 fs timescale contribute to the inhomogeneous broadening derived from our simulation. For all of the flavins including LC, we have determined almost similar inhomogeneous broadening values in spite of different substitutions for different flavins. RF and FMN which has ribtyl chain and also a phosphate

group (for FMN) which can form more number of microsolvated structures compared to that methyl (CH₃) substituent for LF, but the similar inhomogeneous broadening values obtained indicate that they do not affect in our simulated values. Adenine substitution in FAD also do not result in a significant change in the inhomogeneous broadening value for FAD. So, we can conclude that the dynamics of flavin molecules are more complex than that obtained from our work and further investigation is required to understand the processes responsible for the dynamics at different timescales and evaluate the precise role of water in these relaxation processes.

Table 7.1. Parameters obtained from the best fit simulation

	E_0 (cm ⁻¹)	Λ (cm ⁻¹)	τ (fs)	θ (cm ⁻¹)	M (Å)	λ_{int} (cm ⁻¹)	λ_{S} (cm ⁻¹)	λ (cm ⁻¹)
LF	37719	140	37.9	750	1.12	472	1070	1542
RF	37500	200	26.5	880	1.14	594	1110	1704
FMN	37495	200	26.5	890	1.14	550	1080	1630
FAD	37490	210	25.2	870	1.22	543	1370	1913
LC	38210	230	23.1	730	0.84	393	470	863

7.2 Future perspective

Initial excited state parameters measured in the current study proclaims to the foundation for future studies to extract the properties of excited state for flavin and flavin related compounds following UV excitations. **The limitations of our method which neglects interference from nearby electronic states, and ambiguity in the accuracy of DFT and TDDFT calculations regarding the mode compositions and sign of displacements claim more experimental and theoretical investigations.** More advanced experimental techniques such as fs stimulated resonance Raman spectroscopy (FSRS) or pump-probe experiments with sub-ps time resolution can be useful to study the short time dynamics within the UV absorption band of flavins. In combination with these experiments, the use of relevant theoretical methods would be able to produce a general methodology to study the excited states within the UV absorption regions for flavins and other biomolecules.

RR scattering of flavins are strong at UV excitations compare to the visible excitations, and also UVRR spectra are free from fluorescence. **So, our data can be useful in flavoprotein studies, although protein residues of tryptophan, tyrosine and phenylalanine can interfere in the UVRR spectra since they also absorb at UV regions. However, it has been reported that at 266 nm excitation, tryptophan scattering is weaker compared to the flavins and the contributions from tyrosine and phenylalanine are negligible. Therefore, by exciting flavins within their 266 nm absorption band, it can be used as a probe to determine the structure and dynamics of flavoproteins.**

Appendix I

A.I.1 Assignments of UVRR bands of RF

The UVRR bands of RF molecule are assigned (Table A.I.1) based on the comparisons of experimental and theoretical frequencies. Assignments of the experimental UVRR bands between 1300 to 1100 cm^{-1} in H_2O and D_2O solution were taken from Schimdt et al.^{1,2} According to the literature¹ 1256 cm^{-1} band upshifts to 1293 cm^{-1} in D_2O , but here we did not find any match of this band in D_2O spectrum. 1207 cm^{-1} band observed in D_2O spectrum was predicted due to the downshift of a band at 1277 cm^{-1} observed at 488 nm excitation. Raman bands in the lower frequency regions are assigned according to the assignment done for FMN.² Our assignments are consistent with other DFT calculations.²⁻⁶

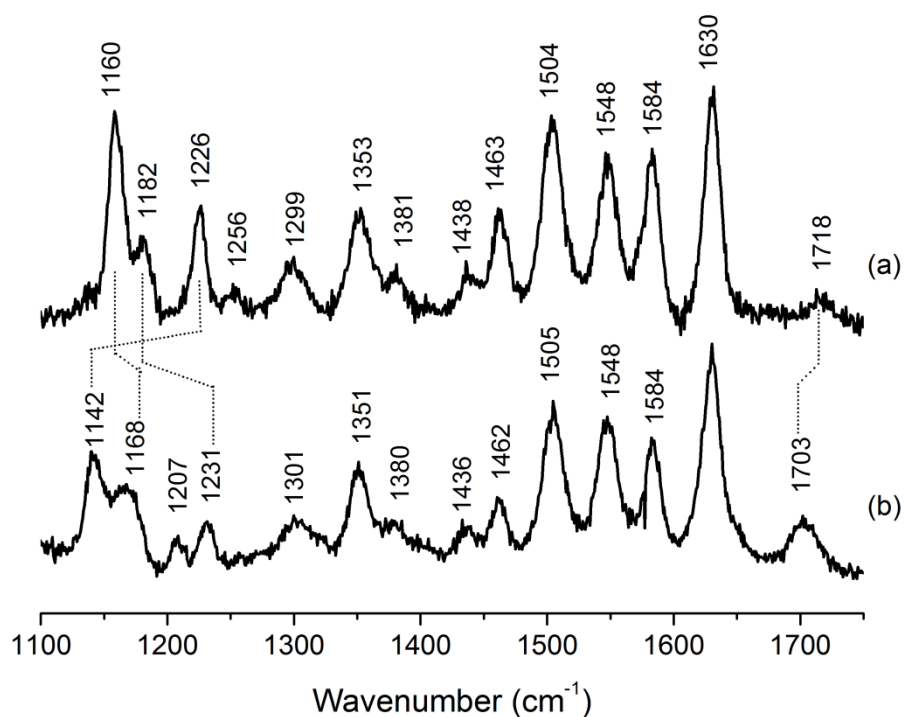


Fig.A.I. 1 UVRR spectra of 100 μM RF obtained at 260 nm excitation in H_2O (a) and in D_2O (b) prepared in pH 7 phosphate buffer solution. Dotted line indicates the shift of the bands in D_2O solution.

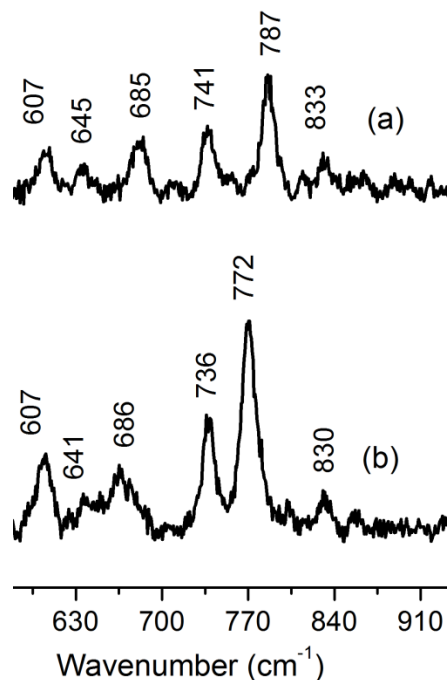


Fig.A.I.2 UVRR spectra of 100 μM RF in lower frequency region obtained at 260 nm excitation in H_2O (a) and in D_2O (b) prepared in pH 7 phosphate buffer solution.

Table A.I.1. UVRR band assignments of Riboflavin by B3LYP/TZVP level of theory using PCM as solvent model

In H_2O					In D_2O			
Exp. UVRR (cm^{-1})	Comp. ^a (cm^{-1})	Comp. freq. ^c	Published, Computed in H_2O^b (cm^{-1})	PED in H_2O^b (%) ^c	Exp. UVRR (cm^{-1})	Comp. after N3-H/D exchange ^a (cm^{-1})	Comp. shifts	PED in D_2O^b (%) ^c
1718	1736	1717	1745(-1)	str C4-O(67)	1703	1734	-2	str C4-O(63) + str C2-O(14)
-	1692	1675	1735 (-11)	str C2-O(62)	-	1678	-14	- str C4-O(17) + str C2-O(55)
1630	1663	1664	1617 (0)	str C6-C7(34) - str C8-C9(15)	1630	1663	0	str C6-C7(33) - str C8-C9(14)
1584	1597	1593	1574 (0)	- str N5-C4a(24) - str C8-C9(15) + str C9a-C5a(19)	1584	1597	0	- str N5-C4a(24) - str C8-C9(15) + str C9a-C5a(18)
1548	1555	1550	1537 (0)	- str N5-C4a(17) + str	1548	1554	-1	str N5-C4a(17) - str N10-

				N10-C10a(11)				C10a(10)
1504	1520	1517	1478 (0)	- be C6-H(13) + be C9-H(24)	1505	1520	0	- be C6-H(12) + be C9-H(23)
1463	1491	1488	1457 (0)	be H-C-H (8-CH3)(46)	1462	1491		be H-C-H (8-CH3)(49)
1438	1457			-	1436	1456	-1	-
1381	1376			- str C8-C9(18) + str N3-C4(12)	1380	1373	-3	- str C8-C9(17) + str N3-C4(12)
1353	1363	1362	1328 (-1)	str N10-C10a(10) + be H-C-H (Ribityl chain)(24)	1351	1364	+1	str N10-C10a(11) + be H-C-H (Ribityl chain)(25)
1299	1320		1304	tors Ribityl chain(16)	1301	1321	+1	- be C4a-N5-C5a(10) + be C6-H(10) + tors Ribityl chain(11)
1256	1232	1252	1266 (+3)	str N1-C2(11) + str N3-C4(15) - str N3-C2(12)	-	1269	+37	- str N3-C4(21) + str N3-C2(16) + be N3-D(15)
1226	1232*	under 1252	1195 (-10)	str N1-C2(11) + str N3-C4(15) - str N3-C2(12)	1142	1269	+37	- str N3-C4(21) + str N3-C2(16) + be N3-D(15)
1182	1192	1205	1174 (-)	str N5-C5a(15) - str N3-C4(14)	1231	1218	+26	str N5-C5a(12)
1160	1167	1166	1149(+12)	str C7-CH ₃ (11)	1168	1167	0	str C7-CH ₃ (11) + be C6-H(10)
1065	1059	1069	1056(-7)	Ribityl chain def.(23)	-	1056	-3	Ribityl chain def. (55)
833	840		837(-4)	-	830	836	-4	-
787	794		758(-22)	be N1-C10a-C4a (10)	772	775	-19	-
741	748		725(0)	str C9a-C5a(11) - be C8-C9-C9a(10) - be C5a-C6-C7(10) + be C9a-C5a-C6(15)	736	747	-1	- be C8-C9-C9a(10) - be C5a-C6-C7(10) + be C9a-C5a-C6(16)
685	682		647(-23)	be C4-O(19) + be C2-O(27) + be N5-C5a-C9a(12)	686	661	-21	be C4-O(18) + be C2-O(25) + be N5-C5a-C9a(13)
645	643		614(-1)	-	641	643	0	-
607	594		579(-4)	be Ribityl chain(10)	607	594	0	-

str: stretching, be: bending vibrations; ^aAll frequency calculations are done using B3LYP/TZVP/PCM level of theory and no scaling factor for theoretical frequencies are used; ^bPEDs (potential energy

distributions) are calculated using the software VEDA; °Optimization and frequency calculations of LF structure were done using B3LYP/6-31G(d,p) method in gas phase, parentheses are the isotope effect of N3-H/D exchange, from ref. 2; °Optimization and frequency calculation of RF structure were done by B3LYP/TZVP/PCM level of theory with addition of four explicit water molecules, from ref. 3.

References

- (1) Schmidt, J.; Coudron, P.; Thompson, A. W.; Watters, K. L.; Mcfarland, J. T. *Biochemistry* **1983**, *22* (1970), 76.
- (2) Eisenberg, A. S.; Schelvis, J. P. M. *J. Phys. Chem. A* **2008**, *112* (27), 6179.
- (3) Weigel, A.; Dobryakov, A.; Klaumünzer, B.; Sajadi, M.; Saalfrank, P.; Ernsting, N. P. *J. Phys. Chem. B* **2011**, *115*, 3656.
- (4) Wolf, M. M. N.; Schumann, C.; Gross, R.; Domratcheva, T.; Diller, R. *J. Phys. Chem. B* **2008**, *112* (42), 13424.
- (5) Wolf, M. M. N.; Zimmermann, H.; Diller, R.; Domratcheva, T. *J. Phys. Chem. B* **2011**, *115* (23), 7621.
- (6) Klaumünzer, B.; Kröner, D.; Saalfrank, P. *J. Phys. Chem. B* **2010**, *114* (33), 10826.

Appendix II

A.II.1 Assignments of UVRR bands of Lumichrome (LC)

Normal mode assignments of all the observed Raman bands using B3LYP functional in conjunction with TZVP basis set in PCM solvent model are described in Table A.II.1. Most of the UVRR bands for LC were previously observed in SERS,¹ FT-IR and FT-Raman spectra.² Normal mode compositions corresponding to UVRR bands of LC drastically changes in D₂O spectrum upon deuteration (D) at N1-H and N3-H positions. So, it is difficult to assign the LC bands by comparing the experimental H₂O and D₂O spectra, because LC bands show large shifts in D₂O solution, specially between 1450 to 1200 cm⁻¹ regions of spectrum. So, we have done the assignment based on the theoretical frequencies in H₂O and D₂O and followed the assignment done for LC in ref. 2. Raman bands below 1000 cm⁻¹ are done according to the previous RF and LF assignments.

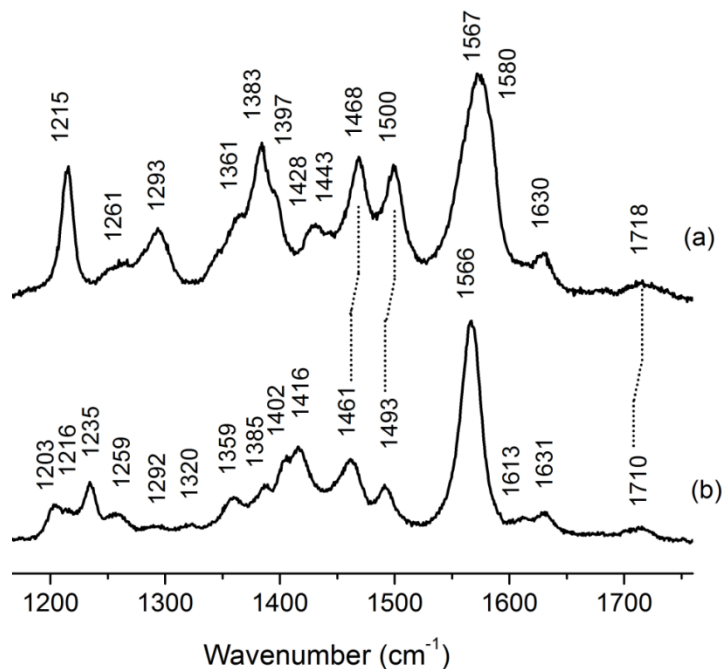


Fig.A.II.1 UVRR spectra of 350 μ M LC obtained at 259 nm excitation in H₂O (a) and in D₂O (b) prepared in pH 7 phosphate buffer solution. Dotted line indicates the shift of the bands in D₂O solution.

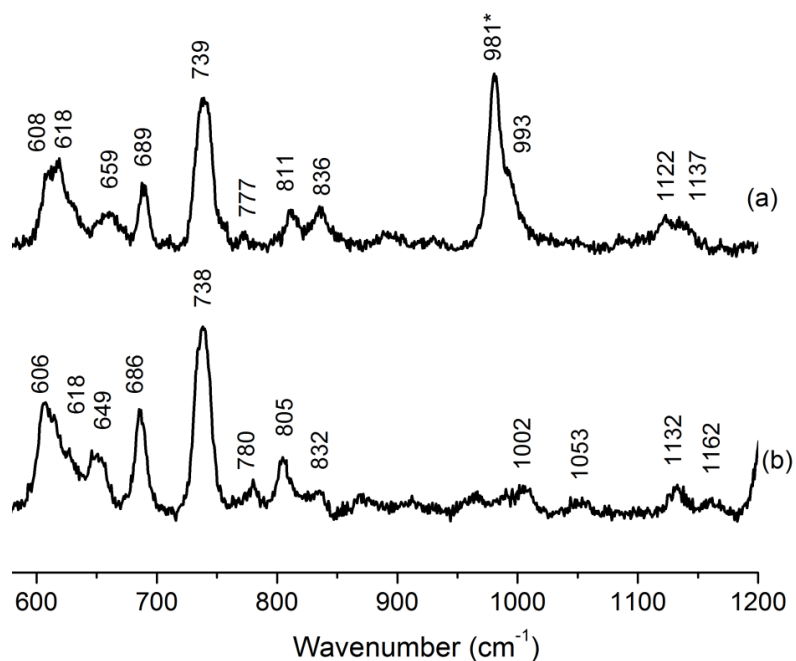


Fig.A.II.2 UVRR spectra of 350 μM LC in lower frequency region obtained at 259 nm excitation in H_2O (a) and in D_2O (b) prepared in pH 7 phosphate buffer solution. 981 cm^{-1} band is the internal standard sulfate band.

Table A.II.1 UVRR band assignments of Lumichrome (LC) by B3LYP/TZVP level of theory using PCM as solvent model

Exp. UVRR in H_2O (cm^{-1})	Comp. in H_2O (cm^{-1}) ^a	FT Raman ^c	FT-IR ^c	SERS ^d	PED (%) ^b	Exp. UVRR in D_2O (cm^{-1})	Comp. after replacing the H by D at N1 and N3 position (cm^{-1})	PED (%) ^b
1718	1756	1723	1725	no	str C2O2(42) + str C4O4(36)	1710	1753	str C2O2(35) + str C4O4(45)
no	1730	1697	1700	no	- str C2O2(29) + str C4O4(44) - be N3H(11)	no	1709	str C2O2(45) - str C4O4(39)
1630	1666	1620	1623	1629	- str C7C6(27) + str C8C9(23)	1631	1665	- str C7C6(29) + str C8C9(23)
1580	1600	1576	1578	1573	str N10C10a(21) - str C4aC10a(12)	-	1589	str N10C10a(18) + str N5C5a(10) - str C4aC10a(13) + be N5C4aC10a(10)
1567	1583	1558	1561	1548	- str N5C4a(11) - str N10C9a(11) + str C4aC10a(14)	1566	1583	str N5C4a(14) + str N10C9a(12) - str C4aC10a(11) + be N10C10aC4a(10)
1500	1523	1496	vw	1525	str N10C9a(13)	1493	1516	be (H-C-H) 8-Methyl(10)

1468	1467	1458	1461	1460	str C7C6(13) + str C4aC10a(11)	1461	1460	str C8C9(15) + str C4aC10a(15)
1443	1439	1441	1447	no	- str C2OC2(10) - str N5C4a(12) + be N1H(13) + be N3H(20)	-	-	
1428	1420	sh	1420	no	be N3H (35)	-	-	
1397	1394	1386	1384	1377	- str C8C9(14) - str N1C2(14)	-	1387	str N5C4a(11) - str C6C5a(13) + str N1C2(16)
1383	1372	1380	vw	1377	- str N10C10a(15) + str C9C9a(17)	-	1371	str C9C9a(17)
1361	1340	1356	1357	1348	str N5C4a(15) - str N1C10a(14) + be N1H (20)	1359	1404	- str N5C4a(18) + str N1C10a(17)
1293	1291	1288	vw	no	- str N5C5a(12) + str N10C9a(14) - be C8C9C9a(12)	-	1297	- str N5C5a(12) + str N10C9a(15) - be C8C9C9a(10)
1261	1267	1261	1261	no	- str N5C5a(10) - str N10C9a(11) - str N3C4(12)	-	1279/ 1258*	str N3C4(24) + be C6HC6C5a(12) - be C9H (10)/ - str N10C10a(17) + str N5C5a(16)
1215	1234	1213	1214	1212	str N10C10a(11) + str N3C4(14) - str N3C2(10)	-	1204	be N3H(12) + be C2N1C10a(15)
1137	1146	vw	1144	1155	- str C8-Methyl(20) + str C7-Methyl(17)	1132	1143	str N10C9a(11) - str C8-Methyl(23) + str C7-Methyl(19)
1122	1138				- str C4aC10a(10) + str N3C4(18)	1162	1171	str N5C5a(12) - be C6HC6C5a(14) + be N1H(13)
993	1041	vw	1006	no	- tors (H-C-H) 8-Methyl(26) - tors (H-C-H) 7-Methyl(30)	1002	1045	- tors (H-C-H) 8-Methyl(20) - tors (H-C-H) 7-Methyl(22)
993*	1019				- tors (H-C-H) 8-Methyl(28) + tors (H-C-H) 7-Methyl(22)	1002	1021	- tors (H-C-H) 8-Methyl(32) + tors (H-C-H) 7-Methyl(24)
836	842				be C9C9aN10(10) - be C2N1C10a(10)	832	813	be N1H(15)
811	801				str C7Me (12) + be N1C10aN10(14)	805	779	str C7Me (12) + be N3H(11)
739	744				be C9aN10C10a(10) - be N10C10aC4a(11) - be N5C4aC10a(11) + be C9C9aN10(10)	738	744	be C9aN10C10a(11) - be N10C10aC4a(12) - be N5C4aC10a(10) + be C9C9aN10(10)
689	687				be C9aN10C10a(14) + be C5aN5C4a(11)	686	684	be C9aN10C10a(17) + be C5aN5C4a(11)
659	655				- be O2C2N3(27) + be O4C4N3(18)	649	625	- be C4N3C2(10) - be O2C2N3(29) + be O4C4N3(17)
618	611				- be C8C9C9a(12) + be C5aN5C4a(16)	618	607	- be C8C9C9a(12) + be C5aN5C4a(14)

608	601				tors N1H (19) + out N1C4aN10C10a(35)	606	603	- tors N5C4aC10aN10(10) - tors C8C9C9aC5a(11) + out N1C4aN10C10a(37)
-----	-----	--	--	--	---	-----	-----	--

^aComputed using B3LYP/TZVP/PCM level of theory; ^busing VEDA 4.0; str: stretching, be: bending, tors: torsional vibrations; n.o.- not observed, *these bands can be assigned with both the frequencies, the dash sign (-) are given where it is difficult to assign the Raman bands; ^csee ref. 2; ^dsee ref. 1.

References

- (1) Lee, N. S.; Sheng, R. S.; Morris, M. D.; Schopfer, L. M. *J. Am. Chem. Soc.* **1986**, *108* (20), 6179.
- (2) Lee, N.-S. *Bull. Korean Chem. Soc.* 1994, Vol. 15, p 1.

Appendix III

Correction for Spectrometer Response

Procedure of intensity correction for wavelength dependent response of spectrometer and detector

- (i) Take the sample spectrum, I_λ at a particular excitation wavelength, say λ . Note down position of both ends of the spectrum in wavelength, say λ_1 and λ_2 nm.
- (ii) NIST calibrated standard D₂O lamp (Ocean Optics Inc, Dunedin, FL, USA) spectrum is recorded at whole wavelength range (255-290 nm) of the spectrometer detection by changing grating position corresponding to each experiment at the different excitation wavelength. Interpolate this spectrum from λ_1 nm to λ_2 nm, in 1024 points to obtain standard lamp response, D_λ .
- (iii) Linearly interpolate the true spectrum of the lamp (expressed as irradiance in $\mu\text{W}/\text{cm}^2/\text{nm}$ unit) from λ_1 nm to λ_2 nm, in 1024 points to obtain true lamp output, T_λ .
- (iv) Calculate the correction factor at current excitation wavelength, λ as $S_\lambda = D_\lambda/T_\lambda$
- (v) Now, correct the sample spectrum by taking into account spectrometer and detector response as,

$$I_{\text{corrected}}(\lambda) = \frac{I(\lambda)}{S(\lambda)}$$

- (vi) Repeat this method for spectra recorded at each excitation.

Appendix IV

Relations between Einstein's coefficient of absorption, transition dipole moment and experimentally measurable quantities, such as, molar extinction coefficient and absorption cross-section

A.IV.1 Einstein's coefficient and transition dipole moment

The relation between Einstein's coefficient for spontaneous absorption (B_{21}) and transition dipole moment, $\vec{\mu}_{fi}$ for a randomly oriented molecule,^[1]

$$B_{21} = \frac{\pi |\vec{\mu}_{fi}|^2}{3\eta^2 \epsilon_0 \hbar^2} \quad (\text{A. IV. i})$$

where, $\vec{\mu}_{fi} = e\vec{M}_{fi}$ is transition electric dipole moment operator. \vec{M}_{fi} is matrix element of the transition length operator = $\langle f | \vec{r} | i \rangle$. $|i\rangle$ and $|f\rangle$ are initial and final eigenstate of the absorbing molecule, \vec{r} is position operator and $|\vec{\mu}_{fi}|^2$ is the transition probability. Transition dipole moment ($\vec{\mu}_{fi}$) characterizes single photon absorption or emission by a molecule. This vector describes in which direction the charge distribution will move in a molecule with respect to that of ground electronic state (S_0) following an absorption of photon to reach a particular excited state (S_N).

A.IV.2 Absorption cross-section and extinction coefficient

In spectroscopy, strength of an absorption band can be related to experimentally measurable quantities like absorption cross-section, $\sigma(\omega)$.

$\sigma(\omega)$ can be determined from molar absorptivity, ϵ_A , of a molecule via following equation^[1],

$$\sigma(\omega) = \frac{2.303 \times 10^{19} \epsilon_A(\omega)}{N_A} \quad (\text{A. IV. ii})$$

Where, if $\epsilon_A(\omega)$, molar extinction coefficient is expressed in $\text{L mol}^{-1} \text{cm}^{-1}$ and N_A is Avogadro number = 6.023×10^{23} , unit of $\sigma(\omega)$ would be $\text{\AA}^2/\text{molecule}$. Extinction coefficient can easily be determined by fitting measured absorbance of a molecule with their concentrations according to Beer-Lambert's law.

A.IV.3 Transition dipole length or dipole strength

Transition dipole moment can be related to measurable integrated $\sigma(\omega)$ using following equation^[1],

$$|\vec{\mu}_{fi}|^2 = \frac{3\hbar c \eta \epsilon_0}{\pi \omega_{fi}} \int \sigma(\omega) d\omega \quad (\text{A. IV. iii})$$

Where, $\int \sigma(\omega) d\omega$ = area under the gaussian fitted absorption spectrum in \AA^2 molecule⁻¹ cm⁻¹.

\hbar = reduced Planck constant = 1.054×10^{-34} J.s

η = refractive index of water = 1.33

ϵ_0 = permittivity of vacuum = 8.85×10^{-12} F.m⁻¹

c = speed of light = 2.99×10^8 m.s⁻¹

ω_{fi} = transition frequency or peak of the absorption band in cm⁻¹

$\vec{\mu}_{fi} = e\vec{M}_{fi}$, where e = charge of electron = 1.60×10^{-19} C and $\vec{M}_{fi} = \langle i|\vec{r}|f \rangle$ is electric dipole moment operator and $\vec{r} = \{rx, ry, rz\}$, position operator.

Magnitude of \vec{M}_{fi} , $|\vec{M}_{fi}|^2 = D_{fi}$ is transition dipole length expressed in \AA .

The transition probability is proportional to the square of the length of the vector. The transition moment vector can be resolved in three cartesian coordinates,

$$\vec{M}_{fi}^2 = M_{fi}^2(x) + M_{fi}^2(y) + M_{fi}^2(z)$$

where $M_{fi}(x) = \langle i|\mu_x|f \rangle$, μ_x being the x component of dipole moment vector.

A.IV.4 Oscillator strength

Another quantity to express the strength of photon absorption by a molecule in state $|i\rangle$ to reach state $|f\rangle$ is oscillator strength, f_{fi} . In classical theory it is the probability of an electronic transition induced by interaction of electrons in a molecule with

incident electromagnetic radiation. Oscillator strength is the popular choice to express strength of absorption line in computational chemistry. Classically f_{fi} means, ratio of the intensity of the measured transition (absorption or emission) by a molecule to the intensity of a ‘harmonically oscillating’ electron in a three-dimensional harmonic potential well. Such an electron is considered a perfect harmonic oscillator or an oscillating dipole with $f_{fi} = 1$.

This dimensionless quantity is defined in terms of dipole strength (or induced transition dipole moment) of a transition^[1] as,

$$f_{fi} = \frac{2m_e\omega_{fi}}{3\hbar e^2} |\vec{\mu}_{fi}|^2 \quad (\text{A. IV. iv})$$

where $\vec{\mu}_{fi}$ is transition electric dipole moment, ω_{fi} is the transition frequency. Derivation of this relation is well documented in many text books^[3]. Substituting equation A.II.iii in A.II.iv and converting unit of ω from Hz to wavenumber, f_{fi} becomes

$$f_{fi} = 1.13 \times 10^{12} \eta \int \sigma(\tilde{\nu}) d\tilde{\nu} \quad (\text{A. IV. v})$$

where $\tilde{\nu}$ is wavenumber in cm^{-1} and $\sigma(\tilde{\nu})$ is in $\text{cm}^2/\text{molecule}$ instead of $\text{\AA}^2/\text{molecule}$ ($1 \text{\AA}^2 = 10^{-16} \text{cm}^2$)

